Reduced Dimensionality Quantum Dynamics of Chemical Reactions

Sarah M. Remmert

Magdalen College, University of Oxford

A thesis submitted for the degree of

Doctor of Philosophy

Hilary Term, 2011

To my parents, who have always taught me the value of education.

Reduced Dimensionality Quantum Dynamics of Chemical Reactions

Sarah M. Remmert, Magdalen College

A thesis submitted in partial fulfillment of the requirements for the degree of Doctor of Philosophy of the University of Oxford

Hilary Term, 2011

Abstract

In this thesis a reduced dimensionality quantum scattering model is applied to the study of polyatomic reactions of type $X + CH_4 \rightleftharpoons XH + CH_3$.

Two dimensional quantum scattering of the symmetric hydrogen exchange reaction CH_3+$CH_4 \rightleftharpoons CH_4$+$CH_3$ is performed on an 18-parameter double-Morse analytical function derived from *ab initio* calculations at the CCSD(T)/cc-pVTZ//MP2/cc-pVTZ level of theory. Spectator mode motion is approximately treated via inclusion of curvilinear or rectilinear projected zero-point energies in the potential surface. The close-coupled equations are solved using R-matrix propagation. The state-to-state probabilities and integral and differential cross sections show the reaction to be primarily vibrationally adiabatic and backwards scattered. Quantum properties such as heavy-light-heavy oscillating reactivity and resonance features significantly influence the reaction dynamics. Deuterium substitution at the primary site is the dominant kinetic isotope effect. Thermal rate constants are in excellent agreement with experiment.

The method is also applied to the study of electronically nonadiabatic transitions in the $CH_3 + HCl \rightleftharpoons CH_4 + Cl(^2P_J)$ reaction. Electrovibrational basis sets are used to construct the close-coupled equations, which are solved via R-matrix propagation using a system of three potential energy surfaces coupled by spin-orbit interaction. Ground and excited electronic surfaces are developed using a 29-parameter double-Morse function with *ab initio* data at the CCSD(T)/cc-pV(Q+d)Z-dk//MP2/cc-pV(T+d)Z-dk level of theory, and with basis set extrapolated data, both corrected via curvilinear projected spectator zero-point energies. Coupling surfaces are developed by fitting MCSCF/cc-pV(T+d)Z-dk *ab initio* spin-orbit constants to 8-parameter functions. Scattering calculations are performed for the ground adiabatic and coupled surface models, and reaction probabilities, thermal rate constants and integral and differential cross sections are presented. Thermal rate constants on the basis set extrapolated surface are in excellent agreement with experiment. Characterisation of electronically nonadiabatic nonreactive and reactive transitions indicate the close correlation between vibrational excitation and nonadiabatic transition. A model for comparing the nonadiabatic cross section branching ratio to experiment is discussed.

Acknowledgements

First and foremost, I would like to thank my supervisor Professor David Clary, for his guidance and support over the past three and a half years. Many members of the Clary group have also contributed to this work, and I am particularly grateful for the scientific guidance, patience and support of Dr. Simon Banks. I would also like to thank Kristjan Alexandersson, Dr. Ivan Ljubic, and especially Dr. Frank von Horsten for many useful scientific discussions.

Professor Mark Child has generously provided scientific advice during the completion of this work. Collaboration with Professor Jeremy Harvey and Professor Andrew Orr-Ewing has been instrumental in the work on nonadiabatic reaction dynamics, and I am very grateful for their detailed and thoughtful input over the past several years.

Above all, I would like to thank my parents and my sister for their love and support. This would not have been possible without you.

Contents

Chapter 1

Introduction

The field of molecular reaction dynamics is the study of fundamental processes contributing to chemical reactivity [1, 2]. The main goal of this field is to gain a detailed understanding of reaction processes on the molecular level, by accurately characterising the probability of different reaction pathways, the transfer of internal and kinetic energy, the geometry of molecular collisions and the angular distribution of product species. Understanding these characteristics can lead to optimal control of chemical reactions and can also be used to develop a macroscopic description of chemical kinetics by statistical averaging. A variety of theoretical approaches to molecular reaction dynamics have been developed to solve these complex problems.

Quantum scattering theory allows for an accurate understanding of state-to-state dynamics of gas phase reactive collisions, and plays a significant role in aiding and interpreting increasingly sophisticated gas phase kinetics and dynamics experiments [3,4]. Atomic motion during a collision process is most accurately described by solving the nuclear Schrödinger equation [1, 2]. Within the Born-Oppenheimer approximation, separating nuclear and electronic motion, this is equivalent to solving for nuclear dynamics on the potential energy surface for a given electronic

state. Both time-independent (TI) and time-dependent (TD) methods have been developed that involve constructing the quantum Hamiltonian operator in an appropriate set of internal coordinates and solving for the scattering (S) matrix, from which all state-to-state properties can be determined. There are advantages to both methods and the selection of which to use depends upon the system and property of interest. Standard TI methods generally solve for the entire S-matrix for a given collision energy. TD methods generally compute one column of a given S-matrix for specific initial reaction conditions, over a range of collision energies. The TD method allows for a more intuitive understanding of the collision process and scales well with molecular size, but can become inefficient for low energy collisions. The stationary state TI approach avoids this inefficiency, but quickly becomes expensive with an increase in system size, requiring the solution of a large number of coupled differential equations [1].

Full dimensional quantum scattering calculations are computationally expensive and are therefore limited to small reaction systems with relatively low values of total angular momentum [4]. Molecular collision problems can instead be approached by solving the classical equations of motion [1]. In one approach, the quasi-classical trajectory (QCT) method, initial reactant conditions are specified and the average of many possible reaction pathways is used to understand the dynamics. This approach is efficient but the neglect of quantum effects such as zero-point energy and tunneling can be problematic, especially in systems involving the transfer of a light atom between two heavy groups [5]. A variety of accurate semi-classical methods have been developed that incorporate zero-point energy and quantum tunneling effects in molecular dynamics simulations. For example, ring-polymer molecular dynamics (RPMD) approaches have been shown to accurately predict thermal rate constants for bimolecular gas phase reactions, even in the

low-temperature tunneling regime; one advantage of this method is the controlled approach to the quantum limit [6].

Developing approximate methods to investigate the TD and TI quantum dynamics of larger systems is an active area of ongoing research [1]. One approach to approximate TD quantum scattering is the multi-configurational time dependent hartree (MCTDH) method, which can be used to treat much larger systems and becomes exact in the limit of a large basis and many configurations. This method has been shown to be highly accurate for predicting thermal rate constants [7]. Another approach, for both TI and TD scattering problems, is to identify a subset of degrees of freedom important in the reaction process, such as the stretching vibrations of forming and breaking bonds. A hierarchy of reduced dimensionality (RD) approximations to quantum scattering theory decrease computational cost by simplifying the description of total angular momentum and prioritizing key internal degrees of freedom, treating the remaining spectator modes in an approximate manner [4, 8].

Classical, semi-classical, and quantum methods for describing nuclear motion during a reaction process all rely on an accurate description of the forces acting on the system, governed by the potential energy surface for each electronic state. Some direct dynamics techniques make use of electronic structure packages to generate potential energy values for each step in trajectory calculations as they are required. This approach can become prohibitively expensive for highly accurate electronic structure methods, and therefore analytical functions are often developed prior to dynamics calculations by fitting functions to *ab initio* data. Development of a $3N-6$ dimensional potential energy surface can be difficult for large polyatomic systems. One approach to overcoming this bottleneck involves developing analytical functions to describe reduced dimensionality potentials for

use in RD time-independent quantum scattering. This method has been shown to be a very efficient approximation for describing the dynamics and kinetics of molecular gas-phase collisions [9–16].

The current study focuses on using this RD time-independent scattering method to characterise polyatomic hydrogen abstraction reactions of type

$$\mathbf{X + HCH_3 \longrightarrow XH + CH_3}, \tag{1.1}$$

where X is taken to be (a) CH_3 or (b) $Cl\,(^2P)$. Both systems are heavy-light-heavy (HLH) in nature and are known to have significant quantum effects; full quantum treatment is highly computationally expensive due to the size of the species involved. In the case of reaction (a), this thesis focuses on extending an RD quantum method that has been previously applied to atom + molecule reactions to the treatment of a molecule + molecule system. In the case of reaction (b) the method is further developed and applied to the investigation of multi-surface reactions and nonadiabatic transitions resulting from spin-orbit coupling.

This thesis is organised as follows. An overview of reduced dimensionality quantum scattering theory is presented in Chapter 2. The hyperspherical coordinate system is defined and single and multiple electronic state problems are discussed with respect to the construction and solution of the close-coupled equations via inelastic R-matrix propagation theory. The application of approximate boundary conditions to extract the scattering S-matrix and assignment of asymptotic states is presented.

Chapter 3 outlines potential energy surface development via partial geometry optimisations, frequency, and single point energy *ab initio* calculations. The approximate treatment of spectator mode vibrations is discussed with respect to the application of rectilinear and curvilinear frequency projection methods. The de-

velopment of an analytical function describing the reaction, as well as a fitting procedure to determine the parameters of the equations, is presented. A detailed summary of the *ab initio* calculations and a physical interpretation of spin-orbit coupling constants is given.

Analysis of the results of the scattering calculation requires additional computation to convert S-matrix elements into important physical quantities comparable to experimental results. Chapter 4 describes the calculation of thermal rate constants, integral cross sections, branching ratios and differential cross sections. J- and energy shifting methods are presented as further simplifications to RD scattering theory. The analysis of resonances in the reaction probability is discussed with respect to time-delay theory.

Chapter 5 describes the analysis of the $CH_3 + CH_4$ reaction system, and its symmetric deuterated variants $CD_3 + CD_4$ and $CH_3 + DCH_3$. The stationary points, potential energy surface, and scattering parameters are all given. Thermal rate constant results show a close correlation to experiment indicating the validity of using this RD theory to study molecule + molecule reaction systems. Kinetic isotope effects (KIE), integral and differential cross sections are discussed. The curvilinear projection method is evaluated relative to the rectilinear approach and found to be more accurate for this reaction.

The final chapter outlines the multi-surface calculations for the $Cl(^2P_J) + CH_4 \rightleftarrows HCl + CH_3$ reaction. The model of coupled potential energy surfaces (PES) is presented in detail, along with background literature regarding the importance of the reaction system and the results of past experimental and theoretical studies characterising nonadiabatic transitions in this and other systems. Basis set tests, intrinsic reaction coordinate (IRC) calculations, stationary point properties, and an evaluation of the frequency projection methods are presented. Thermal rate

constants for a basis set extrapolated (BSE) surface are reported and are in excellent agreement with experiment. The scattering results of ground and multi-surface calculations are presented, and a model for comparing the nonadiabatic branching ratio with experiment is developed. The correlation between vibrational energy transfer and nonadiabatic transition is discussed.

1.1 Publications

The following publications have resulted from the work discussed in this thesis:

- Banks, S. T.; Tautermann, C. S.; Remmert, S. M.; Clary, D. C. An improved treatment of spectator mode vibrations in reduced dimensional quantum dynamics: Application to the hydrogen abstraction reactions μ+CH_4, H +CH_4, D +CH_4, and CH_3+CH_4. *Journal of Chemical Physics*, **2009**, *131*, 044111.

- Remmert, S. M.; Banks, S. T.; Clary D. C. Reduced Dimensionality Quantum Dynamics of $CH_3 + CH_4 \longrightarrow CH_4 + CH_3$: Symmetric Hydrogen Exchange on an *Ab Initio* Potential. *Journal of Physical Chemistry A*, **2009**, *113*, 4255.

The following paper is in preparation for publication:

- Remmert, S. M.; Banks, S. T.; Harvey, J. M.; Orr-Ewing, A.J.; Clary, D. C. Reduced dimensionality spin-orbit dynamics of $HCl + CH_3 \rightleftarrows CH_4 + Cl(^2P_J)$ on *ab initio* surfaces. *Journal of Chemical Physics*, **2011**, *134*, 204311.

Chapter 2

Reduced Dimensionality Quantum Scattering Theory

2.1 Introduction

2.1.1 A history of reduced dimensionality theory

Exact solutions for the quantum scattering of triatomic collision processes are reasonably straightforward to compute. This is generally achieved via the so-called coupled channel (CC) approach [17], where the exact solution for the three-dimensional problem may be obtained by expanding the total wavefunction in an appropriate basis set, propagating the resulting close-coupled equations, and applying asymptotic boundary conditions to obtain the scattering S-matrix, from which all other properties can be derived. The size of the problem – and thus the ease of its solution – depends upon the number of close-coupled second order differential equations necessary to describe the energetically accessible states [18]. In the case of exact treatment of a three dimensional collision process, the number of coupled equations to propagate becomes large when all energetically accessible

vibrational-rotational channels must be considered. This is especially true when all (including degenerate) projection rotational states are treated in the description.

Because of computational limitations concerning the size of the scattering problem, approximations suitable to larger collision processes were first developed and tested on triatomic reactions of type A + BC $\longrightarrow$ AB + C. There is therefore a hierarchy of approximations to improve the computational efficiency the CC approach [17, 18]. The first method assumes that the different projection quantum states can be decoupled in the calculation; this is known as the coupled states approximation (CS) [19], and vastly reduces the computational effort required. An additional family of methods build upon the foundation of the CS approach and involve approximations to the treatment of the overall rotation and bending motions of the triatomic reaction species. These approaches are termed reduced dimensionality exact quantum (RDEQ) methods.

One RDEQ approximation assumes that the reaction only progresses along a collinear pathway, and is named the rotating linear model (RLM) [20–23]. In the RLM model, the internal bending of the A−B−C angle (which asymptotically correlates to the rotation of the diatomic reactant or product, depending on the arrangement channel) is treated adiabatically. That is, the doubly degenerate bending vibrational motion is assumed to be slow in relation to the other internal degrees of freedom, and neglected in the scattering calculations. There are therefore only two vibrational degrees of freedom remaining to be treated. Furthermore, assuming that the total molecular rotation can be approximated as a linear rigid rotor affords an analytical expression for the total angular momentum operator in the scattering Hamiltonian. Partial wave expansion of the scattering Hamiltonian thus yields a series of easily solvable, two-dimensional collinear scattering calculations – one for each value of the total angular momentum, J. The partial wave

Hamiltonian (in atomic units) is given in hyperspherical coordinates (defined in section 2.2) as

$$\mathrm{H} = -\frac{1}{2\mu}\frac{\partial^2}{\partial\rho^2} - \frac{1}{2\mu\rho^2}\frac{\partial^2}{\partial\delta^2} + \frac{3}{8\mu\rho^2} + \frac{J(J+1)}{2\mu\rho^2} + V(\rho,\delta), \tag{2.1}$$

where the $\frac{J(J+1)}{2\mu\rho^2}$ term is the centrifugal potential ($J = 0, 1, 2...$), and $V(\rho,\delta) = V_{\mathrm{coll}}(\rho,\delta)$ is the potential energy surface neglecting any effects of the bending modes, i.e. for collinear geometries. Note that this Hamiltonian has been weighted by a factor of $\rho^{-3/2}$ for ease of solution, which is discussed in detail in Appendix A.2. The surface is two-dimensional and reflects the motion of the two internal degrees of freedom explicitly accounted for in the scattering calculations. The close-coupled equations must therefore only be solved in two dimensions – one scattering coordinate and one internal vibration. The system is thus represented by

$$\mathrm{A} \;+\; \mathrm{BC}(m) \;\longrightarrow\; \mathrm{AB}(n) \;+\; \mathrm{C}, \tag{2.2}$$

where m and n are the initial and final internal vibrations of the diatomic species BC and AB, respectively [23]. It is easy to ascertain that the RLM approach yields a significant reduction in computational effort. In this approach, only two degrees of freedom are coupled, and the number of close-coupled equations reflects only the number of energetically accessible vibrational states m and n at a particular collision energy [18]. This is in stark contrast to the number of equations that would be required for all vibrational-rotational states including all possible projection quantum numbers.

Though computationally efficient, the RLM model is generally insufficient in predicting dynamical properties due to its complete neglect of the internal bending degrees of freedom – most notably, this approximation underestimates the

threshold to reaction [24]. A useful improvement upon this model is the bending corrected rotating linear model (BCRLM), which also assumes adiabatic separability of the bending motions, but accounts approximately for their effects via addition of a zero-point energy (ZPE) potential energy surface to the scattering Hamiltonian. This ZPE potential energy consists of the bending zero-point energies evaluated as a function of geometry within the collinear constraint [23]. Ideally, this approximation should result in a family of BCRLM calculations for each excitation value of the bending vibrational energy, however, in practice only the ground state ZPE is generally used. It should be noted that an obvious drawback of using the RLM or BCRLM approaches involves the requirement of collinearity, a requirement that many reactive systems do not fulfil [24, 25]. It should also be noted that the RLM/BCRLM methods are similar in spirit to the collinear exact quantum (CEQ), and collinear exact quantum with bending corrections (CEQB) methods [26,27]; however, they differ slightly in terms of the treatment of the total angular momentum. The CEQB method is generally associated with the use of energy shifting methods to describe reaction probabilities for $J > 0$, whereas the cetrifugal barrier is explicitly included in the Hamiltonian in the BCRLM approach (equation (2.1)) [24].

In the BCRLM Hamiltonian, the collinear potential is replaced by a total, effective potential defined by the addition of the collinear potential energy surface and the ground-state ZPE of the bending internal vibrations, $V^{\mathrm{ZPE}}_{\mathrm{bending}}(\rho, \delta)$:

$$\mathrm{V}(\rho, \delta) = \left[V_{\mathrm{coll}}(\rho, \delta) + V^{\mathrm{ZPE}}_{\mathrm{bending}}(\rho, \delta)\right]. \tag{2.3}$$

The extension of these RDEQ concepts to four-atom and polyatomic collision processes has resulted in a series of additional approximations where varying numbers of degrees of freedom are treated in the exact quantum scattering calculations (*act-*

ive modes) and the remainder approximated via inclusion of ground-state ZPEs in the effective potential (*spectator modes*) [28]. In the current study, a method is applied that extends the two-dimensional BCRLM approach to polyatomic reaction systems $X + HCH_3$ [11]. A collinear RLM is assumed for the close-coupling equations and treatment of the total angular momentum, and only two degrees of freedom are treated in the quantum calculations. An adiabatic approximation is therefore made with respect to the motion of all the spectator modes, in addition to the bending modes specified in the BCRLM approach. Therefore in the current method, the *bending correction* incorporates not only the ground state ZPE of the bending vibrations, but the geometry-dependent ZPE of all the spectator vibrational modes not explicitly included in the scattering calculation. For a polyatomic system of N atoms, the ground-state ZPE of the $3N - 8$ spectator vibrational modes are included in the effective potential. Thus, the potential is given according to

$$\mathrm{V}(\rho, \delta) = \left[V_{\mathrm{coll}}(\rho, \delta) + V^{\mathrm{ZPE}}_{\mathrm{spectator}}(\rho, \delta)\right]. \tag{2.4}$$

Early implementation of RD methods used analytical potential energy surfaces and did not exploit the efficiency of an *ab initio* driven approach [29]. The collinear PES and the spectator ZPE PES can be generated efficiently via *ab initio* calculations, and the combination of *ab initio* data points with an analytical, physically relevant potential function provides an effective approach to polyatomic reduced dimensionality dynamics [12]. The following sections outline this method.

2.1.2 Current study: $\mathbf{X + HCH_3}$

$X + CH_4$ reactions contain $3N - 6$ internal vibrational degrees of freedom (DOF), where N is the number of atoms in each system. For reaction (a) (X=CH_3), this

is 21 DOF; for reaction (b) (X=Cl), this pertains to 12 DOF. Both systems are large for exact quantum treatment, and therefore only two degrees of freedom are considered explicitly in the CC calculations. The reduction of a generic system to a triatomic collision process appropriate for use of the BCRLM Hamiltonian is shown in Figure 2.1. Molecular units CH_3 and, in the case of reaction (a), X, are considered to be pseudo-atoms, thus reducing the reaction system to the familiar A + BC form. The two DOF explicitly considered then pertain to the reaction coordinate and one internal vibration. In the reactant channel, the internal mode is the B–C vibration (or the H–C in the full dimensional picture), whereas in the product channel, the internal mode is the A–B (or X–H) vibration.

Though Figure 2.1 reduces the system to the triatomic form assumed by the scattering Hamiltonian kinetic energy operator (KEO), the effective potential used for the reaction system accounts for the ZPE of all $3N - 8$ spectator modes, not just the bending vibrations as for the A–B–C case. This amounts to 19 spectator modes for reaction (a), and 10 spectator modes for reaction system (b).

For single-surface application of the extended-BCRLM approach, the Hamiltonian is as given in equation (2.1) with the effective potential as described in equation (2.4). The potential surface is thus a two-dimensional PES in hyperspherical coordinates ρ and δ, with the inclusion of geometry dependent zero-point energy corrections. $V(\rho, \delta)$ thus has a single value for the effective (corrected) potential energy at each value of the hyperspherical coordinates.

Multi-surface studies are a simple extension of these ideas. The principles regarding reduction in the number vibrational DOF continue to apply, and therefore the same KEO described in equation (2.1) is used. The difference is that for each geometry (ρ, δ), there exist multiple two-dimensional effective potential energy surfaces corresponding to different electronic states. There are also geometry

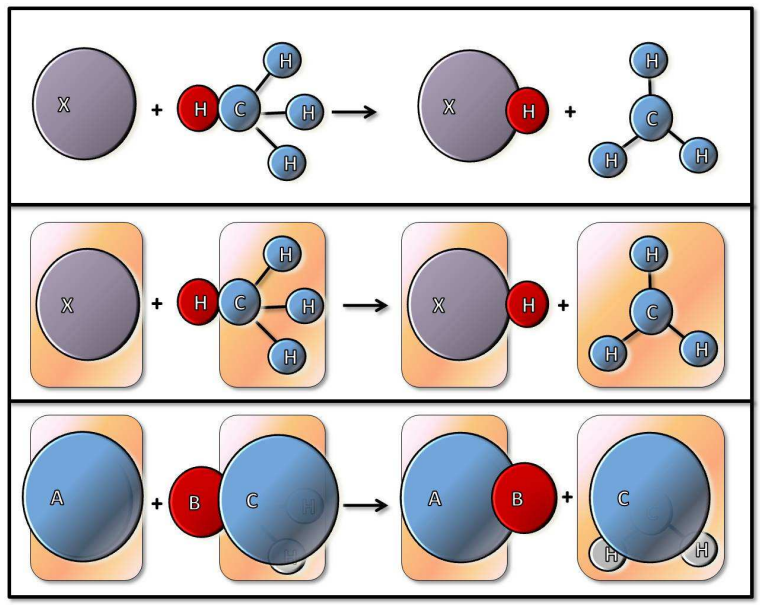

Figure 2.1: Reduced dimensionality psuedo-atom approach to the study of $X+CH_4$ reactions.

dependent potentials that describe the coupling between electronic states.

This results in a potential $\mathbf{V}(\rho, \delta)$ that is a matrix rather than a single-valued function. Thus, at a given geometry (ρ, δ), the potential in equation (2.1) is given according to

$$\mathbf{V}(\rho,\delta) = \begin{pmatrix} V_{11} & V_{12} & \cdots & V_{1n} \\ V_{21} & V_{22} & \cdots & V_{2n} \\ \vdots & \vdots & \ddots & \vdots \\ V_{n1} & V_{n2} & \cdots & V_{nn} \end{pmatrix}, \tag{2.5}$$

where the V_{nn} terms correspond to the values of each 2D PES for electronic state n, and where the cross terms $V_{n,m\neq n}$ correspond to coupling between electronic states n and m.

Considering the 2D Hamiltonian $\mathrm{H} = \mathrm{T} + V(\rho, \delta)$, the KEO then takes the form of a diagonal matrix and the problem is thus expressed in terms of *vibronic* channels. The increased dimensionality of a multi-surface problem makes the two-

dimensional (vibrational) approach even more essential for polyatomic systems.

2.1.3 Nonadiabatic reaction dynamics

The multi-surface approach to characterising nonadiabatic transitions of polyatomic reactions is an important theoretical development. Highly accurate, full dimensional, multi-surface studies have been performed for many $X + H_2$ (X=Cl, Br, F) reaction systems [30–45], however, computational limitations have restricted the study of larger polyatomic collisions. Incorporating the effects of multiple electronic states for atom + molecule reactions, such as $O(^3P) + CH_3 \longrightarrow CH_3O$, has required reduced dimensionality approximations in combination with simplifications concerning surface couplings, in order to achieve computational feasibility [46]. Several approaches may be taken to studying nonadiabatic reaction processes, including time-dependent and time-independent quantum scattering, surface hopping, and semi-classical approaches, as summarised in reference [47]. The current study, however, utilises the 2D, BCRLM approach within a multi-surface framework.

Adiabatic and nonadiabatic transitions.

Throughout this thesis, the terms adiabatic and nonadiabatic are used extensively, and in several different contexts. For clarity, the different uses are summarised briefly.

In defining an *adiabatic approximation*, it is useful to first describe the most famous example: the Born-Oppenheimer (BO) approximation [47]. The total system Hamiltonian is defined as the sum of the nuclear kinetic energy operator, T,

and the electronic Hamiltonian H_e[1]:

$$H(\mathbf{R}, \mathbf{r}) = T(\mathbf{R}) + H_e(\mathbf{R}, \mathbf{r}). \tag{2.6}$$

In the BO formalism, the motion of the nuclei and electrons can be decoupled because of the large mass difference between slow nuclei and fast electrons; nuclear positions can be treated as constant with respect to the motion of the electrons. The Schrödinger equation can then be solved for the electronic coordinates with parametric dependence on nuclear coordinates $\mathbf{R}$. Therefore, it is possible to define a potential energy surface,$V(\mathbf{R})$, which represents the energy of a particular electronic state as a function of the nuclear geometry. The BO approximation breaks down when, at a specific nuclear configuration, multiple PESs closely approach one another; in this case, only a small amount of energy (derived from nuclear motion) is required to transfer from one surface to the other. This is a so-called *electronically nonadiabatic transition*. In the context of quantum scattering calculations, an *electronically adiabatic transition* occurs when the electronic state is conserved, but may involve changes in vibrational excitation.

Another example of an adiabatic approximation may be found in the treatment of spectator mode vibrations. The motion of the two active, stretching vibrations is assumed to be slow relative to the $3N - 8$ spectator vibrations. Therefore, the ZPE of the spectator mode is assumed to be constant relative to the vibration of the active modes. In the current study, only the ground state ZPE is considered, though it would be feasible to define separate scattering problems for discrete excited state spectator vibrations – one for each degree of excitation, analogous to the electronic PESs defined in the BO approximation.

Finally, as discussed in section 2.3.3, an adiabatic approximation can be made

[1] $\mathbf{R}$ and $\mathbf{r}$ refer to the nuclear and electronic coordinates, respectively.

in the treatment of hyperspherical coordinates ρ and δ (defined in section 2.2). Motion in δ can be assumed to be fast relative to corresponding motion in scattering coordinate ρ, and therefore the one dimensional Schrödinger equation can be solved for the terms dependent upon δ, with parametric ρ dependence. This leads to one dimensional potential surfaces $\varepsilon_s(\rho)$, termed *hyperspherical adiabats*. In the context of scattering calculations based on vibrational coordinates, a *vibrationally adiabatic transition* does not involve a transfer between hyperspherical adiabats of different quantum numbers s, whereas a *vibrationally nonadiabatic transition* does. For the remainder of this work, adiabatic or nonadiabatic transitions refer to electronic transitions unless otherwise specified as referring to vibrational motion.

Adiabatic and diabatic representations.

Furthermore, it is possible to define *adiabatic* and *diabatic* representations in approaching the solution of multi-surface time-independent quantum scattering. These representations differ according to the choice of the electronic basis set [47]. Judicious choice of representation can allow for neglect of different terms in the total Hamiltonian (equation (2.6)), thereby simplifying the solution of the scattering problem [48]. The most chemically intuitive, straightforward choice for the electronic basis set is eigenfunctions of the electronic matrix H_e (essentially, the BO approximation). In this *adiabatic representation*, the potential matrix (including surface couplings) is diagonal [48], and the diagonal terms are the adiabatic potential energy surfaces readily available from *ab initio* calculations. Surfaces interact through conical intersections and sometimes complicated series of avoided crossings. In this formalism, the nonadiabatic coupling between surfaces is described in the KEO. The complexity of the nonadiabatic coupling terms, especially in the vicinity of an avoided crossing or conical intersection, is often considered a disadvantage of this representation [47].

The *diabatic representation* involves choosing electronic basis functions such that the nonadiabatic coupling terms in the KEO are sufficiently small in comparison with the coupling in the electronic Hamiltonian that they can be neglected in scattering calculations [48]. The advantage of neglecting these terms is offset by the difficulty in obtaining diabatic surfaces, which are not available from *ab initio* calculations and must be generated by a unitary transformation (rotation) of the adiabatic potential matrix[2] [47]. As the diabatic basis functions are not eigenfunctions of H_e, the diabatic potential matrix is no longer diagonal. Diabatic potentials (which vary smoothly and allow for curve crossing [47]) fall along the diagonal of the potential matrix, with electronic surface coupling terms as off-diagonal matrix elements. Diagonalisation of the diabatic potential energy matrix at each geometry yields the adiabatic potential energy surfaces.

In reaction systems where spin-orbit coupling dominates the electronic surface coupling terms[3], an *approximate diabatic representation* may be used [48]. This approach combines the advantageous use of *ab initio* surfaces (adiabatic representation) with the more simple form of the KEO used in the diabatic formalism. The assumption is made that the internal Hamiltonian can be divided into electronic and spin-orbit components ($H_e = H_{elec} + H_{SO}$). This results in a potential matrix where the diagonal terms (from H_{elec}) are the spin-free electronic energies generated from *ab initio* calculations, and the off-diagonal terms (from H_{SO}) are the spin-orbit coupling terms (which can also be generated from *ab initio* calculations). In the current study, it is this approximate diabatic representation that is implemented, although it is hereafter simply referred to as the diabatic representation.

[2]The transformation is not unique, and thus there is some ambiguity in the choice of diabatic representation.

[3]A complete summary of the surface coupling terms necessary for accurate multi-surface molecular scattering calculations is presented in reference [49]; exact treatment would involve consideration of all nuclear and electronic angular momenta couplings, such as spin-orbit, electronic, rotational, and Coriolis couplings.

2.2 Coordinate system

Solving a scattering problem in the 2D BCRLM approximation depends upon an appropriate definition for the coordinate system. In this work, hyperspherical coordinates are used to describe the motion of the X + CH_4 reactions. Though summarised in detail elsewhere [3, 50], the hyperspherical coordinate definition is reproduced here first for a triatomic collinear reaction, and subsequently this definition is extended for polyatomic collision processes.

Hyperspherical coordinates provide the advantage of allowing for a smooth description of the reaction system from reactants to products without requiring coordinate transformation or matching in the interaction region. Furthermore, the mathematical form of the KEO is simplified in the hyperspherical coordinate representation, thereby enabling ease of solution of the CC equations. These coordinates are thus widely used in a variety of scattering methodologies [3].

2.2.1 The triatomic reaction case: $\mathbf{A + BC \longrightarrow AB + C}$

Hyperspherical coordinates can be derived by considering the reactant and product Jacobi coordinates, defined according to Figure 2.2. The Jacobi coordinates best describing the reactants (A + BC) involve R_A, the distance between A and the centre of mass of fragment BC, and r_{BC}, the bond length between atoms B and C. For large atom-diatom separations, R_A roughly describes to the translational motion of the atom A towards the diatom BC, whereas the smaller distance r_{BC} can be used to describe the vibrational motion of the diatom. The product Jacobi coordinates R_C and r_{AB} are similarly defined, and accurately describe the situation where atom C and diatom AB are far apart.

In order to convert to a representation that equally describes both the reactant and product arrangement channels, the Jacobi coordinates must first be mass

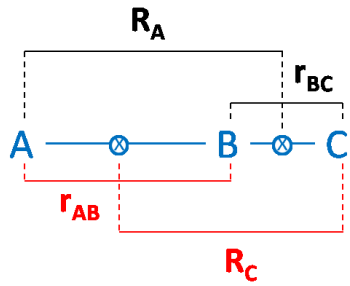

Figure 2.2: Jacobi coordinate system for triatomic reaction A + BC ⟶ AB + C. The x's correspond to the location of the centre of mass of fragments AB and BC. Reactant Jacobi coordinates shown in black, product Jacobi coordinates shown in red.

weighted. Therefore the reduced masses are defined as

$$M_A = m_A m_{BC}/m_{ABC} \tag{2.7}$$

$$M_{BC} = m_B m_C/m_{BC} \tag{2.8}$$

$$M_C = m_C m_{AB}/m_{ABC} \tag{2.9}$$

$$M_{AB} = m_A m_B/m_{AB} \tag{2.10}$$

where the total reduced mass μ is independent of the arrangement channel:

$$\mu = \left(\frac{m_A m_B m_C}{m_{ABC}}\right)^{\frac{1}{2}}. \tag{2.11}$$

The corresponding mass weighted Jacobi coordinates are defined by the equations

$$R_r = \left(\frac{M_A}{\mu}\right)^{\frac{1}{2}} R_A \tag{2.12}$$

$$r_r = \left(\frac{M_{BC}}{\mu}\right)^{\frac{1}{2}} r_{BC} \tag{2.13}$$

$$\mathrm{R_p} = \left(\frac{\mathrm{M_C}}{\mu}\right)^{\frac{1}{2}} \mathrm{R_C} \tag{2.14}$$

$$\mathrm{r_p} = \left(\frac{\mathrm{M_{AB}}}{\mu}\right)^{\frac{1}{2}} \mathrm{R_{AB}} \tag{2.15}$$

where the sub-labels "r" and "p" refer to the reactant and product arrangement channels, respectively. Conversion between the reactant and product Jacobi coordinate system is performed through the orthogonal transformation [3]

$$\begin{pmatrix} \mathrm{R_r} \\ r_r \end{pmatrix} = \begin{pmatrix} \cos\theta & \sin\theta \\ \sin\theta & -\cos\theta \end{pmatrix} \begin{pmatrix} R_p \\ r_p \end{pmatrix}, \tag{2.16}$$

where the transformation is defined according to the skewing angle, θ:

$$\theta = \delta_{\max} = \tan^{-1}\left[\sqrt{\frac{\mathrm{m_B m_{ABC}}}{\mathrm{m_A m_C}}}\right]. \tag{2.17}$$

Finally, the hyperspherical coordinates can be calculated using the mass weighted Jacobi coordinates. The hyperradius, ρ, is independent of the arrangement channel (where i indicates the arrangement channel r or p), whereas the hyperangle δ_i remains dependent upon the arrangement channel as indicated:

$$\rho = \left(\mathrm{R}_i^2 + \mathrm{r}_i^2\right)^{\frac{1}{2}} \tag{2.18}$$

$$\delta_i = \tan^{-1}\left(\frac{\mathrm{r}_i}{\mathrm{R}_i}\right). \tag{2.19}$$

The hyperangle δ_i is, however, bound to the skewing angle such that

$$\delta_{\max} = \delta_r + \delta_p \tag{2.20}$$

and it is therefore possible to define a hyperangle, δ, ranging from 0 to $\delta_{\max}$ that

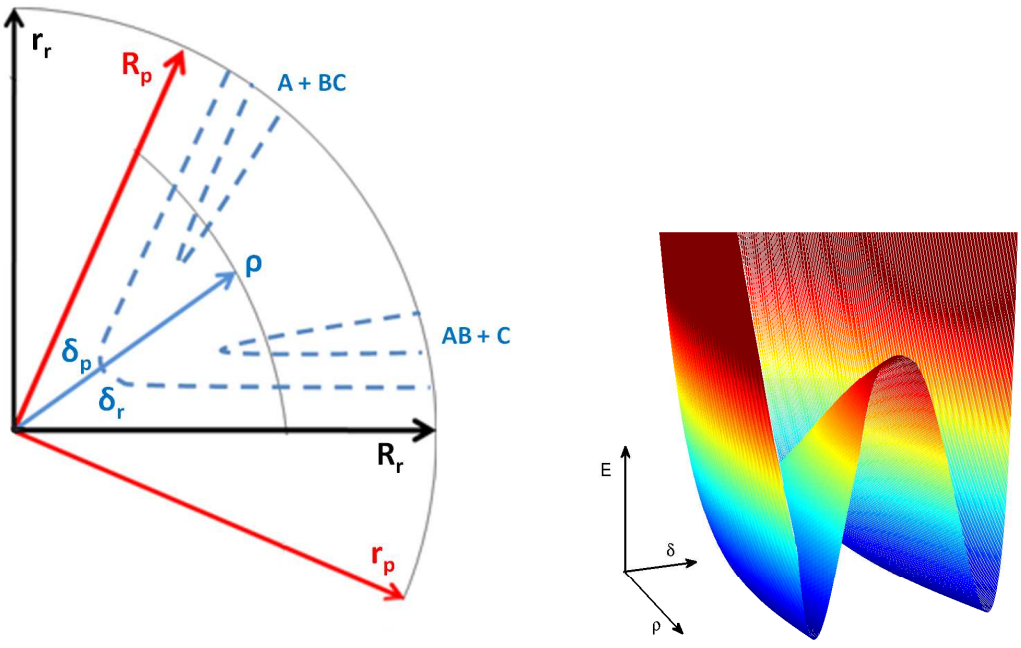

Figure 2.3: Hyperspherical coordinates. Left: Mass-weighted Jacobi and hyperspherical coordinate definition for reaction A + BC, with contour diagram of the potential energy surface (blue). Product mass-weighted Jacobi coordinates (red axis); reactant mass-weighted Jacobi coordinates (black axis); hyperspherical coordinates (blue). Figure adapted from reference [3]. Right: Example double-Morse PES.

varies smoothly from reactants to products. It is therefore clear that the Jacobi coordinates of either arrangement channel can be used to construct the hyperspherical cooridnates ρ and δ.

The reactant and product mass weighted Jacobi coordinates and corresponding hyperspherical coordinates are displayed in Figure 2.3. The transition from the reactant mass weighted Jacobi coordinates to the corresponding product definition is achieved via rotation through angle $\delta_{\max}$. At small values of hyperradius ρ, the hyperspherical coordinates display little correspondence to the mass weighted Jacobi coordinates. At large values of ρ, however, ρ resembles R_i, thereby correlating to translational motion of the atom towards the diatomic fragment, whereas

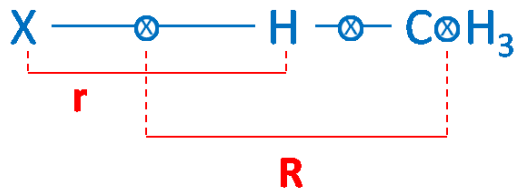

Figure 2.4: Product Jacobi coordinate system for the X + H−CH_3 reaction system. x's indicate centre of masses of fragments XH, CH_4 and CH_3.

δ resembles the vibrational coordinate, r_i [3].

2.2.2 $X + CH_4 \longrightarrow XH + CH_3$ hyperspherical coordinates

Extending the definition of the triatomic collinear hyperspherical coordinate system to the current X + CH_4 reaction (X = CH_3, Cl) is a simple matter of adjusting the definitions of the Jacobi coordinates and reduced masses to reflect the pseudo-atom approximation. Approximating the X + H−C−H_3 reaction system as an A + BCD pseudo-atom reaction, the following definitions for the product Jacobi coordinates result (Figure 2.4): R is adjusted to be the centre of mass distance between fragments XH and CH_3, while r is given as the distance between abstracting atom X and the atom being transferred, H.

Furthermore, the reduced masses used to define the hyperspherical coordinates and the skewing angle must also be adjusted:

$$M_1 = m_{XH}m_{CH_3}/m_{XHCH_3} \tag{2.21}$$

$$M_2 = m_X m_H/m_{XH} \tag{2.22}$$

$$M_3 = m_C m_{H_3}/m_{CH_3} \tag{2.23}$$

$$\mu = (M_1 M_2 M_3)^{1/3} \tag{2.24}$$

$$\delta_{max} = \tan^{-1}\left[\sqrt{\frac{m_H m_{tot}}{m_X m_{CH_3}}}\right]. \tag{2.25}$$

Subsequently, conversion to hyperspherical coordinates is achieved via the transformation equations [12, 13, 16, 51]:

$$\rho = \sqrt{\left(\frac{\mathrm{M_1}}{\mu}\right)\mathrm{R}^2 + \left(\frac{\mathrm{M_2}}{\mu}\right)\mathrm{r}^2} \tag{2.26}$$

$$\delta = \tan^{-1}\left(\frac{\mathrm{r}}{\mathrm{R}}\sqrt{\frac{\mathrm{M_2}}{\mathrm{M_1}}}\right). \tag{2.27}$$

The definition of the reduced mass, μ, is dependent upon the choice of a four pseudo-atom definition of the reaction system; however, in terms of the scattering calculations it is a scaling mass that does not alter the calculation results, as shown in Appendix A.1.

Finally, it should also be noted that for reaction systems where X and CH_3 are much heavier than the transferring atom, H – a so-called heavy-light-heavy (HLH) system – hyperspherical coordinates are particularly suited. This is due to the fact that HLH systems have a large skewing angle, which indicates a greater separability of motion between the coordinates ρ and δ [52].

2.3 Solution of the 2D scattering problem

2.3.1 Discrete variable representation

A judicious choice of a primitive basis for the close-coupled equations can aid in the diagonalisation of the coupling matrix in the R-matrix procedure, and thereby drastically influence the efficiency of the scattering calculations. In this study, a primitive basis χ_k is used, comprised of a discrete variable representation (DVR) constructed from particle-in-a-box (PIB) sine functions [53, 54]. The choice of this basis allows for the construction of analytical δ-dependent Hamiltonian matrix elements, thereby negating the need for numerical evaluation of primitive basis

overlap integrals. This basis is dependent only upon the angular coordinate, δ.

The fixed-node DVR basis described by Muckerman *et al.* [53], is used in this study. Sine PIB functions are chosen to construct the DVR basis because of the physical properties of the PIB eigenfunctions, which have nodes at each end of the interval over which the functions are specified. They are constructed specifically to retain the Kronecker δ property of the sinusoidal PIB basis.

For an interval from a to b, the PIB basis functions are given by

$$\Psi_n(\delta) = \sqrt{\frac{2}{b-a}} \sin\left[\frac{n\pi(\delta - a)}{b-a}\right], \tag{2.28}$$

where $a \leq \delta \leq b$ and $n = 1, \ldots, N_\delta$. The DVR basis function then becomes:

$$\chi_k(\delta) = \frac{2w_k}{b-a} \sum_{n=1}^{N_\delta} \sin\left[\frac{n\pi(\delta - a)}{b-a}\right] \sin\left[\frac{n\pi\,(\delta_k - a)}{b-a}\right]. \tag{2.29}$$

Making the substitutions for the quadrature points $\delta_k = a + k(b-a)/(N_\delta + 1)$ and weights $w_k = \sqrt{(b-a)/(N_\delta + 1)}$ in (2.29) yields

$$\chi_k(\delta) = \sqrt{\frac{4}{(N_\delta + 1)(b-a)}} \sum_{n=1}^{N_\delta} \sin\left(\frac{n\pi(\delta - a)}{b-a}\right) \sin\left(\frac{n\pi k}{N_\delta + 1}\right), \tag{2.30}$$

where $k = 1, \ldots N_\delta$ and where hereafter R is assigned the value of $\sqrt{\frac{4}{(N_\delta+1)(b-a)}}$.

An illustration of the Kronecker delta property of the basis is given in Figures 2.5(a)–2.5(b), with $a = 0$, $b = \pi$, and $N_\delta = 13$. At each grid point δ_l, the basis functions satisfy the condition[4]

$$\chi_k(\delta_l) = \frac{1}{\sqrt{w_k}} \delta_{kl}. \tag{2.31}$$

[4]It is important to note that in the creation of these figures, δ is displayed as a continuous variable, whereas in reality in the DVR calculations δ only has discrete values at each quadrature point. The δ interval is $\delta_{\text{inc}} = (\delta_{\max} - \delta_{\min})/(N_\delta + 1)$, and the quadrature points range from $1 \times \delta_{\text{inc}}$ to $N_\delta \times \delta_{\text{inc}}$.

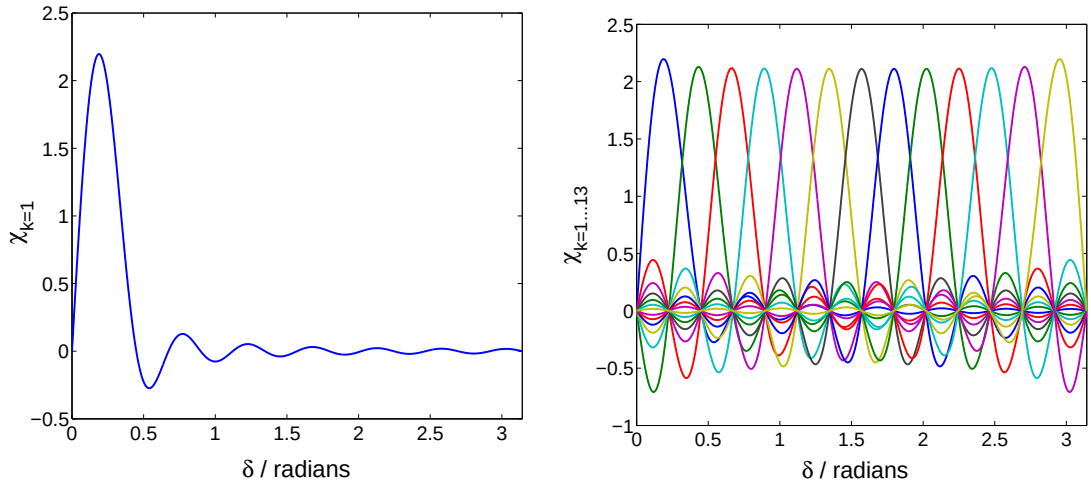

(a) Single DVR basis wavefunction.

(b) Nodal properties of full DVR basis.

Figure 2.5: Discrete variable representation basis functions constructed from PIB sine functions.

Therefore, each function has non-zero magnitude only at the grid point $k = l$. The basis functions satisfy the orthonormality condition when the volume element w_k is included in integration.

Solution of the one-dimensional Schrödinger equation in the basis of the discrete variable representation requires construction of the δ dependent Hamiltonian matrix elements. The Hamiltonian is given according to (in atomic units)

$$\mathrm{H}_\delta = -\frac{1}{2\mu\rho^2}\frac{\partial^2}{\partial\delta^2} + V(\delta;\rho_i), \tag{2.32}$$

and the elements are constructed as follows:

$$\mathrm{H}_{ij} = \langle\chi_i|\mathrm{H}|\chi_j\rangle \tag{2.33}$$

$$= \langle\chi_i(\delta)| - \frac{1}{2\mu\rho^2}\frac{\partial^2}{\partial\delta^2} + V(\delta)|\chi_j(\delta)\rangle \tag{2.34}$$

$$= -\frac{1}{2\mu\rho^2}\langle\chi_i(\delta)|\frac{\partial^2}{\partial\delta^2}|\chi_j(\delta)\rangle + V(\delta_i)\delta_{ij}, \tag{2.35}$$

where the second derivative of the DVR basis function is defined as

$$\frac{\partial}{\partial\delta}\chi_j(\delta) = R\sum_{n=1}^{N_\delta}\left(\frac{n\pi}{b-a}\right)\cos\left(\frac{n\pi(\delta-a)}{b-a}\right)\sin\left(\frac{n\pi j}{N_\delta+1}\right) \tag{2.36}$$

$$\frac{\partial^2}{\partial\delta^2}\chi_j(\delta) = -R\sum_{n=1}^{N_\delta}\left(\frac{n\pi}{b-a}\right)^2\sin\left(\frac{n\pi(\delta-a)}{b-a}\right)\sin\left(\frac{n\pi j}{N_\delta+1}\right), \tag{2.37}$$

and the KE matrix element, T_{ij}, is thus given by

$$\begin{aligned}
T_{ij} &= -\frac{1}{2\mu\rho^2}\int_a^b \chi_i(\delta)\frac{\partial^2}{\partial\delta^2}\chi_j(\delta)d\delta \\
&= -\frac{1}{2\mu\rho^2}\int_a^b\left(R\sum_{n_i=1}^{N_\delta}\sin\left[\frac{n_i\pi(\delta-a)}{b-a}\right]\sin\left[\frac{n_i\pi i}{N_\delta+1}\right]\right) \\
&\quad\times\left(-R\sum_{n_j=1}^{N_\delta}\left(\frac{n_j\pi}{b-a}\right)^2\sin\left(\frac{n_j\pi(\delta-a)}{b-a}\right)\sin\left(\frac{n_j\pi j}{N_\delta+1}\right)\right)d\delta \\
&= \frac{1}{2\mu\rho^2}R^2\left(\frac{\pi}{b-a}\right)^2\int_a^b\sum_{n_i=1}^{N_\delta}\sin\left(\frac{n_i\pi(\delta-a)}{b-a}\right)\sin\left(\frac{n_i\pi i}{N_\delta+1}\right) \\
&\quad\times\sum_{n_j=1}^{N_\delta}n_j^2\sin\left(\frac{n_j\pi(\delta-a)}{b-a}\right)\sin\left(\frac{n_j\pi j}{N_\delta+1}\right)d\delta \\
&= \frac{1}{2\mu\rho^2}R\left(\frac{\pi}{(b-a)}\right)^2\sum_{n_i=1}^{N_\delta}\sum_{n_j=1}^{N_\delta}n_j^2\sin\left(\frac{n_i\pi i}{N_\delta+1}\right)\sin\left(\frac{n_j\pi j}{N_\delta+1}\right) \\
&\quad\times\int_a^b\sin\left(\frac{n_i\pi(\delta-a)}{b-a}\right)\left(\frac{n_j\pi(\delta-a)}{b-a}\right)d\delta.
\end{aligned} \tag{2.38}$$

Using the standard integral definition

$$\int\sin(px)\sin(rx)dx = \frac{\sin(p-r)x}{2(p-r)} - \frac{\sin(p+r)x}{2(p+r)} + C, \tag{2.39}$$

for $p = \frac{n_i\pi}{b-a}$, $r = \frac{n_j\pi}{b-a}$ and making the substitution $x = \delta - a$, the integral over the interval $a \leq x \leq b$ yields:

$$\int_0^{(b-a)} \sin(px)\sin(rx)dx = \frac{\sin(p-r)x}{2(p-r)} - \frac{\sin(p+r)x}{2(p+r)}$$

$$\begin{aligned}
&= \left[\frac{\sin\left(x(n_j-n_i)\frac{\pi}{b-a}\right)}{2(n_j-n_i)\frac{\pi}{b-a}} - \frac{\sin\left(x(n_i+n_j)\frac{\pi}{b-a}\right)}{2(n_i+n_j)\frac{\pi}{b-a}}\right]_0^{(b-a)} \\
&= \left[\frac{\sin(\pi(n_j-n_i))}{2(n_j-n_i)\frac{\pi}{b-a}} - \frac{\sin(\pi(n_i+n_j))}{2(n_i+n_j)\frac{\pi}{b-a}}\right] \\
&= \left(\frac{b-a}{2}\right)\left[\frac{\sin(\pi(n_j-n_i))}{\pi(n_j-n_i)} - \frac{\sin(\pi(n_i+n_j))}{\pi(n_i+n_j)}\right] \qquad (2.40) \\
&= \left(\frac{b-a}{2}\right)\left[\delta_{n_i n_j}\right], \qquad (2.41)
\end{aligned}$$

where $\delta_{n_i n_j}$ is the Kronecker delta[5]. Substituting this result into (2.38) yields the following KEO matrix elements[6]:

$$\begin{aligned}
T_{ij} =& \frac{1}{2\mu\rho^2}R^2\left(\frac{\pi}{b-a}\right)^2 \sum_{n_i=1}^{N_\delta}\sum_{n_j=1}^{N_\delta} n_j^2 \sin\left(\frac{n_i\pi i}{N_\delta+1}\right)\sin\left(\frac{n_j\pi j}{N_\delta+1}\right)\left(\frac{b-a}{2}\right)\left[\delta_{n_i n_j}\right] \\
&= \frac{1}{2\mu\rho^2}R^2\left(\frac{\pi}{b-a}\right)^2\left(\frac{b-a}{2}\right)\times\left[\sum_{n_i=1}^{N} n_i^2 \sin\left(\frac{n_i\pi i}{N_\delta+1}\right)\sin\left(\frac{n_i\pi j}{N_\delta+1}\right)\right] \\
&= \frac{1}{\mu\rho^2}\frac{1}{(N_\delta+1)}\left(\frac{\pi}{b-a}\right)^2\left[\sum_{n_i=1}^{N_\delta} n_i^2 \sin\left(\frac{n_i\pi i}{N_\delta+1}\right)\sin\left(\frac{n_i\pi j}{N_\delta+1}\right)\right].
\end{aligned}$$

[5]The sine expression in equation (2.40) is equivalent to the Kronecker delta, and yields zero in all cases except for $n_i = n_j$, where it becomes 1. The integers n_i, n_j are restricted to the range 1, ..., N_δ. The second sine function thus results in an argument of an integer multiple of π for all $n_{i,}, n_j$, and will thus be zero. The first sine function argument will yield an integer multiple of π (and thus 0) for all n_i and n_j except in the special case $n_i = n_j$; here the expression reduces to 1, because the limit $\lim(\sin[x]/x) \to 1$ as $x \to 0$.

[6]If desired, the closed form expression for this sum is given by Colbert and Miller [54].

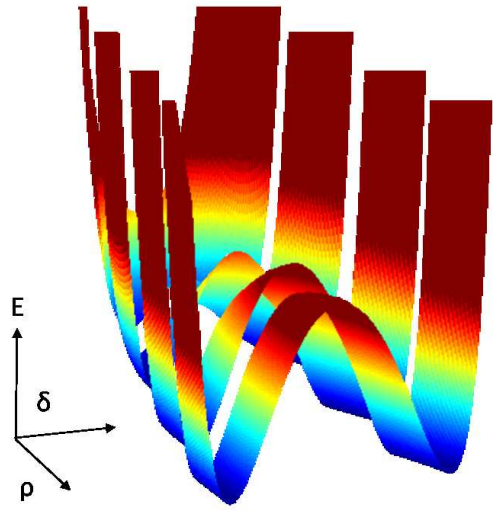

Figure 2.6: Even-width sectors in ρ-space defined for R-matrix propagation. The coupling matrix is constructed and diagonalised in the centre of each sector.

2.3.2 Close-coupled equations for single-surface scattering

The BCRLM Hamiltonian is used to construct the close-coupled equations in terms of the scattering coordinate ρ and angular coordinate δ (in atomic units),

$$H = -\frac{1}{2\mu}\frac{\partial^2}{\partial\rho^2} - \frac{1}{2\mu\rho^2}\frac{\partial^2}{\partial\delta^2} + \frac{3}{8\mu\rho^2} + \frac{J(J+1)}{2\mu\rho^2} + V(\rho,\delta), \tag{2.42}$$

and the close-coupled equations are constructed and solved according to the inelastic R-matrix propagation scheme [55]. This scheme involves dividing the reaction surface into even-width sectors of the scattering coordinate ρ (Figure 2.6).

Within each ρ-sector, the system wavefunction is given by the expansion

$$\Psi_k(\rho,\delta;\rho_i) = \sum_{k'}^{N} f_{k'k}(\rho;\rho_i)\chi_{k'}(\delta;\rho_i), \tag{2.43}$$

where the basis functions χ_k are the primitive DVR basis functions defined in Section 2.3.1. Applying the Hamiltonian operator to this wavefunction expansion

yields

$$
\begin{aligned}
&(H - E_k)\Psi_k = 0 \qquad (2.44)\\
&= \left(-\frac{1}{2\mu}\frac{\partial^2}{\partial\rho^2} - \frac{1}{2\mu\rho^2}\frac{\partial^2}{\partial\delta^2} + \frac{3}{8\mu\rho^2} + \frac{J(J+1)}{2\mu\rho^2} + V(\rho,\delta) - E_k\right)\Psi_k\\
&= \frac{d^2}{d\rho^2}\Psi_k + 2\mu\left[E_k - \frac{3}{8\mu\rho^2} - \frac{J(J+1)}{2\mu\rho^2} + \frac{1}{2\mu\rho^2}\frac{\partial^2}{\partial\delta^2} + V(\rho,\delta)\right]\Psi_k\\
&= \frac{d^2}{d\rho^2}\sum_{k'} f_{k'k}|\chi_{k'}\rangle + 2\mu\\
&\times\left[E_k - \frac{3}{8\mu\rho^2} - \frac{J(J+1)}{2\mu\rho^2} + \frac{1}{2\mu\rho^2}\frac{\partial^2}{\partial\delta^2} + V(\rho,\delta)\right]\sum_{k'} f_{k'k}|\chi_{k'}\rangle. \qquad (2.45)
\end{aligned}
$$

Left multiplying this result by $\langle\chi_k|$ yields

$$
\begin{aligned}
&\frac{d^2}{d\rho^2}\sum_{k'} f_{k'k}\langle\chi_k|\chi_{k'}\rangle +\\
&\sum_{k'} f_{k'k}\langle\chi_k|2\mu\left[E_k - \frac{3}{8\mu\rho^2} - \frac{J(J+1)}{2\mu\rho^2} + \frac{1}{2\mu\rho^2}\frac{\partial^2}{\partial\delta^2} + V(\rho,\delta)\right]|\chi_{k'}\rangle = 0\\
&\frac{d^2}{d\rho^2}\sum_{k'} f_{k'k}\delta_{k'k} + \sum_{k'} f_{k'k}W_{kk'} = 0\\
&\frac{d^2}{d\rho^2}f_{kk} + \sum_{k'} f_{k'k}W_{kk'} = 0, \qquad (2.46)
\end{aligned}
$$

which are the close-coupled equations. In order to apply the R-matrix propagation scheme to solve these coupled differential equations, a basis transformation to an uncoupled representation must be made, where the matrix **W** is diagonal. This is achieved by assuming the new target basis can be expressed as an expansion in the primitive DVR basis as

$$\phi_k = \sum_{k'} T_{k'k}\chi_{k'}. \qquad (2.47)$$

As the only δ-dependent components of the **W**-matrix (and thus the only components that act on the primitive basis functions χ_k) are $H_\delta = -\frac{1}{2\mu\rho^2}\frac{\partial^2}{\partial\delta^2} + V(\rho,\delta)$,

diagonalising the **W**-matrix is equivalent to diagonalising H_δ to obtain the eigenvalues[7] ϵ_k and eigenvectors ($T_{k'k}$). This equivalence arises from the following property of eigenvalue matrix problems:

$$\mathbf{AX} = \lambda\mathbf{X} \tag{2.48}$$

$$(\mathbf{A} + c\mathbf{I})\mathbf{X} = (\lambda + c)\mathbf{X}, \tag{2.49}$$

which dictates that the eigenvectors arising from diagonalisation of H_δ are equivalent to diagonalisation of the total coupling matrix. This is particularly convenient as H_δ-diagonalisation and subsequent computation of the sector transformation (overlap) matrix are only required once and can therefore be separated from the bulk of the R-matrix calculation. This is because the ρ and translational energy dependent components of the coupling matrix enter only on the diagonal and therefore do not affect the resulting eigenvectors.

Thus, the matrix elements of the transformed (diagonal) **W**-matrix in the uncoupled representation can be calculated as

$$W_{kk'}(\rho_i) = 2\mu\left(E - \epsilon_k(\rho_i) - \frac{3}{8\mu\rho_i^2} - \frac{J(J+1)}{2\mu\rho_i^2}\right). \tag{2.50}$$

It is the diagonal elements of the **W**-matrix – the eigenvalues λ_k – that are used to construct the R-matrix. The coupling matrix and its eigenvalues are parametrically dependent upon J, though subscripts are not included for simplicity of notation.

2.3.3 Close-coupled equations for multi-surface scattering

The close-coupled model for the multi-surface case is similarly constructed; however, in the scattering Hamiltonian the potential term $V(\rho, \delta)$ is replaced with the

[7]The eigenvalues ϵ_k are called hyperspherical adiabats.

electronic Hamiltonian (in atomic units):

$$H = -\frac{1}{2\mu}\frac{\partial^2}{\partial\rho^2} - \frac{1}{2\mu\rho^2}\frac{\partial^2}{\partial\delta^2} + \frac{3}{8\mu\rho^2} + \frac{J(J+1)}{2\mu\rho^2} + H_{el}. \tag{2.51}$$

H_{el} acts upon the diabatic wavefunctions to yield the diabatic or coupling potentials. Following the formalism of Lepetit *et al.* [56], the total scattering wavefunction is expanded in a product *vibronic* basis of diabatic (Φ_i^d for electronic state i) and vibrational DVR ($\chi_{(i\nu)}$ for vibrational state ν) basis functions:

$$\Psi_k(\rho,\delta;\rho_i) = \sum_{k'=1}^{N} f_{k'k}(\rho;\rho_i)\Phi_{i'}^d\chi_{(i\nu)'}(\delta;\rho_i). \tag{2.52}$$

The primitive vibrational basis functions $\chi_{(i\nu)}$ are constructed as DVR basis functions in the δ-coordinate, and are therefore identical for each electronic state i at discrete value δ_k. Thus the vibrational basis functions retain their Kronecker delta property $\langle\chi_{i\nu}\chi_{(i\nu)'}\rangle = \delta_{\nu\nu'}$.

The close-coupled equations are constructed by applying the Hamiltonian in equation (2.51) to the total scattering wavefunction:

$$\begin{aligned}
&(H - E_{i\nu})\Psi_{i\nu} = 0 \\
&= \left(-\frac{1}{2\mu}\frac{\partial^2}{\partial\rho^2} - \frac{1}{2\mu\rho^2}\frac{\partial^2}{\partial\delta^2} + \frac{3}{8\mu\rho^2} + \frac{J(J+1)}{2\mu\rho^2} + H_{el} - E_{i\nu}\right)\Psi_{i\nu} \\
&= \frac{d^2}{d\rho^2}\Psi_{i\nu} + 2\mu\left[E_{i\nu} - \frac{3}{8\mu\rho^2} - \frac{J(J+1)}{2\mu\rho^2} + \frac{1}{2\mu\rho^2}\frac{\partial^2}{\partial\delta^2} + H_{el}\right]\Psi_{i\nu} \\
&= \frac{d^2}{d\rho^2}\sum_{(i\nu)'} f_{(i\nu)'i\nu}|\Phi_{i'}^d\chi_{(i\nu)'}\rangle \\
&\quad + 2\mu\left[E_{i\nu} - \frac{3}{8\mu\rho^2} - \frac{J(J+1)}{2\mu\rho^2} + \frac{1}{2\mu\rho^2}\frac{\partial^2}{\partial\delta^2} + H_{el}\right]\sum_{(i\nu)'} f_{(i\nu)'i\nu}|\Phi_{i'}^d\chi_{(i\nu)'}\rangle.
\end{aligned} \tag{2.53}$$

Left multiplying by $\langle \chi_{i\nu} \Phi_i^d |$ yields

$$\frac{d^2}{d\rho^2} \sum_{(i\nu)'} f_{(i\nu)'i\nu} \langle \chi_{i\nu} \Phi_i^d | \Phi_{i'}^d \chi_{(i\nu)'} \rangle \tag{2.54}$$
$$+ \sum_{(i\nu)'} f_{(i\nu)'i\nu} \langle \chi_{i\nu} \Phi_i^d | 2\mu \left[E_{i\nu} - \frac{3}{8\mu\rho^2} - \frac{J(J+1)}{2\mu\rho^2} + \frac{1}{2\mu\rho^2} \frac{\partial^2}{\partial \delta^2} + H_{el} \right] | \Phi_{i'}^d \chi_{(i\nu)'} \rangle = 0.$$

As the vibrational and electronic diabatic wavefunctions are separable and orthonormal within each basis, the first term in this expansion becomes

$$\begin{aligned} &\frac{d^2}{d\rho^2} \sum_{(i\nu)'} f_{(i\nu)'i\nu} \langle \chi_{i\nu} | \chi_{(i\nu)'} \rangle \langle \Phi_i^d | \Phi_{i'}^d \rangle \\ &= \frac{d^2}{d\rho^2} \sum_{(i\nu)'} f_{(i\nu)'i\nu} \delta_{\nu\nu'} \delta_{ii'} = \frac{d^2}{d\rho^2} f_{i\nu i\nu} = \frac{d^2}{d\rho^2} f_{kk}. \end{aligned} \tag{2.55}$$

The second term in the expansion is then

$$\begin{aligned} &2\mu \left[\sum_{(i\nu)'} f_{(i\nu)'i\nu} \left\{ \langle \Phi_i^d \Phi_{i'}^d \rangle \langle \chi_{i\nu} | \frac{1}{2\mu\rho^2} \frac{\partial^2}{\partial \delta^2} | \chi_{(i\nu)'} \rangle \right. \right. \\ &\left. \left. + \left(\frac{3}{8\mu\rho^2} - \frac{J(J+1)}{2\mu\rho^2} \right) \langle \Phi_i^d \Phi_{i'}^d \rangle \langle \chi_{i\nu} \chi_{(i\nu)'} \rangle + \langle \Phi_i^d | H_{el} | \Phi_{i'}^d \rangle \langle \chi_{i\nu} \chi_{(i\nu)'} \rangle \right\} \right] \end{aligned} \tag{2.56}$$
$$\begin{aligned} &= 2\mu \left[\sum_{(i\nu)'} f_{(i\nu)'i\nu} \left\{ \delta_{ii'} \langle \chi_{i\nu} | \frac{1}{2\mu\rho^2} \frac{\partial^2}{\partial \delta^2} | \chi_{(i\nu)'} \rangle \right. \right. \\ &\left. \left. + \left(\frac{3}{8\mu\rho^2} - \frac{J(J+1)}{2\mu\rho^2} \right) \delta_{ii'} \delta_{\nu\nu'} + V_{ii'} \delta_{\nu\nu'} \right\} \right]. \end{aligned} \tag{2.57}$$

Thus, the final form of the close-coupled equations is

$$\frac{d^2}{d\rho^2} f_{i\nu i\nu} + \sum_{(i\nu)'} f_{(i\nu)' i\nu} 2\mu \left[\delta_{ii'} \langle \chi_{i\nu} | \frac{1}{2\mu\rho^2} \frac{\partial^2}{\partial \delta^2} | \chi_{(i\nu)'} \rangle \right. \tag{2.58}$$
$$\left. + \left(\frac{3}{8\mu\rho^2} - \frac{J(J+1)}{2\mu\rho^2} \right) \delta_{ii'} \delta_{\nu\nu'} + V_{ii'} \delta_{\nu\nu'} \right] = 0$$
$$\frac{d^2}{d\rho^2} f_{i\nu} + \sum_{(i\nu)'} f_{(i\nu)' i\nu} W_{i\nu(i\nu)'} = 0. \tag{2.59}$$

It is necessary to evaluate the coupling matrix in a manner that minimises computational effort. There are three terms, which survive or disappear according to the nature of overlap of the primitive basis (equation (2.58)). The state labels of the coupling matrix range from $k_1 \ldots k_{N_e \times N_\delta}$, where N_e is the number of electronic states[8]. The first term represents the KEO and survives in block diagonal form for each electronic state ($i = i'$). The second term survives only for diagonal elements where both quantum numbers agree ($i = i'$,$\nu = \nu'$). The third term either corresponds to the diabatic potential energy surface ($i = i'$) or the spin-orbit coupling potential ($i \neq i'$), in both cases only surviving along the diagonals of each matrix block ($\nu = \nu'$).

This construction is equivalent to writing the three-electronic surface model equations more intuitively as [43]

$$T \begin{pmatrix} \Psi_{1\nu} \\ \Psi_{2\nu} \\ \Psi_{3\nu} \end{pmatrix} + \begin{pmatrix} V_{11} & V_{12} & V_{13} \\ V_{12} & V_{22} & V_{32} \\ V_{13} & V_{23} & V_{33} \end{pmatrix} \begin{pmatrix} \Psi_{1\nu} \\ \Psi_{2\nu} \\ \Psi_{3\nu} \end{pmatrix} = E \begin{pmatrix} \Psi_{1\nu} \\ \Psi_{2\nu} \\ \Psi_{3\nu} \end{pmatrix}, \tag{2.60}$$

where $\Psi_{i\nu}$ is the total wavefunction, V_{ii} are the diabatic surfaces and $V_{ii'}$ are the coupling surfaces.

[8] In terms of electronic and vibrational quantum numbers, N_e ranges from $i_1\nu_1, \ldots, i_1\nu_{N_\delta}, \ldots, i_{N_e}\nu_1, \ldots, i_{N_e}\nu_{N_\delta}$.

As with the single surface case, R-matrix propagation requires diagonalisation of the coupling matrix to transform from the primitive coupled vibronic basis $|\Phi_i^d \chi_{i\nu}\rangle$ to the target uncoupled vibronic basis, $\phi_{i\nu}$:

$$\phi_k = \sum_{k'} T_{k'k}(\phi_{i'}^d \chi_{k'}). \tag{2.61}$$

In this formalism, the construction and solution of the close-coupled equations is identical to the single-surface case; the eigenvalues of the **W**-matrix in the uncoupled representation are used in R-matrix propagation as before, with the exception that the state label k refers to the collective vibronic index $i\nu$. In this uncoupled representation, the asymptotically diagonal states correlate to the adiabatic ones, and thus transitions between diabatic states $k \rightarrow k'$ may be interpreted as transitions between electronically adiabatic energy states.

2.3.4 Inelastic R-matrix propagation

Because of the implementation of hyperspherical coordinates, where the same Hamiltonian may be used in the reactant and product arrangement channels, the inelastic R-matrix propagation method may be used in place of the reactive scattering version [55]. The inelastic method provides the advantage that the same Hamiltonian and therefore basis functions may be applied to describe reactants and products, as well as that the total scattering energy appears as a diagonal element in the scattering matrix, thereby increasing method efficiency.

The inelastic R-matrix propagation scheme is an iterative algorithm used to solve coupled second order linear differential equations in the scattering coordinate, ρ, of the form

$$\frac{d^2}{d\rho^2}\mathbf{f}(\rho;\rho_i) + \mathbf{W}\mathbf{f}(\rho;\rho_i) = 0, \tag{2.62}$$

or, equivalently, expressed in terms of each energy state k,

$$\frac{d^2}{d\rho^2}\mathbf{f_k}(\rho;\rho_i) + \sum_{k'=1}^{N} W_{kk'}(\rho_i)\mathbf{f_{k'}}(\rho;\rho_i) = 0, \tag{2.63}$$

where the functions $f_{kk'}(\rho)$ comprising the vector $\mathbf{f}$ are the translational scattering functions, and the matrix elements $W_{kk'}(\rho)$ of matrix $\mathbf{W}$ couple all system states to each other during the calculation. Indeed, $\mathbf{W}$ is referred to as the coupling matrix, and is by definition a symmetric matrix for most scattering problems, because of the hermiticity requirement of the Hamiltonian for motion with respect to the angular coordinates.

In essence, the R-matrix scheme relies upon division of the scattering coordinate space into sectors over which $\mathbf{W}$ is assumed to be constant with respect to ρ. Solution of the close-coupled equations is initiated in the interaction region where an approximate form of the initial wavefunction is assumed, and these solutions are propagated from sector to sector via the R-matrix to the asymptotic region, where scattering boundary conditions are applied and the S-matrix can be extracted. Thus, the coupling matrix and translational functions in equations (2.62) and (2.63) are given with parametric ρ-sector dependence, i.e., dependence on the ρ value located at the centre of sector i, ρ_i. Though sector width can be varied in different regions of the scattering coordinate space according to the behaviour of the system, in the current approach this parameter is held fixed, resulting in constant sectors of width h.

Application of the R-matrix propagation method necessitates diagonalisation of the coupling matrix, $\mathbf{W}$, in the centre of each sector. Effectively, this results in a transformation from the primitive basis[9] $\chi_k(\delta;\rho_i)$ to a new basis, $\phi_k(\delta;\rho_i)$, where the off-diagonal coupling of the second order linear differential equations is

[9]For the multi-surface case, the primitive basis is defined as $\Phi^d_{i'}\chi_{(i\nu)'}(\delta;\rho_i)$.

removed:

$$\mathbf{T}^{iT}\mathbf{W}(\rho_i)\mathbf{T}^i = \lambda^2(i). \tag{2.64}$$

$\mathbf{T}^i$ is the orthogonal matrix required to diagonalise $\mathbf{W}(\rho_i)$, and $\lambda^2(i)$ is a diagonal matrix containing the sector-dependent eigenvalues (λ_k) of the coupling matrix, which are needed to construct the R-matrix recursion. It should be noted that this diagonalisation is not necessarily ρ-independent; the assumption is made that h is small enough for the diagonalisation of the coupling matrix to remain constant over the entire width of the sector.

The transformation is also applied to the basis wavefunctions

$$\phi_k^i(\delta;\rho_i) = \sum_{k'} T_{k'k}^i \chi_{k'}(\delta;\rho_i), \tag{2.65}$$

and the new translational functions (used in the expansion of Ψ) are given according to the transformation

$$g_k^i(\rho) = \sum_{k'} T_{k'k}^i f_{k'}(\rho). \tag{2.66}$$

The R-matrix propagation takes place in the uncoupled representation. For a given sector (i), we define the translational functions evaluated at the *left* ($\mathbf{g}_L(i)$) and *right* ($\mathbf{g}_R(i)$) boundaries of sector (i) according to

$$\mathbf{g}_L(i) = \mathbf{g}^{(i)}(\rho_i - \frac{1}{2}h) \tag{2.67}$$

$$\mathbf{g}_R(i) = \mathbf{g}^{(i)}(\rho_i + \frac{1}{2}h). \tag{2.68}$$

The global $N \times N$ R-matrix is then defined as the ratio of the translational functions to their outward normal derivatives evaluated at the right sector boundary:

$$\mathbf{g}_R(\rho;\rho_i) = \mathbf{R}(i)\mathbf{g}_R^{'}(\rho;\rho_i). \tag{2.69}$$

R-matrix propagation is initiated in sector (1) near the origin, where – because of the repulsive nature of the potential – it is assumed that the translational functions $\mathbf{g}(\rho)$ tend to zero, allowing an initial construction of the R-matrix in terms of the eigenvalues of the diagonalised coupling matrix:

$$R_{jk}^{(1)} = \delta_{jk}|\lambda_j|^{-1}. \tag{2.70}$$

For each subsequent sector (i), a local $2N \times 2N$ R-matrix $\mathbf{r}^{(i)}$ is constructed which contains information about the propagation step from sector $i-1$ to i,

$$\begin{bmatrix} \mathbf{g}_L(\rho;\rho_i) \\ \mathbf{g}_R(\rho;\rho_i) \end{bmatrix} = \begin{bmatrix} \mathbf{r}_1(i) & \mathbf{r}_2(i) \\ \mathbf{r}_3(i) & \mathbf{r}_4(i) \end{bmatrix} \begin{bmatrix} -\mathbf{g}_L^{'}(\rho;\rho_i) \\ \mathbf{g}_R^{'}(\rho;\rho_i) \end{bmatrix}, \tag{2.71}$$

where the elements of the local R-matrix $\mathbf{r}^{(i)}$ are given by

$$(r_1^{(i)})_{jk} = (r_4^{(i)})_{jk} = \delta_{jk} \begin{cases} |\lambda_j|^{-1} \coth|h_i\lambda_j|, & \lambda_j^2 < 0 \\ -|\lambda_j|^{-1} \cot|h_i\lambda_j|, & \lambda_j^2 \geq 0 \end{cases}, \tag{2.72}$$

$$(r_2^{(i)})_{jk} = (r_3^{(i)})_{jk} = \delta_{jk} \begin{cases} |\lambda_j|^{-1}\mathrm{csch}|h_i\lambda_j|, & \lambda_j^2 < 0 \\ -|\lambda_j|^{-1} \csc|h_i\lambda_j|, & \lambda_j^2 \geq 0 \end{cases}. \tag{2.73}$$

The translational functions and their derivatives at the boundary between sectors

$i-1$ and i must also satisfy the continuity condition

$$\mathbf{g}_R(i) = \mathcal{T}(i,i-1)\mathbf{g}_L(i-1) \tag{2.74}$$

$$\mathbf{g}_R^{'}(i) = \mathcal{T}(i,i-1)\mathbf{g}_L^{'}(i-1), \tag{2.75}$$

where the orthogonal transformation matrix [57] is comprised of three components

$$\mathcal{T}(i,i-1) = \mathbf{T}^{iT}\mathcal{O}^{i,i-1}\mathbf{T}^{(i-1)}, \tag{2.76}$$

where:

1. The matrix $\mathbf{T}^{(i-1)}$ transforms the functions in sector $i-1$ from the uncoupled, ϕ_k basis to the coupled ψ_k basis.

2. The matrix $\mathcal{O}^{i,i-1}$ relates to the basis function overlap between sectors (for normalised and unchanging basis functions such as those used for the DVR vibrational basis, this entity is a unit operator), with matrix elements

$$\mathcal{O}_{kk'}^{i,i-1} = \langle \phi_k^i | \phi_{k'}^{i-1} \rangle. \tag{2.77}$$

3. The matrix $\mathbf{T}^{(iT)}$ transforms the functions in sector i from the coupled, ϕ_k basis back to the uncoupled ψ_k basis.

Finally, the propagation step from sector $i-1$ to sector i is achieved as follows: the transformation matrix $\mathcal{T}(i,i-1)$ is used in combination with the new sector R-matrix $\mathbf{r}^{(i)}$ and the old global R-matrix $\mathbf{R}^{(i-1)}$ to construct the new global R-matrix in sector i:

$$\mathbf{R}^i = \mathbf{r}_4^i - \mathbf{r}_3^i\mathbf{Z}^i\mathbf{r}_2^i, \tag{2.78}$$

where

$$\mathbf{Z}^i = \left[\mathbf{r}_1^i + \mathcal{T}_{i,i-1}\mathbf{R}^{i-1}\mathcal{T}_{i,i-1}^{\mathrm{T}}\right]^{-1}. \tag{2.79}$$

A final transformation back to the coupled representation may be required at the final asymptotic sector, N_ρ, in order to apply boundary conditions:

$$\mathbf{R}^{\mathrm{final}} = \mathcal{T}^{\mathbf{N}_\rho\mathbf{T}}\mathbf{R}\mathcal{T}^{\mathbf{N}_\rho}, \tag{2.80}$$

where $\mathbf{R}^{\mathrm{final}}$ is the ratio of the coupled translational functions and their outward normal gradients in the final sector N_ρ:

$$\mathbf{f}(\rho;\rho_{N_\rho}) = \mathbf{R}^{\mathrm{final}}\mathbf{f}'(\rho;\rho_{N_\rho}). \tag{2.81}$$

However, the final transformation back to the coupled representation is dependent upon the manner in which asymptotic boundary conditions are applied. The application of boundary conditions directly in hyperspherical coordinates, by assuming incoming and outgoing plane waves in ρ, necessitates remaining in the uncoupled representation, and therefore this final conversion is not performed in the current approach.

2.3.5 Assignment of reactant and product states

An additional level of assessment required during the R-matrix propagation procedure is the identification of reactant and product states (for the single-surface scattering problem), and an additional identification of the corresponding electronic states (for the multi-surface problem). It is necessary to identify the state labels in the scattering matrix in order to extract the reactive scattering matrix from the result of the R-matrix propagation scheme. In the following sections, the

orthonormality of the basis functions is presented alongside the method of calculating the expectation value of δ for both the single and multi-surface approach.

2.3.5.1 Orthonormality

One-state. The orthonormality condition of the basis functions is satisfied in the following way (where k refers to the state of the system):

$$\langle\psi_k|\psi_k\rangle = \sum_{j=1}^{N_\delta} c_j^k \sum_{j'=1}^{N_\delta} c_{j'}^k \langle\chi_j|\chi_{j'}\rangle = \sum_{j,j'=1}^{N_\delta} c_j^k c_{j'}^k \delta_{jj'} = \sum_{j=1}^{N_\delta} (c_j^k)^2 = 1, \quad (2.82)$$

$$\langle\psi_k|\psi_{k'}\rangle = \sum_{j=1}^{N_\delta} c_j^k \sum_{j'=1}^{N_\delta} c_{j'}^{k'} \langle\chi_j|\chi_{j'}\rangle = \sum_{j,j'=1}^{N_\delta} c_j^k c_{j'}^{k'} \delta_{jj'} = \sum_{j=1}^{N_\delta} c_j^k c_j^{k'} = 0. \quad (2.83)$$

Three-state. For the three state system, the total wavefunction in the vibronic basis is given by $|\Psi_k\rangle = \sum_{i=1}^{3} |\Phi_i\rangle|\psi_k\rangle$, where the vibrational basis is given by an expansion into $\{|\chi_j\rangle\}$, the set of primitive DVR basis functions, such that $|\psi_k\rangle = \sum_{j=1}^{N_\delta} c_j^{i,\nu}|\chi_j\rangle$. The normalisation condition is defined according to

$$\begin{aligned}
\langle\Psi_k|\Psi_k\rangle &= \sum_{i=1}^{3} \langle\Phi_i|\Phi_i\rangle\langle\psi_{i\nu}|\psi_{i\nu}\rangle \\
&= \sum_{i=1}^{3} (1) \sum_{j=1}^{N_\delta} \sum_{j'=1}^{N_\delta} c_j^{i\nu} c_{j'}^{i\nu} \langle\chi_j|\chi_{j'}\rangle \\
&= \sum_{i=1}^{3} \sum_{j=1}^{N_\delta} \sum_{j'=1}^{N_\delta} c_j^{i\nu} c_{j'}^{i\nu} \delta_{jj'} = \sum_{i=1}^{3} \sum_{j=1}^{N_\delta} (c_j^{i\nu})^2 = 1, \quad (2.84)
\end{aligned}$$

and the orthogonality condition is presented as follows:

$$\langle \Psi_k | \Psi_{k'} \rangle = \sum_{i=1}^{3} \sum_{i'=1}^{3} \langle \Phi_i | \Phi_{i'} \rangle \langle \psi_{i,\nu} | \psi_{i',\nu'} \rangle \tag{2.85}$$

$$= \sum_{i,i'=1}^{3} \delta_{ii'} \sum_{j=1}^{N_\delta} \sum_{j'=1}^{N_\delta} c_j^{i,\nu} c_{j'}^{i',\nu'} \langle \chi_j | \chi_{j'} \rangle \tag{2.86}$$

$$= \sum_{i=1}^{3} \sum_{j,j'=1}^{N_\delta} c_j^{i,\nu} c_{j'}^{i,\nu'} \delta_{jj'} = \sum_{i=1}^{3} \sum_{j=1}^{N_\delta} c_j^{i,\nu} c_j^{i\nu'} = 0. \tag{2.87}$$

2.3.5.2 Expectation value of δ

In the asymptotic region, decreased coupling between motion in ρ and δ results in increased δ-dependence of the scattering wavefunction [14]. The expectation value $\langle \delta \rangle_k$ therefore enables the assignment of reactant and product states for each state, k, which can be used to eliminate nonreactive transitions from the scattering matrix. $\langle \delta \rangle_k$ is calculated in the basis of the δ-dependent wavefunctions.

One-state.

$$\langle \delta \rangle_k = \langle \psi_k | \hat{\delta} | \psi_k \rangle = \sum_{j,j'=1}^{N_\delta} c_j^k c_{j'}^k \langle \chi_j | \delta | \chi_{j'} \rangle \tag{2.88}$$

Three-state.

$$\begin{aligned} \langle \delta \rangle_k &= \sum_{i=1}^{3} \langle \Phi_i \psi_{i\nu} | \hat{\delta} | \Phi_i \psi_{i\nu} \rangle \\ &= \sum_{i=1}^{3} \langle \Phi_i | \Phi_i \rangle \sum_{j,j'=1}^{N_\delta} c_j^{i,\nu} c_{j'}^{i,\nu} \langle \chi_j | \hat{\delta} | \chi_{j'} \rangle \\ &= \sum_{i=1}^{3} (1) \sum_{j,j'=1}^{N_\delta} c_j^{i,\nu} c_{j'}^{i,\nu} \langle \chi_j | \hat{\delta} | \chi_{j'} \rangle \end{aligned} \tag{2.89}$$

2.3.6 Boundary conditions

The scattering, or S-matrix, is the fundamental quantity resulting from solution of the close-coupled equations, and allows for computation of all state-to-state properties of interest. The probability of state-to-state transitions is given as the square modulus of the state-to-state S-matrix elements. R-matrix propagation proceeds into the asymptotic region, where boundary conditions, derived from the assumed behaviour of the asymptotic wavefunction, must be applied in order to extract the S-matrix from the final-sector R-matrix.

In exact calculations, the R-matrix must first be projected from hyperspherical coordinates to the asymptotic reactant or product Jacobi coordinates, and only then can boundary conditions be applied. This projection of the hyperspherical R-matrix into the Jacobi coordinate system is a time consuming and complicated procedure [23]. To avoid the lengthy coordinate projection method, several studies have instead applied approximate boundary conditions directly in hyperspherical coordinates [14, 16]. The justification for this approach is that for large values of hyperradius, ρ and δ become approximately separable and in each arrangement channel ρ corresponds closely to the largest internuclear distance, thereby allowing for approximate treatment [29, 58]. Negligible difference has been reported for the $Cl + CH_4$ reaction between the thermal rate constant results of the accurate hyperspherical projection method and the approximate (sector averaging) approach [59].

The approximate application of boundary conditions in hyperspherical coordinates assumes that the incident and outgoing wavefunctions resemble exactly out of phase plane waves in ρ. Though ρ and δ are approximately separable asymptotically, they are not exactly so; this has been shown to yield oscillations in the resulting reaction probability as a function of ρ when the procedure is applied directly in hyperspherical coordinates [29]. Therefore boundary conditions are applied

over a large number of asymptotic sectors, and the probability matrix elements are averaged [29, 60].

In hyperspherical coordinates, the **S**-matrix is derived according to[10]

$$\mathbf{S}(E,n) = \left[\mathbf{R}(\rho_n)\mathbf{O}'(\rho_n) - \mathbf{O}(\rho_n)\right]^{-1}\left[\mathbf{R}(\rho_n)\mathbf{I}'(\rho_n) - \mathbf{I}(\rho_n)\right], \tag{2.90}$$

where n corresponds to a sector i in the asymptotic region, and where $\mathbf{S}^J(E,n)$ is the energy and sector-dependent S-matrix for a particular total angular momentum value J. For each E, J, and sector n, the incident ($I_{kk'}$) and outgoing ($O_{kk'}$) wavefunctions are plane waves with respect to ρ, but also depend upon the square root of the elements of the coupling matrix in the diagonal representation (λ_k):

$$I_{kk'} = \lambda_k^{-1/2}\exp\left(-i\lambda_k\rho_n\right)\delta_{kk'} \tag{2.91}$$

$$O_{kk'} = \lambda_k^{-1/2}\exp\left(i\lambda_k\rho_n\right)\delta_{kk'} \tag{2.92}$$

$$\lambda_k = \sqrt{W_{kk}}. \tag{2.93}$$

It is important to recall the parametric dependence of the coupling matrix, and therefore also the scattering matrix, on total angular momentum. Therefore the scattering matrix $\mathbf{S}(E,n)$ in equation (2.90) is more accurate rendered $\mathbf{S}^J(E,n)$. The partial wave probability matrix elements can then be defined according to the square modulus of the sector-dependent scattering matrix elements:

$$P^J_{kk'}(E;n) = |S^J_{kk'}(E;n)|^2. \tag{2.94}$$

In the current study, the primary interest is in understanding the dynamics of reactive collisions, and therefore the probability matrix can be reduced by removing

[10]The procedure is identical for the single and multi-surface reaction cases.

all elements that do not correspond to reactant to product transitions. Therefore, considering a transition from initial reactant state s to final product state s', the reactive probability matrix elements are labelled $P^J_{ss'}(E;n)$, and are taken to be an average over a number of final-sector probability matrix elements:

$$P^J_{ss'}(E) = \overline{P^J_{ss'}(E;n)} \; . \tag{2.95}$$

It is this quantity which serves the basis for the derivation of state-to-state dynamical properties, which are discussed in detail in Chapter 4.

Chapter 3

Potential energy surface development

3.1 Overview

In addition to the computational bottleneck arising from the number of coupled equations, the development of a multi-dimensional potential energy surface also remains a limiting factor in the size of the scattering problem. Though work in the area of PES development is expanding[1], the reduced dimensionality approach significantly mitigates the computational cost of investigating polyatomic systems.

The RD approach implemented in this work relies on a combination of high level geometry, single point energy, and frequency *ab initio* data with an analytical double-Morse PES function derived from physical considerations of triatomic reaction surface behaviour. This method has been successfully applied in a number of recent studies [12, 13, 16]. Fitting *ab initio* data to an analytical double-Morse function is useful in providing accuracy and efficiency, especially given that interpolation cannot be used as electronic structure packages do not allow for geometry

[1]For example, full dimensional surfaces have been computed for nine atom systems [30].

optimisation in hyperspherical coordinates. Furthermore, the approach also allows for the use of fewer grid points; higher level *ab initio* calculations may thus be performed to characterise the most important regions of the surface (e.g. the minimum energy path), without significantly increasing computational cost.

The general method of ground state surface development is described in the following sections.

Geometry Optimisation. A two dimensional grid of *ab initio* points in hyperspherical coordinates is developed by performing constrained (partial) geometry optimisations using commercial electronic packages, such as Gaussian [61] or Molpro [62]. Geometry optimisations directly in hyperspherical coordinates are not possible in these programs, so in order to develop a 2D grid of geometries, X–H and H–C bond lengths are held fixed while allowing spectator modes to relax to the minimum energy configuration. Hyperspherical coordinates may then be calculated to yield an (irregular) grid in ρ and δ. Care is taken to ensure that all relevant areas of the hyperspherical grid space are well represented in the final *ab initio* data.

Spectator ZPE Calculation. Frequency calculations must be performed at the same level of theory and basis set as the constrained geometry calculations. A cartesian Hessian is generated at each of the partially optimised geometries in the 2D grid, and extracted for further analysis. The ZPE correction to the surface is computed by projecting the contribution of the two active modes from the Hessian in rectilinear or curvilinear coordinates, described in detail in Section 3.2. Following projection of the active modes, the spectator mode ZPE corrections can be calculated and added to the *ab initio* energies for each grid point. In this way the effect of the spectator DOF are approximately included in the PES.

Single Point Energy Correction. The accuracy of the *ab initio* energies are improved by performing single point energy (SPE) calculations at a higher level of theory for each grid point geometry. Furthermore, this provides the opportunity to additionally improve the quality of the energies by using basis set extrapolation (BSE) methods. Thus, the total energy of each data point is given by the addition of the higher level single point energies and the spectator mode zero point energy corrections.

Surface Fitting. The *ab initio* data is fit to an analytical double-Morse function via a nonlinear least squares regression algorithm implemented in Matlab [63]. Initial parameter values are taken from previous studies or optimised based upon physical considerations to give a good initial representation of surface behaviour.

3.2 Frequency calculations

3.2.1 Harmonic oscillator model: diatomic case

The harmonic oscillator (HO) model [64] is the most widely used approximation in representing vibrational motion of molecular systems. This model amounts to describing the vibrational potential about a stationary point as a Taylor series expansion and truncating to second order. In terms of a diatomic system, this is equivalent to approximating the vibrational motion as that of a harmonic spring using Hooke's law, $F = -kx$, where k is the force constant and x is the cartesian displacement coordinate in the centre of mass frame. The Taylor series expansion

about stationary point x_0 is therefore given as

$$\begin{aligned} V(x) &= V(x_0) + \left(\frac{dV}{dx}\right)\Big|_{x=x_0}(x-x_0) + \frac{1}{2!}\left(\frac{d^2V}{dx^2}\right)\Big|_{x=x_0}(x-x_0)^2 \\ &\quad + \frac{1}{3!}\left(\frac{d^3V}{dx^3}\right)\Big|_{x=x_0}(x-x_0)^3 + \dots \ . \end{aligned} \tag{3.1}$$

The first term is constant and can be set to zero by judicious choice of the zero of energy. The second term (the derivative of the potential with respect to x) is by definition zero at a stationary point, indicating that there is no force acting upon the system at equilibrium. The HO approximation involves truncating to second order, leading to the familiar expression $V(x) = \frac{1}{2}kx^2$. A diatomic potential energy curve is accurately represented by a Morse function, therefore the HO approach is valid only at low energies where a parabola reproduces the behaviour of the potential. All terms of higher order in the truncation – those not considered in the HO approximation – are termed *anharmonic* contributions to vibrational motion.

3.2.2 Solving for the vibrational frequencies

The HO approximation is easily extended to molecular problems with multiple degrees of vibrational freedom [65]. Considering a system with $3N$ dimensions (where N is the number of atoms), the Taylor series expansion of the potential $V(\mathbf{x})$ in cartesian coordinates $\mathbf{x} = (x_1, x_2, ..x_{3N})$ about equilibrium geometry $\mathbf{x_0} = (x_1^0, x_2^0, ..x_{3N}^0)$ [15] is as given in equation (3.1). Truncating this expansion to second order, and choosing $V(\mathbf{x_0})$ as the zero of energy, the expansion reduces to

$$\begin{aligned} V &\approx \sum_{i=1}^{3N}\left(\frac{\partial V}{\partial x_i}\right)\Big|_{x_i=x_i^0}(x_i - x_i^0) \\ &\quad + \sum_{i=1}^{3N}\sum_{j=1}^{3N}\frac{1}{2!}\left(\frac{\partial^2 V}{\partial x_i \partial x_j}\right)\Big|_{x_i=x_i^0, x_j=x_j^0}(x_i - x_i^0)(x_j - x_j^0), \end{aligned} \tag{3.2}$$

where the first term becomes zero at a stationary point and the expression becomes

$$V \approx \sum_{i=1}^{3N}\sum_{j=1}^{3N} \frac{1}{2!}\left(\frac{\partial^2 V}{\partial x_i \partial x_j}\right)\Big|_{x_i=x_i^0, x_j=x_j^0} (x_i - x_i^0)(x_j - x_j^0). \tag{3.3}$$

The terms $f_{\mathrm{cart},ij} = \left(\frac{\partial^2 V}{\partial x_i \partial x_j}\right)$ are elements of the cartesian force constant matrix evaluated by most electronic structure packages (through the analytical or numerical calculation of derivatives of the electronic potential as a function of nuclear coordinates) [65]. Transformation to mass-weighted cartesian coordinates necessitates determining the mass weighted Hessian matrix

$$f_{\mathrm{MWC},(ij)} = \frac{f_{\mathrm{cart},ij}}{\sqrt{m_i m_j}}, \tag{3.4}$$

from which the contribution of translational and rotational motion can be removed by projection from $3N$ to $3N-6$ dimensional space[2]. Diagonalisation of the post-projected Hessian yields the normal modes of vibrational motion (eigenvectors) and eigenvalues λ_i, which are used to compute the vibrational frequencies (cm^{-1})

$$\tilde{\nu}_i = \sqrt{\frac{\lambda_i}{4\pi^2 c^2}}. \tag{3.5}$$

3.2.3 Projection methods

Harmonic vibrational analysis is only valid at a global stationary points, where the gradient with respect to all coordinates is zero. However, the partially-optimised geometries for the RD surface have non-zero gradient with respect to the two active (frozen) modes treated explicitly in the scattering calculations. Inclusion of the spectator ZPE thus requires projection of the active mode vibrations from the $3N-6$ dimensional Hessian. The $3N-8$ dimensional projected Hessian can then

[2]This projection is described in detail by Ochterski [65] but not discussed here.

be diagonalised to yield spectator-only ZPE.

In the present work, two projection methods are implemented. The first method is performed in rectilinear coordinates as outlined by Lu and Truhlar [66]. The second is performed in curvilinear coordinates as introduced by Banks and Clary [14, 15].

3.2.3.1 Rectilinear projection

Definition of subspace. Assuming F represents the full $3N - 6$ degrees of internal freedom, and d the dimensions of the reduced dimensionality scattering problem[3], the Hessian matrix consists of four distinct blocks (Figure 3.1). The $(F - d) \times (F - d)$ block, $\mathrm{H_I}$, is composed of the spectator degrees of freedom. The $d \times d$ block $\mathrm{H_{III}}$ consists of the active degrees of freedom treated in the scattering calculations, while the two blocks $\mathrm{H_{II}} = \mathrm{H_{II}^T}$ contain the coupling of the active and spectator coordinates. The goal of projection is thus to remove coupling between blocks $\mathrm{H_I}$ and $\mathrm{H_{III}}$ such that the former can be diagonalised independently; the resulting eigenvalues are for the spectator mode frequencies only [15].

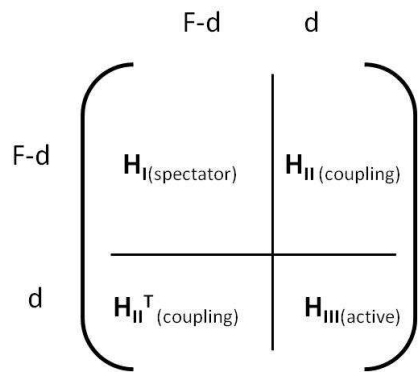

Figure 3.1: Analysis of the Hessian matrix, showing spectator modes (F-d), active modes (d) and the spectator-active mode coupling. Figure adapted from reference [15].

[3] d=2 for the present work.

In projection operator formalism, the total space containing all internal vibrational degrees of freedom is labelled $\mathbf{R}^{F=3N-6}$. Within this space, subspace $\mathbf{C}$ and complementary subspace $\mathbf{C}_1$ contain degrees of freedom associated with the d active modes and $F-d$ spectator modes, respectively. Isolation of the spectator ZPE requires projection of the F-dimensional Hessian from $\mathbf{R}$ onto the $F-d$ dimensional subspace $\mathbf{C}_1$ [66].

Consider a vector $\mathbf{u}$ in $\mathbf{R}^{3N-6}$, which has projections $\mathbf{u}^{\mathbf{C}}$ in subspace $\mathbf{C}$ and $\mathbf{u}^{\mathbf{C}_1}$ in subspace $\mathbf{C}_1$, and can be written as the sum of these two components, i.e. $\mathbf{u} = \mathbf{u}^{\mathbf{C}} + \mathbf{u}^{\mathbf{C}_1}$. The two projections of $\mathbf{u}$ are uniquely determined by projection operators $\mathbf{P}^{\mathbf{C}}$ and its orthogonal complement $\mathbf{P}^{\mathbf{C}_1}$

$$\mathbf{u}^{\mathbf{C}} = \mathbf{P}^{\mathbf{C}}\mathbf{u} \tag{3.6}$$

$$\mathbf{u}^{\mathbf{C}_1} = \mathbf{P}^{\mathbf{C}_1}\mathbf{u} \tag{3.7}$$

and have three main properties, namely

$$(\mathbf{P}^{\mathbf{C}})^{\mathbf{2}} = \mathbf{P}^{\mathbf{C}} \tag{3.8}$$

$$\mathbf{P}^{\mathbf{C}} + \mathbf{P}^{\mathbf{C}_1} = \mathbf{1} \tag{3.9}$$

$$\mathbf{P}^{\mathbf{C}}\mathbf{P}^{\mathbf{C}_1} = 0. \tag{3.10}$$

As motion in subspace $\mathbf{C}$ corresponds to motion in the two constrained coordinates, the operator $\mathbf{P}^{\mathbf{C}}$ describes motion in these DOF. The operator projecting to the desired $\mathbf{C}_1$ subspace can then be defined, following equation (3.9), as

$$\mathbf{P}^{\mathbf{C}_1} = \mathbf{1} - \mathbf{P}^{\mathbf{C}}. \tag{3.11}$$

Correspondingly, in the $F-d$ dimensional subspace $\mathbf{C}_1$, the reduced dimensionality

system gradient ∇V^P and projected force constant matrix $\mathbf{F}^P$ may be defined as

$$\nabla V^P = (\mathbf{1} - \mathbf{P^C})\nabla V \tag{3.12}$$

$$\mathbf{F}^P = (\mathbf{1} - \mathbf{P^C})\mathbf{F}(\mathbf{1} - \mathbf{P^C}), \tag{3.13}$$

where ∇V and $\mathbf{F}$ are the full dimensional gradient and Hessian, respectively.

Projection operator construction. The rectilinear projection operator for bond-stretching constraints is constructed in mass-weighted cartesian coordinates. Given k bond-distance constraints, the total projection operator is a sum over the adjoint products of the individual orthonormalised projection operators for each constraint i (where † indicates a vector transpose):

$$\mathbf{P^C} = \sum_{i=1}^{k} \mathbf{e}_i \mathbf{e}_i^{\dagger}. \tag{3.14}$$

The vectors $\mathbf{e}_i$ are constructed individually for each constraint i and then orthonormalised via the Gram-Schmidt procedure. Prior to orthonormalisation, the vectors

are constructed according to

$$\mathbf{e}_i^0 = \begin{pmatrix} 0 \\ \vdots \\ \chi_{Ax}^{AB} \\ \chi_{Ay}^{AB} \\ \chi_{Az}^{AB} \\ \vdots \\ \chi_{Bx}^{AB} \\ \chi_{By}^{AB} \\ \chi_{Bz}^{AB} \\ \vdots \end{pmatrix} \tag{3.15}$$

where the 0 superscript of $\mathbf{e}_i^0$ denotes pre-orthonormalisation, and A and B are the atoms of the bond distance constraint i. Only six non-zero elements are present in this vector, positioned according to the ordering of atoms A and B in the Z-matrix. These elements are given by

$$\chi_{A\alpha}^{AB} = \left[\frac{\eta_B}{\eta_A}\chi_{A\alpha} - \chi_{B\alpha}\right] / d_{AB} \tag{3.16}$$

$$\chi_{B\alpha}^{AB} = \left[\frac{\eta_B}{\eta_A}\chi_{B\alpha} - \chi_{A\alpha}\right] / d_{AB}, \tag{3.17}$$

where d_{AB} is the distance between atoms A and B, and $\chi_{A\alpha} = \eta_A R_{A\alpha}$ is the mass weighted cartesian coordinate $\alpha = x, y, z$ for atom A. $R_{A\alpha}$ is the cartesian coordinate α for atom A and $\eta_A = \sqrt{m_A}$.

The projected Hessian, $\mathbf{F}^P$, is then obtained according to equations (3.13) and (3.14).

3.2.3.2 Curvilinear projection

In the following discussion, the cartesian displacement coordinates are defined by the set $\{x_i\}$, whereas the curvilinear coordinates are given according to the set $\{q_i, r_u\}$, where $r_u, u = 1, \ldots, d$ are the active scattering coordinates and $q_i, i = 1, \ldots, F - d$ are the spectator curvilinear coordinates. A vector, $\mathbf{a}$, of the F-dimensional curvilinear coordinates is therefore defined as

$$\mathbf{a} = (q_1, q_2, \ldots, q_{F-d}, r_1, r_2, \ldots, r_d). \tag{3.18}$$

The curvilinear coordinates implemented in the present study are bond stretches, angle bends, and doubly degenerate linear angle bends.

Conversion to curvilinear coordinates. Most electronic structure packages calculate the force constant matrix in cartesian coordinates. The curvilinear projection method thus first requires transformation of the gradient and the Hessian matrix to curvilinear coordinates according to the following relations [14, 15]:

$$\mathbf{g} = \mathbf{A}^T \tilde{\mathbf{g}} \tag{3.19}$$

$$\mathbf{F} = \mathbf{A}^T \tilde{\mathbf{F}} \mathbf{A} - \sum_{i=1}^{F} g_i \mathbf{A}^T \mathbf{C}^i \mathbf{A}, \tag{3.20}$$

where $\mathbf{g}$ and $\mathbf{F}$ are the gradient and Hessian, respectively, and where the tilde indicates these quantities in cartesian coordinates. $\mathbf{C}^i$ is a rank two tensor with elements

$$C^i_{jk} = \left(\frac{\partial^2 q_i}{\partial x_j \partial x_k} \right); \quad i = 1, \ldots, F; \quad j, k = 1, \ldots, 3N, \tag{3.21}$$

and **A** is defined according to (where **B** is the Wilson B matrix)

$$\mathbf{A} = \mathbf{u}\mathbf{B}^T\mathbf{G}^{-1} \tag{3.22}$$

$$\mathbf{G}^{ij} = (\mathbf{B}\mathbf{u}\mathbf{B}^T)^{ij} \tag{3.23}$$

$$\mathbf{B}_{ij} = \left(\frac{\partial q_i}{\partial x_j}\right). \tag{3.24}$$

The diagonal matrix **u** has $3N$ nonzero elements comprised of the inverse masses of the atom of the corresponding displacement motion.

Projection operator construction. The projection operator in curvilinear coordinates is constructed as [15]

$$\mathbf{P} = \sum_{u,\nu}^{d} \left[\mathbf{O}(r_1, r_2, \ldots, r_d)^{-1}\right]_{u,\nu} \mathbf{a}'_u \otimes \mathbf{a}'_\nu, \tag{3.25}$$

where $\otimes$ is a dyadic product, and where the derivative of the position vector with respect to active coordinate u is given by $\mathbf{a}'_u = (\partial\mathbf{a}/\partial r_u)$. The overlap matrix elements are defined as

$$O_{u,\nu}(r_1, r_2, \ldots, r_d) = G^{ij} a'_{ui} a'_{\nu j}. \tag{3.26}$$

In a fashion similar to the rectilinear projection representation, the projected curvilinear Hessian is given according to

$$\mathbf{F_P} = (\mathbf{I} - \mathbf{P}\mathbf{G})\mathbf{F}(\mathbf{I} - \mathbf{G}\mathbf{P}). \tag{3.27}$$

The derivatives a'_u can be calculated either numerically [14] or analytically [15]; the latter approach makes use of the fact that

$$\mathbf{T} = -\mathbf{H_I^{-1}}\mathbf{H_{II}}, \tag{3.28}$$

where $\mathbf{H_I}$ and $\mathbf{H_{II}}$ are the matrix blocks defined in Figure 3.1. The first $F - d$ elements of a'_u are defined as the elements i of the u^{th} column of matrix $\mathbf{T}$. The last d elements of a'_u are given as the Kronecker delta $\delta_{u,\nu}$, with ν defined as the position label in the vector $(1, 2, \ldots, d)$.

3.3 Analytical potential energy surface

A potential function capable of describing a 2D reactive scattering problem should have several key properties, as highlighted for the triatomic case by Figure 3.2(a). In addition to being well behaved and single valued, there should be two distinct minima in an asymptotic cut through ρ, corresponding to reactant (A + BC) and product (AB + C) geometries. These minima are separated by the high energy fragmentation zone (A + B + C). In the interaction region, a saddle point TS should correspond to a minimum in ρ and a maximum along the MEP. The function should also have the correct high-energy behaviour; as $\delta \to 0$, and $\delta \to \delta_{\max}$, the potential should smoothly extend to asymptotically high energies. This should also be the case for $\rho \to \rho_{\min}$ behind the TS saddle point. Furthermore, as $\rho \to \infty$ in the asymptotic region, the potential energy should stabilise with respect to the scattering coordinate, i.e. $V(\rho, \delta) \to V(\delta)$. The surface should approach all limits with physical behaviour devoid of unphysical oscillations or singularities.

Because of the required double well behaviour of the PES in the asymptotic region, it is logical to express the potential energy function in terms of Morse func-

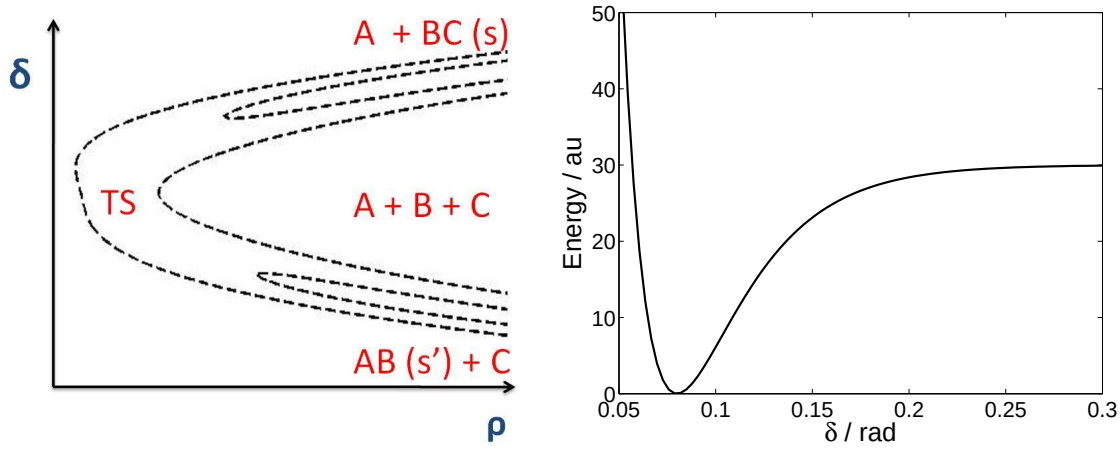

(a) (b)

Figure 3.2: (a): Example two dimensional potential energy surface contour for $V(\rho, \delta)$. Double Morse behaviour is evident in the asymptotic region. (b): Example single Morse potential ($c_1 = 30$, $c_2 = -30$, $c_3 = 0.08$; Eq. (3.29)).

tions dependent upon hyperangle δ. A single Morse potential – which adequately reproduces the behaviour of half of the 2D PES in the asymptotic region – is given according to the following expression:

$$V(\delta) = c_1 \left[1 - \exp\left(c_2(\delta - c_3)\right)\right]^2, \tag{3.29}$$

where the parameter c_1 controls the well depth (or dissociation energy), the magnitude of c_2 influences the narrowness of the potential minimum while its sign dictates the orientation of the function, and c_3 influences the δ location of the potential minimum. An example of a single Morse function is shown in Figure 3.2(b).

It is logical to choose a PES function that is the sum of oppositely orientated Morse functions, with additional parameters added to account for the influence of the hyperradius ρ on well depth, narrowness, and location of the potential minimum in δ. The use of a weighting factor is particularly important, as this

counterbalances the decrease in the PES which naturally occurs as the opposing Morse functions coalesce. This factor is thus necessary to ensure that the TS location exhibits the correct saddle point behaviour for the reaction barrier.

In the current study, two different functions which satisfy the above criteria have been used. In the case of the CH_3+CH_4 reaction system, a symmetric potential with 18 variable parameters is used, while for the Cl+CH_4 ground and excited state surfaces, an asymmetric function with 29 parameters is implemented. These functions are presented in Chapters 5 and 6, respectively.

The surfaces are fit to *ab initio* data using a nonlinear least squares regression analysis algorithm in Matlab, as well as the use of the Surface Fitting Toolbox [63] to identify outlying points. In general, more *ab initio* points are generated than are used in the final fit; a serial fitting procedure is used such that a highly accurate potential surface is developed for low energies.

3.4 Multi-surface potential models

Calculation of multiple potential energy surface models is performed using the same form of the potential function for the ground and excited diabatic surfaces. As a result of computational limitations, the geometry and frequency are assumed fixed at ground state values, with the excited electronic energies computed as stationary point corrections. Furthermore, in the approximate diabatic representation introduced in section 2.1.3, spin-orbit coupling potentials must be derived to describe interaction between the surfaces. In the current study, these surfaces are generated by fitting *ab initio* constants to eight parameter functions; calculation and physical interpretation of the *ab initio* constants is presented in section 3.4.1.

3.4.1 The Breit-Pauli spin-orbit Hamiltonian

Ab initio evaluation of spin-orbit coupling (SOC) constants remains an active area of research [67–70]. Several advances have made the evaluation of the SOC matrix from first principles computationally feasible [67], and thus researchers have gradually moved away from the empirically based, phenomenological operator ($\mathrm{H_{SO}} = A_{\mathrm{SO}}\mathbf{L}\cdot\mathbf{S}$) to the spin-orbit (SO) component of the Breit-Pauli (BP) relativistic multi-electron Hamiltonian. Furthermore, improvements in the spin-free description of electron correlation effects have allowed for a more accurate description of correlation in SOC; this is achieved by treating the SO operator as a first order energy perturbation and solving it in a 0^{th} order basis comprised of eigenfunctions of the spin-free Hamiltonian. Additional simplifications such as frozen-core or mean-field approximations can also be used to simplify evaluation of two electron integrals in SOC calculations [69].

In Molpro [62], SOC is described by the Breit-Pauli operator ($\mathrm{H_{BP}^{SO}}$) and solved as a perturbation to the spin-free electronic Schrödinger Hamiltonian:

$$\mathrm{H} = \mathrm{H_{el}} + \mathrm{H_{BP}^{SO}} \,. \tag{3.30}$$

The SOC contribution is calculated by diagonalising $\mathrm{H_{BP}^{SO}}$ in the basis of eigenfunctions of $\mathrm{H_{el}}$. As described in a thorough review of the subject by Marian [69], $\mathrm{H_{BP}^{SO}}$

is given as follows:

$$\mathrm{H}_{\mathrm{BP}}^{\mathrm{SO}} = \frac{e^2}{2m_e^2c^2}\left\{\sum_i\left(-\hat{\nabla}_i\left(\sum_I \frac{Z_I}{\hat{r}_{iI}}\right)\times\vec{\hat{p}}_i\right)\cdot\vec{\hat{s}}_i \right. \tag{3.31}$$

$$+\sum_i\sum_{j\neq i}\left(\hat{\nabla}_i\left(\frac{1}{\hat{r}_{ij}}\right)\times\vec{\hat{p}}_i\right)\cdot\vec{\hat{s}}_i \tag{3.32}$$

$$+\sum_i\sum_{j\neq i}\left(\hat{\nabla}_j\left(\frac{1}{\hat{r}_{ij}}\right)\times\vec{\hat{p}}_j\right)\cdot\vec{\hat{s}}_i \tag{3.33}$$

$$\left.+\sum_i\sum_{i\neq j}\left(\hat{\nabla}_i\left(\frac{1}{\hat{r}_{ji}}\right)\times\vec{\hat{p}}_i\right)\cdot\vec{\hat{s}}_j\right\}, \tag{3.34}$$

where (3.31) and (3.32) are the so-called *spin-same orbit* SOC terms, and (3.33) and (3.34) are the *spin-other orbit* terms. Term (3.31) describes the interaction between the orbital angular momentum of electron i moving in the field created by nucleus I, with the spin angular momentum of electron i, while (3.32) describes orbital angular momentum of electron i moving in the field created by electron j, interacting with the spin of electron i. Conversely, the spin-other orbit term (3.33) refers to the coupling of the spin angular momentum of electron i with the orbital angular momentum of electron j, and term (3.34) describes the reverse scenario. In this study, Molpro [62] is used to compute MCSCF wavefunctions of states of interest[4]. The $\mathrm{H}_{\mathrm{BP}}^{\mathrm{SO}}$ Hamiltonian is then solved in this 0^{th} order basis. The full BP Hamiltonian is used for the internal configurations, with a mean-field Fock operator for external configurations [68, 71].

3.4.2 The phenomenological operator: the Cl atom

Evaluating the BP Hamiltonian for polyatomic species in a cartesian basis is a complex process. For clarity, the SOC of the Cl atom is summarised in detail in

[4]These states are recomputed with the MRCI method without excitation in order to generate the proper input form for the SOC calculation.

the spherical harmonic and cartesian basis, given that the Cl atom is the major contributing factor to spin-orbit interaction in the $Cl + CH_4$ reaction system.

The phenomenological spin-orbit operator is given by [69]

$$\mathrm{H_{SO}} = A_{\mathrm{SO}}\mathbf{L}\cdot\mathbf{S}, \tag{3.35}$$

where A_{SO} is the empirical spin-orbit coupling parameter, $\mathbf{L}$ is the total orbital angular momentum operator and $\mathbf{S}$ is the total spin angular momentum operator. Expanding $\mathbf{L}$ and $\mathbf{S}$ into their cartesian (x, y, z) components yields:

$$\mathrm{H_{SO}} = A_{\mathrm{SO}}\left(l_x s_x + l_y s_y + l_z s_z\right). \tag{3.36}$$

Angular momentum ladder operators can be defined ($l_+ = l_x + il_y$, $l_- = l_x - il_y$ and so forth) and substituted into equation (3.35) such that (in atomic units):

$$\begin{aligned}\mathbf{L}\cdot\mathbf{S} &= l_z s_z + \frac{1}{2}\left((l_x + il_y)(s_x - is_y) + (l_x - il_y)(s_x + is_y)\right)\\ &= l_z s_z + \frac{1}{2}(l_+ s_- + l_- s_+).\end{aligned} \tag{3.37}$$

The l_z, s_z and the ladder operators l_+, l_-, s_+, and s_- yield the following eigenvalues

in the basis of spherical harmonic angular momentum eigenfunctions (in au):

$$
\begin{aligned}
l_z|lm_l\rangle &= m_l|lm_l\rangle \qquad (3.38)\\
l_+|lm_l\rangle &= \sqrt{l(l+1)-m_l(m_l+1)}|lm_{l+1}\rangle\\
l_-|lm_l\rangle &= \sqrt{l(l+1)-m_l(m_l-1)}|lm_{l-1}\rangle\\
s_z|sm_s\rangle &= m_s|sm_s\rangle\\
s_+|sm_s\rangle &= \sqrt{s(s+1)-m_s(m_s+1)}|sm_{s+1}\rangle\\
s_-|sm_s\rangle &= \sqrt{s(s+1)-m_s(m_s-1)}|sm_{s-1}\rangle.
\end{aligned}
$$

Considering only the unpaired valence electron of the Cl atom 3p orbital ($3p^5$), the possible quantum states for the system are $l = 1$, $m_l = -1, 0, 1$, $s = \frac{1}{2}$, and $m_s = +\frac{1}{2}, -\frac{1}{2}$. Table 3.1 summarises the possible resulting states, from which it is possible to derive spin-orbit coupling patterns.

Table 3.1: Orbital and spin angular momentum microstates for the Cl atom.

m_l	m_s	m_j
1	1/2	3/2
1	-1/2	1/2
0	1/2	1/2
-1	1/2	-1/2
0	-1/2	-1/2
-1	-1/2	-3/2

Applying equation (3.37) to the microstates of Table 3.1 indicates that state $m_j = \frac{3}{2}$ cannot couple with any other state, as l_+s_- or l_-s_+ cannot operate on a state already at the maximum values of l and s. By the same analysis, state $m_j = -\frac{3}{2}$ also does not couple to another state. However, the $m_j = \frac{1}{2}$ states will couple, as will the $m_j = -\frac{1}{2}$ states.

Using the formula in equation (3.38), the coupling pattern for the $m_j = \frac{1}{2}$ states is analysed by computing the matrix elements $\langle m_l, m_s|\mathbf{L}\cdot\mathbf{S}, |m_l, m_s\rangle$; the

individual ladder operations are given according to

$$l_z s_z|1,-\frac{1}{2}\rangle = -\frac{1}{2}|1,-\frac{1}{2}\rangle \tag{3.39}$$

$$l_z s_z|0,\frac{1}{2}\rangle = 0 \tag{3.40}$$

$$l_+ s_-|1,-\frac{1}{2}\rangle = 0 \tag{3.41}$$

$$l_- s_+|1,-\frac{1}{2}\rangle = (1)|0,\frac{1}{2}\rangle \tag{3.42}$$

$$l_+ s_-|0,\frac{1}{2}\rangle = \sqrt{2}|1,-\frac{1}{2}\rangle \tag{3.43}$$

$$l_- s_+|0,\frac{1}{2}\rangle = 0. \tag{3.44}$$

Thus, the $\mathbf{L}\cdot\mathbf{S}$ matrix elements are given according to[5]

$$\langle 1,-\frac{1}{2}|l_z s_z + \frac{1}{2}(l_+ s_- + l_- s_+)|1,-\frac{1}{2}\rangle = -\frac{1}{2} \tag{3.45}$$

$$\langle 0,\frac{1}{2}|l_z s_z + \frac{1}{2}(l_+ s_- + l_- s_+)|0,\frac{1}{2}\rangle = 0 \tag{3.46}$$

$$\langle 0,\frac{1}{2}|l_z s_z + \frac{1}{2}(l_+ s_- + l_- s_+)|1,-\frac{1}{2}\rangle = \frac{1}{\sqrt{2}} \tag{3.47}$$

$$\langle 1,-1/2|l_z s_z + 1/2(l_+ s_- + l_- s_+)|0,\frac{1}{2}\rangle = \frac{1}{\sqrt{2}}. \tag{3.48}$$

Therefore, the SOC matrix for the Cl atom is defined

$$\mathrm{H_{SO}} = A_{\mathrm{SO}} \begin{pmatrix} -\frac{1}{2} & -\frac{1}{\sqrt{2}} \\ \frac{1}{\sqrt{2}} & 0 \end{pmatrix}, \tag{3.49}$$

where the same coupling pattern can be shown to occur for the $m_j = -\frac{1}{2}$ states.

However, it is useful to express the SOC in a basis of cartesian states, as Molpro reports *ab initio* results in this representation. The cartesian basis $\{\mathrm{p}_x, \mathrm{p}_y, \mathrm{p}_z\}$ is

[5]Note that the z-component of the angular momentum operators only contributes to diagonal terms (matrix element of a spin-orbit state with itself).

defined according to the following convention:

$$|1\rangle = \frac{1}{\sqrt{2}}(p_x + ip_y) \tag{3.50}$$

$$|0\rangle = p_z \tag{3.51}$$

$$|-1\rangle = \frac{1}{\sqrt{2}}(p_x - ip_y). \tag{3.52}$$

These definitions can be used to derive the cartesian coupling constants. The matrix element

$$\langle 0, \frac{1}{2}|\mathbf{L}\cdot\mathbf{S}|1, -\frac{1}{2}\rangle = \frac{1}{\sqrt{2}} \tag{3.53}$$

can be expressed as (where α is an $m_s = \frac{1}{2}$ state and β is an $m_s = -\frac{1}{2}$ state)

$$\langle p_z\alpha|\mathbf{L}\cdot\mathbf{S}|\frac{1}{\sqrt{2}}(p_x + ip_y)\beta\rangle = \frac{1}{\sqrt{2}}. \tag{3.54}$$

Given that

$$\langle 0, \frac{1}{2}|\mathbf{L}\cdot\mathbf{S}| - 1, -\frac{1}{2}\rangle = 0 \tag{3.55}$$

$$\langle p_z\alpha|\mathbf{L}\cdot\mathbf{S}|\frac{1}{\sqrt{2}}(p_x - ip_y)\beta\rangle = 0, \tag{3.56}$$

the addition of equations (3.54) and (3.56) results in the following relations:

$$\langle p_z\alpha|\mathbf{L}\cdot\mathbf{S}|\frac{1}{\sqrt{2}}(2p_x)\beta\rangle = \frac{1}{\sqrt{2}} \tag{3.57}$$

$$\langle p_z\alpha|\mathbf{L}\cdot\mathbf{S}|p_x\beta\rangle = \frac{1}{2}. \tag{3.58}$$

Equation (3.58) is the SOC constant for the interaction between states p_x and p_z. Correspondingly, by subtracting equation (3.56) from equation (3.54), the SOC

between states p_y and p_z is described by

$$\langle p_z\alpha|\mathbf{L}\cdot\mathbf{S}|\frac{1}{\sqrt{2}}(2ip_y)\beta\rangle = \frac{1}{\sqrt{2}} \tag{3.59}$$

$$\langle p_z\alpha|\mathbf{L}\cdot\mathbf{S}|p_y\beta\rangle = -\frac{i}{2}. \tag{3.60}$$

Derivation of the p_x and p_y coupling terms is also straightforward. Defining the matrix elements

$$\langle 1,-\frac{1}{2}|\mathbf{L}\cdot\mathbf{S}|1,-\frac{1}{2}\rangle = -\frac{1}{2} \tag{3.61}$$

$$\langle -1,-\frac{1}{2}|\mathbf{L}\cdot\mathbf{S}|-1,-\frac{1}{2}\rangle = \frac{1}{2} \tag{3.62}$$

$$\langle 1,-\frac{1}{2}|\mathbf{L}\cdot\mathbf{S}|-1,-\frac{1}{2}\rangle = 0 \tag{3.63}$$

and taking the addition of equations (3.61) and (3.62) results in

$$\langle\frac{1}{\sqrt{2}}(p_x+ip_y)\beta|\mathbf{L}\cdot\mathbf{S}|\frac{1}{\sqrt{2}}(2p_x)\beta\rangle = -\frac{1}{2}. \tag{3.64}$$

Then, computing the addition of equations (3.62) and (3.63) yields

$$\langle\frac{1}{\sqrt{2}}(p_x-ip_y)\beta|\mathbf{L}\cdot\mathbf{S}|\frac{1}{\sqrt{2}}(2p_x)\beta\rangle = \frac{1}{2}. \tag{3.65}$$

Finally, subtracting equation (3.65) from equation(3.64) gives

$$\begin{aligned}\langle\frac{1}{\sqrt{2}}(2ip_y)\beta|\mathbf{L}\cdot\mathbf{S}|\frac{1}{\sqrt{2}}(2p_x)\beta\rangle &= -1\\ \langle p_y\beta|L\cdot S|p_x\beta\rangle &= \frac{i}{2}.\end{aligned} \tag{3.66}$$

Therefore, the SOC matrix (expressed in order of states (1) $p_x\beta$; (2) $p_y\beta$; and (3)

$p_z\alpha$), is given by:

$$H_{SO} = A_{SO} \begin{pmatrix} 0 & -i/2 & 1/2 \\ i/2 & 0 & i/2 \\ 1/2 & -i/2 & 0 \end{pmatrix} = \begin{pmatrix} 0 & -iA & A \\ iA & 0 & iA \\ A & -iA & 0 \end{pmatrix}, \tag{3.67}$$

where the constant $A = A_{SO}/2$. Diagonalising the SOC matrix should predict the splitting between energy levels caused by spin-orbit interaction. The characteristic equation $\det(H_{SO} - \lambda I) = 0$ is constructed as

$$H_{SO} - \lambda I = \begin{pmatrix} -\lambda & -iA & A \\ iA & -\lambda & iA \\ A & -iA & \lambda \end{pmatrix}, \tag{3.68}$$

and

$$\det(H_{SO} - \lambda I) = -\lambda(\lambda^2 - A^2) + 2A^2(\lambda + A) = 0 \tag{3.69}$$

$$= -\lambda(\lambda + A)(\lambda - A) + 2A^2(\lambda + A) = 0 \tag{3.70}$$

$$= (\lambda + A)(-\lambda^2 + A\lambda + 2A^2) = 0 \tag{3.71}$$

$$= (\lambda + A)^2(\lambda - 2A) = 0. \tag{3.72}$$

Therefore, $\lambda = -A$ is a double root, and $\lambda = +2A$ is a single root, thus indicating that one state shifts up by $2A$, and two states shift down by A. The total energy splitting is $3A$. Given an experimental splitting for the Cl atom of 882 cm^{-1} [72], the parameter A is $882/3 = 294$ cm^{-1}. Therefore $A_{SO} = 588$ cm^{-1}.

The Molpro [62] output for the Cl atom produces an SOC of six states of the form:

	(1) $p_x\alpha$	(2) $p_x\beta$	(3) $p_y\alpha$	(4) $p_y\beta$	(5) $p_z\alpha$	(6) $p_z\beta$
(1) $p_x\alpha$	0	0	iA	0	0	$-A$
(2) $p_x\beta$	0	0	0	$-iA$	A	0
(3) $p_y\alpha$	$-iA$	0	0	0	0	iA
(4) $p_y\beta$	0	iA	0	0	iA	0
(5) $p_z\alpha$	0	A	0	$-iA$	0	0
(6) $p_z\beta$	$-A$	0	$-iA$	0	0	0

This matrix can be decomposed into two distinct blocks of equal coupling – states 1, 3, and 6 couple separately while states 2, 4, and 5 couple with an identical pattern. In analysing the coupling scheme of states 2, 4, and 5, it is easy to see that Molpro exactly reproduces the predicted coupling interaction for the Cl atom in the cartesian basis:

	(2) $p_x\beta$	(4) $p_y\beta$	(5) $p_z\alpha$
(2) $p_x\beta$	0	$-iA$	A
(4) $p_y\beta$	iA	0	iA
(5) $p_z\alpha$	A	$-iA$	0

The Cl atom SOC calculation was performed using MCSCF wavefunctions (in MRCI formalism) as basis states for evaluation of the BP Hamiltonian, with the cc-pV(T+d)Z basis. The resulting coupling constant A_{calc} was determined to be 278.18 cm^{-1}, which produces a low splitting energy of 834.55 cm^{-1}. It is possible to scale the coupling constant A_{calc} to reproduce the experimental splitting value and associated SOC experimental constant of $A = 294$ cm^{-1}. This scaling factor is given by the ratio $A/A_{\text{calc}} = 1.05687$, a result which is subsequently used to scale the SOC constants for the polyatomic reaction system $\text{Cl} + \text{CH}_4$.

3.4.3 Cl + CH_4 spin-orbit coupling

The analysis in section 3.4.2 is very relevant to the calculation of SOC constants for the reactant channel of the $\text{Cl} + \text{CH}_4$ reaction; the spin-orbit coupling arising from the Cl atom remains the dominant feature in this region of the PES. However,

the presence of the incident CH_4 molecule breaks the symmetry of the SOC. The p_z state ($1A'$ symmetry), corresponding to the electron hole orientated along the principle symmetry axis and the direction of CH_4 approach, has identical coupling interaction with the degenerate excited states p_x and p_y ($2A'+1A''$ symmetry). The latter two states, however, have different SO interaction with each other. Though six states are present for the molecular system as for the Cl atom, symmetry exists in the coupling pattern as before, requiring only 1/2 of the SOC matrix to be considered. This is shown with state ordering (1) $1A'(\alpha)$, (4) $2A'(\beta)$, and (6) $1A''(\beta)$[6]:

	(1) $1A'\ \alpha$	(4) $2A'\ \beta$	(6) $1A''\ \beta$
(1) $1A'\ \alpha$	0	A	$-iA$
(4) $2A'\ \beta$	A	0	$-iB$
(6) $1A''\ \beta$	iA	iB	0

In the asymptotic limit of large separation between Cl and CH_4, the coupling terms tend towards the Cl atom values and the B coupling constant value approaches that of A. For example, far into the reactant asymptotic region ($\rho = 18.7$; $\delta = 0.214$), the magnitude of the scaled coupling constants $A = 293.99$ cm^{-1}, while the magnitude of the coupling constant B is slightly lower at 293.93 cm^{-1}. The magnitudes of both A and B decrease rapidly in the interaction region as a function of hyperspherical coordinates ρ and δ. Potential functions describing this variation are described in Chapter 6.

The SOC terms form the off-diagonal coupling surfaces between the diabatic potential energy surfaces in the scattering problem. Only three states are considered in the scattering, as the coupling scheme is identical in the two subsets of states; this drastic reduction of the dimensionality of the problem significantly improves computational feasibility of the approach. Furthermore, the complex

[6]The numbering scheme reflects the state ordering for the majority of grid points resulting from the *ab initio* calculations.

nature of four of the coupling constants can introduce complex eigenvectors in the R-matrix propagation. This effect is trivial, however, if working with purely real eigenvectors is desirable, it is possible to instead consider the coupling between states $|(1)\rangle$, $|(4)\rangle$, and $|i(6)\rangle$, such that all the terms of the SOC matrix are real.

Chapter 4

Analysis

Following development of the potential energy surface(s) (Chapter 3) and application of the quantum scattering calculations (Chapter 2), it is possible to derive physical quantities that link to experimental observables and enable analysis of the reaction mechanism and thermal rate constants. These expressions are summarised in the following sections.

4.1 Thermal rate constant

From full dimensional models to transition state theory. The thermal rate constant (TRC) for a full dimensional quantum scattering calculation is given as the integral of the reaction probability over the collision energy, weighted by a pre-exponential factor of reactant partition functions [73][1](in $\mathrm{cm^3 molecule^{-1} s^{-1}}$):

$$k(T) = \frac{1}{hQ^{\mathrm{int}}_{\mathrm{react}}(T)Q^{\mathrm{rel}}_{\mathrm{trans}}(T)} \int_0^\infty dE\ P_c(E)\ e^{-E/k_B T}, \tag{4.1}$$

[1]For the purposes of this derivation, the electronic partition function of the TS is not explicitly included. This is remedied in the final expression for the thermal rate constant, where Q^{int}=$Q_{\mathrm{vib}} \times Q_{\mathrm{rot}} \times Q_{\mathrm{elec}}$.

where h is Planck's constant, $Q^{\text{int}}_{\text{react}}(T)$ is the temperature dependent partition function of the reactant species for internal rotation, vibration, and electronic state and $Q^{\text{rel}}_{\text{trans}}(T)$ is the relative translational partition function. $P_c(E)$ is the cumulative reaction probability (CRP), defined as the sum of the state-to-state partial wave probabilities over all quantum states and total angular momentum:

$$P_c(E) = \sum_s \sum_{s'} \sum_{J=0} (2J+1) P^J_{ss'}(E). \tag{4.2}$$

As the reduced dimensionality method calculates the TRC using a combined scattering and transition state theory (TST) approach, it is useful to derive the TST rate constant from the expression for the full dimensional TRC. This is achieved by assuming the CRP may be described by a sum of unit step functions for each bending and rotational degree of freedom [74]:

$$P_c(E) = \sum_m \Theta(E - V_0 - E^{TS}_m), \tag{4.3}$$

where V_0 is the vibrationally adiabatic barrier height of the reaction, the energies E^{TS}_m are the transition state energies associated with quantum state m for rotational or vibrational motion, and the unit step function is defined according to

$$\Theta(x) \;=\; \begin{cases} 0 & x \leq 0 \\ 1 & x > 0 \end{cases} . \tag{4.4}$$

This approximation yields a thermal rate constant as:

$$\begin{aligned} k(T) &= \frac{1}{hQ^{\text{int}}_{\text{react}}(T)Q^{\text{rel}}_{\text{trans}}(T)} \int_0^\infty dE \sum_m \Theta(E - V_0 - E_m^{TS})\, e^{-E/k_BT} \\ &= \frac{1}{hQ^{\text{int}}_{\text{react}}(T)Q^{\text{rel}}_{\text{trans}}(T)} \sum_m \int_0^\infty dE\, \Theta(E - V_0 - E_m^{TS})\, e^{-E/k_BT} \\ &= \frac{1}{hQ^{\text{int}}_{\text{react}}(T)Q^{\text{rel}}_{\text{trans}}(T)} \sum_m \int_{V_0+E_m^{TS}}^\infty dE\, e^{-E/k_BT} \\ &= \frac{1}{hQ^{\text{int}}_{\text{react}}(T)Q^{\text{rel}}_{\text{trans}}(T)} \sum_m k_BT e^{-(V_0+E_m^{TS})/k_BT} \\ &= \frac{k_BT e^{-V_0/k_BT}}{hQ^{\text{int}}_{\text{react}}(T)Q^{\text{rel}}_{\text{trans}}(T)} \sum_m e^{-E_m^{TS}/k_BT}. \end{aligned} \tag{4.5}$$

Given that the internal partition function of the transition state is given according to $Q^{\text{int}}_{TS}(T) = \sum_m e^{-E_m^{TS}/k_BT}$,

$$k(T) = \frac{k_BT}{h} \frac{Q^{\text{int}}_{TS}}{Q^{\text{int}}_{\text{react}}(T)Q^{\text{rel}}_{\text{trans}}(T)} e^{-V_0/k_BT}, \tag{4.6}$$

which is the standard expression for TST. The forms of the partition functions are defined in section 4.1.1. TST is an extremely useful method that allows for prediction of the TRC while only requiring knowledge of the barrier height and stationary point geometries and frequencies. However, it neglects the possibility for recrossing [2]; once a collision overcomes the barrier height necessary to proceed to products, it must always continue to reaction completion. This leads to an overestimation of the reaction rate at high temperature. Quantum effects such as hydrogen tunnelling are also not treated, and thus the rate constant is underestimated at low temperatures.

Reduced dimensionality thermal rate constants. Reduced dimensionality quantum scattering provides a compromise between the efficiency of TST and the

accuracy of full dimensional quantum scattering. This is achieved by using TST-like approximations for a reduced subset of spectator degrees of freedom, while treating the active modes in an accurate manner. The family of approximations are generally referred to as energy shift approximations, such as the *J-shifting approximation* [27, 74] for the treatment of total molecular rotation, or the *bend-energy shift approximation* [27, 74] to account for spectator degrees of vibrational freedom. Both of these methods reduce computational effort by allowing for the calculation of a total TRC from the ground state CRP.

The J-shifting approximation computes the TRC from the $J = 0$ partial wave of the CRP, and thus considerably mitigates computational effort. The following energy shift approximation to the reaction probability is assumed:

$$P_c^J(E) \simeq P_c^{J=0}(E - E_J^{TS}), \tag{4.7}$$

where E_J^{TS} is the rotational energy of the transition state, which is assumed to be a linear rigid rotor. This approximation leads to the thermal rate constant expression

$$\begin{aligned} k^{\mathrm{J-shift}}(T) &= \frac{1}{hQ^{\mathrm{int}}_{\mathrm{react}}(T)Q^{\mathrm{rel}}_{\mathrm{trans}}(T)} \int_0^\infty dE\ P_c^{J=0}(E - E_J^{TS})\ e^{-E/k_BT} \\ &= \frac{Q^{TS}_{\mathrm{rot}}(T)}{hQ^{\mathrm{int}}_{\mathrm{react}}(T)Q^{\mathrm{rel}}_{\mathrm{trans}}(T)} \int_0^\infty dE\ P_c^{J=0}(E)\ e^{-E/k_BT} \\ &= Q^{TS}_{\mathrm{rot}} k^{J=0}(T). \end{aligned} \tag{4.8}$$

Therefore, the total TRC is the product of the TS rotational partition function with $k^{J=0}(T)$, the TRC computed from the $J = 0$ partial wave reaction probability.

Similarly, an energy shift approximation can be made for the spectator vibra-

tional modes, such that

$$P_c^J(E;\ n_b) \ \simeq \ P_c^J(E - n\hbar\omega^{TS};\ n_b = 0), \tag{4.9}$$

where n_b is the quantum number associated with the spectator vibrational motion and $n\hbar\omega^{TS}$ is the harmonic energy of the spectator vibration at the TS. The energy shift assumes that the probability is computed for the ground state vibration only ($n_b = 0$):

$$\begin{aligned} k^{\mathrm{RD}}(T) &= \frac{Q_{\mathrm{vib}}^{TS}(T)}{hQ_{\mathrm{react}}^{\mathrm{int}}(T)Q_{\mathrm{trans}}^{\mathrm{rel}}(T)} \int_0^\infty dE\ P_c^J(E;\ n_b = 0)\ e^{-E/k_BT} && (4.10)\\ &= Q_{\mathrm{vib}}^{TS} k(T), && (4.11) \end{aligned}$$

where $Q_{\mathrm{vib}}^{TS}(T)$ is the vibrational partition function associated with the spectator vibrations not treated explicitly in the quantum calculations.

A combination of J- and energy shifting methods result in the following expression for the TRC:

$$k_{\mathrm{J-shift}}^{\mathrm{RD}}(T) = Q_{\mathrm{vib}}^{TS} Q_{\mathrm{rot}}^{TS} k^{J=0}(T). \tag{4.12}$$

The bend-energy shift is always implemented in the current study to account for the 2D nature of the scattering calculations. However, both the J-shifting ($k(T)$) and explicitly summed ($k^{\mathrm{ex}}(T)$) thermal rate constants may be computed as

$$\begin{aligned} k(T) &= \frac{Q_{\mathrm{int}}^{TS}(T)}{hQ_{\mathrm{react}}^{\mathrm{int}}(T)Q_{\mathrm{trans}}^{\mathrm{rel}}(T)} \int_0^\infty dE\ P_c^{J=0}(E)\ e^{-E/k_BT} && (4.13)\\ k^{\mathrm{ex}}(T) &= \kappa \frac{Q_{\mathrm{elec}}^{TS} Q_{\mathrm{vib}}^{TS}(T)}{hQ_{\mathrm{react}}^{\mathrm{int}}(T)Q_{\mathrm{trans}}^{\mathrm{rel}}(T)} \int_0^\infty dE\ \sum_J (2J+1) P_c^J(E)\ e^{-E/k_BT}, && (4.14) \end{aligned}$$

where the latter expression must be weighted by a factor, κ, to account for the

number of identical hydrogens available to abstract[2]. Finally, the state-to-state thermal rate constant within the J-shifting framework is given by:

$$k_{ss'}(T) = \frac{Q_{\text{int}}^{TS}(T)}{hQ_{\text{react}}^{\text{int}}(T)Q_{\text{trans}}^{\text{rel}}(T)} \int_0^\infty dE\ P_{ss'}^{J=0}(E)\ e^{-E/k_BT}. \tag{4.15}$$

4.1.1 Canonical partition functions

Electronic Partition Function. Electronic partition functions are generated by summing over degeneracy weighted low energy electronic states [75]. In general, the excited electronic states are very high in energy in comparison with the ground electronic states, and thus, only the ground state need be included in the partition function in the temperature range of interest. The expression for the partition function is given according to

$$\begin{aligned} Q_{\text{el}} &= \sum_i \text{g}_i e^{-\varepsilon_{\text{el},i}/k_{\text{B}}T} && (4.16)\\ &= \text{g}_0 e^{-0} + 0 \times \sum_{i>0} \text{g}_i e^{-\varepsilon_{\text{el},i}/k_{\text{B}}T} = \text{g}_0 && (4.17) \end{aligned}$$

where g_0 indicates the degeneracy of the ground state and $\varepsilon_{el,i}$ is the electronic energy of state i. The second line of the equation introduces the assumption that the excited electronic states are too high in energy to influence system behaviour, and thus the partition function reduces to the degeneracy of the ground electronic state. For atoms, this degeneracy is $g_0 = 2J + 1$; for molecules, the degeneracy is $g_0 = 2S + 1$, where S is the total spin angular momentum. Thus, for a closed shell molecule $Q_{\text{el}} = 1$; for a doublet radical (such as CH_3), $Q_{\text{el}} = 2(\frac{1}{2}) + 1 = 2$.

For a system where the first excited state is sufficiently low to be of influence,

[2]This factor is normally accounted for in the rotational partition function of the transition state, and is therefore not included in the J-shifted thermal rate constant expression.

the electronic partition function is given by

$$Q_{\mathrm{el}} = \sum_i \mathrm{g}_i e^{-\varepsilon_{\mathrm{el},i}/k_{\mathrm{B}}T} = \mathrm{g}_0 + \mathrm{g}_1 e^{-\Theta_{\mathrm{el}}/T}, \tag{4.18}$$

where g_1 is the degeneracy of the first excited state, T is the temperature and Θ_{el} is the energy gap (in K) between the first excited electronic state and the ground electronic state ($\Theta_{\mathrm{el}} = \Delta\mathrm{E}/k_{\mathrm{B}}$).

Translational Partition Function. The relative translational partition function is given according to [75, 76]

$$Q^{\mathrm{rel}}_{\mathrm{trans}}(T) = q_{trs,x} \times q_{trs,y} \times q_{trs,z} = \left(\frac{2\pi\mu k_{\mathrm{B}}T}{h^2}\right)^{3/2}, \tag{4.19}$$

where μ is the reduced mass of the reactant system.

Vibrational Partition Function. The vibrational partition function is constructed via harmonic oscillator normal mode analysis for polyatomic systems [76]. The individual partition function for each normal mode i is given by

$$q^i_{\mathrm{vib}} = \frac{1}{1 - e^{-hc\nu_i/k_{\mathrm{B}}T}} = \frac{1}{1 - e^{-\Theta_{\mathrm{vib}}/T}}\ , \tag{4.20}$$

where $\beta = 1/k_{\mathrm{B}}T$ and the characteristic vibrational temperature is $\Theta^i_{\mathrm{vib}} = \frac{hc\nu_i}{k_{\mathrm{B}}}$. The total vibrational partition function is the product of the individual vibrational partition functions for each mode:

$$Q_{\mathrm{vib}} = \prod_i^{3N-5(6)} q^i_{\mathrm{vib}}, \tag{4.21}$$

where the 5(6) is for linear (non-linear) molecules, respectively. For TST calculations, the imaginary reaction coordinate frequency is removed and therefore the total number of vibrations in the partition function reduces to $3N-6(7)$. For the energy shifted reduced dimensionality case, one additional mode is projected from the frequencies, and therefore the total number of vibrations in the partition function is further reduced to $3N-7(8)$.

Rotational Partition Function. For a diatomic molecule, the rotational partition function is approximately given according to [75]

$$Q_{\text{rot}} = \frac{T}{\sigma\Theta_r}, \tag{4.22}$$

where σ is the rotational symmetry number, the characteristic rotational temperature is $\Theta_r = \frac{h^2}{8\pi^2 I k_B} = \frac{\hbar^2}{2Ik_B}$, and I is the rotational moment of inertia. For nonlinear molecules, the rotational partition function is extended to

$$Q_{\text{rot}} = \frac{\sqrt{\pi}}{\sigma}\left[\left(\frac{T}{\Theta_{r,x}}\right)\left(\frac{T}{\Theta_{r,y}}\right)\left(\frac{T}{\Theta_{r,z}}\right)\right]^{1/2}, \tag{4.23}$$

where the characteristic rotational temperatures are given according to $\Theta_{r,i}=\frac{h^2}{8\pi^2 I_i k_B}$.

4.2 Dynamics

Conversion of the S and probability matrix elements into dynamical properties such as the integral (σ) and differential $\left(\frac{\mathrm{d}\sigma}{\mathrm{d}\Omega}\right)$ cross sections allow for comparison with experimental results. They are thus useful in providing some information regarding the mechanism of the reaction system. The details of these quantities are presented elsewhere [2,77,78]; it is sufficient here to note that the integral cross section provides a measure of the reactivity of a particular system by predicting

the effective size of its molecular components in the reaction process [78] (it thus has units of area). The differential cross section, on the other hand, is the derivative of the integral cross section with respect to the solid angle, $d\Omega$. It provides information regarding the probability that a product of reaction is scattered in a given solid angle, and has the units area per unit solid angle [2]. The solid angle depends on angles (ϕ, θ). However, for cylindrically symmetric potentials there is no ϕ dependence because of symmetry considerations, and so the differential cross section becomes a function of the deflection angle θ, which is the angle difference between the incident and outgoing trajectories of the collision partners [78]. Both the integral and the differential cross sections can be computed for initial state selected or state to state transitions.

The initial state selected integral reaction cross section, $\sigma_s(E_c^s)$, is calculated according to (in au^2) [2]

$$\sigma_s(E_c^s) = \frac{\pi}{q_s^2} \sum_{s'} \sum_{J=0}^{J_{\max}} (2J+1) P_{ss'}^J(E), \tag{4.24}$$

where the initial translational wavenumber, q_s^2, is computed as

$$q_s^2 = 2\mu_R(E - \varepsilon_s) \tag{4.25}$$

and where the reduced mass of the reactant complex is (for the A + BC reaction)

$$\mu_R = \frac{m_{\mathrm{A}} m_{\mathrm{BC}}}{m_{\mathrm{total}}}. \tag{4.26}$$

The integral cross section is plotted as a function of the collision energy for each initial state, where the collision energy is defined as the initial internal energy of a particular vibrational state s subtracted from the total energy: $E_c^s = E - \varepsilon_s$.

Because of this dependence, a total integral cross section at a given collision energy, $\sigma_{\text{tot}}(E_c^s)$, can only be defined provided the initial population of internal reactant vibrations is known [1]. If such fractions are known for specific experimental conditions, then the total integral cross section may be calculated as the weighted sum

$$\sigma_{\text{tot}} = a\sigma_0(E_c^0) + b\sigma_1(E_c^1) + \dots \ . \tag{4.27}$$

The integral cross section branching ratio provides a useful approach to categorising the relative importance of particular reaction pathways to the overall mechanism. Initial state selected branching ratios may be defined at the same collision energy for different final state distributions, or a total branching ratio may be defined provided the appropriate initial state weighting factors ($a,\ b,\ \dots$) are known. As an example, the branching ratio for nonadiabatic transition in comparison with total reaction may be defined according to the ratio of weighted state selected integral cross sections for the production of nonadiabatic (nonad) products, to the weighted integral cross sections for the production of all available product states.

$$\sigma_{\text{branching}} = \frac{\sigma_{\text{nonad}}}{\sigma_{\text{tot}}} = \frac{a\sigma_{0\to\text{nonad}}(E_c^0) + b\sigma_{1\to\text{nonad}}(E_c^1) + \dots}{a\sigma_{0\to\text{all}}(E_c^0) + b\sigma_{1\to\text{all}}(E_c^1) + \dots} \tag{4.28}$$

The state-to-state differential cross section is defined as follows (in atomic units):

$$\frac{\mathrm{d}\sigma_{ss'}}{\mathrm{d}\Omega}(\theta; E) = \frac{1}{4q_s^2}\left|\sum_J (2J+1) S_{ss'}^J(E) P_J(\cos\theta)\right|^2 , \tag{4.29}$$

where $S_{ss'}$ is the S matrix element for the transition from state s to s', q_s^2 is the translational wavenumber defined in equation (4.25), J is the total angular momentum, and $P_J(\cos\theta)$ is a Legendre polynomial of order J. The differential cross section has parametric energy dependence. It should be noted that in the

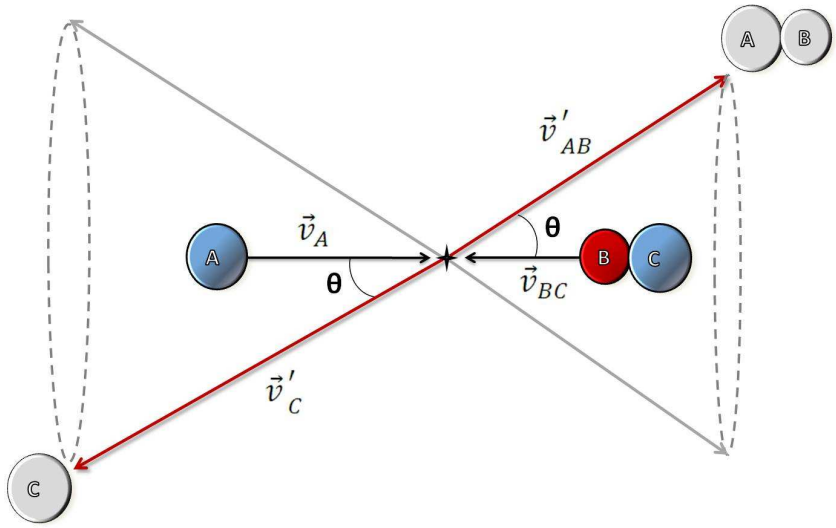

Figure 4.1: Differential cross section deflection angle, θ, for reactive collision A + BC $\rightarrow$ AB + C on a cylindrically symmetric potential. Adapted from reference [78].

present study, because of the complex nature of the scattering S matrix elements, the differential cross sections are not averaged over a number of ρ sectors, but are instead taken from the final sector in ρ.

The angular dependence of a scattering event is shown in Figure 4.1. Reactants A and B–C approach with relative, centre of mass frame velocities $\overrightarrow{v_A}$ and $\overrightarrow{v_{BC}}$, and the products of reaction rebound with velocities $\overrightarrow{v_C}$ and $\overrightarrow{v_{AB}}$. The angular distribution does not depend upon ϕ when the potential is cylindrically symmetric, thus leading to a cone of products with a particular angular distribution with respect to θ. As shown in Figure 4.1, product A–B leaves the reaction complex with an angle θ with respect to the straight-line approach of diatom B–C. In the case of forward scattering (as depicted), this angle is acute; in the case of backwards scattering, the angle becomes obtuse.

4.3 Resonances

Resonances also play a key role in understanding the dynamics of polyatomic collision processes, although with limited quantitative applicability to reduced dimensionality quantum studies. Resonances occur when the system becomes trapped in a particular motion during the reaction process, and lead to sharp Feshbach resonance peaks in the cumulative reaction probability[3]. Analysis of resonances can be performed by analysing the hyperspherical adiabats (δ-dependent eigenvalues as a function of ρ) and predicting bound states in the interaction region where the reactant and product channels coalesce. Furthermore, time-delay analysis can also be used for identification of resonances, along with various other indications, such as shoulders in the integral cross sections [79], or forward-backward peaks in the differential cross section [79].

4.3.1 Time-delay theory

A number of different recent studies use collision time delay as a method of interpreting whether features present in reaction probabilities, integral and differential cross sections pertain to resonances in the reaction process. A good overview of the time-delay method is presented in reference [80], where it is noted that the approach is approximate and is occasionally subject to false positive and negative results. The latter was clearly demonstrated, for example, in the F + HD reaction, where spectral quantisation was instead necessary to identify a peak as a resonance structure [79, 81]. Complications in the time-delay approach may also arise because of overlapping resonances [82]. In the current study, the time-delay analysis is applied cautiously as a first approximation to the interpretation of peaks

[3]In the current study, a Feshbach resonance is taken to mean a resonance occurring due to a reactive transition between two hyperspherical adiabatic channels.

in the CRP.

Physically, a resonance in the context of this study occurs during a reactive collision where energy becomes trapped in a particular motion along the reaction path, or in van der Waals wells in the entrance or exit channels. Such processes can be observed as sharp peaks in the reaction probability. Mathematically, resonances are, by definition, poles in the complex-plane scattering matrix elements and are therefore open to theoretical characterisation [82]. However, identification of resonances experimentally is made more difficult by smearing out of the effects over a large number of rotational (J) and collision energies [80, 83].

The collision time delay method enables one to differentiate resonant and direct scattering mechanisms. The collision time delay (in the Smith formalism [84]) is defined as the amount of time a collision process takes relative to the amount of time that the collision would require if there were no interaction between the particles (essentially, the hypothetical non-existence of the reaction potential) [80, 81].

In order to calculate the collision time delay, one must construct the matrix, $\mathbf{Q}$, such that (assuming a constant value of J)

$$\mathbf{Q} = i\hbar\mathbf{S}^{\dagger}\frac{d\mathbf{S}}{dE}, \tag{4.30}$$

where E is the collision energy, and the $\mathbf{S}^{\dagger}$ is the adjoint of the total scattering matrix. Diagonalization of $\mathbf{Q}$ leads to eigenvalues which are the resonant lifetimes. The resonance lifetime and width may be obtained by fitting a Lorentzian to the largest eigenvalue of the $\mathbf{Q}$-matrix as a function of collision energy [82]. However, this analysis is limited by the fact that it is computationally costly to construct the full $\mathbf{Q}$-matrix, and often only the $\mathbf{S}$-matrix elements associated with reactive collisions are available for analysis. Therefore only the components of $\mathbf{Q}$ pertaining

to reactive collisions are calculated, such that [84][4]

$$Q_{ii}^{R} = i\hbar \sum_{n}^{R \to P} S_{i,n}^{\dagger} \frac{dS_{n,i}}{dE}. \tag{4.31}$$

The elements $\mathbf{Q}_{ii}$ pertain to the average time delay for scattering from initial reactant state i to all final product channels, n [84]. A further simplification involves calculating the total average reactant to product collision time delay, which is weighted by the CRP [81]:

$$\Delta t^{J}(E) = \frac{1}{P_{c}^{J}(E)} \sum_{s's} Re \left[S_{s's}^{J}(E)^{*} \times -i\hbar \frac{d}{dE} S_{s's}^{J}(E) \right], \tag{4.32}$$

where the asterisk signifies complex conjugate. Plotting the collision time delay as a function of energy can identify resonance features; they are interpreted as positive maxima relative to the time-delay baseline [80].

[4]In the present study, the collision time-delay must be calculated by taking numerical finite difference derivatives of the S-matrix elements, which can lead to inaccuracies around narrow isolated resonances [82].

Chapter 5

$CH_3 + CH_4 \longrightarrow CH_3 + CH_4$

The reduced dimensionality method and analysis described in detail in Chapters 2-4 has primarily been restricted to the study of atom + molecule collisions [9–11,13]. In this chapter, application of this method to the title reaction provides the opportunity to evaluate the suitability of generalising the two-dimensional approach to the characterisation of larger, polyatomic reactions. In the following sections, the kinetic (thermal rate constant) and dynamical information concerning this symmetric hydrogen exchange process is computed and compared with available experimental data.

5.1 Introduction

The title reaction and two symmetric isotopic variants:

$$CH_3+CH_4 \rightarrow CH_4+CH_3 \tag{5.1}$$

$$CH_3+DCH_3 \rightarrow CH_3D+CH_3 \tag{5.2}$$

$$CD_3+CD_4 \rightarrow CD_4+CD_3 \tag{5.3}$$

are investigated in order to characterise the reaction rates and dynamics for the main reaction 5.1, and the primary and secondary kinetic isotope effects through study of reactions 5.2 and 5.3, respectively.

This system is of particular importance as it is the simplest reaction of type $CH_3 + RH \longrightarrow CH_4 + R$, a reaction class which is essential for understanding hydrocarbon combustion and thermal decomposition processes [85]. Furthermore, reaction 5.1, along with the ethane + methyl reaction system, forms the basis from which properties of the entire CH_3+RH reaction class may be understood [86]. An increased knowledge of the dynamical and kinetic properties of this reaction class is essential for the accurate modelling of combustion mechanisms, though despite their importance, reactions of this type are not well understood. Clearly detailed quantum characterisations of elementary hydrogen exchange processes are necessary for the continued development of accurate reaction models. Reaction 5.1 is particularly suited to the use of a quantum-based method, given the importance of quantum effects in describing the dynamics of heavy-light-heavy (HLH) reaction systems [52].

A number of different experimental studies have been performed on the reactions 5.1-5.3 [87–91], although because of symmetry, these studies generally involved indirect derivation of the rate constant via comparison with a well characterised reference reaction. Kerr and Parsonage [92], and Arthur and Bell [93], provided separate evaluations of the available experimental data, providing "best estimates" of the thermal rate constant; Kerr suggested a rate constant on the order of 10^{-19} to 10^{-17} cm^3 $molecule^{-1}$ s^{-1} for temperatures ranging between 450 to 800 K, with up to 30% estimated error limits.

There have also been numerous theoretical characterisations of reactions 5.1-5.3 [86,94–101]. The most sophisticated treatment was that of Kungwan *et al.* [86],

where the thermal rate constant of the reaction was predicted by using canonical variational transition state theory (CVT) with small curvature tunnelling corrections (SCT). It was reported that low-temperature tunnelling was a significant effect. Because of the quantum nature of the HLH reaction system, the demonstrated importance of low temperature tunnelling, and the lack of low-temperature experimental TRC data, it is evident that additional characterisation of this reaction with a quantum-based approach is necessary.

The following sections outline the *ab initio* characterisation of reaction 5.1, frequency projection, surface characteristics, and the results of the scattering calculations in comparison with both previous theoretical works as well as experimental studies.

5.2 Potential energy surface development

5.2.1 *Ab initio* calculations

Stationary point characterisation. Geometry optimisations and frequency calculations for stationary points were calculated at the MP2/cc-pVTZ level of theory, with single-point energy corrections at the CCSD(T)//cc-pVTZ level of theory. All calculations were performed using the Gaussian 03 electronic structure package [61], without symmetry constraints. Geometry and frequency calculations compared favourably with high level QCISD/cc-pVDZ calculations [86], thus providing justification for the choice of basis set method. The reactant molecules were characterised assuming infinite separation in the asymptotic region. The stationary point geometries are given in Figure 5.1, where it is easy to see that the TS has a collinear geometry. Furthermore, intrinsic reaction coordinate calculations characterising the minimum energy path indicated a collinear reaction path, thus providing further justification for the current choice of a collinear 2D scattering method.

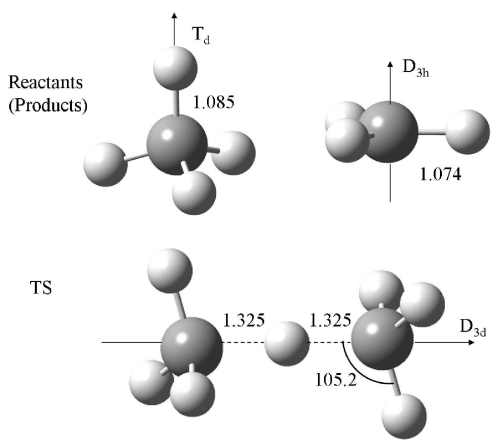

Figure 5.1: Stationary points geometries and symmetry point groups for the $CH_3 + CH_4 \rightarrow CH_4 + CH_3$ reaction. Bond lengths and angles given in angstroms and degrees, respectively.

Table 5.1: Rotational moments of inertia for stationary points of reaction CH_3 + CH_4 (amu Bohr^2).

Species	Point Group	σ	I_a	I_b	I_c
CH_3	D_{3h}	6	6.23	6.23	12.46
CH_4	D_{3h}	12	11.31	11.31	11.31
TS 5.1 [a]	D_{3h}	6	23.59	218.16	218.16
CH_3D	D_{3h}	3	11.31	15.29	15.29
CD_4	D_{3h}	12	22.60	22.60	22.60
CD_3	D_{3h}	6	12.45	12.46	24.91
TS 5.2 [b]	D_{3h}	6	23.59	218.16	218.16
TS 5.3 [c]	D_{3h}	6	47.15	285.73	285.73

[a] CH_3HCH_3; [b] CH_3DCH_3; [c] CD_3DCD_3

The point groups, symmetry numbers, and rotational moments of inertia of the reactants and transition states are given in Table 5.1. The harmonic frequencies for the stationary points of the three abstraction reactions are given in Table 5.2, along with the pre and post- projected frequencies of the transition state using the rectilinear projection method.

The CCSD(T) single point energy corrections for the stationary points are presented in Table 5.3, along with the *ab initio* barrier heights of reactions 5.1-5.3. The zero-point energy corrected barrier height for the main reaction is 17.7 kcal mol^{-1}, in comparison with 18.6 and 17.9 kcal mol^{-1} for reactions 5.2 and 5.3, respectively. Isotopic substitution leads to an increase in the barrier height in both cases, though the effect is greater in the case of substituting the transferring deuterium only (reaction 5.2) as the zero-point energy decrease in the reactants is more pronounced relative to the transition state.

Grid development. The grid points for the construction of the PES were developed using the same CCSD(T)/cc-pVTZ//MP2/cc-pVTZ approach. Furthermore, the process was simplified because of the symmetry of the reaction system, such that only 1/2 of the grid points were required to be computed explicitly with

Table 5.2: Stationary point harmonic frequencies at the MP2/cc-pVTZ level, in cm^{-1}. (Degeneracy in parentheses). TS frequencies prior to (pre) and following (post) rectilinear projection.

Species	Frequencies				
CH_3	486.2	1445.4	1445.5	3177.9	3368.9 (2)
CH_4	1350.1 (3)	1586.3 (2)	3075.0	3210.8 (3)	
CD_3	376.9	1063.5 (2)	2248.0	2510.8 (2)	
CD_4	1020.5 (3)	1122.1 (2)	2175.2	2377.3 (3)	
CH_3D	1193.3 (2)	1344.3	1522.1 (2)	2321.3	3115.0
	3210.5 (2)				
TS 5.1 (pre)	1949.8 i	48.5	322.5 (2)	540.8	706.2 (2)
	1164.5	1197.7	1375.7 (2)	1463.1 (2)	1489.9 (2)
	3109.2	3110.6	3257.4 (2)	3257.8 (2)	
TS 5.1 (post)		48.5	322.5 (2)		706.2(2)
	1052.3	1074.6	1375.7(2)	1463.1(2)	1489.9(2)
	3109.2	3090.0	3257.4(2)	3257.8(2)	
TS 5.2 (pre)	1454.0 i	48.5	295.8 (2)	540.8	706.2 (2)
	1098.1 (2)	1154.5	1164.5	1462.9 (2)	1463.1 (2)
	3108.8	3110.6	3257.4 (2)	3257.8 (2)	
TS 5.2 (post)		48.5	295.8 (2)		706.2 (2)
	1098.1 (2)	1052.3	1070.8	1462.9 (2)	1463.1 (2)
	3108.5	3090.0	3257.4 (2)	3257.8 (2)	
TS 5.3 (pre)	1434.5 i	34.3	228.6 (2)	477.0	528.7 (2)
	897.0	927.1	1012.8 (2)	1065.5 (2)	1066.5 (2)
	2212.4	2216.7	2419.4 (2)	2420.0 (2)	
TS 5.3 (post)		34.3	228.6 (2)		528.7 (2)
	744.4	820.7	1012.8 (2)	1065.5 (2)	1066.5 (2)
	2212.2	2185.8	2419.4 (2)	2420.0 (2)	

electronic structure theory calculations. Furthermore, the T_1 diagnostic [102, 103] was monitored throughout in order to test the applicability of the single reference CCSD(T) method; it was determined that this value ranged from 0.01 in the interaction region to 0.06 for asymptotic values of ρ. This indicates that the accuracy of the energies decreases far into the asymptotic region, where the system possesses more radical-like behaviour. However, the T_1 diagnostic remained below 0.02 along the MEP, thus justifying the use of the single reference approach [102, 103]. Grid points were developed from $\delta = 0$ to $\delta = \delta_{\max}$ and from $\rho = 8.87$ to $\rho = 15$

Table 5.3: Single point and zero-point energies for reaction stationary points at CCSD(T)/cc-pVTZ//MP2/cc-pVTZ level of theory.

	Energies	ZPE
Molecular energies (Hartree)		
CH_3	-39.7609	0.03028
CH_4	-40.4381	0.04540
CH_3–H_a–CH_3 (TS 5.1)	-80.1701	0.07499
CD_3	-39.7609	0.02228
CD_4	-40.4381	0.03331
CH_3D	-40.4381	0.04247
CH_3–D_a–CH_3 (TS 5.2)	-80.1701	0.07343
CD_3–D_a–CD_3 (TS 5.3)	-80.1701	0.05527
Reaction energetics (kcal mol^{-1})		
ΔV (TS5.1)	18.1422	
ΔV_a^G (TS5.1)	17.7048	
ΔV_a^G (TS5.2)	18.5633	
ΔV_a^G (TS5.3)	17.9322	

au. Points generated from the MEP calculation were included, as were grid values perpendicular to the MEP at the saddle point. In addition to the frequency and geometry calculations and the subsequent single point energy calculations, projection of the active modes from the ZPE was required in order to obtain the corrected grid points to fit an effective potential energy surface.

5.2.2 Frequency projection

Development of an effective potential energy surface requires projection of the active modes from the Hessian to calculate the spectator-mode zero-point energy corrections. Both the rectilinear and curvilinear schemes can be used in this projection, and in order to evaluate the efficacy of the projection schemes, both are implemented and the scattering results are compared. At stationary points such as the TS, the pre-projected frequencies should be identical in both the curvilinear and rectilinear schemes. The pre- and post- projected frequencies displayed

in Table 5.2 are from the rectilinear method, and can be used to interpret the effect of projection on active mode contributions. Two active modes are projected – the imaginary frequency corresponding to the reaction coordinate, and the stretch vibration at 540.8 cm^{-1}. In general, it can be seen that the active modes do not couple substantially to the spectator modes, thus validating the use of the two-dimensional scattering approach. There is minor coupling associated with the modes at 1164.5 and 1197.7 cm^{-1}, which decrease by 9.6 and 10.3% post-projection. These vibrational modes correspond to umbrella motion of the methyl groups (with additional vibration of the transferring hydrogen in the case of the latter mode), and therefore it is unsurprising that this degree of coupling is observed. The symmetric CH_3 stretch at 3110.6 cm^{-1}, corresponding to motion of the carbon atoms along the D_{3d} axis, also has minor coupling leading to a 0.6% post-projection frequency reduction. The combined effect of the reduction due to coupling of the active modes to these three vibrations likely causes a ZPE decrease across the potential (i.e. 5.8×10^{-4} au at TS). Similar trends are seen for coupling in the deuterated reaction systems.

The current application of the curvilinear projection method defines eight internal bond lengths, one doubly-degenerate linear angle bend, six bond angles, and four bond angles from the methyl moieties (two from each). In this description, the mode associated with hindered internal rotation is neglected (48.5 cm^{-1} at the TS). In the curvilinear approach, the neglect of this mode is considered to have minimal effect across the surface; however, for computing the TS vibrational partition function, the post-projected rectilinear frequencies are used to calculate the thermal rate constants for both projection scheme results.

One of the disadvantages of the rectilinear projection scheme is the tendency to introduce unphysical imaginary frequencies across the grid of the PES. Imaginary

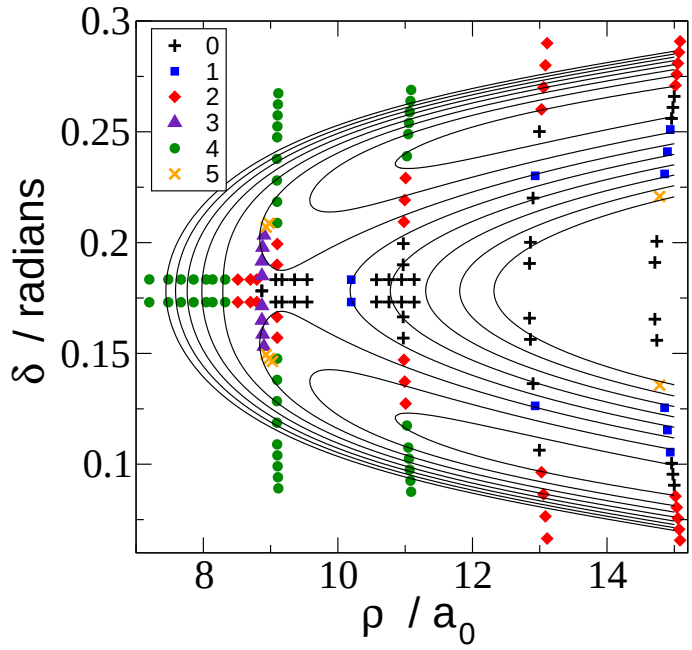

Figure 5.2: Rectilinear projection scheme applied to *ab initio* grid points for the $CH_3 + CH_4 \longrightarrow CH_4 + CH_3$ reaction. Number of post-projection imaginary frequencies greater than 100 cm^{-1} as indicated in legend. Contour of the symmetric potential energy surface is shown in solid black in the background.

frequencies are set to zero in determining the ZPE correction and therefore result in a decrease in the ZPE correction to the effective potential [14, 15]. Across the two dimensional potential energy grid, the number of imaginary frequencies with respect to geometry is plotted in Figure 5.2. There is a clear trend for an increased number of imaginary frequencies along the outer edges of the potential and along the minimum energy path near the transition state. This is indicative that use of the rectilinear approach could result in a loss of ZPE in these regions, thereby rendering inaccurate in the final fit the surface barrier height and the steepness of the outer edges of the double-Morse wells. The curvilinear approach, on the other hand, did not result in any imaginary frequencies for this system, and thus the ZPE corrections along the outer edges of the surface and along the MEP are higher for the curvilinear than the rectilinear approach [15].

Table 5.4: Potential energy function and definitions. ($\delta_{\min}$ location is defined as the location of the δ minimum of the Morse function as ρ varies.)

	Expression	Description
f	$(1 + c_1(\rho)^{c_2} e^{c_3(\rho)})c_4$	TS location
g	$c_5 + c_6\rho + c_7\rho^2$	Well width
h_1	$\frac{(c_8+c_9\rho+c_{10}\rho^2)-\log(c_{11}+c_{12}\rho+c_{13}\rho^2)}{c_{14}+c_{15}\rho+c_{16}\rho^2}$	$\delta_{\min}$ location
h_2	$\delta_{\max} - h_1$	$\delta_{\min}$ location
c	c_{17}	Well depth
c''	c_{18}	Well depth

5.2.3 Potential energy surface function

The symmetric analytical double Morse function used in the current study is given according to equation (5.4) and Table 5.4. The form of the function chosen enforces the inherent symmetry of the reaction system. The parameters used in the final fit of the curvilinear and rectilinear surfaces for the main reaction 5.1 are given in Table 5.5.

$$V(\rho, \delta) = f\left[\left(1 - e^{g(h_1-\delta)}\right) + \left(1 - e^{g(\delta-h_2)}\right)^2 - 2c\right] + c'' \tag{5.4}$$

Initial input parameters were generated by eye and based upon physical significance (Table 5.4). A serial nonlinear least squares regression fitting procedure was used [13] such that the surface was fit accurately for low energies (but the final energy cut-off was high enough to be above the total energy ($E_c + \varepsilon_s$)). Convergence was monitored by noting the physical correspondence between the potential and the *ab initio* points, as indicated by the sum of squared residuals (SSR). A total of 138 grid points were used in the fit, resulting in an SSR of 9×10^{-4} and 1.1×10^{-3} au^2 for the curvilinear and rectilinear surfaces, respectively.

As the curvilinear surface more accurately reflects the behaviour of the spectator ZPEs, this surface is used to generate the majority of the dynamics results

Table 5.5: Potential energy surface parameters for $CH_3 + CH_4 \longrightarrow CH_4 + CH_3$.

	Curvilinear	Rectilinear
c_1	14.566357	13.278464
c_2	-0.474389	-0.248734
c_3	-0.484526	-0.534803
c_4	0.332118	0.309091
c_5	1.121871	0.197754
c_6	2.504157	2.738426
c_7	-0.086424	-0.094994
c_8	11.311948	11.297201
c_9	0.279914	0.284996
c_{10}	-0.009328	-0.009161
c_{11}	8503.881320	8503.839979
c_{12}	1882.029393	1882.063888
c_{13}	-37.722341	-37.737967
c_{14}	-0.607851	-0.807658
c_{15}	3.118215	3.118229
c_{16}	-0.046316	-0.039376
c_{17}	-2.972006	-2.996391
c_{18}	-82.423837	-82.280410

in the following sections (though the thermal rate constants for both surfaces are compared). Therefore, the properties and quality of the curvilinear surface are analysed in detail. The close correspondence between the analytical surface and the *ab initio* data points used in the fitting procedure is shown via analysis of slices through ρ in the interaction and asymptotic regions in Figure 5.3(a). The typical double-Morse behaviour in the asymptotic region is observed, with the wells coalescing near the transition state. A contour diagram of this potential is given in Figure 5.3(b), from which the symmetry about the transition state is obvious.

The properties of both potentials are summarised in Table 5.6, where E_{shift} represents the zero of energy on the surface, E_{TS} is the transition state energy, $E_{vdw,r/p}$ is the minimum of energy in the reactant or product wells (van der Waal (vdW) energy, where present), $E_{r/p}$ is the asymptotic reactant or product minimum energy, $\Delta V_{rev/for}$ is the barrier height on the surface, ΔH is the reaction

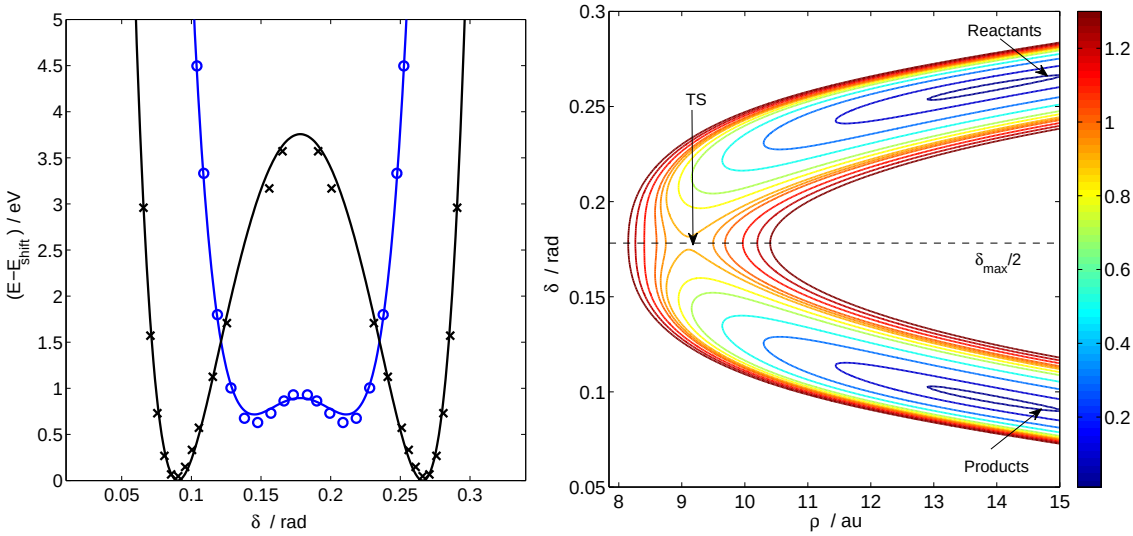

Figure 5.3: **Left:** Fitted $V(\rho, \delta)$ (lines) and *ab initio* grid data (points) for values of ρ approximately pertaining to the asymptotic and interaction regions. Black lines: $\rho = 15$, blue lines: $\rho = 9.1$. Data points: Black crosses: *ab initio* data ranging from 14.9-15.1 au; blue circles: *ab initio* data at 9.1 au. **Right:** Contour diagram of the symmetric fitted potential $V(\rho, \delta)$ for the $CH_3 + CH_4$ reaction at hyperspherical coordinate values surrounding the TS. Relative energies for contour height, $E\text{-}E_{shift}$, are given in eV. The contours are not evenly spaced, but are shown for energies: 0.01, 0.1, 0.3, 0.5, 0.7, 0.8, 0.9, 0.95, 1.0, 1.1, 1.2, 1.3 eV.

enthalpy, $E_{r/p} - E_{vdW,r/p}$ is the depth of the vdW well, and ΔV_{vdW} is the barrier height from the bottom of the vdW well. Furthermore, the locations of the transition state (surface saddle point) and vdW well are given (ρ_{TS}, δ_{TS} and ρ_{vdw}, δ_{vdw}, respectively). The barrier height on the curvilinear surface, 20.6 kcal mol^{-1}, is larger than that predicted by *ab initio* methods; this is certainly due to the projection of the active mode contribution from the ZPE. The use of the more accurate analytical curvilinear method to develop the surface leads to an increase in the surface barrier height of 0.44 kcal mol^{-1}. The δ-coordinate of the TS on the surface is unaffected by the projection method, though a slightly different ρ value is obtained on the rectilinear surface as compared to its curvilinear analogue, though this could be an artifact of the surface fitting procedure.

Table 5.6: Energetic properties of curvilinear and rectilinear potential energy surfaces for reaction $CH_3 + CH_4$. Energies given in kcal mol^{-1} .

	Curvilinear	Rectilinear
E_{shift}	-80.1325592	-80.1316579
$E_{TS} - E_{shift}$	20.8379	20.4489
$E_{vdw,r/p} - E_{shift}$	0.0000	0.0000
$E_{r/p} - E_{shift}$	0.2065	0.2528
$\Delta V_{rev/for}$	20.6314	20.1962
ΔH	0.0000	0.0000
$E_{r/p} - E_{vdW,r/p}$	0.2065	0.2528
ΔV_{vdW}	20.8379	20.4489
ρ_{TS} / au	9.1053	8.9850
δ_{TS} / rad	0.1788	0.1788
$\rho_{vdw,r}$ / au	13.8772	13.5363
$\delta_{vdw,r/p}$ / rad	0.0965/0.2598	0.0977/0.2586

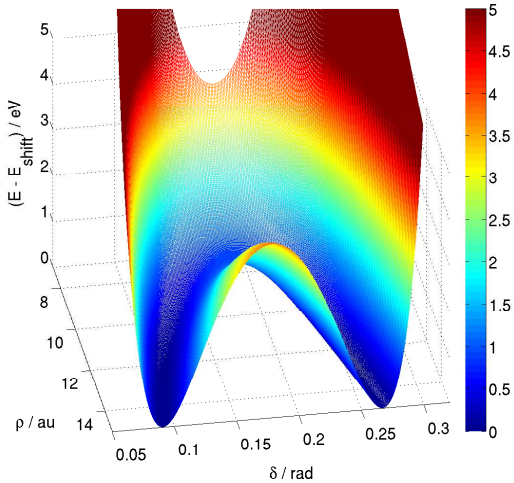

(a) Curvilinear symmetric potential $V(\rho, \delta)$.

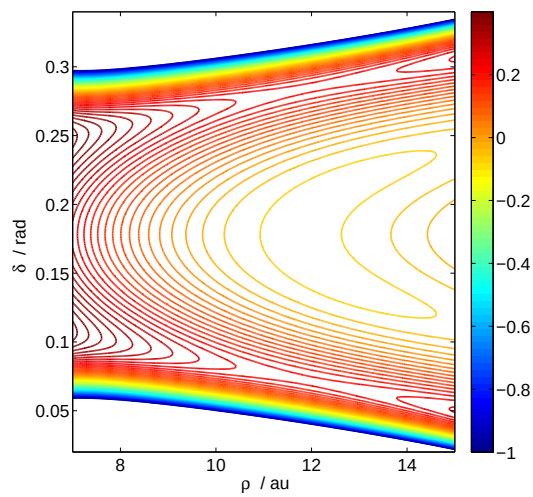

(b) Contour diagram of the energy difference between the curvilinear and rectilinear potential energy surfaces. (Curvilinear – rectilinear). 70 contour lines are evenly spaced from -1.0 eV to 0.4 eV.

Figure 5.4: Curvilinear and rectilinear potential energy surfaces for the $CH_3 + CH_4 \rightarrow CH_4 + CH_3$ reaction.

The curvilinear surface is displayed in Figure 5.4(a). Comparison of the properties of the rectilinear and curvilinear surfaces is exhibited in Figure 5.4(b). It is clear to see that the curvilinear surface has a positive difference along the MEP

and especially behind the transition state in comparison with the rectilinear surface. This is consistent with the conclusions concerning the loss of magnitude of ZPE in the rectilinear scheme because of imaginary frequencies in this region (section 5.2.2). In the centre, asymptotic fragmentation zone, there is little difference between the two approaches. At very high energies along the edge of the coordinate space, the rectilinear surface has increased magnitude, but this effect would not be significant for low energy scattering results.

5.3 Scattering results

5.3.1 Numerical details

Scattering was performed with the inelastic single surface R-matrix propagation described in Chapter 2. Tests monitored the convergence of the cumulative reaction probabilities, hyperspherical adiabatic energies, and integral and differential cross sections with respect to the scattering parameters and definitions listed in Table 5.7. Although symmetrisation of the DVR basis eigenfunctions would be required for this symmetric reaction [104], in the current study degeneracy is instead lifted by adding a slight perturbation of 1×10^{-5} au to the potential $V(\rho,\delta)$ for δ values greater than $\frac{\delta_{\max}}{2}$. Minimum oscillatory behaviour of the hyperspherical adiabats was observed in the asymptotic region. The probability matrix elements were therefore averaged over the final 15% of ρ sectors, a value consistent with that used in previous studies [12, 13]. At 2.17 eV, there is a maximum of 14 open channels for the $J = 0$ calculation (this decreases with J due to an increase in the centrifugal barrier height), and therefore the size of the contracted basis is held at $N = 16$ for all J values.

Table 5.7: Scattering numerical parameters for the $CH_3 + CH_4 \longrightarrow CH_4 + CH_3$ calculation.

Parameter	Final Value	Description
$\rho_{\min}$	7.4 au	First ρ sector (behind TS)
$\rho_{\max}$	15 au	Final asymptotic ρ sector
N_ρ	400	Number of ρ sectors
S_{num}	60	Number of ρ sectors to average $P_{ss'}$
N_δ	300	Size of DVR basis
$E_{\max}$	2.17 eV	Maximum incident KE
E_{inc}	0.001 eV	Energy scaling
N	16	Contracted basis size
$J_{\max}$	250	Maximum total angular momentum

5.3.2 Hyperspherical adiabats

The open channel hyperspherical adiabats for the $J = 0$ results are shown in Figure 5.5. Asymptotic degeneracy of reactant and product hyperspherical adiabats arises from the symmetry of the reaction system, though this degeneracy is broken in the interaction region, where adiabats form deep wells capable of supporting bound states. These wells are present from the third reactant hyperspherical adiabat. Note that the first and second reactant hyperspherical adiabats (corresponding to the first two reaction channels) open at approximately the same total energy level. The TS energy occurs just at the opening of the first reaction channel, thus indicating that reactions out of state $s = 0$ are the main contribution to tunnelling effects.

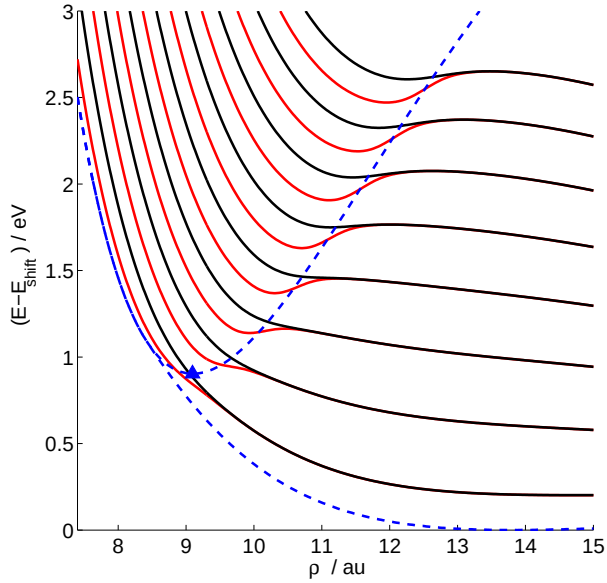

Figure 5.5: Hyperspherical adiabats for scattering on the symmetric potential $V(\rho, \delta)$ for the $CH_3 + CH_4$ reaction. Blue triangle is the TS; lower blue dashed line is the minimum energy path along the reactant channel and upper blue dashed line is the potential as a function of ρ along the δ value of the TS.

5.3.3 Reaction probabilities

The cumulative reaction probability is shown in Figure 5.6, where inclusion of the surface barrier height highlights the importance of quantum tunnelling to the reaction process[1]. Broad oscillations are a prominent feature in the CRP, along with the presence of clusters of sharp resonance peaks that increase in number with energy. The state-to-state reaction probabilities (SSRP) are shown in Figure 5.7. The reaction is seen to be primarily vibrationally adiabatic with only minor contributions from vibrationally non-adiabatic transitions, contributions which increase with collision energy. Oscillations evident in the CRP are also present in the state-to-state probabilities; these are especially clear for the $0 \rightarrow s'$ and $1 \rightarrow s'$ transitions. Oscillating reaction probability arises because of the symmetry of the reaction system, which causes quantum interference effects between the degenerate

[1]Note that the barrier height is shifted by 0.2017 eV because the CRP is plotted in an $E - E_0$ scale; the barrier height for this plot is thus 0.7019 eV.

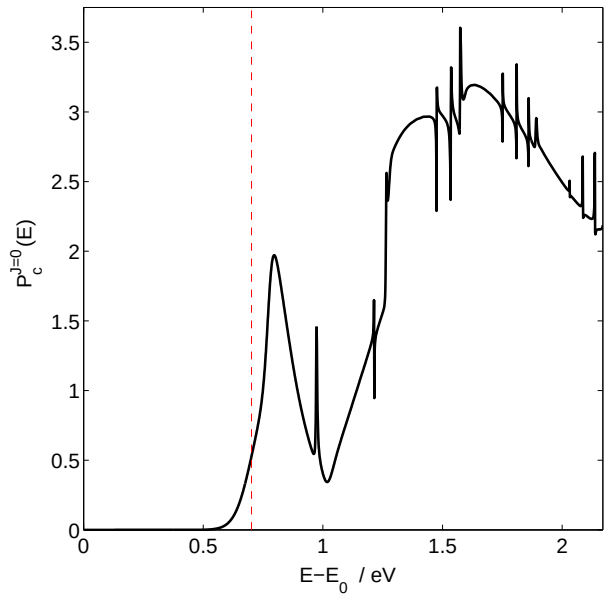

Figure 5.6: Cumulative reaction probability ($J = 0$) for the $CH_3 + CH_4$ reaction as a function of total energy (solid line). The surface barrier height of 0.7019 eV is included to highlight tunnelling probability (dashed red line).

hyperspherical adiabatic potentials. This effect has been studied extensively for triatomic HLH collision processes [52, 105].

5.3.4 Resonances

The presence of clusters of sharp peaks in the CRP indicated the possibility of bound state resonances in the interaction region. In order to further analyse the presence of resonances, 13 of the peaks were characterised by predicting bound state energies in the hyperspherical adiabatic wells in combination with the time delay analysis discussed in Chapter 4.

Analysis of the bound states on the hyperspherical adiabatic potentials involved using one-dimensional DVR to predict the bound state energies. The potential for the one-dimensional DVR was restricted to the ρ interval below the local maximum, as indicated by a red star in Figure 5.8. It was found that the predicted bound states agreed favourably with the location of the resonance peaks in the CRP,

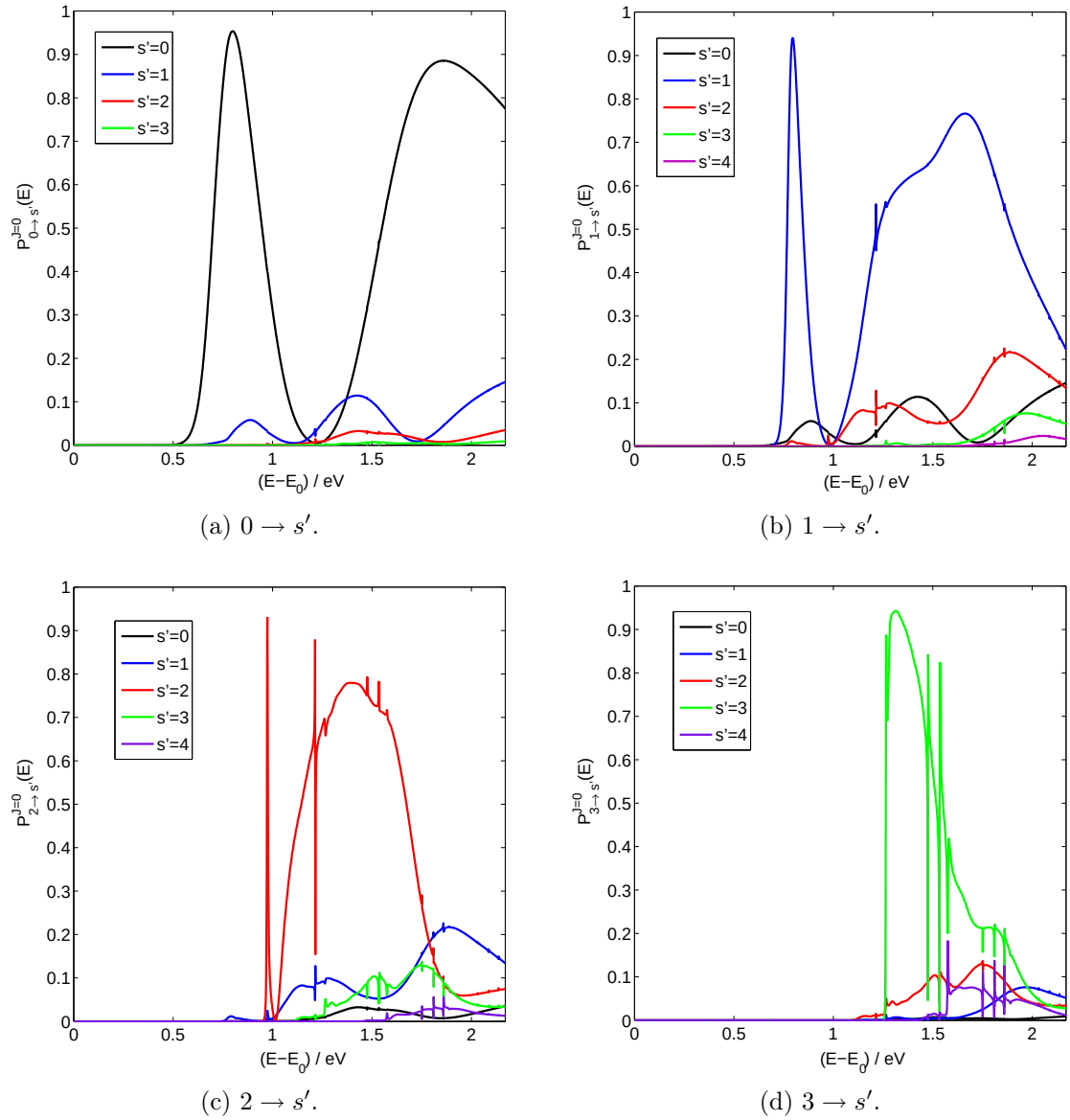

(a) $0 \to s'$. (b) $1 \to s'$.

(c) $2 \to s'$. (d) $3 \to s'$.

Figure 5.7: State-to-state ($s \to s'$) reaction probabilities for $CH_3 + CH_4 \longrightarrow CH_4 + CH_3$ for $J = 0$.

within a given energy correction most likely relating to inaccuracy in assuming a cut-off potential. The semi-quantitative assignment of resonance features is given in Table 5.8, where it can be seen that the mean energy correction factor is 0.014 eV.

Time-delay analysis was also used to analyse the presence of resonances in the

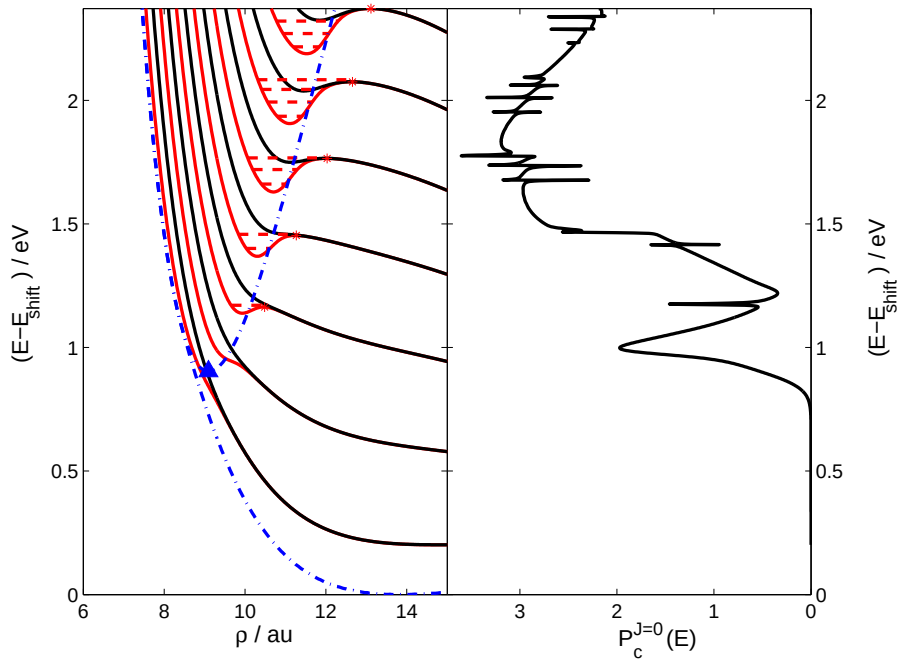

Figure 5.8: **Left**: Hyperspherical adiabatic potentials in the interaction region (solid lines); potential exit well minimum and potential along ρ at fixed δ TS location (dotted blue lines); potential TS (blue triangle); and predicted metastable bound state energies (dashed red lines). **Right**: Cumulative $J = 0$ reaction probability for the $CH_3 + CH_4$ reaction (solid line).

Table 5.8: Hyperspherical adiabat bound state energies for the CH_3+CH_4 reaction. Energies given relative to potential minimum, E_{shift}. TD refers to the confirmation of resonance via time delay. E_{Diff}=E_{CRP}− E_{DIVAH}.

Transition	Level	E_{DIVAH} / eV	E_{CRP} / eV	E_{Diff} / eV	TD (y/n)
$\nu = 2$	0	1.171	1.176	0.005	y
$\nu = 3$	0	1.401	1.416	0.015	y
	1	1.458	1.468	0.010	y
$\nu = 4$	0	1.661	1.677	0.016	y
	1	1.720	1.736	0.016	y
	2	1.768	1.775	0.007	y
$\nu = 5$	0	1.936	1.953	0.017	y
	1	1.993	2.011	0.018	y
	2	2.044	2.061	0.017	y
	3	2.084	2.094	0.010	n
$\nu = 6$	0	2.217	2.233	0.016	y
	1	2.271	2.288	0.017	y
	2	2.321	2.339	0.018	y

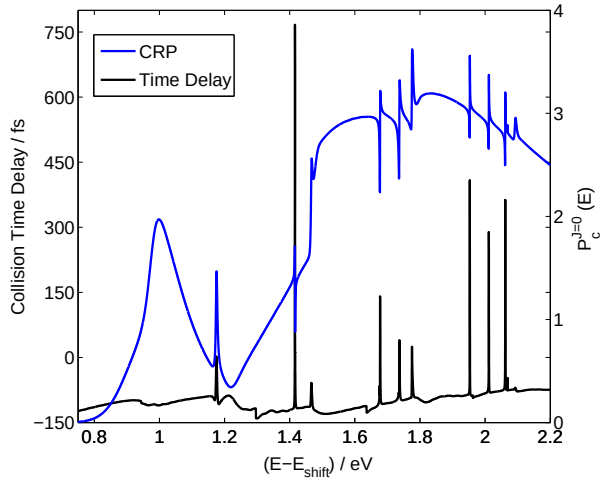

Figure 5.9: Time delay analysis for identification of resonances in the $CH_3 + CH_4 \rightarrow CH_4 + CH_3$ reaction (black). $J = 0$ cumulative reaction probability (blue).

CRP[2]. Positive maxima were used to confirm resonant behaviour[3], all resonances bar one predicted by analysis of the hyperspherical adiabats were confirmed by time-delay analysis (Table 5.8).

A qualitative physical interpretation of the type of motion associated with the resonances can be made. The current study only treats two active modes associated with C-H-C stretching vibrations, and therefore the bound state resonances must be interpreted as energy trapped in motion in both ρ and δ in the TS region. Thus, a combination of H chattering between the two heavy groups and heavy atom breathing of the two methyl groups towards each other must contribute to the resonance features in the CRP. Vibrationally bonded states for HLH reactions have been investigated in detail – for example, for the I + HI reaction system [106]. For the current system, bound states resonances are only observed for $s \geq 2$, and therefore experimentally accessible vibrationally bonded states are unlikely.

[2]For time-delay calculations increased resolution with $E_{\text{inc}} = 1 \times 10^{-4}$ eV was required in order to obtain accurate finite difference derivatives of the S-matrix elements.

[3]Positive relative to the negative time-delay baseline. The well defined time-delay maximum at 1.468 eV pertains to a resonance despite the time-delay peak not extending above 0 on a total energy scale.

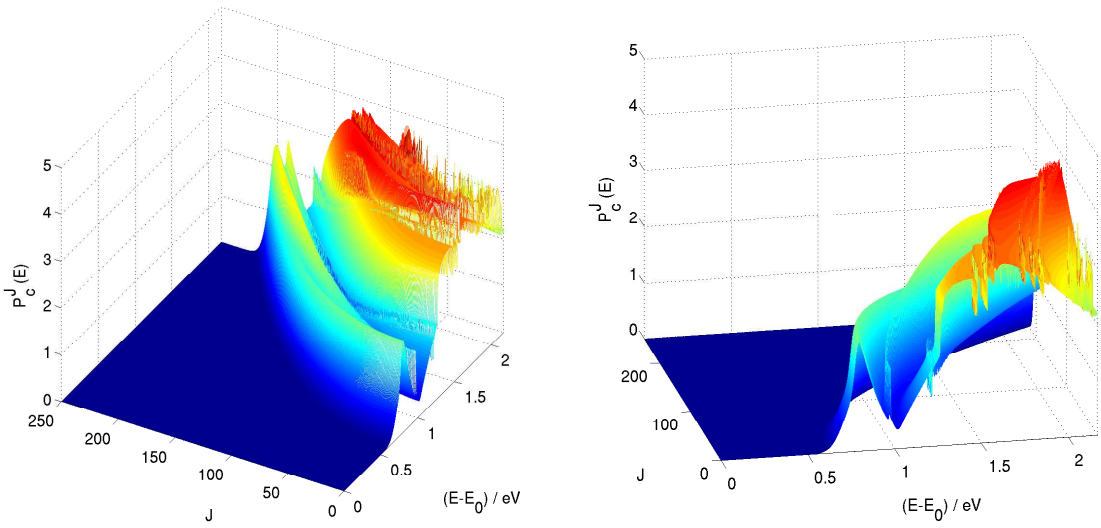

Figure 5.10: Two perspectives of the angular momentum (J) dependence of the $CH_3 + CH_4$ cumulative reaction probability.

5.3.5 J>0 Dynamics: Integral and differential cross sections

Angular dependence of the CRP. Scattering calculations were performed up to a total angular momentum value of $J = 250$. The J-dependence of the cumulative reaction probability from two different perspectives is shown in Figure 5.10. Many of the resonance features are preserved for higher angular momentum values, but shifted to higher collision energies because of the effect of the centrifugal barrier.

Integral Cross Section. The initial state selected (ISS) integral cross sections were calculated as described in Chapter 4 and are shown in Figure 5.11 as a function of collision energy[4]. The integral cross sections show a number of features, most notably a delay in the onset of reaction after the total energy reaches the level of the initial vibrational state $E - E_i = 0$ – a feature that is not, for example, reproduced in the exothermic $CH_3 + HCl$ study discussed in Chapter 6. This

[4]Note that as calculations are performed on a total energy scale, the collision energy data available varies for each initial state.

onset does, however, decrease with the level of initial vibrational excitation, s. Furthermore, each ISS cross section is associated with a sharp rise in the cross section value, followed by levelling out at high collision energies. As with the reaction probabilities, the main contribution to the ISS cross sections occurs via vibrationally adiabatic pathways.

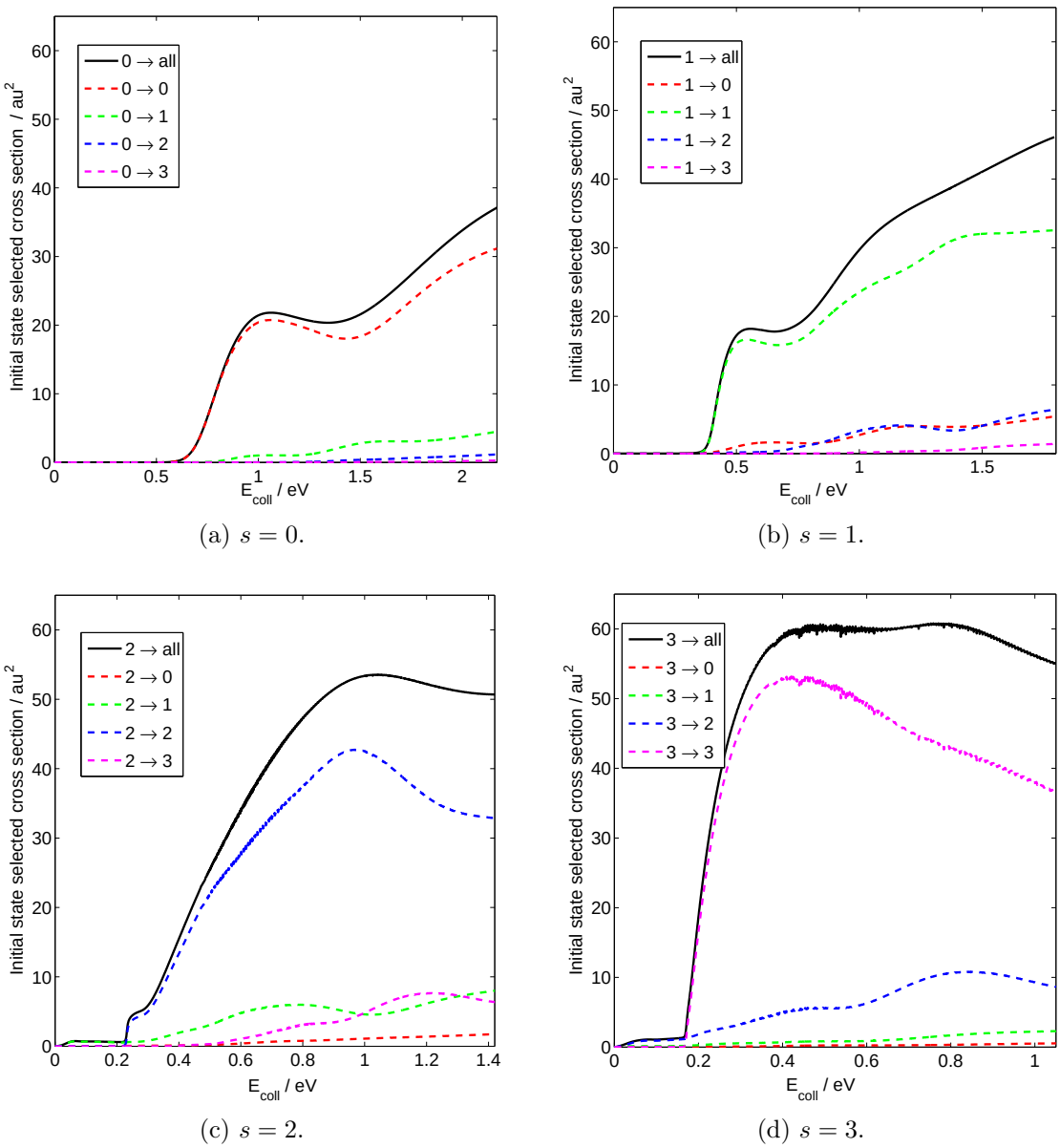

(a) $s = 0$.

(b) $s = 1$.

(c) $s = 2$.

(d) $s = 3$.

Figure 5.11: Initial state (s) selected integral cross sections for the $CH_3 + CH_4$ reaction system.

Differential Cross Section. The differential cross section was calculated for the 0→0 transition, and was shown to be exclusively backward scattered, with increased sideways scattering at higher collision energies (though the majority of the cross section magnitude occurred for reactive scattering angles above 170^{o}). This trend is expected, given that this system involves the collinear collision of two bulky polyatomic groups. The restriction to collinearity neglects the effects of stripping mechanisms. Therefore the current differential cross section predictions can only be qualitatively interpreted with the caveat that some forward scattering mechanisms are neglected in the model.

The 0→0 differential cross section is shown in Figure 5.12, for select collision energies in (a) and as a contour diagram to highlight dependence on collision energy in (b). In (a), the large value of the differential cross section at 180 degrees is expected; integration including the volume element $\sin\theta$ reproduces integral cross section values.

At high collision energies, there appear to be broad oscillations present in the differential cross section. In some studies on HLH systems, these oscillatory features have been indicative of resonance structure [107].

5.3.6 Thermal rate constant

The thermal rate constant was calculated and compared with available experimental and theoretical kinetic data, both of which are summarised for completeness in the following sections.

Experimental Kinetic Results. The experimental kinetic data is evaluated from indirect experimental studies for reaction 5.1. Estimates for the parameters for the Arrhenius expression, $k(T) = A\mathrm{e}^{-\mathrm{E_a/RT}}$, were obtained in two separate studies. For Arthur and Bell [93], the rate constant expression over the temperature

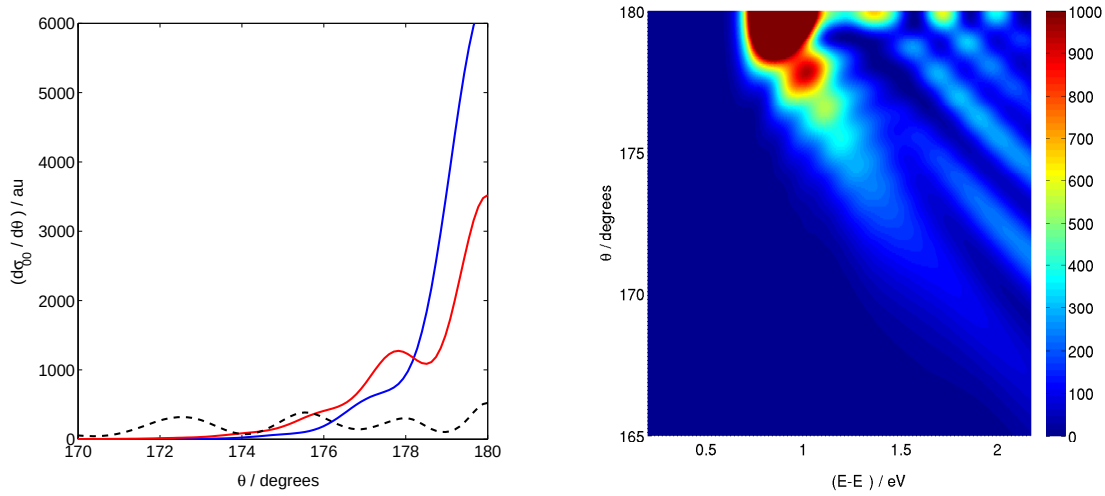

(a) (b)

Figure 5.12: Energy dependence of the $0 \rightarrow 0$ differential cross section for the $CH_3 + CH_4 \longrightarrow CH_4 + CH_3$ reaction system. (a): For three collision energies, E_c (eV): 0.886 (blue), 0.995 (red) and 2.000 (black). (b): As a function of collision energy.

range $298 - 473$ K was determined as given by equation (5.5), and by equation (5.6) for Kerr and Parsonage [92] over the temperature range $450 - 800$ K (where R is the universal gas constant).

$$k(T) = 10^{11.8} e^{\frac{-14.51 \text{kcal mol}^{-1}}{RT}} \text{cm}^3 \text{ mol}^{-1} \ s^{-1} \tag{5.5}$$

$$k(T) = 10^{(8.60 \pm 0.2 - 14.0 \pm 0.5 \text{ kcal mol}^{-1}/(2.3RT))} \text{dm}^3 \text{ mol}^{-1} \ s^{-1} \ . \tag{5.6}$$

The independent TRC evaluations in these two studies give nearly identical results over the reduced temperature range specified by Kerr.

Theoretical Kinetic Results. The J-shifted thermal rate constant results for both rectilinear and curvilinear surfaces are given in Table 5.9 along with the CVT/SCT/HR[5] results of Kungwan and Truong [86]. Transition state theory

[5]Canonical variational transition state theory with small curvature tunnelling correction and hindered rotor treatment of one vibrational mode.

Table 5.9: Theoretical thermal rate constants for $CH_3 + CH_4 \longrightarrow CH_4 + CH_3$ (cm^3 $molecule^{-1}$ s^{-1}, powers of 10 in parentheses) .

T / K	TST	CVT/SCT/HR	Curvilinear	Rectilinear
150	7.44(-38)		5.55(-29)	1.57(-28)
180	1.27(-33)		2.57(-27)	6.69(-27)
200	1.67(-31)		2.43(-26)	6.00(-26)
250	1.11(-27)		2.74(-24)	6.10(-24)
300	4.08(-25)	2.21(-23)	1.12(-22)	2.30(-22)
400	7.24(-22)	7.13(-21)	2.30(-20)	4.09(-20)
500	7.23(-20)	3.10(-19)	8.21(-19)	1.31(-18)
600	1.71(-18)	4.62(-18)	1.06(-17)	1.57(-17)
800	1.072(-16)	1.82(-16)	3.29(-16)	4.39(-16)
1000	1.52(-15)	2.07(-15)	3.06(-15)	3.82(-15)
1500	7.64(-14)	8.29(-14)	8.11(-14)	9.28(-14)
2000	7.23(-13)	7.10(-13)	5.29(-13)	5.80(-13)
2500	3.29(-12)	3.04(-12)	1.88(-12)	2.01(-12)

Table 5.10: Thermal and state-to-state rate constants (cm^3 $molecule^{-1}$ s^{-1}, powers of 10 in parentheses).

T / K	k_{00}	k_{01}	k_{10}	k_{11}	k_{22}
150	5.54(-29)	2.81(-32)	2.79(-32)	2.08(-34)	1.54(-41)
180	2.56(-27)	4.89(-30)	4.87(-30)	3.74(-32)	2.38(-37)
200	2.41(-26)	7.25(-29)	7.23(-29)	8.75(-31)	2.99(-35)
250	2.72(-24)	1.37(-26)	1.37(-26)	1.86(-27)	2.02(-31)
300	1.10(-22)	6.88(-25)	6.88(-25)	5.23(-25)	1.00(-28)
400	2.20(-20)	1.75(-22)	1.75(-22)	6.93(-22)	5.21(-25)
500	7.48(-19)	7.37(-21)	7.37(-21)	5.63(-20)	1.32(-22)
600	9.23(-18)	1.10(-19)	1.10(-19)	1.12(-18)	6.15(-21)
800	2.66(-16)	4.29(-18)	4.29(-18)	5.25(-17)	9.48(-19)
1000	2.33(-15)	4.67(-17)	4.67(-17)	5.84(-16)	2.35(-17)
1500	5.54(-14)	1.56(-15)	1.56(-15)	1.83(-14)	2.44(-15)
2000	3.23(-13)	1.15(-14)	1.14(-14)	1.25(-13)	3.17(-14)
2500	1.02(-12)	4.35(-14)	4.34(-14)	4.52(-13)	1.65(-13)

(TST) was also calculated as part of the current study, using the ZPE corrected *ab initio* barrier height and the properties of the stationary points presented in Section 5.2.1. The state-to-state rate constants for the curvilinear surface are given in Table 5.10.

Comparison. The experimental and theoretical thermal rate constants are plotted in Figure 5.13(a), where it is easy to see that low temperature tunneling plays an important role in the reaction dynamics, as noted by the difference between the RD quantum and the TST results of this study. The curvilinear results agree well with the evaluated kinetic data, although slightly overestimate the thermal rate constant at intermediate temperatures in comparison with Kungwan's [86] CVT/SCT/HR results. It is difficult to evaluate the extent of tunnelling because of the absence of low temperature kinetic data. Extrapolation of the available evaluated data suggests that the CVT results underestimate low temperature rate constants. High temperature recrossing is also predicted by the current RD quantum study, for which the predicted rate constants are low in comparison with TST (a theory for which recrossing is forbidden). Finally, it should be noted that both the J-shifted and the J-summed thermal rate constants for the curvilinear surface are plotted in Figure 5.13(a); they are very similar with only a small deviation at low temperatures, indicating the applicability of the J-shifting method in predicting RD rate constants for this polyatomic collision process.

The J-shifted, curvilinear state-to-state thermal rate constants are also plotted, in Figure 5.13(b). The importance of tunneling is highlighted by the fact that the $0 \rightarrow 0$ thermal rate constant dominates the total TRC, the main contribution to the tunnelling probability. It is clear that the $0 \rightarrow 1$ and $1 \rightarrow 0$ rate constants are in excess of an order of magnitude slower than the vibrationally adiabatic ground state TRC.

Comparison of the J-shifted thermal rate constants for the curvilinear and rectilinear surfaces can also be made (Figure 5.14). The thermal rate constant of the curvilinear surface is significantly lower than its rectilinear counterpart, especially at low temperatures, bringing it into closer agreement with experimental

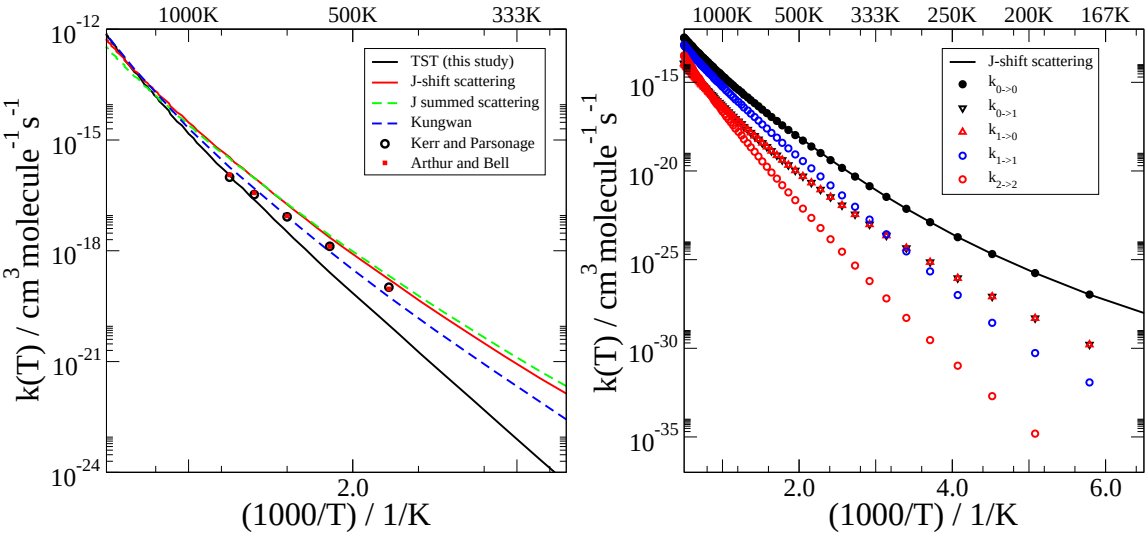

Figure 5.13: Thermal rate constants for the $CH_3 + CH_4 \longrightarrow CH_4 + CH_3$ reaction. (a): Total thermal rate constants are shown for reduced dimensionality J-shifted, J-summed, and TST (this study), as well as for CVT/SCT/HR [86], and evaluated experimental kinetic data [92, 93]. (b): State-to-state thermal rate constants for the J-shifted reduced dimensionality scattering results.

data. This indicates an improvement in the quality of the surface with the use of the curvilinear projection method [14, 15]. This trend is expected, given the increased barrier height on the curvilinear surface (Figure 5.4(b)).

5.4 Deuterated studies

Reactions 5.2 and 5.3 were chosen in order to investigate the effects of primary and secondary kinetic isotope effects, respectively. The latter reaction possesses both primary and secondary effects, but an approximate evaluation of the importance of secondary effects can be made by comparing the differences between these two reaction systems. Kinetic isotope effects generally provide an indication of the quality of the surface via comparison with experimental results; in the present case this comparison is only approximate given that zero-point energy corrections

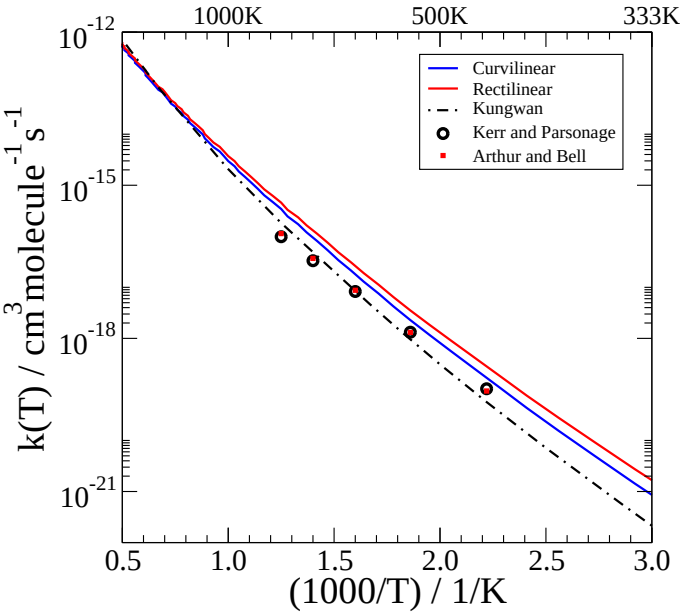

Figure 5.14: Thermal rate constants for the $CH_3 + CH_4 \longrightarrow CH_4 + CH_3$ reaction. Comparison of curvilinear (blue) and rectilinear (red) J-shifted reduced dimensionality thermal rate constants with previous experimental [92,93] and theoretical [86] results.

to the surface necessitate a new fit for each isotopic substitution. For an approximate evaluation of the type of double-Morse symmetric potential function chosen, the rates of these two symmetric variations were calculated and compared. Only symmetric reactions were studied so that the same form of the potential function could be used.

The reaction energies are presented in Table 5.3, the frequencies are given in Table 5.2 and the rotational constants in Table 5.1.

Potential energy surfaces. The analytical curvilinear surface parameters[6] are presented in Table 5.11. Both surfaces were fit using 151 points across the symmetric grid, and resulted in an SSR of 9.53×10^{-4} au^2 for surface 5.2, with a slightly higher error fit for reaction 5.3, with an SSR of 2.15×10^{-3} au^2.

The properties of the two surfaces are given in Table 5.12 in comparison with the

[6]Updated from the numerical curvilinear surfaces presented by Remmert *et al.* [16].

Table 5.11: Potential energy surface parameters for the symmetric deuterated reactions.

	$CH_3 + DCH_3$	$CD_3 + DCD_3$
c_1	12.230878	11.1040008
c_2	0.096547	-0.1546578
c_3	-0.628928	-0.5887360
c_4	0.307556	0.3237088
c_5	-0.438458	1.4745618
c_6	2.250075	2.2177430
c_7	-0.084667	-0.0853670
c_8	11.035490	10.7537934
c_9	0.876202	1.0544656
c_{10}	-0.007315	-0.0059363
c_{11}	8506.427613	8507.6236532
c_{12}	1880.241297	1880.5104660
c_{13}	-39.100533	-39.3421489
c_{14}	3.317668	5.2153628
c_{15}	2.323395	2.1340906
c_{16}	0.323631	0.4770869
c_{17}	-2.015876	-2.8187435
c_{18}	-81.669316	-82.2866747

main reaction. The depression associated with a van der Waals well is shallower for both deuterated systems, and the surface barrier height is lower for both reactions in comparison with the main reaction. The surface barrier height is lowest for reaction 5.3 at 19.96 kcal mol^{-1}, followed by reaction 5.2 at 20.41 kcal mol^{-1}, and the main reaction at 20.63 kcal mol^{-1}. This is not an expected trend, given that the *ab initio* calculations predicted barrier heights of 17.9, 18.6, and 17.7 kcal mol^{-1}, respectively. However, it is difficult to predict the effect that spectator mode (as opposed to total) ZPEs will have on the surface barrier height. Furthermore, as the hyperspherical coordinates are dependent upon the reduced mass of the system, direct comparison of the surfaces is made even more difficult.

Numerical details. Scattering for reaction 5.2 was performed with the same scattering parameters as before (Section 5.3.1), with the exception of $\rho_{\min} = 6.5$

Table 5.12: Energetic properties of surfaces for reactions 5.2 and 5.3. Energies given in kcal mol^{-1}.

	$CH_3 + CH_4$(curv)	$CH_3 + DCH_3$	$CD_3 + CD_4$
E_{shift}	-80.1325592	-80.133663	-80.150887
$E_{TS} - E_{shift}$	20.8379	20.5904	20.0837
$E_{vdW,r/p} - E_{shift}$	0.0000	0.0000	0.0000
$E_{r/p} - E_{shift}$	0.2065	0.1827	0.1222
$\Delta V_{rev/for}$	20.6314	20.4077	19.9615
ΔH	0.0000	0.0000	0.0000
$E_{r/p} - E_{vdW,r/p}$	0.2065	0.1827	0.1222
ΔV_{vdW}	20.8379	20.5904	20.0837
ρ_{TS}(au)	9.1053	8.1602	8.1667
δ_{TS}(rad)	0.1788	0.2463	0.2267
$\rho_{vdW,r}$(au)	13.8772	12.4910	12.5702
$\delta_{vdW,r/p}$(rad)	0.0965/0.2598	0.1314/0.3596	0.1224/0.3295

to $\rho_{max} = 13.7$ au, as well as using an increased contracted basis size of $N = 19$ to account for the increased number of accessible states. For reaction 5.3, these were held constant but the final value of ρ_{max} was reduced to 13.5 au. Calculations were only performed to compute the $J = 0$ partial wave probabilities.

Hyperspherical adiabats. The hyperspherical adiabats for reactions 5.2 and 5.3 are displayed in Figures 5.15(a) and 5.15(b), respectively. It is easy to see that in both cases the hyperspherical adiabats are shifted to lower values of ρ compared to the main reaction, but maintain the same functional form. Furthermore, the levels are more closely spaced leading to additional open channels for the same collision energy.

Reaction probabilities. State-to-state reaction probabilities exhibited the same preference for vibrationally adiabatic transitions as was witnessed for the main reaction. For comparison purposes, the cumulative reaction probabilities of all three processes are shown in Figure 5.16. The presence of sharp resonances remains in all CRPs; however, the pattern of oscillating reactivity, though present, is less

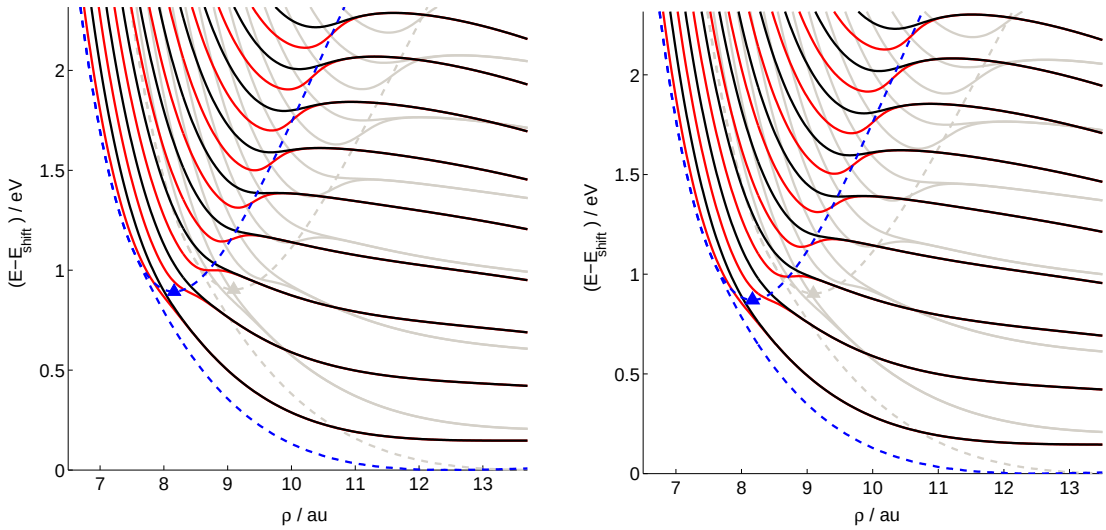

(a) CH_3+DCH_3→CH_3D+CH_3. (b) CD_3+CD_4→CD_4+CD_3.

Figure 5.15: Hyperspherical adiabats for deuterated reactions. The blue triangle corresponds to the TS; lower blue dashed line is the minimum energy path along the reactant channel, and upper blue dashed line is the potential as a function of ρ along the δ value of the TS. Grey: hyperspherical adiabats for the CH_3+CH_4→CH_4+CH_3 reaction.

pronounced for the deuterated reactions. This is attributed to the larger number of states accessible at high energies – overlapping probabilities for different transitions makes the effects of oscillating reactivity less visible in the CRP, though these effects remain present in the state-to-state probabilities [not shown].

Thermal rate constants. The J-shifted thermal rate constants and their KIEs in comparison with the main reaction are presented in Table 5.13, and plotted in Figure 5.17.

Experimental data [108], also included in Figure 5.17 for the CD_3+CD_4 reaction system[7], predicted the Arrhenius equation (473 - 623 K)

$$k(T) = 6.76 \times 10^{-12} \exp[\frac{(-74.50 \pm 2.24)\ \text{kJ mol}^{-1}}{RT}]\ \text{cm}^3\ \text{molecule}^{-1}\ \text{s}^{-1}. \quad (5.7)$$

[7]Experiments were performed using ^{14}C as a tracer.

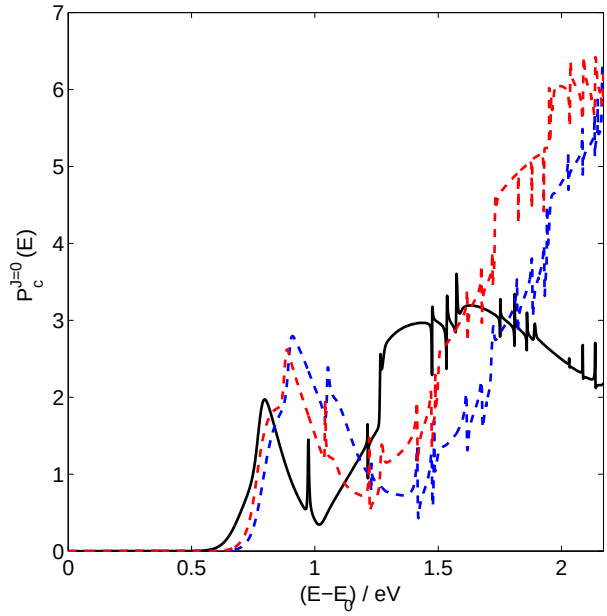

Figure 5.16: Cumulative reaction probabilities for CH_3+CH_4 $\longrightarrow$ CH_4+CH_3 (black solid), CH_3+DCH_3 $\longrightarrow$ CH_3D+CH_3 (blue dashed) and CD_3+CD_4 $\longrightarrow$ CD_4+CD_3 (red dashed).

Table 5.13: J-shifted thermal rate constants and kinetic isotope effects. (Rates given in cm^3 $molecule^{-1}$ s^{-1}; powers of ten in parentheses).

T / K	$CH_3 + CH_4$	$CH_3 + DCH_3$	KIE (D/H)	$CD_3 + CD_4$	KIE (D/H)
150	5.55(-29)	6.280(-32)	0.0011	8.08(-32)	0.0015
180	2.57(-27)	3.99(-31)	0.0002	1.92(-30)	0.0007
200	2.43(-26)	7.25(-30)	0.0003	3.92(-29)	0.0016
250	2.74(-24)	3.72(-27)	0.0014	1.93(-26)	0.0071
300	1.12(-22)	4.41(-25)	0.0039	2.12(-24)	0.0188
400	2.30(-20)	3.31(-22)	0.0144	1.42(-21)	0.0617
500	8.21(-19)	2.43(-20)	0.0296	9.89(-20)	0.1205
600	1.06(-17)	4.96(-19)	0.0468	1.95(-18)	0.1844
800	3.29(-16)	2.65(-17)	0.0806	1.00(-16)	0.3050
1000	3.06(-15)	3.37(-16)	0.1103	1.23(-15)	0.4026
1500	8.11(-14)	1.32(-14)	0.1623	4.36(-14)	0.5376
2000	5.29(-13)	9.93(-14)	0.1876	3.00(-13)	0.5666
2500	1.88(-12)	3.71(-13)	0.1971	1.03(-12)	0.5489

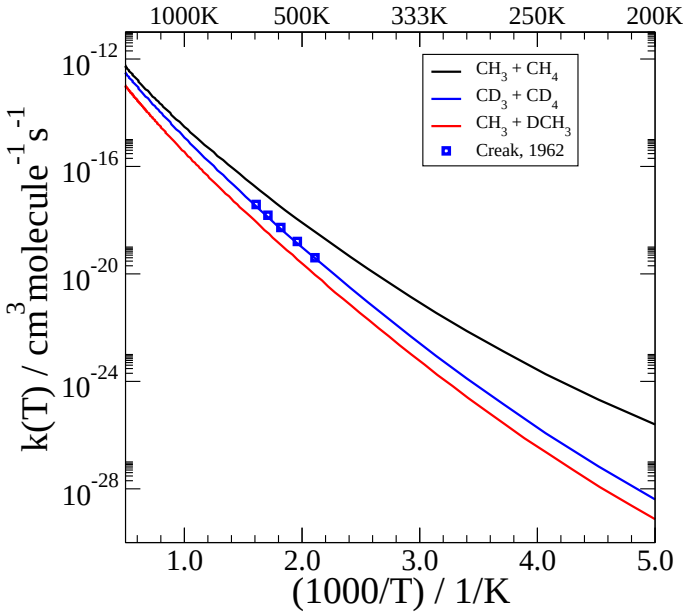

Figure 5.17: J-shifted thermal rate constants for CH_3+CH_4 $\longrightarrow$ CH_4+CH_3 (black), CD_3 + CD_4 $\longrightarrow$ CD_4 + CD_3 (blue) and CH_3 + DCH_3 $\longrightarrow$ CH_3D + CH_3 (red), in comparison with experimental kinetic data [108].

It is clear to see that the effect of both deuterium substitutions results in a large decrease in the thermal rate constant, especially at low temperatures. This is expected given the lower probability of deuterium tunnelling as compared to hydrogen, and is further evidenced by the delayed onset of the deuterated reaction probabilities in Figure 5.16. The much lower reaction rate observed for the CH_3+DCH_3 process arises because of symmetry considerations; in this case only the transfer of the single deuterium atom is investigated, whereas there are four sites for abstraction in the other processes. The CH_3+DCH_3 rates are approximately 1/4 of the rates for CD_3+CD_4 indicating that the primary deuterium substitution is the most important factor. Thus secondary deuterium effects are not anticipated to play a substantial role in the reaction process, within the current reduced dimensionality model.

Finally, the excellent agreement between the experimentally derived rate constant for CD_3+CD_4 and that predicted by the current study should be noted.

Thus, two reactions using the same fitting procedure and analytical function both result in good correlation with experiment, indicating that the current approach is indeed sufficient for characterisation of polyatomic processes.

5.5 Conclusions

In this chapter, the quantum scattering results for the symmetric reactions $CH_3 + CH_4$, $CH_3 + DCH_3$ (D abstraction only), and $CD_3 + CD_4$ were presented. It was found that the two dimensional quantum scattering approach to the study of this polyatomic reaction system was very effective in reproducing experimental thermal rate constants. The curvilinear and rectilinear projection schemes were both tested for surface development, and it was found that the curvilinear method offered significant improvement in terms of eliminating the presence of unphysical imaginary frequencies across the surface grid, thus more accurately representing the effective potential barrier height. Furthermore, the J-shifted rate constant was found to be an adequate approximation in comparison with the J-summed thermal rate constant, thereby validating the use of this approximation for the deuterated systems. The $0 \rightarrow 0$ transition was found to dominate the thermal rate constant.

A number of sharp resonance peaks in the cumulative reaction probability were analysed by predicting the energies of bound states in the deep wells of the hyperspherical adiabats in the interaction region. Resonances were also confirmed via time delay analysis. Physically, these resonances were attributed to a mixture of stretching motion – heavy atom breathing and light atom chattering between the two heavy groups. Broad oscillations in the cumulative and state-to-state reaction probabilities were witnessed and attributed to quantum interference effects due to the symmetry of the reaction system. Furthermore, the reaction was determined to be primarily vibrationally adiabatic, with only minor contributions to the reaction

probability for vibrationally non-adiabatic pathways.

Partial wave probabilities were computed up to $J = 250$ and it was determined that, for higher collision energies, resonant features in the CRP were preserved but shifted to higher energy. Differential and integral cross sections were also computed; the reaction was determined to be exclusively backwards scattering for the ground state collision process, with an increase in the amount of sideways scattering with increasing collision energy.

Deuterated reactions CH_3+DCH_3 (D abstraction only), and CD_3+CD_4 enabled evaluation of the applicability of the symmetric form of the potential chosen. The close correlation of the thermal rate constant results for CD_3+CD_4 to experiment validated the choice of surface and provided additional evidence of the applicability of the 2D quantum scattering method. Primary and secondary kinetic isotope effects were studied; it was determined that the effect of substituting the transferring hydrogen with a deuterium was the dominant factor in reducing the thermal rate constant. Secondary isotope effects were significantly less important.

This study is the first extension of the current method to polyatomic hydrogen transfer processes. As such, it has successfully shown the applicability of the reduced dimensionality quantum scattering approach to molecule + molecule reactions.

Chapter 6

$Cl(^2P_J) + CH_4 \rightleftarrows HCl + CH_3$

6.1 Introduction

Chapter 5 involved the detailed application of a two-dimensional quantum scattering technique to the study of a ground state reaction. In this chapter, the method is extended to include characterisation of electronically adiabatic and nonadiabatic quantum dynamics, through the explicit inclusion of multiple potential energy surfaces.

Reactions involving hydrogen transfer between chlorine radicals and hydrocarbon molecules are widely studied both theoretically and experimentally. In particular, the reaction process:

$$Cl(^2P) + CH_4 \rightarrow HCl + CH_3 \qquad \text{(F1)}$$

and its reverse:

$$HCl + CH_3 \rightarrow Cl(^2P) + CH_4 \qquad \text{(R1)}$$

have been the focus of intense investigation[1].

[1] A note concerning notation: Forward and reverse reactions are discussed at length – R1

Accurate description of the forward reaction (F1) is essential in polar atmospheric chemistry; it is a major sink for chlorine radicals and hinders competing processes which lead to the degradation of the stratospheric ozone [109–111]. Hence, accurate knowledge of the reaction rate, particularly at low temperatures, is necessary for modelling ozone depletion [112]. Conversely, the reaction can also be viewed as a major sink for the greenhouse gas methane, second only to the destruction of methane via reaction with the OH radical [113]. Furthermore, it is hypothesised that F1 is essential in interpreting the combustion of chlorinated hydrocarbons – a topic necessary for understanding the consequences of toxic waste incineration [114].

In addition to its physical importance, this reaction has emerged in the laboratory as a prototype for understanding basic principles regarding reaction dynamics in polyatomic systems. Numerous sophisticated experiments have been performed in recent years, designed not only to measure the forward and reverse reaction rates, but to probe in detail the transfer of internal and kinetic energy. Theory has in turn followed, resulting in a variety of experimental and theoretical studies analysing angular distributions, isotope effects and the influence on reactivity of vibrational excitation and redistribution. The majority of studies have focused on the ground state reaction, however, several recent experiments investigated the role of nonadiabatic processes involving spin-orbit state Cl ($^2P_{\frac{1}{2}}$). The reverse reaction (R1) was found to be especially useful in quantifying the extent of nonadiabatic reaction [115–118].

Explicitly studying the influence of electronically excited states allows for more accurate characterisation of collision dynamics. Furthermore, it provides the opportunity to draw general conclusions regarding the influence of nonadiabatic

refers to the reverse process and F1 to the forward process. To avoid confusion, in the following discussion mention of "reactant" or "product" channels will be preceded by the label of the reaction process in question. Thus, the $HCl+CH_3$ channel may be labelled as R1 reactants or F1 products.

transitions on polyatomic reaction dynamics. Though this influence has been theoretically characterised for triatomic collision processes [38], multiple-surface quantum scattering studies of polyatomic reactions have been rare [46]. To the best of my knowledge, no such investigations have been performed for reactions F1 and R1. Thus, the current study not only provides insight into the role of non-adiabatic transitions in a prototype polyatomic reaction, but allows for comparison with increasingly sophisticated experimental characterisations.

6.1.1 Multi-surface reaction model

The F1 reaction system contains three, two-fold degenerate potential energy surfaces[2]. In the diabatic, C_{3v} symmetric representation[3], all three states are degenerate in the asymptotic limit of infinite separation of the Cl atom from methane. The ground state reaction occurs along the doubly-degenerate A_1 potential ($1A'$ in C_s symmetry). The four-fold degenerate E potential ($2A' + 1A''$ in C_s symmetry) correlates instead to the excited state F1 products, which are sufficiently high in energy to be negligible in the study of low to moderate collision energy dynamics.

A qualitative representation of the diabatic potential energy along the reaction coordinate is given in Figure 6.1(a). The reaction can be considered physically on the basis of where the so-called $\pi-$hole (the orbital containing the unpaired electron) is in the Cl atom relative to the incident CH_4. The primary axis, z, is defined as the collinear Cl–H–C axis, and thus the ground state corresponds to the electron hole in the p_z orbital. The $\pi-$hole is located in the (indistinguishable) p_x or p_y orbitals for the E states correlating to the excited F1 products.

[2]The two-fold degeneracy arises from the spin states of the unpaired electron in the valence p orbital of the Cl radical.

[3]As in Chapter 5, a central assumption is that F1/R1 occurs via a collinear C_{3v} symmetric reaction path. C_s symmetries are also introduced as Molpro [62] calculations require Abelian point group symmetry.

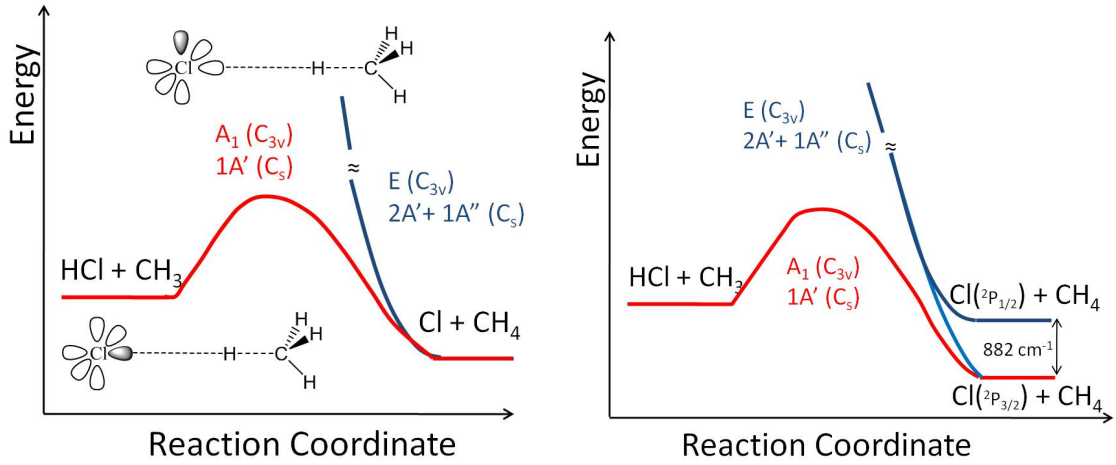

(a) Diabatic representation: $g = 6$.

(b) Adiabatic representation: $g = 4 + 2$.

Figure 6.1: Diagram of the three $Cl + CH_4 \rightleftharpoons HCl + CH_3$ potential energy surfaces as a function of reaction coordinate. The two excited states in the diabatic representation (a) break degeneracy due to spin-orbit coupling in the adiabatic representation (b). g is the degeneracy of the electronic states in the asymptotic $Cl + CH_4$ channel.

Complexity arises when spin-orbit coupling splits the degeneracy of the asymptotic states into the four-fold degenerate Cl ($^2P_{\frac{3}{2}}$) (ground) state and the two-fold degenerate ($^2P_{\frac{1}{2}}$) (excited) states, as shown in Figure 6.1(b). In the asymptotic limit, the splitting between the states equals ΔE_{SOC} =882 cm^{-1}, the spin-orbit splitting of the Cl atom [72]. The two lower states decrease by 1/3 of ΔE_{SOC}, whereas the upper state increases by 2/3 of ΔE_{SOC}. Because of this energy splitting, any reaction from (to) Cl ($^2P_{\frac{1}{2}}$)+ CH_4 to (from) ground state $HCl + CH_3$ must involve a nonadiabatic transition, which occurs in the $Cl + CH_4$ channel. A primary interest of multi-surface scattering calculations is understanding these nonadiabatic interactions. In all subsequent discussion, the excited spin-orbit state Cl ($^2P_{\frac{1}{2}}$) will be abbreviated as Cl*, and ground state Cl ($^2P_{\frac{3}{2}}$) will be referred to as Cl.

6.1.2 Literature survey

General background. A variety of theoretical and experimental studies have characterised the properties of the ground state $Cl + CH_4 \rightleftharpoons HCl + CH_3$ reaction. It is a mildly endothermic reaction process [119, 120] with a late (product-like) transition state [121] as expected by the Hammond postulate [122]. The reaction is collinear along the angle of abstraction (Cl−H−C) [119, 123–125] and C_{3v} symmetry is found to be maintained along the reaction path [13, 123] (consistent with the assumptions of the current study). Additionally, steric hindrance is expected to have a significant effect; the pre-exponential factor (1×10^{-11}) is approximately 30 times less than the hard sphere collision rate [126]. Steric effects lead to a tight structure at the TS, indicating that only certain collision configurations will result in reaction [127]. Furthermore, because of the HLH nature of this system, quantum effects such as oscillating reactivity and resonance features govern the kinetics and dynamics [13, 128]. Several theoretical studies have shown the presence of quasi-bound states in the TS region [129] corresponding to HLH "chattering" of the light atom [128].

***Ab initio* calculations.** *Ab initio* characterisation of reaction stationary points and barrier heights have been performed at various levels of theory; for an extensive comparison, the reader is referred to the work of Troya *et al* [130]. The best reported estimates for the vibrationally adiabatic F1 reaction barrier height were 2.64 kcal mol^{-1} at CCSD(T)/CBL//CCSD(T)/aug-cc-pVTZ level of theory [130], and 3.58 kcal mol^{-1} at QCISD(T)/aug-cc-pVTZ//QCISD/cc-pVTZ level of theory [123]. In comparison, the experimental barrier height was estimated to be 2.6±0.4 kcal mol^{-1} [121], though accurate prediction of the barrier height from experiment is difficult given the non-Arrhenius curvature of the thermal rate constant.

In general, the following basis set trends were reported. MP2 geometry characterisations underestimated C−H_a bond lengths thereby decreasing the F1 product-like nature of the TS in comparison with higher levels of theory [120]. Accurate energetic analysis required the use of perturbative triple excitations in coupled-cluster (CC) and quadratic configuration interaction (QCI) methods. Perturbative triples were found to lower the F1 reaction barrier by $\sim$ 2 kcal mol^{-1}(in the QCISD(T) case [123]) but were not found to be necessary for geometry optimisations [130]. Diffuse functions also had significant impact, lowering the F1 barrier height by $\sim$ 2 kcal mol^{-1} [130]. In comparison with experiment, two-point basis set extrapolated methods underestimated the reaction enthalpy [130] and the F1 barrier height, the latter as evidenced by overestimation of rate constants for 2D quantum scattering on a BSE surface[4] [13].

van der Waals minima. F1 entrance [124, 125, 131] and exit [125, 131] channel van der Waals (vdW) minima have been hypothesised to have a strong influence in driving the dynamics – a so-called "steering" effect on the reaction [130]. Resonances corresponding to motion trapped in the vdW complexes could also influence the reaction dynamics [132]. However, the exact influence of these pre- and post-reaction complexes is unknown, as their properties vary widely with theoretical method. Though some studies do not locate vdW minima along the MEP [133], the majority do at least predict an F1 exit valley complex characteristic of a variety of Cl + hydrocarbon reactions [134]. This exit vdW complex arises from a stabilising interaction between the HCl dipole moment and the CH_3 quadrupole moment [123, 130, 131]. Though some studies have found two F1 reactant vdW wells [119], only one is relevant as it possesses a collinear geometry; it is relatively

[4]The former inaccuracy was attributed to inadequacy of the harmonic approximation [130], while a potential source of error in the case of the latter effect was the relatively small size of the basis set used in the extrapolation [13].

shallow in comparison with the product complex.

Potential energy surfaces developed. Many full and reduced dimensional ground state potential energy surfaces have been developed and used in classical, quasi-classical trajectory (QCT) and RD quantum studies. The full dimensional surfaces are generally semi-empirical – *ab initio* results parametrised to reproduce rate constants and kinetic isotope effects [119, 123, 133, 135–137]. The most recently published full dimensional PES is a re-calibrated surface based upon CCSD(T)/aug-cc-pVTZ calculation of the reactants, products and TS [119]. Reduced dimensional, effective (ZPE-corrected) potential energy surfaces were also developed [13, 59, 121, 132]; the most recently published surface by Banks and Clary [13] used the same 2D approach as the current study and reported a CCSD(T)/cc-pVTZ analytical PES.

A more detailed theoretical treatment involves discussion of the excited state surfaces. To the best of my knowledge, there has been no development of a multiple potential energy surface description of this reaction system. Spin-orbit splitting of the Cl atom has generally only been treated statistically[5], though it is hypothesised that explicit inclusion of spin-orbit effects on the surface would raise the barrier height by approximately 1/3 of the value of the SO splitting, i.e, by 0.8 kcal mol^{-1} [136][6].

Dynamics. A variety of single-surface theoretical and experimental studies have probed the dynamics of the reaction in order to characterise reaction mechanism, integral and differential cross sections, thermal rate constants, and vibrational reaction enhancement. For detailed information, readers are referred to Teslja *et*

[5]For example, in calculation of the thermal rate constant. See for example reference [13].

[6]This is because the ground state surface should be shifted down by 1/3 of the SO splitting in the asymptotic Cl + CH_4channel, but should not be affected at the location of the TS.

al. for a review of Cl + RH reaction dynamics [138]. Two possible forward reaction mechanisms have been predicted in the literature. Small impact parameter (b) collisions result in a rebound mechanism and produce backwards scattered products [119, 128]. However, peripheral (high impact parameter) collisions can lead to a so-called "stripping" mechanism, which results in more forward scattered products [119, 128, 139]. In general, the incidence of peripheral reactions increases with collision energy [140, 141], leading, for example, to a more forward scattered differential cross section for the ground vibrational state reaction [129]. Theoretical results have predicted backwards scattered products at low energies (for the vibrational ground state, [142]), with an increase in sideways [13, 123] or forward [129] scattering with collision energy, a pattern which is also present for the deuterated $Cl + CD_4$ reaction [132].

The importance of accurate theoretical treatment of the methyl group has also been investigated. A series of different dimensionality surfaces for classical trajectory calculations were developed by Wang *et al.* [128]: (1) Cl–H–"CH_3" (2D), (2) Cl–H–C–"H_3" (3D), and (3) Cl–H–CH_3(full D). The two dimensional, pseudo-atom treatment of the methyl group in surface (1) was found to adequately describe the classical dynamics – potentially providing justification for the RD quantum approximation used in the current study.

Numerous QCT studies have been performed [119, 121, 123, 129, 130, 133–135, 143–145] and are in generally good agreement with experiment, although low QCT reaction probabilities in comparison with quantum results highlighted the need for additional accurate quantum treatment [129]. Furthermore, ZPE-leakage has proved to be a formidable challenge to this theory because of low experimental collision energy relative to the barrier height[7]. Time-dependent and -independent

[7]Many experimental studies generate Cl radicals via 355 nm photodissociation of Cl_2 [121,130]; collision energies of 3.67 kcal mol^{-1} (0.159 eV in the centre of mass frame [121]) result. This

reduced dimensionality ground state quantum scattering calculations were also in relatively good agreement with each other and with experiment concerning dynamic and kinetic properties of the system. Time-dependent 4D wavepacket [125], 3D wavepacket [129,146], time independent 2D rotating line approximation (RLA) [59], 3D rotating line umbrella (RLU) [147] and 4D rotating bond umbrella (RBU) approximations [142] have all been implemented on various surfaces. However, a recent 2D time-independent study with an analytical double-Morse PES is most comparable to the current approach [13]. Within a two dimensional framework, the reaction was found to be primarily vibrationally adiabatic with respect to the two explicitly treated stretching vibrations [13].

Thermal rate constants. A number of different experimental studies have measured the thermal rate constants for the forward [148–152] and reverse reactions [153–155]; these results are generally in good agreement with one another and are displayed in Figures 6.2 and 6.3, respectively. Curvature of the Arrhenius plot for F1 and R1 reactions is significant, further emphasising the need for quantum treatment in a theoretical approach[8].

Theoretical rate constants have been predicted by a variety of TST based and quantum methods [59, 119, 121, 122, 132, 135, 136, 142, 157, 158]. In general, tunnelling was shown to be very important at low temperatures [13], and recrossing dynamics were found to play a large role in the reaction mechanism [59, 158]. The theoretical rate constants[9] for the forward reaction are in good agreement with each other and experiment (Figure 6.2), although the 4D RBU quantum scattering result [142] underestimates the low temperature rate constant, while the 2D

energy is above the adiabatic barrier height but below the classical one. Loss of ZPE is thus more problematic for accurate QCT simulations at this collision energy [123].

[8]For a detailed investigation of the causes of F1 non-Arrhenius curvature, see references [126, 156].

[9]Only a subset of the available theoretical rate constant data is included.

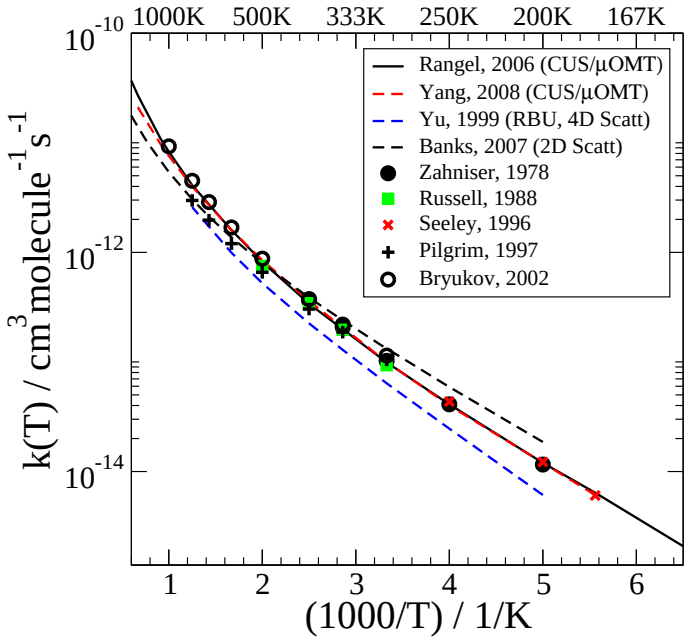

Figure 6.2: Theoretical [13, 119, 125, 142] and experimental [148, 150–152, 154] thermal rate constants for reaction $Cl + CH_4 \longrightarrow HCl + CH_3$.

quantum scattering of Banks and Clary [13] slightly overestimates the low temperature rate constant. The CUS/μOMT results of Rangel *et al.* [119] and the 4D time-dependent scattering results of Yang *et al.* [125] agree quite well with experiment. The estimated room temperature thermal rate constant is predicted by Rangel to be 9.90×10^{-14} cm^3 molecule^{-1} s^{-1} at 300 K.

Though less extensively studied than the forward reaction, reverse rate constants are shown in Figure 6.3. The experimental results are more widely distributed for this process. In general, the theoretical results do not as consistently reproduce the non-Arrhenius behaviour of the reverse thermal rate constant as for the forward reaction and are not in as good agreement with each other. As for F1, the RBU 4D scattering results [142] underestimate rate constants, while the CUS/μOMT approach of Corchado *et al.* [136] overestimates the reaction rate. The CUS/μOMT method with the updated surface of Rangel, *et al.* [119] results in much better agreement, though the extent of low temperature tunnelling is un-

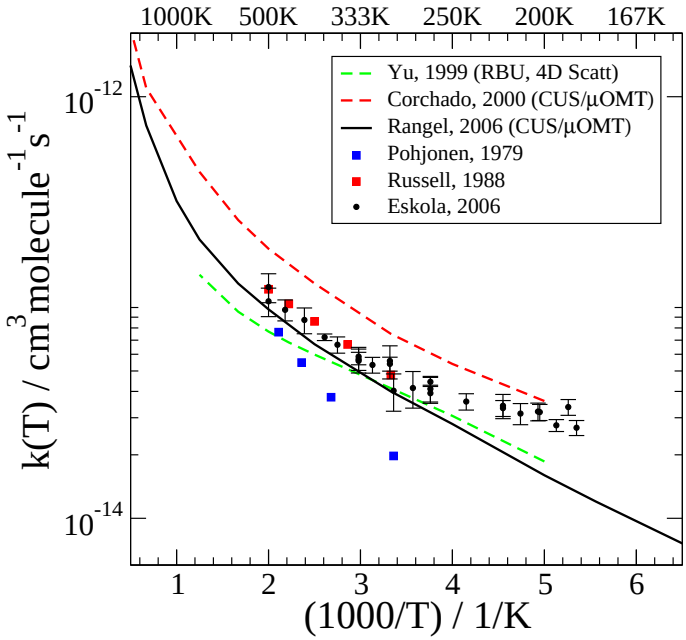

Figure 6.3: Theoretical [119, 136, 142] and experimental [153–155] thermal rate constants for reaction $HCl + CH_3 \longrightarrow Cl + CH_4$.

derestimated in comparison with the results reported by Eskola, *et al* [155]. The rate constant predicted by Rangel is 4.00×10^{-14} cm^3 molecule^{-1} s^{-1} at 300 K.

Vibrational coupling and reaction enhancement. The effect of vibrational excitation on reaction efficiency and dynamics has been frequently investigated. The F1 reaction is preferentially enhanced by vibrational excitation [121,158]. The forward reaction is enhanced by excitation in both the C–H symmetric stretch and the umbrella excitation of the CH_4 group, whereas the reverse reaction is enhanced by excitation of the H–Cl vibration but decreased by umbrella excitation of the CH_3 [122, 136, 142].

The degree of reaction enhancement for the stretching, bending, and torsional modes for this reaction system is well studied experimentally and theoretically [121, 122, 127, 135, 136, 139, 144, 145, 159–161]. The most relevant conclusions from these studies involve the analysis of intramolecular vibrational redistribution [144]

driven by coupling between vibrational degrees of freedom. The reaction path coordinate couples to the CH_4 symmetric stretch and umbrella mode in the F1 entrance channel [135, 136], and to the H–Cl stretch and CH_3 bending modes in the F1 exit channel [135]. Thus, one would expect coupling between bending and stretch motions along the reaction path to significantly influence the reaction process.

6.1.3 Excited state dynamics

There have been several sophisticated experimental studies probing nonadiabatic transitions in this system. Liu, *et al.* have characterised the ground state and nonadiabatic reaction dynamics of the forward F1 process and deuterated variants in a series of recent studies [140, 141, 162–167]. Initial crossed beam experiments indicated Cl* quenching occurred at a faster rate than its reaction with CH_4, thus resulting in a very small Cl* reactivity [162]. However, subsequent ion imaging experiments [163] noted the presence of an isotropic ring corresponding to reaction of Cl* + CH_4 $\rightarrow$ HCl (ν=1) + $CH_3(\nu = 0)$[10]. Interestingly, the reaction of ground state Cl with methane to produce HCl (ν=1) + $CH_3(\nu = 0)$ was found to be associated with a reactive resonance – it was hypothesised that vibration to translational coupling is responsible for excitation of the symmetric C–H stretch along the reaction path. The reactive resonance would therefore consist of H-chattering between the heavy groups prior to the system decaying to H–Cl stretch excited products.

Subsequent work on the Cl + CH_2D_2 reaction system [166] provided further justification for the reaction of Cl* and the correlation between nonadiabatic reaction and production of HCl or DCl with one quantum of stretch excitation. Though

[10] At collision energies of 9.7 kcal mol^{-1}.

limited by lack of exact knowledge of the initial population of Cl*, it was estimated that this pathway is small but significant, comprising up to 9% of total reactivity at high collision energies ($\sim$ 20 kcal mol^{-1}). As with the Cl + CH_4 reaction, a resonance pathway was indicated for production of HCl ($\nu = 1$)[11]. It was hypothesised that the resonance pathway involved relaxation from the Cl*–$HCHD_2$ excited state surface to the ground state Cl–$HCHD_2$ surface in the entrance channel before the TS, where release of energy due to this transition excites the C–H symmetric stretch thus leading to the ground state resonance pathway observed in previous studies [163].

Conversely, Orr-Ewing and coworkers have approached the study of nonadiabatic dynamics in this reaction system by instead monitoring the production of Cl* from the reverse reaction of CH_3+HCl [115–118]. In these experiments, the incident methyl radicals were generated by photolysis of CH_3I at 266 nm and therefore possess vibrational excitation in the umbrella mode due to relaxation from tetrahedral to planar geometry[12]. Furthermore, photolysis results in a bimodal distribution of CH_3 radicals; the slow distribution (co-product I*) has an average centre of mass collision energy of 18.6 kcal mol^{-1}, while the fast distribution with (co-product I) has centre of mass speed of 30.3 kcal mol^{-1}, produced in ratio 2.1:1[13]. Various assumptions can be made regarding the extent of nonadiabatic reactivity of each distribution (see section 6.5.3.3).

Detection of Cl* products relative to ground state Cl afforded the opportunity to quantify the extent of nonadiabatic reaction according to the cross section

[11]Both resonance and non-resonance pathways were indicated for the channel involving production of DCl ($\nu = 1$). Resonance pathways were indicated by forward-backward peaking differential cross sections. Peripheral mechanisms were instead characterised by evolution of the differential cross section from backwards to sideways scattering with increasing collision energy.

[12]The predicted degree of vibrational excitation is discussed in section 6.5.3.3

[13]Thus resulting in an average collision energy 22.3 kcal mol^{-1}.

branching ratio[14]

$$\Gamma = \frac{\sigma(Cl^*)}{\sigma(Cl) + \sigma(Cl^*)} , \tag{6.1}$$

which was determined to be $\Gamma = 0.14 \pm 0.02$ [115] at an average collision energy of 22.3 kcal mol^{-1}. The differential cross sections for production of Cl and Cl* were found to be similar (with a preference for high-energy stripping dynamics), indicating that the same mechanism exists for the adiabatic and nonadiabatic pathways [117]. This finding supports the assertion of Zhang *et al.* [163] that the reactions proceed through the same TS and undergo nonadiabatic transitions in the $Cl + CH_4$ channel.

Clearly, both experimental approaches indicate that reaction to (or from) the excited spin-orbit state Cl* + CH_4 plays a significant, albeit small, role in the overall reaction process. However, direct comparison between the forward and reverse nonadiabatic results is difficult given that Liu *et al.* predict the release of vibrationally excited HCl ($\nu = 1$) with $CH_3(\nu = 0)$, whereas Orr-Ewing's reaction system is comprised of vibrationally cold HCl ($\nu = 0$) with umbrella excited CH_3 [117].

Despite the numerous experimental studies, many questions remain regarding the nonadiabatic properties of $Cl + CH_4 \rightleftharpoons HCl + CH_3$. Most notably, the lack of multi-surface theoretical characterisations means the relative importance of nonadiabatic coupling mechanisms such as spin-orbit coupling, Coriolis coupling, and electronic mixing has not been evaluated. Furthermore, although experiments indicate the nonadiabatic transition takes place in the $Cl + CH_4$ channel, the exact location – and thus, the geometric configurations necessary to achieve transition between electronic states – is unclear. The role of vibrational motion in mediating nonadiabatic transfer has been indicated in both forward and reverse experiment,

[14]Where $\sigma(Cl^*)$ refers to the cross section for nonadiabatic production of Cl* + CH_4, and $\sigma(Cl)$ is the reaction cross section for adiabatic production of Cl + CH_4.

although the exact mechanism of this influence has yet to be studied theoretically. Theory would provide a degree of state-to-state specificity seldom available to experimental studies. It is evident that an accurate theoretical approach to this problem could provide a means of bridging the gap of understanding between these two sets of sophisticated experiments.

6.1.4 Scattering background: $\mathbf{X + H_2 \longrightarrow XH + H}$

Many experimental and theoretical studies have also been performed to investigate the role of nonadiabatic transitions in the reactions $X + H_2 \longrightarrow XH + H$, with X=Cl [30–33, 35, 36], X=F [38–40, 45], and X=Br [41–43]. The detailed nonadiabatic dynamics of these systems are relevant to the current study, as these reactions possess the same asymptotic spin-orbit splitting behaviour and surface symmetries as the $X + CH_4$ system. Reaction to and from the excited spin-orbit state X* for reactions $X + H_2 \longrightarrow XH + H$ is thus also mediated by a nonadiabatic transition.

Though experiment initially indicated Cl* as more reactive than the ground state Cl [36], subsequent theoretical and experimental characterisations ascertained that reaction from the Cl* state comprises approximately 10% of the total reaction probability [30,35]. Sophisticated full dimensional quantum scattering calculations were performed, explicitly including the effects of Coriolis coupling, electronic mixing, and spin-orbit coupling [31]. The Cl* pathway dominated only at low collision energies below the zero-point corrected barrier height, where it was hypothesised that the additional internal energy in the Cl* contributed towards overcoming the barrier. Spin-orbit coupling was found to be the most important type of nonadiabatic coupling, and neglect of Coriolis coupling, electronic mixing of the A' states, or geometry dependence of the spin-orbit coupling were not found to significantly alter the reaction probability [33].

Similar conclusions were found for nonadiabatic reaction in the $F + H_2$ reaction system, with F* reactions accounting for 10% [40] to 25% of the total reactivity [38]. F* reactions were also seen to dominate at low collision energies. Furthermore, there was significant probability of reaction associated with the nearly thermoneutral release of energy into H–F vibration: F* + H_2 ($\nu = 0, j = 0$) $\longrightarrow$ HF ($\nu' = 3$) + H [38]. Oscillatory features observable in the excited state reaction probability supported a two step mechanism – electronic transition followed by reaction on the ground state surface [45]. Comparatively, nonadiabatic reaction of Br* in the Br+H_2 $\longrightarrow$ BrH+H reaction comprised 10-40% of total reactivity [41]. A dominant spin-orbit relaxation inelastic transition Br* + $H_2$$\rightarrow$ Br + H_2($\nu = 1$) was determined [42]. The dominant mechanism for nonadiabatic reaction was deemed to involve electronic relaxation in the entrance valley combined with simultaneous excitation of one quantum of vibrational H–H stretch, followed by subsequent reaction on the ground state surface [43]: Br* + H_2($\nu = n$) $\rightarrow$[Br − H_2($\nu = n + 1$)] $\rightarrow$HBr + H, where $n = 0$ or 1.

6.2 Potential energy surface development

A multi-surface description of the Cl + CH_4 $\rightleftharpoons$ HCl + CH_3 within the diabatic framework (Figure 6.1(a)) necessitates the construction of three diabatic surfaces and three potentials describing the spin-orbit coupling between them. Because of the degeneracy of the excited states (and thus the symmetry of spin-orbit interaction), only four surfaces are required – describing the ground diabatic state (A_1), the excited diabatic states (E), the spin-orbit coupling between the A_1 and E states, and the spin-orbit coupling between the degenerate E states.

The approximate diabatic representation is assumed, such that the diabatic surfaces are taken to be the spin-free electronic energies determined by fitting a

29-parameter function to *ab initio* data. A single-reference *ab initio* method can be used, because of the different symmetries of the ground and excited states[15]. Geometry optimisations and frequency calculations were performed for the ground state only, and assumed to be valid for the $Cl + CH_4$ channel, where behaviour on both diabatic surfaces should be very similar. The spin-orbit coupling potentials were also calculated via *ab initio* calculations in Molpro [62] (as discussed in section 3.4.1) and fit to an 8-parameter potential function.

6.2.1 Basis set tests

Basis set tests were performed in order to determine the most appropriate method for development of the ground and excited state diabatic potential energy surfaces. The resulting classical forward (ΔV) and reverse (ΔV_r) barrier heights, the zero-point corrected forward (ΔV^a) and reverse (ΔV_r^a) barrier heights, the classical forward reaction energy (ΔE), and the zero-point corrected forward reaction energy (ΔH) for each basis set are given in Table 6.1. Geometry calculations were performed at the MP2 level of theory; CCSD(T) was used for single point energy calculations. Correlation consistent basis sets were used, defined according to cc-pVXZ-dk (X = D, D+d, T, T+d, Q, Q+d), where (+d) indicates the addition of polarisation functions to the Cl atom description and the (-dk) label refers to the use of Douglas-Kroll scalar relativistic basis sets. In Table 6.1, the basis sets for geometry and single point energy calculations are labelled according to X. The notation X//X′ indicates the use of cc-pV(X′)Z-dk for geometries and cc-pV(X)Z-dk for energies, and X,X',X'' indicates the use of cc-pV(X)Z-dk for geometries with X′–X″ basis set extrapolated energies. Basis set exponents for the additional

[15]All calculations are performed with the Molpro electronic structure package [62]; C_s symmetry is used and therefore the ground and excited states are described by A′ and A″ symmetry, respectively.

d-polarisation functions for the Cl atom were obtained from the basis set exchange website of Pacific Northwest National Laboratory [168, 169].

Two-point basis set extrapolation methods differed depending upon the series used; the Truhlar method [170] was implemented for the D-T series, whereas the method proposed by Halkier *et al.* [171] was used for the T-Q extrapolation energies. As total energy is the sum of the Hartree-Fock (HF) and correlation energies, the Truhlar extrapolation method can be given according to

$$E_\infty^{\text{tot}} = \frac{3^\alpha}{3^\alpha - 2^\alpha} E_3^{\text{HF}} - \frac{2^\alpha}{3^\alpha - 2^\alpha} E_2^{\text{HF}} + \frac{3^\beta}{3^\beta - 2^\beta} E_3^{\text{cor}} - \frac{2^\beta}{3^\beta - 2^\beta} E_2^{\text{cor}}, \tag{6.2}$$

where (for CCSD(T) energies) $\alpha = 3.4$, $\beta = 2.4$ and, for basis X $=i$, E_i^{HF} is the HF energy and E_i^{cor} is the correlation energy. The Halkier basis set extrapolated method is alternately defined as

$$E_\infty^{\text{tot}} = E_X^{\text{HF}} + \frac{X^\beta}{X^\beta - (X-1)^\beta} E_X^{\text{cor}} - \frac{(X-1)^\beta}{X^\beta - (X-1)^\beta} E_{X-1}^{\text{cor}}. \tag{6.3}$$

As shown in Table 6.1, increasing the accuracy of the basis set generally decreases the forward and – to a lesser extent – reverse barrier heights and reaction energies. The largest effect occurs as the order X increases. Inclusion of additional polarisation functions for the Cl atom also lowers the forward (F1) barrier height, though the effect is less pronounced for large X. However, polarisation functions raise the reverse (R1) barrier height for low-order basis sets, but result in a slight increase for X=Q+d compared to Q. Finally, extrapolation methods further decrease ΔV^a and ΔV_r^a, though there is little difference between using the higher or lower basis in the geometry calculation[16].

[16]It should be noted that the zero-point correction for the forward reaction is much larger than for the reverse as the zero point energy of Cl + CH_4 is much larger than that of CH_3+ HCl.

Table 6.1: Basis set tests for reaction $Cl + CH_4 \longrightarrow HCl + CH_3$. CCSD(T) energies in kcal mol^{-1}.

Series	ΔV	ΔV^a	ΔE	ΔH	ΔV_r	ΔV_r^a
D	12.3948	8.0677	9.9805	4.7319	2.4142	3.3359
D+d	11.9249	7.4714	8.9549	3.7258	2.9700	3.7456
T	9.6785	5.5001	7.5751	2.4452	2.1035	3.0550
T+d	9.4111	5.1059	7.0414	1.9173	2.3697	3.1886
Q	8.0357	4.1676	6.2691	1.4072	1.7666	2.7604
Q+d	7.8603	3.8006	5.9322	1.0783	1.9281	2.7223
Q+d//T+d	7.8759	3.5707	5.9187	0.7946	1.9572	2.7761
D,D,T	8.2681	3.9410	6.6425	1.3939	1.6256	2.5472
T,D,T	8.3103	4.1318	6.6471	1.5171	1.6633	2.6147
D+d,D+d,T+d	8.0377	3.5842	6.2224	0.9933	1.8153	2.5909
T+d,D+d,T+d	8.0780	3.7728	6.2544	1.1303	1.8236	2.6425
Q,T,Q	7.0530	3.1849	5.7247	0.8629	1.3283	2.3221
T,T,Q	7.0757	2.8973	5.7137	0.5838	1.3620	2.3135
Q+d,T+d,Q+d	6.8589	2.7992	5.3370	0.4831	1.5219	2.3161
T+d,T+d,Q+d	6.8801	2.5749	5.3303	0.2062	1.5498	2.3687

Current results compare favourably with previous studies. Troya *et al.* [130] also reported low F1 barrier height (2.64 kcal mol^{-1}) and forward reaction enthalpy (-0.16 kcal mol^{-1}) for basis set extrapolated energies (CCSD(T)/CBL//CCSD(T)/aug-cc-pVTZ), thus suggesting, as consistent with this study, that basis set extrapolated energies are prone to systematic underestimation of the F1 barrier height. However, the Q+d//T+d vibrationally corrected barrier height (3.5707 kcal mol^{-1}) is similar to the CCSD(T)/aug-cc-pVTZ and CCSD(T)/aug-cc-pVQZ//CCSD(T)/aug-cc-pVTZ results of Troya *et al.* [130], which were found to be 3.64 and 3.06 kcal mol^{-1}, respectively. This correspondence indicates that the Q+d//T+d basis set and method – despite the use of less accurate MP2 geometries – is an adequate choice for PES development, providing a reasonable compromise between computational efficiency and accuracy. As T+d,T+d,Q+d energies are readily available from the Q+d//T+d calculations, a basis set extrapolated surface is also developed; however, the main conclusions of this study are based upon the Q+d//T+d surface.

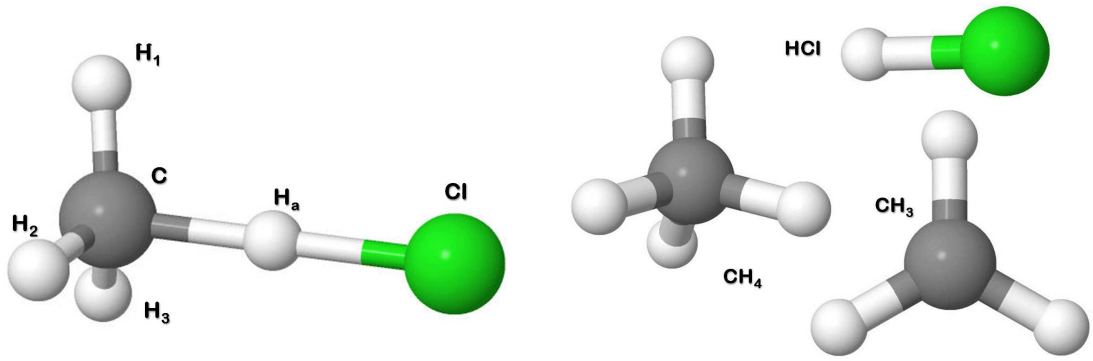

(a) Transition state. (b) Reactant and product geometries.

Figure 6.4: $Cl + CH_4 \rightleftharpoons HCl + CH_3$ reaction stationary point geometries.

6.2.2 Stationary point characterisation

6.2.2.1 Stationary point geometries

Ground state stationary point geometries and frequencies were calculated at the MP2/cc-pV(T+d)Z-dk level of theory, with CCSD(T)/cc-pV(Q+D)Z-dk energy corrections. The transition state and reactant/product geometries are shown in Figures 6.4(a) and 6.4(b), respectively. Corresponding bond lengths and angles are given in Table 6.2.

Comparison of TS geometry to that of the reactants and products affords an approximate manner of determining the nature of the transition state. The active mode bond lengths at the TS geometry are more similar to the HCl + CH_3 channel, with a larger C–H_a than H_a–Cl distance. This result is expected by the Hammond postulate given that the F1 reaction process is endothermic [122].

6.2.2.2 Intrinsic reaction coordinate calculations

Intrinsic reaction coordinate (IRC) calculations were performed at the UMP2/cc-pV(T+d)Z-dk level of theory in Molpro [62]. C_{3v} geometry (and therefore collinear

Table 6.2: Geometric parameters for reaction $Cl + CH_4 \rightleftharpoons HCl + CH_3$ at MP2/cc-pV(T+d)Z-dk level of theory.

Molecule	Molecular parameter	Value	Experiment (Å)
HCl	Cl - H	1.27 Å	1.275 [172]
CH_4	C-H	1.09 Å	1.087 [172]
	H-C-H	109.5°	
CH_3	C-H	1.07 Å	1.079 [173]
	H-C-H	120.0°	
TS	$Cl_6-H_2-C_1$	180.0°	
	$H_5-C_1-H_4$	116.1°	
	$H_3-C_1-H_4$	116.1°	
	$H_3-C_1-H_5$	116.1°	
	$H_3-C_1-H_2$	101.6°	
	Cl_6-H_2	1.45 Å	
	H_2-C_1	1.36 Å	
	C_1-H_5	1.08 Å	
	C_1-H_3	1.08 Å	
	C_1-H_4	1.08 Å	

approach) was assumed, and the numerical Hessian for reaction path following was computed with a central difference approximation and updated every five steps from the starting TS geometry for the F1 forward reaction path, and every three steps for the F1 reverse reaction path. The energy as a function of the reaction coordinate, s (Figure 6.5(a)) shows that the endothermic forward reaction process possesses an (F1) product-like TS. The variation in geometric parameters also supports this assertion; the H_a–C–H angle is seen to approach a 90° angle from the tetrahedral reference angle of 109.5° as the umbrella angle quickly flattens post-TS, allowing for a planar CH_3 configuration (Figure 6.5(b)). Furthermore, analysis of the H_a–Cl and H_a–C bond lengths show that they approach the reference molecular bond lengths of CH_4 and HCl in the asymptotic F1 reactant and product channels, respectively (Figure 6.5(c)).

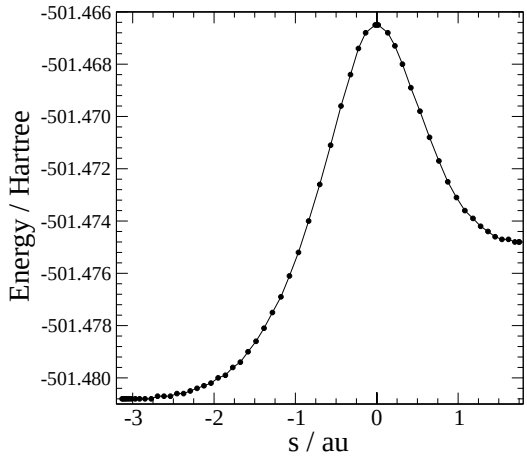

(a) Energy as a function of reaction coordinate.

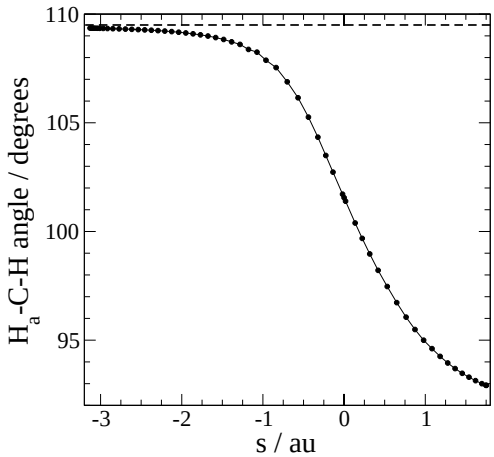

(b) Black dots: variation of H_a–C–H angle along the reaction coordinate; black dashed: reference tetrahedral angle.

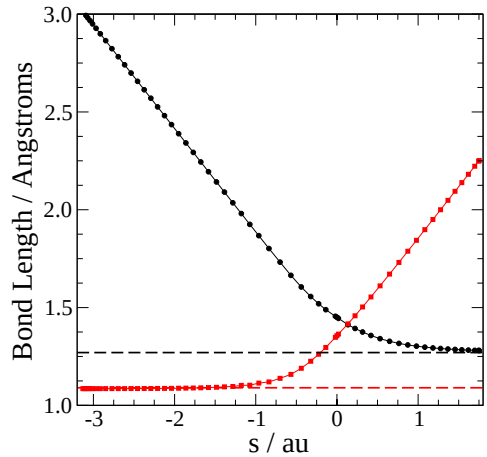

(c) Variation of bond lengths along the reaction coordinate: black dots (Cl–H_a), red dots (H_a–C), black dashed (HCl reference), red dashed (CH_4 reference)

Figure 6.5: Intrinsic reaction coordinate calculations for $Cl + CH_4 \rightleftharpoons HCl + CH_3$ ($s > 0$: $CH_3 + HCl$ channel, $s < 0$: $Cl + CH_4$ channel).

6.2.2.3 Reaction energies and frequencies

The values of the frequencies for the reactant and product molecules for this reaction system are given in Table 6.3. The moments of inertia associated with the reaction stationary points are given in Table 6.4.

The *ab initio* stationary point energies are given in Table 6.5. The forward and reverse classical barrier heights (ΔV_f and ΔV_r), as well as the zero-point corrected

Table 6.3: Reactant and product frequencies and zero-point energies.

	CH_3	HCl	CH_4
Frequency (cm^{-1})	486.0	3054.327	1349.6
	1445.4		1349.7
	1445.7		1349.7
	3177.9		1586.3
	3368.7		1586.4
	3368.7		3075.7
			3211.3
			3211.3
			3211.3
ZPE (au)	0.0303	0.0070	0.0454

Table 6.4: Stationary point moments of inertia (amu $bohr^2$).

Species	I_a	I_b	I_c
CH_3	6.23	6.23	12.46
HCl	5.67		
TS	12.10	314.65	314.65

Table 6.5: Stationary point energies at UCCSD(T)-cc-pV(Q+d)Z//UMP2-cc-pV(T+d)Z level of theory. Harmonic zero point energies computed with a UMP2-cc-pV(T+d)Z basis.

Species	**Energy / au**	**ZPE / au**
Reactant 1 (CH_4)	-40.4656	0.0454
Reactant 2 (Cl)	-461.1050	0
Product 1 (CH_3)	-39.7872	0.0303
Product 2 (HCl)	-461.7740	0.0070
Transition State	-501.5581	0.0386
Barrier Heights		
ΔV_f / kcal mol^{-1}	7.88	
ΔV_r / kcal mol^{-1}	1.96	
ΔV_f^a / kcal mol^{-1}	3.57	
ΔV_r^a / kcal mol^{-1}	2.77	
ΔE / kcal mol^{-1}	5.92	
ΔH / kcal mol^{-1}	0.79	

forward and reverse barrier heights (ΔV_f^a and ΔV_r^a), are presented alongside the classical (ΔE) and zero-point corrected reaction forward energy (ΔH).

Table 6.6: Harmonic frequencies for stationary points at the UMP2-UHF/cc-pV(T+d)Z-dk level of theory, in cm^{-1}. TS frequencies are given prior to (pre) and following (post) projection of explicitly treated vibrational modes, for the rectilinear (rt) and curvilinear (cv) methods.

TS (pre, rt)	TS (post, rt)	TS (pre, cv)	TS (post, cv)
$1232.5i$		$1232.5i$	
324.6	324.574	324.5	324.5
334.3	334.302	334.1	336.7
512.1		512.1	
959.4	958.6	959.4	888.1
965.4	965.4	965.3	965.3
1214.0	1014.0	1214.0	973.3
1442.8	1443.0	1442.7	1433.7
1446.7	1446.7	1446.6	1446.6
3127.0	3118.0	3127.0	3113.9
3294.7	3294.7	3294.7	3294.7
3296.3	3296.3	3296.3	3296.2

6.2.3 Frequency projection and grid development

6.2.3.1 Transition state

Zero-point energy correction necessitates projection of the two active modes (C–H_a and H_a–Cl stretching vibrations) from the Hessian. Both curvilinear [14, 15] and rectilinear [66] projection methods are applied in order to evaluate the most appropriate method for PES development. Pre- and post-projected frequencies for both methods are shown in Table 6.6. At a stationary point, the pre-projected frequencies should be coordinate independent; slight differences between the rectilinear and curvilinear descriptions are most likely related to inaccuracies introduced due to use of a numerical gradient in the curvilinear description[17]. The following observations can be made regarding TS normal mode behaviour:

- The reaction coordinate, at $1232i$ cm^{-1}, corresponds to motion of the transferring hydrogen between the two heavy groups, with some umbrella-like

[17]Molpro [62] only allows for numerical Hessians and gradients with UMP2 theory.

bending motion of the CH_3 group. This mode is correctly projected out in both the curvilinear and rectilinear schemes.

- At approximately 320–330 cm^{-1}, two modes correspond to rocking of the CH_3 group, combined with some linear angle bend of the central Cl–H_a–C angle. These modes are not projected.
- The second reactive mode is a heavy atom breathing motion at 512 cm^{-1} , and is projected in both schemes.
- A doubly degenerate linear angle bend (with some CH_3 group rocking) occurs at approximately 959–965 cm^{-1}. These vibrational modes are not coupled to the reaction coordinate and therefore do not lose magnitude post-projection.
- At 1214 cm^{-1}, there is an umbrella bending mode (with some C–H_a stretch) that is reduced post-projection, indicating some degree of coupling between the two active modes and the umbrella bending mode. This coupling appears to be stronger in the curvilinear scheme, resulting in a lower post-projection frequency.
- There are two C–H bending vibrations in the CH_3 moiety at approximately 1442–1446 cm^{-1}, which remain relatively unaffected by projection.
- At approximately 3127 cm^{-1}, there is a symmetric CH_3 stretch which is also shown to have (minor) coupling with the active coordinates, losing magnitude post-projection.
- Finally, there are two degenerate asymmetric C–H stretching vibrations at approximately 3294–3296 cm^{-1}, which are not coupled to the reactive modes.

Hydrogen chattering ($1232i$ cm^{-1}) and heavy atom breathing (512 cm^{-1}) are the two active modes completely removed in both projection schemes. However, there

is also coupling between the spectator and active modes as observed by post-projection decrease of several additional vibrational modes. This is evidenced by a 19.8% (16.4%) and 0.4% (0.3%) decrease of the modes at $\sim$ 1214 cm^{-1} and $\sim$ 3127 cm^{-1} in the curvilinear (rectilinear) method, respectively. Furthermore, two additional modes also decrease following projection in the curvilinear but not rectilinear scheme: the 959 cm^{-1} linear angle bend decreases by 7.4% while the 3296 cm^{-1} C–H stretch decreases by 0.6%. At the transition state, this amounts to a loss of approximately 334.071 cm^{-1} (209.37 cm^{-1}) for the curvilinear (rectilinear) method. It is possible that this coupling is present across the surface, resulting in an overall decrease in zero point energy.

6.2.3.2 PES frequency projection

Previous studies have shown that the curvilinear projection method is an improvement upon the rectilinear scheme; the latter was shown to result in the unphysical loss of vibrational energy due to the introduction of large imaginary frequencies post-projection [14, 15]. In order to evaluate the best projection method for the current system, both methods were implemented across a grid of PES *ab initio* points. The number of post-projection imaginary frequencies greater than tolerance threshold 100 cm^{-1} for the rectilinear and curvilinear methods are shown in Figures 6.6(a) and 6.6(b), respectively. The curvilinear scheme produces fewer imaginary frequencies than the rectilinear scheme, however, the improvement is not as promising as for previous studies [15]. For the rectilinear scheme, 160/363 grid points possessed post-projected imaginary frequencies larger than the tolerance value; this was reduced to 69/363 for the curvilinear scheme. Rectilinear imaginary frequencies primarily occur along the outer edges of the PES and along the MEP, as consistent with past comparisons [15]. The curvilinear scheme, while

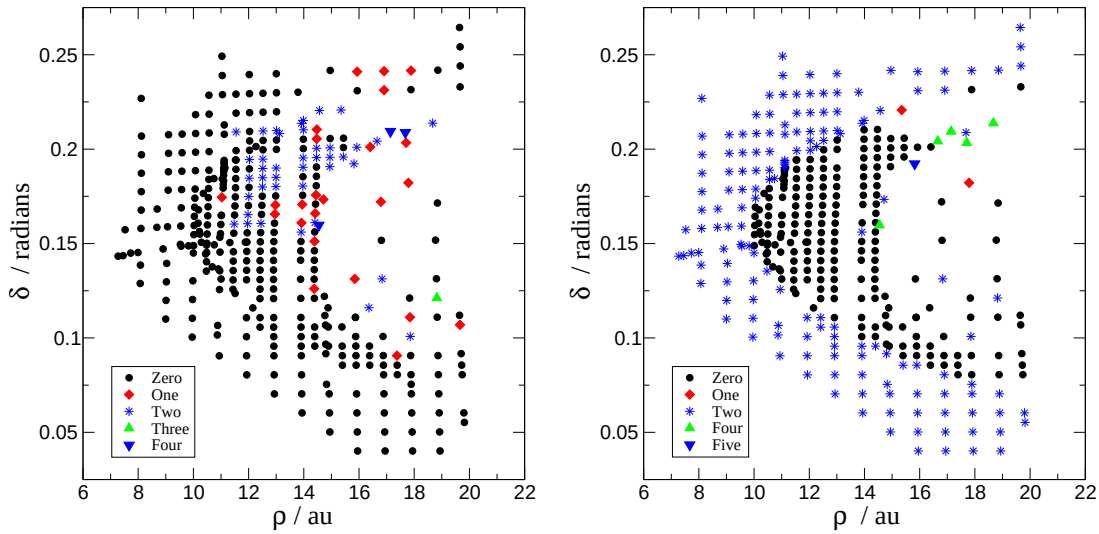

(a) Curvilinear projection method.

(b) Rectilinear projection method.

Figure 6.6: Curvilinear and rectilinear projection scheme applied to *ab initio* grid points for the $Cl + CH_4 \longrightarrow HCl + CH_3$ reaction. Number of post-projection imaginary frequencies greater than 100 cm^{-1} as indicated in legend.

a significant improvement along the outer walls of the PES, does predict unphysical imaginary frequencies in the $Cl + CH_4$ channel and the high energy region between the two asymptotic channels. This is most likely related to treatment of the linear angle bend motion, which is believed to follow a rectilinear path when lifting off the RD PES (S.T. Banks, private communication). Despite this inaccuracy, the curvilinear projection method generally performs better than its rectilinear counterpart, and is therefore implemented in the development of the current potential system.

6.2.3.3 Grid development

Hyperspherical coordinates were defined according to section 2.2. Preliminary tests showed that the reaction maintained a collinear Cl–H_a–C angle across the grid, and therefore C_{3v} symmetry was subsequently enforced in calculation of the *ab initio* PES. Data points were calculated on a grid ranging from $\delta_{\min} = 0$ to

δ_{max}, and from behind the TS $\rho \sim 7$ au to $\rho \sim 21$ au. Hyperspherical coordinate values were recomputed following centre of mass changes after partial optimisation calculations.

6.2.4 Potential energy model

An analytical 29-parameter double-Morse function (Section 3.3) is used to construct the ground and excited state diabatic potential surfaces. An 8-parameter analytical function describing the decay of the spin-orbit coupling constants in the vicinity of the transition state is also developed. For all four surfaces, a nonlinear least squares regression algorithm in Matlab [63] was used to determine surface parameters; the surface fitting toolbox was also used to identify and exclude outliers.

The final PES is presented in the following section, and is valid from $\rho = 8$ to 16 au. The ground state diabatic surface is valid from $\delta = 0$ to δ_{max}. Though the excited state diabatic surface was only fit to low energy data in the F1 reactant channel ($\delta > 0.16$ rad), it smoothly extends to high energy in the F1 product channel and is therefore valid across the entire δ range. Similarly, the two SOC surfaces are fit to data for $\delta > 0.15$ rad; for geometries below this, the potentials are set to zero.

6.2.4.1 Diabatic surface models

The diabatic potential function and parameters are given by

$$\begin{aligned} V(\rho,\delta) &= f_1\left[(1-\exp((g_1)\delta+h_1))^2-c_{14}\right] \\ &\quad + f_2\left[(1-\exp(-((g_2)\delta+(h_2))))^2-c_{28}\right]+c_{29} \\ f_1 &= (1+c_1\rho^{c_2}\exp(c_3\rho))c_4 \\ f_2 &= (1+c_{15}\rho^{c_{16}}\exp(c_{17}\rho))c_{18} \\ g_1 &= c_5+c_6\rho+c_7\rho^2 \\ g_2 &= c_{19}+c_{20}\rho+c_{21}\rho^2 \\ h_1 &= c_8+c_9\rho+c_{10}\rho^2-\log(c_{11}+c_{12}\rho+c_{13}\rho^2) \\ h_2 &= c_{22}+c_{23}\rho+c_{24}\rho^2+\log(c_{25}+c_{26}\rho+c_{27}\rho^2). \end{aligned} \tag{6.4}$$

An initial guess for the parameters for the ground state surface was taken from previous studies [13]; parameters were subsequently adjusted to ensure correct asymptotic high energy limits and then modified in the least squares fitting procedure (lsqcurvefit in Matlab [63]). The surface fitting toolbox [63] was used to identify outliers for low-energy fitting; the final data set contained 171 points with a sum of squared residuals (SSR) of 2.2×10^{-4} au^2. The final parameters for all four surfaces, including the A_1 ground state surface, are shown in Table 6.7 (the SOC surfaces are explained in section 6.2.4.2).

The parameters for the excited diabatic E surface were determined using a similar fitting procedure described above. In the current diabatic model, it is particularly important that the two surfaces become degenerate in the asymptotic $Cl + CH_4$ channel, as consistent with *ab initio* data. Developing a model with this behaviour proved difficult, because of the large number of degrees of freedom in equation (6.4), as well as a reduction in the number of data points available because

Table 6.7: PES parameters for the $Cl + CH_4 \rightleftharpoons HCl + CH_3$ reaction.

	$\mathbf{A}_1$	**E**	**A**	**B**
c_1	33.7091791	33.7104657	1.0278043×10^{-4}	1.7837221×10^{-5}
c_2	-9.4137823	-9.4985922	1.6730222×10^{-1}	8.8885700×10^{-2}
c_3	-0.2984860	-0.3120208	1.9180895	1.1052732
c_4	0.3408111	0.4585513	-7.6335945×10^{-1}	-4.0910503×10^{1}
c_5	21.8665166	18.6354881	-1.1925541×10^{2}	4.1022580×10^{2}
c_6	-0.6199417	-0.1178949	6.2782817×10^{2}	-8.8115621×10^{2}
c_7	0.0475726	0.0287326	2.8241506×10^{-1}	3.6444004×10^{-3}
c_8	3.8801101	4.6419913	1.2686625×10^{-3}	1.3401619×10^{-3}
c_9	0.2009703	0.0489267		
c_{10}	-0.0127017	-0.0072190		
c_{11}	52.8669116	53.3500438		
c_{12}	252.1119879	252.6919904		
c_{13}	27.9679782	21.1239275		
c_{14}	12.6352265	16.1588000		
c_{15}	133.4455751	135.0406265		
c_{16}	-5.4623009	-4.9110332		
c_{17}	0.2436439	0.0536798		
c_{18}	0.3520120	0.4571251		
c_{19}	12.9251918	17.4120445		
c_{20}	0.8651841	-0.1331262		
c_{21}	-0.0228559	-0.0119515		
c_{22}	-7.5700022	-6.8890311		
c_{23}	-0.0180181	-0.1982455		
c_{24}	0.0019791	0.0066089		
c_{25}	-87.2670480	-83.8842875		
c_{26}	34.5437230	42.2120505		
c_{27}	-0.8172033	0.3440478		
c_{28}	-122.9947167	-121.4651824		
c_{29}	-540.9150587	-549.8423194		
Ab initio #	171 (171)	142 (585)	199 (199)	199 (199)
SSR (au^2)	2.2×10^{-4}	1.6×10^{-3}	2.1×10^{-9}	9.0×10^{-11}

of convergence issues in the asymptotic region for the E *ab initio* calculations. Therefore, prior to fitting, additional data points were included from evaluating the A_1 potential in the region of degeneracy indicated by comparison of A_1 and E *ab initio* results: 0.21 rad $< \delta < \delta_{max}$; 14 au $< \rho <$ 21 au. A total of 585 final data points were used in the fit; 142 were included directly from *ab initio* calculations,

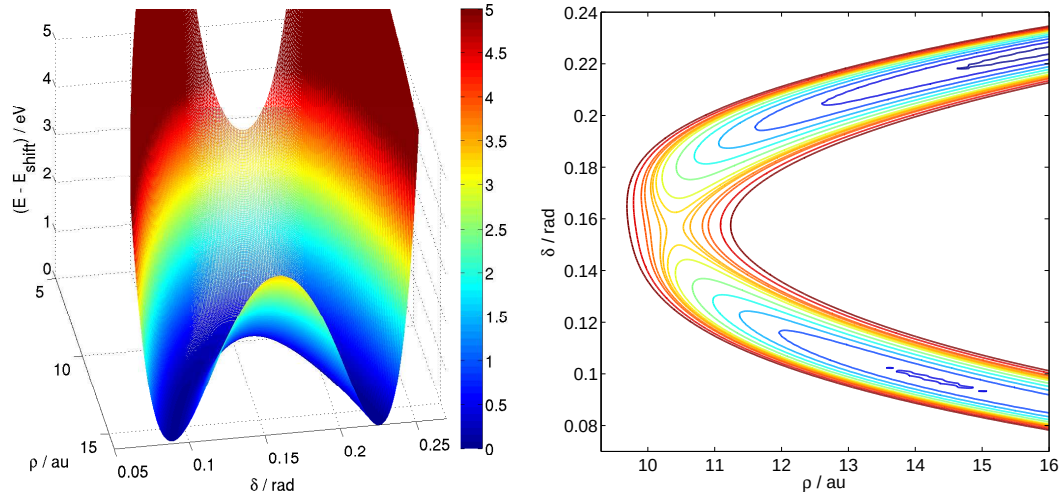

(a) A_1 ground state diabatic surface. (b) Contour diagram of A_1 surface.

Figure 6.7: A_1 ground state potential energy surface for the $Cl + CH_4 \longleftrightarrow HCl + CH_3$ reaction. The energy in the contour diagram (b) ranges from 0 to 0.5 eV; contour lines are unevenly spaced to highlight surface properties. Lines are drawn at 0.010, 0.050, 0.100, 0.150, 0.200, 0.250, 0.300, 0.325, 0.340, 0.350, 0.380, 0.400, 0.450, 0.500 eV.

while the remainder were evaluated data points from the A_1 surface in the region of overlap. The SSR of the E surface was determined to be 1.6×10^{-3} au^2; the parameters are given in Table 6.7. Though the surface was fit only for $\delta > 0.16$, it extends smoothly to high energies, and reaches an F1 product plateau at 5 eV, an energy which is too high to be of influence in the current study.

Correct asymptotic surface behaviour was observed up to $\rho = 16$, and therefore the surface system is restricted to $\rho \leq 16$ au. Both surfaces are plotted on an energy scale shifted with respect to the minimum of the ground state potential[18].

A_1 surface. The ground state PES and contour diagram are shown in Figure 6.7. The TS location slightly favours the $HCl + CH_3$ channel, and there is evidence of van der Waals minima, especially in the R1 reactant channel.

[18] $E_{shift} = -501.53431035$ au; $\rho = 15.8184$ au, $\delta = 0.2242$ rad.

E surface. The excited state (E) diabatic surface and contour diagram are shown in Figure 6.8. The surface is plotted on the same energy scale as the A_1 surface and the same contour settings are applied. Though not shown, the surface plateaus at approximately 5 eV in the $CH_3 + HCl$ channel.

The overlap of the two contour diagrams yields information concerning the interaction between the surfaces (Figure 6.9). The excited diabatic state becomes much higher in energy than the ground state surface before the TS is reached, thus indicating that nonadiabatic transition is likely to occur in the $Cl + CH_4$ channel.

6.2.4.2 SOC potentials

The *ab initio* spin-orbit constants were found to remain fairly constant across the $Cl + CH_4$ channel, but decrease quickly with δ and ρ at the approach of the interaction region[19]. A, the potential describing the spin-orbit interaction of states E and A_1, was found to have more pronounced changes as a function of geometry than B, the potential describing the spin-orbit interaction between the degenerate states E. A function of the form $-1/(\rho+\delta)+C$ was chosen in order to adequately describe the decay of the SOC constants in the interaction region; 8 parameters were included to allow for increased flexibility with respect to variation in ρ and δ:

$$\begin{aligned} \mathrm{A/B}(\rho,\delta) &= \frac{c_1}{(c_2\rho + c_3\delta)^C} + c_8 \\ C &= (c_4 + c_5\delta + c_6\delta^2 + c_7\rho). \end{aligned} \tag{6.5}$$

These functions were found to adequately represent geometric changes in the coupling constants in the $Cl + CH_4$ channel. A nonlinear least squares regression algorithm was used to fit the surfaces [63] for δ >0.15 rad. For $\delta \leq$0.15 rad, the *ab*

[19]The *ab initio* spin-orbit coupling constants are the positive, scaled (1.05687) spin-orbit coupling constants in atomic units.

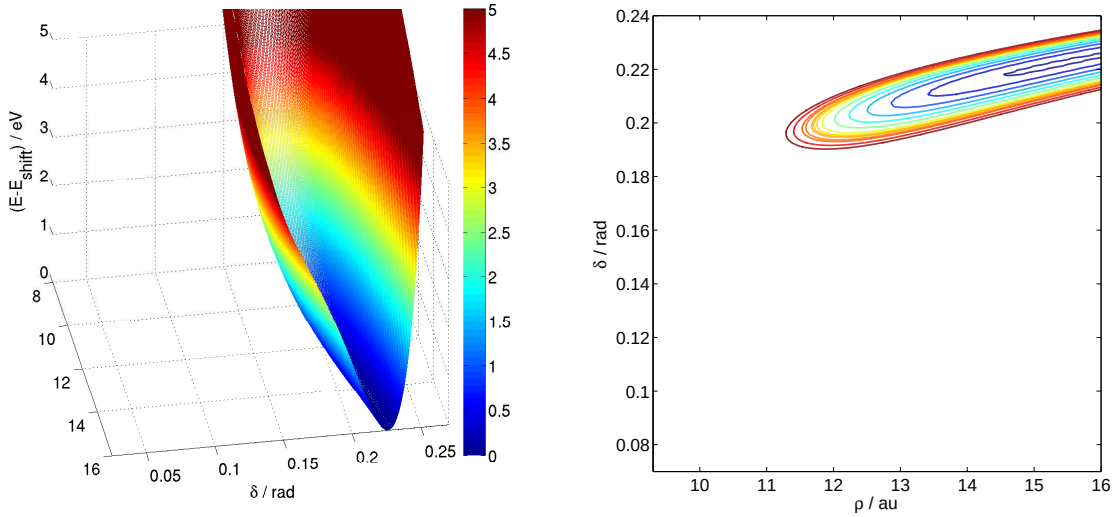

(a) E excited state diabatic surface.

(b) Contour diagram of E surface.

Figure 6.8: E excited state potential energy surface for the $Cl+CH_4 \rightleftharpoons HCl+CH_3$ reaction. The surface extends smoothly to plateau at 5eV in the CH_3+HCl channel (small δ).

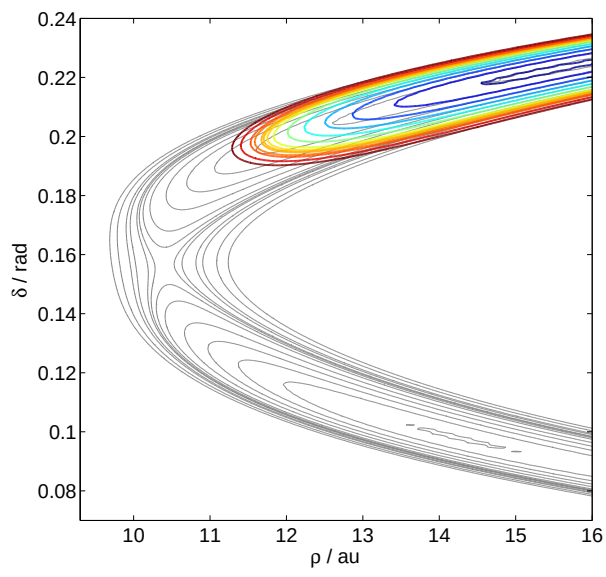

Figure 6.9: Contour diagram of ground and excited diabatic states for the $Cl + CH_4 \rightleftharpoons HCl + CH_3$ reaction. Gray (A_1 surface); Colour (E surface). The E surface extends smoothly to high energies for small values of δ.

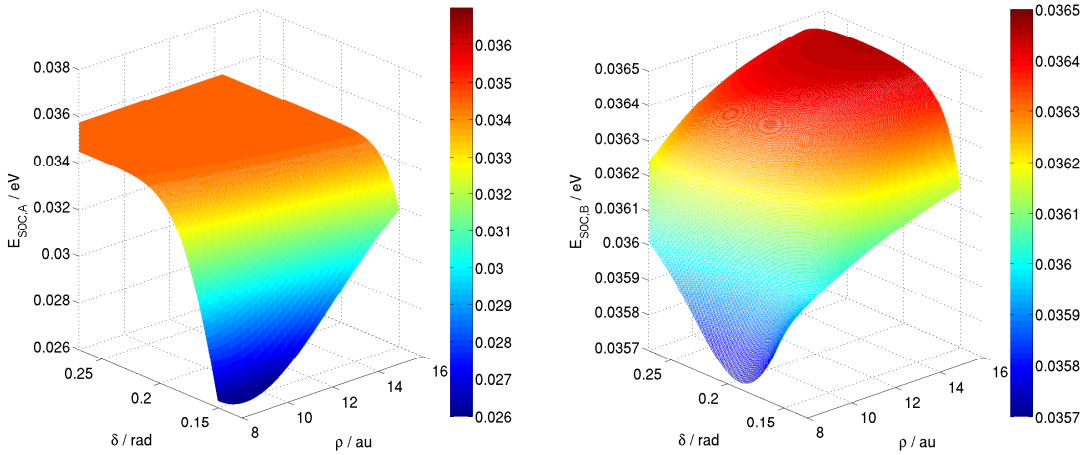

(a) A (b) B

Figure 6.10: Geometry dependent spin-orbit coupling potential energy surfaces.

initio coupling constants were found to abruptly decrease to zero, and therefore were set to be zero in this region. Introduction of this discontinuity had negligible effect, as the diabatic excited state is much higher in energy than the ground state at this geometry, making the possibility of a transition highly unlikely. The surface parameters are given in Table 6.7 and the surfaces are shown in Figure 6.10.

6.3 Surface characterisation

The multi-surface potential model ($\mathbf{V}(\rho, \delta)$) is constructed as a matrix containing the diabatic ground state ($V^{d}_{A_1}(\rho, \delta)$), the diabatic excited states ($V^{d}_{E}(\rho, \delta)$) and the coupling potentials (A and B), according to equation (6.6). For each geometry (ρ_i, δ_i), the potential matrix $\mathbf{V}(\rho_i, \delta_i)$ can be diagonalised (indicated by an arrow) to yield eigenvalues corresponding to the adiabatic potential surfaces that explicitly include the effects of spin-orbit coupling: adiabatic ground ($V^{ad}_{A_1}$) and excited ($V^{ad}_{E_{low}}$ and $V^{ad}_{E_{high}}$) states.

$$\mathbf{V}(\rho,\delta) = \begin{bmatrix} V^{\mathrm{d}}_{\mathrm{A_1}} & \mathrm{A} & \mathrm{A} \\ \mathrm{A} & V^{\mathrm{d}}_{\mathrm{E}} & \mathrm{B} \\ \mathrm{A} & \mathrm{B} & V^{\mathrm{d}}_{\mathrm{E}} \end{bmatrix} \longrightarrow \begin{bmatrix} V^{\mathrm{ad}}_{\mathrm{A_1}} & 0 & 0 \\ 0 & V^{\mathrm{ad}}_{\mathrm{E_{low}}} & 0 \\ 0 & 0 & V^{\mathrm{ad}}_{\mathrm{E_{high}}} \end{bmatrix} \tag{6.6}$$

Explicit inclusion of spin-orbit effects should increase the barrier height of $V^{\mathrm{ad}}_{\mathrm{A_1}}$ relative to $\mathrm{V}^{\mathrm{d}}_{\mathrm{A_1}}$; scattering on the ground adiabatic in comparison with the multi-state potential should elucidate the relative importance of adiabatic versus non-adiabatic spin-orbit effects. Furthermore, spin-orbit interaction splits the diabatic excited state surfaces into $V^{\mathrm{ad}}_{\mathrm{E_{low}}}$ (asymptotically degenerate with $V^{\mathrm{ad}}_{\mathrm{A_1}}$ and corresponding to the $\mathrm{Cl}(^2\mathrm{P}_{\frac{3}{2}})$ ground state) and $V^{\mathrm{ad}}_{\mathrm{E_{high}}}$ (corresponding to the $\mathrm{Cl}(^2\mathrm{P}_{\frac{1}{2}})$ state).

6.3.1 Minimum energy path

The minimum energy path (MEP) of the diabatic and ground adiabatic surfaces in the $\mathrm{Cl} + \mathrm{CH_4}$ channel is shown as a function of ρ in Figure 6.11. In general, the surfaces were found to reproduce the expected behaviour. The three diabatic states are approximately degenerate in the asymptotic region, whereas the lower two adiabatic surfaces ($V^{\mathrm{ad}}_{\mathrm{A_1}}$ and $\mathrm{V}^{\mathrm{ad}}_{\mathrm{E_{low}}}$) are shifted down by $\sim$1/3 of the spin-orbit splitting value and the upper adiabatic surface ($\mathrm{V}^{\mathrm{ad}}_{\mathrm{E_{high}}}$) is shifted up by $\sim$2/3 of the same value. The diabatic surfaces are not exactly degenerate and thus result in slightly disproportionate splitting, which is given in Table 6.8. The average final sector ($\rho = 16$) splitting is 853 cm^{-1}, which is close to the experimentally predicted splitting for the Cl atom, 882 cm^{-1} [72].

Table 6.8: Adiabatic surface spin-orbit splitting at $\rho = 16$ in the $Cl + CH_4$ channel.

	E / kcal mol^{-1}	E / cm^{-1}
$V^{ad}_{A_1}$	-0.7285	-254.7996
$V^{ad}_{E_{low}}$	-0.6699	-234.2911
$V^{ad}_{E_{high}}$	1.7399	608.5397
Average shift		-244.5454
Average split		853.0851

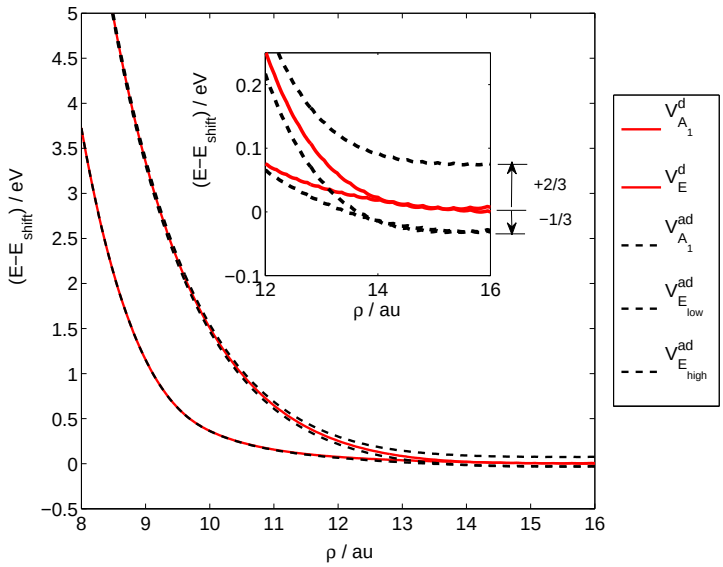

Figure 6.11: Minimum energy path for the diabatic and adiabatic surfaces in $Cl + CH_4$ channel. Spin orbit splitting for the adiabatic surfaces (-1/3, +2/3) shown for the asymptotic region in the inset.

6.3.2 Surface properties

Properties of the diabatic and adiabatic ground state surfaces are summarised in Table 6.9 (where the labels "forward" and "reverse" correspond to reactions F1 and R1, respectively, "r" designates $Cl + CH_4$, "p" designates $CH_3 + HCl$, and "vdW,r/p" designates the r or p vdW wells). The energies of the TS (E_{TS}), vdW wells ($E_{vdw,r/p}$), and reactant and product species ($E_{r/p}$) are all given relative to the potential minimum of the diabatic surface (E_{shift}) and used to calculate the

barrier heights ($\Delta V_{\text{reverse/forward}}$), enthalpy of reaction (ΔH), the depth of the vdW wells relative to asymptotic limits ($E_{r/p} - E_{vdW,r/p}$), and the barrier heights relative to the vdW wells ($\Delta V_{\text{reverse/forward,vdW}}$). These surface barrier heights include the effects of spectator mode vibrations and therefore cannot be directly compared to *ab initio* results.

As shown in Table 6.9, the reverse barrier height is the same for both surfaces (6.4332 kcal mol^{-1})[20], indicating that the spin-orbit effects do not contribute to changes in the $CH_3 + HCl$ channel or at the TS. Other properties such as the depth of the F1 product vdW well ($E_p - E_{vdW,p}$) and the location of the transition state (ρ_{TS} and δ_{TS}) are similarly unchanged, thereby indicating that spin-orbit interaction primarily affects the F1 reactant channel.

Surface properties in the F1 reactant channel are influenced by inclusion of spin-orbit coupling on the surface. The adiabatic forward barrier height increases to 8.4639 kcal mol^{-1} from the diabatic value of 7.7354 kcal mol^{-1}. Van der Waals wells are seen to be shallow, with a depression of only 0.2099 kcal mol^{-1} relative to asymptotic F1 products in the $CH_3 + HCl$ channel, and only 0.0029 kcal mol^{-1} relative to asymptotic F1 reactants in the $Cl+CH_4$ channel on the diabatic surface. The location and depth of the F1 reactant vdW well changes for the adiabatic surface, potentially indicating that the diabatic E surface drops slightly below the A_1 surface in this asymptotic region.

Furthermore, the TS saddle point ($\rho = 10.4032$ au, $\delta = 0.1565$ rad) is similar to the *ab initio* predicted hyperspherical coordinate TS values ($\rho = 10.2399$ au, $\delta = 0.1554$ rad), thereby providing evidence that the surface accurately represents the physical behaviour of the system. This TS location corresponds to **R** and **r** Jacobi coordinate values of 2.854 and 1.484 Å, respectively. **r** directly correlates

[20]The best comparison that can be made involves constructing the approximate surface barrier height predicted by *ab initio*; that is: $(E_{TS} + ZPE_{projected}) - (E_{reactants} + ZPE_{CH_3}) = 5.9093$ kcal mol^{-1}, which is slightly lower than the surface reverse barrier height of 6.4332 kcal mol^{-1}.

Table 6.9: Energetic properties of ground state diabatic and adiabatic surfaces. Quantities defined in text. Energies given in kcal mol^{-1}.

	Diabatic Ground	Adiabatic Ground
$E_{TS} - E_{shift}$	7.7383	7.7383
$E_{vdW,p} - E_{shift}$	1.0953	1.0953
$E_{vdW,r} - E_{shift}$	0.0000	-0.7401
$E_p - E_{shift}$	1.3052	1.3052
$E_r - E_{shift}$	0.0029	-0.7256
$\Delta V_{reverse}$	6.4332	6.4332
$\Delta V_{forward}$	7.7354	8.4639
ΔH	1.3023	2.0308
$E - E_{vdW,p}$	0.2099	0.2099
$E_r - E_{vdW,r}$	0.0029	0.0145
$\Delta V_{reverse,vdW}$	6.6430	6.6430
$\Delta V_{forward,vdW}$	7.7383	8.4784
ρ_{TS}/ au	10.4032	10.4032
δ_{TS} / rad	0.1565	0.1565
$\rho_{vdW,p}$ / au	14.2697	14.2697
$\delta_{vdW,p}$ / rad	0.0978	0.0978
$\rho_{vdW,r}$ / au	15.8184	15.8077
$\delta_{vdW,r}$ / rad	0.2242	0.2242

to the H_a–Cl distance, which is 1.275 Å for the gas phase molecule [172]. $\mathbf{R} - \mathbf{r}$ (1.370 Å) approximately corresponds to the C–H_a distance, which is 1.087 Å for gas phase methane [172]. Thus the surfaces transition states, as with the *ab initio* TS, are more similar to the F1 product geometries.

6.4 Hyperspherical adiabats

6.4.1 Assignment

Hyperspherical adiabats (δ-dependent eigenvalues, ε_s) are visualised as a test of model applicability prior to scattering, where vibronic state $s = i, \nu$ refers to the ν^{th} vibrational level of the i^{th} electronic state. An adiabat may be characterised according to the expectation value of δ as an R1 reactant ($< \frac{1}{2}\delta_{max}$) or R1 product

($> \frac{1}{2}\delta_{max}$) state. However, as mentioned in 2.3.3, no automatic method exists for determining the electronic state of a particular hyperspherical adiabat. It is possible to manually assign quantum numbers i, ν according to the following guidelines:

1. In the R1 reactant channel, the excited state is too high to influence the dynamics; therefore any R1 reactant state must belong to the ground, A_1 state.

2. In the asymptotically diagonal representation resulting from R-matrix propagation, ε_s values at large ρ become degenerate with their adiabatic, single surface counterparts. Thus, hyperspherical adiabats computed from the ground adiabatic surface should be asymptotically degenerate with the A_1 hyperspherical adiabat, thereby distinguishing the two lower Cl + CH_4 states from the upper Cl* + CH_4 state.

3. The number of nodes in the $\delta-$dependent wavefunction increases for each vibrational mode but is independent of electronic state; thus, for the A_1, E_{low}, and E_{high} asymptotic electronic states, the ground vibrational state has zero nodes.

The hyperspherical adiabat vibronic states are assigned in Table 6.10 (where R refers to R1 reactants, and P refers to R1 products). Though some crossings between the A_1 and E_{low} hyperspherical adiabats occur at long range, this subtle effect is not the focus of the current investigation. Thus, the asymptotically degenerate A_1 and E_{low} are treated as indistinguishable; the adiabats are labelled according to whether they correspond to an R1 product state of $Cl(^2P_{\frac{3}{2}})$ or $Cl(^2P_{\frac{1}{2}})$. The asymptotic ordering of the states is for $14 < \rho < 15.9$; in final sectors states

Table 6.10: Vibronic states assignments for $HCl + CH_3 \rightleftharpoons Cl + CH_4$.

Diabatic				Adiabatic		
N	Label of States	R	P	N	R	P
1	A_1/E (Cl; $^2P_{\frac{3}{2}}$)		0	1		0
2	A_1/E (Cl; $^2P_{\frac{3}{2}}$)		1	2	0	
3	Reactant	0		3		1
4	E (Cl*; $^2P_{\frac{1}{2}}$)		2	4	1	
5	A_1/E (Cl; $^2P_{\frac{3}{2}}$)		3	5		2
6	A_1/E (Cl; $^2P_{\frac{3}{2}}$)		4	6	2	
7	Reactant	1		7	$3^\ddagger$	
8	E (Cl*; $^2P_{\frac{1}{2}}$)		5	8		$3^\ddagger$
9	A_1/E (Cl; $^2P_{\frac{3}{2}}$)		6	9	4	
10	A_1/E (Cl; $^2P_{\frac{3}{2}}$)		$7^\ddagger$	10		4
11	Reactant	$2^\ddagger$				
12	E (Cl*; $^2P_{\frac{1}{2}}$)		8			
13	Reactant	$3^\ddagger$				
14	A_1/E (Cl; $^2P_{\frac{3}{2}}$)		$9^\ddagger$			
15	A_1/E (Cl; $^2P_{\frac{3}{2}}$)		10			
16	E (Cl*; $^2P_{\frac{1}{2}}$)		11			
17	Reactant	4				
18	A_1/E (Cl; $^2P_{\frac{3}{2}}$)		12			
19	A_1/E (Cl; $^2P_{\frac{3}{2}}$)		13			
20	E (Cl*; $^2P_{\frac{1}{2}}$)		14			

labelled ($\ddagger$) cross[21]. For comparison, the assignment of the ground state adiabatic hyperspherical adiabats is also given in Table 6.10.

Comparison of the multi-surface hyperspherical adiabats to the ground adiabatic scattering results shows the expected asymptotic degeneracy between the single-state hyperspherical adiabats and the R1 reactant (Figure 6.12(a)) and A_1/E R1 product (Figure 6.12(b)) results.

The lowest 12 (multi-surface) hyperspherical adiabats are shown in Figure 6.13 alongside the potential ridge and the MEP in the R1 product channel ($\delta > \frac{\delta_{\max}}{2}$). It is clear that in the low energy region, the reactant states are higher in energy than

[21] This crossing prohibits averaging of the total probability matrix elements, but not the reactive probability matrix.

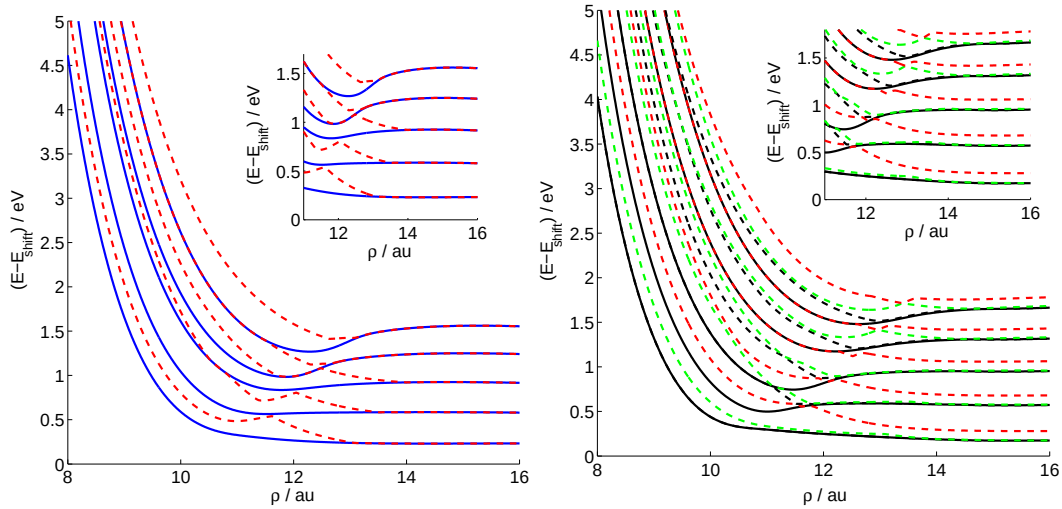

Figure 6.12: Hyperspherical adiabats for the $CH_3 + HCl \rightleftharpoons CH_4 + Cl$ reaction. **Left:** R1 reactant states. Solid blue: adiabatic reactant states; dashed red: diabatic reactant states. **Right:** R1 product states. Solid black: adiabatic product states, dashed black: diabatic Cl ($^2P_{\frac{3}{2}}$; A_1), dashed green: diabatic Cl ($^2P_{\frac{3}{2}}$; E), dashed red: diabatic Cl ($^2P_{\frac{1}{2}}$; E).

the degenerate $Cl(^2P_{\frac{3}{2}})$ product states but fall below the excited product states $Cl(^2P_{\frac{1}{2}})$.

The hyperspherical adiabats shown in Figure 6.13(a) neglect additional diagonal terms in the Hamiltonian (equation (2.1)), and thus the diagonally corrected hyperspherical adiabats are given according to

$$\varepsilon_s^{\text{corr}} = \varepsilon_s + \frac{3}{8\mu\rho^2} + \frac{J(J+1)}{2\mu\rho^2}. \tag{6.7}$$

The second term makes negligible difference in plotting the hyperspherical adiabats; therefore for $J = 0$, $\varepsilon_s^{\text{corr}} \approxeq \varepsilon_s$. However, for large values of total angular momentum, the third term significantly influences $\varepsilon_s^{\text{corr}}$, resulting in a shift of the adiabats to higher energy (because of an increase in the centrifugal barrier). Furthermore, the shape of the hyperspherical adiabats also changes because of the ρ

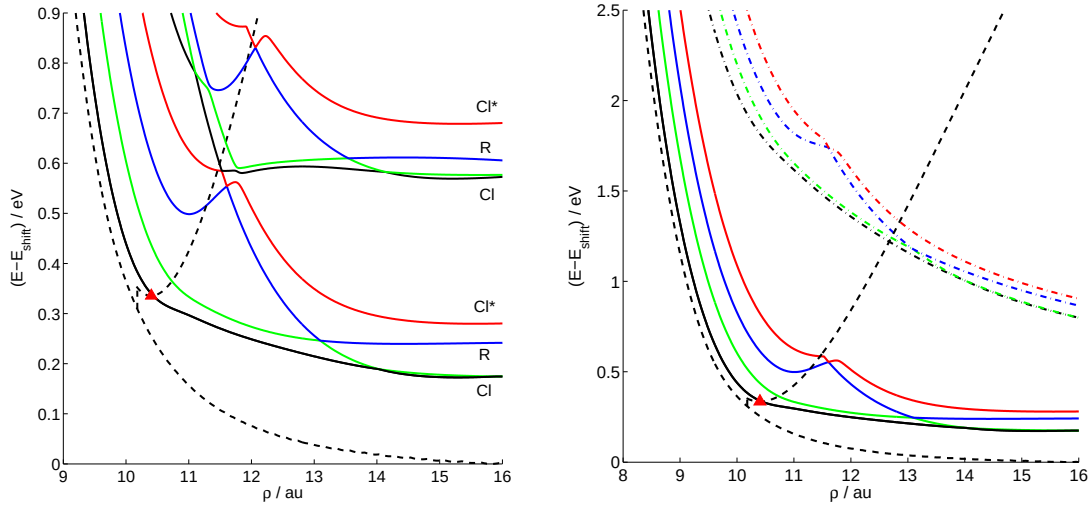

(a) $J = 0$ hyperspherical adiabats. (b) Solid lines: $J = 0$. Dashed: $J = 250$.

Figure 6.13: Hyperspherical adiabats for the $CH_3 + HCl \rightleftharpoons CH_4 + Cl$ reaction. Black: A_1 (Cl*; $^2P_{\frac{3}{2}}$), Green: E (Cl; $^2P_{\frac{3}{2}}$), Blue: reactant (R), Red: E (Cl*; $^2P_{\frac{1}{2}}$). Dashed black: potential ridge and R1 product MEP. TS location shown by red triangle.

dependence of this term (Figure 6.13(b)). Thus, for large values of J one would expect the number of open channels to decrease substantially (at ρ_{max}).

6.4.2 Identifying nonadiabatic transitions

6.4.2.1 Avoided crossings

Determining the location and mechanism of nonadiabatic transition is a major goal of this study. It is possible to specify the approximate site of reactive transfer by the location of avoided crossings between product and reactant hyperspherical adiabats [174]. Specifically, a major advantage of using hyperspherical coordinates in collinear reactive scattering problems is the ability to analyse reactive transitions in terms of the proximity of the avoided crossings to the potential ridge, defined as the dividing line between the reactant and product valleys [175]. It has been shown that reactive transitions often correlate to vibrationally nonadiabatic transitions

occurring in the vicinity of this mountain ridge line.

The potential ridge as shown in Figure 6.13 is defined for all values of ρ for which there is a local maximum separating the reactant and product valleys (and hence is not necessarily a straight line with respect to δ as is sometimes assumed[22] [175]). Below this ρ value, a straight line joins the potential ridge to the minimum energy path of the R1 product channel, thus separating the ρ-space into condensation (small ρ) and fragmentation (large ρ) zones. In the former, all atoms move in the same potential well as a function of δ, whereas in the latter the system exists in distinct product or reactant forms well described by a double-Morse potential [175]. Thus, the hyperspherical adiabats in the fragmentation zone correspond to vibrational states of the product or reactant molecules, and avoided crossings in this region are not meaningful because of the lack of interaction between reactant and product states. However, at intermediate values of ρ near the dividing ridge line, the hyperspherical adiabats interact strongly, leading to sharp avoided crossings [175].

For the *vibronic* hyperspherical adiabats (quantum state $s = i, \nu$), the same principles apply. A series of complex avoided crossings take place near the potential ridge (Figure 6.13), especially between the R1 reactant and the excited-Cl* product states, for example at $\rho = 11.62$ au / 0.549 eV and $\rho = 12.06$ au / 0.830 eV (Figure 6.13). It is likely that these avoided crossings indicate the location of (vibronic) nonadiabatic transition to produce Cl* product states.

6.4.2.2 Diabatic wavefunctions

The third diabatic state, $i = 3$, correlates asymptotically to the excited Cl* + CH_4 states, and therefore plotting the magnitude of the diabatic wavefunction ($|\Psi^d_{s=3,\nu}|^2$) should also indicate the location of nonadiabatic transition. This is

[22] However, assuming fixed $\delta = \delta_{\mathrm{TS}}$ would be a good approximation for the current system.

given by

$$|\Psi^d_{s=3,\nu}|^2 = \left(\sum_{j=1}^{N_\delta} c^\nu_{3j}\Phi^{\mathrm{d}}_3\chi_j \times \sum_{j=1}^{N_\delta} c^\nu_{3j}\Phi^{\mathrm{d}}_3\chi_j\right) \tag{6.8}$$
$$= |\Phi^{\mathrm{d}}_3|^2\left(\sum_{j=1}^{N_\delta} c^\nu_{3j}\chi_j\right)^2 = |\Phi^{\mathrm{d}}_3|^2|\phi_\nu|^2.$$

Contour diagrams of the vibrational component ($|\phi_\nu|^2$) are shown for $\nu = 0$ and 1 in Figures 6.14(a) and 6.14(b), respectively (contour energies are not evenly spaced). Both states commence with an initial sharp peak followed by growth of the wavefunction, a pattern that is also observed for $\nu > 1$ diabatic wavefunctions. The peaks occur in the $Cl + CH_4$ channel, and their location approximately coincides with the hyperspherical adiabat avoided crossings between the R1 reactant and Cl* product states (Figure 6.13).

These results are summarised in Table 6.11, where the average hyperspherical coordinate values for the growth of $|\Psi^d_{s=3,\nu}|^2$ ($\nu = 0,\ 1,\ 2,$ and 3) are given along with the geometry associated with the transition. As the level of vibrational excitation increases, nonadiabatic transition can occur at increasingly large H–Cl separation, potentially indicating that H–Cl stretch excitation makes transition possible at longer distances. The ground state transition occurs for H–Cl bond lengths as small as 2.075 Å.

6.5 Scattering calculations

Scattering calculations are performed for both single-surface (ground adiabatic and diabatic) and multi-surface models, in an effort to characterise the dynamics and kinetics of the forward (F1) and reverse (R1) processes.

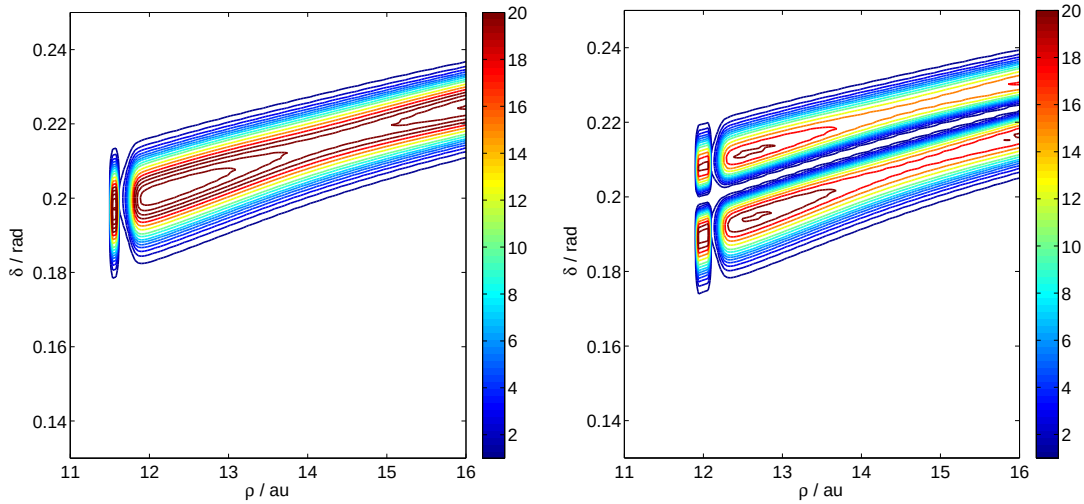

(a) $|\Psi^d_{s=3,1}|^2$. (b) $|\Psi^d_{s=3,2}|^2$.

Figure 6.14: Contour diagrams of diabatic wavefunction magnitudes for $i = 3$ ($|\Psi^d_3|^2$) in the $Cl + CH_4$ channel.

Table 6.11: Approximate location of nonadiabatic transition for the $HCl+CH_3 \longrightarrow Cl^* + CH_4$ reaction.

State	ρ / au	δ / radians	R_1 / Å	R_2 (H–Cl) / Å	∼C–H / Å
TS	10.4032	0.1565	2.8538	1.4841	1.3698
$Cl^*_{s:i,\nu=4:3,0}$	11.5779	0.1971	3.1531	2.0751	1.0780
$Cl^*_{s:i,\nu=8:3,1}$	12.0000	0.1986	3.2671	2.1674	1.0997
$Cl^*_{s:i,\nu=12:3,2}$	12.4087	0.2002	3.3773	2.2580	1.1193
$Cl^*_{s:i,\nu=16:3,3}$	12.8040	0.2013	3.4841	2.3428	1.1412

6.5.1 Numerical details

Scattering was performed using the multi-surface inelastic R-matrix propagation technique described in Chapter 2. Despite the asymptotic degeneracy of the ground $Cl + CH_4$ hyperspherical adiabats, symmetrised wavefunctions were not used as it was not necessary to distinguish between the A_1 and E_{low} states. Convergence of cumulative reaction probabilities, hyperspherical adiabatic energies and cross sections were monitored with respect to the scattering parameters shown in Table 6.12. The parameter E_{inc} was chosen to be small enough for resonances in the $J = 0$ CRP to be resolved, although for computational efficiency the increment

Table 6.12: Numerical parameters for scattering calculations for reaction $Cl + CH_4 \rightleftharpoons HCl + CH_3$.

Parameter	Description	Final Value
E_{inc} $(J = 0)$	Energy grid spacing	0.0001 eV
E_{inc} $(J > 0)$	Energy grid spacing	0.001 eV
ρ_{min}	First ρ sector (behind TS)	8 au
ρ_{max}	Final asymptotic ρ sector	16 au
N_δ	Size of DVR basis	200
E_{max}	Maximum incident KE	1.4 eV
N	Contracted basis size	20
N_{ad}	Contracted basis size (adiabatic calculation)	10
N_ρ	Number of ρ sectors	750
S_{num}	Number of ρ sectors to average $P_{ss'}$	100
J_{max}	Maximum angular momentum	250

was increased for $J > 0$ calculations. Convergence of ε_s was achieved by varying N_δ and the contracted basis set size (N) for all calculations was chosen to be sufficient to describe all open channels in the final sector at $E = E_{\text{max}}$. N_ρ and S_{num} were varied to achieve convergence of the CRP; the latter was chosen to 13.3% of N_ρ which is also consistent with previous studies [12, 13, 16]. The convergence of the integral and differential cross sections were monitored with respect to increasing J_{max}. For higher collision energy calculations (up to 2.4 eV for vibrationally excited states, N and J_{max} were increased to 35 and 300, respectively).

6.5.2 Single surface models

6.5.2.1 Adiabatic: $\mathbf{CH_3 + HCl \longrightarrow CH_4 + Cl\ (^2P_{\frac{3}{2}})\ (J = 0)}$.

Reaction Probabilities. The cumulative reaction probability (CRP) for scattering on the ground adiabatic surface is given in Figure 6.15, plotted on a total energy scale shifted by the energy of the ground state reactants, E_0. The reaction is dominated at high energies by the presence of sharp resonances.

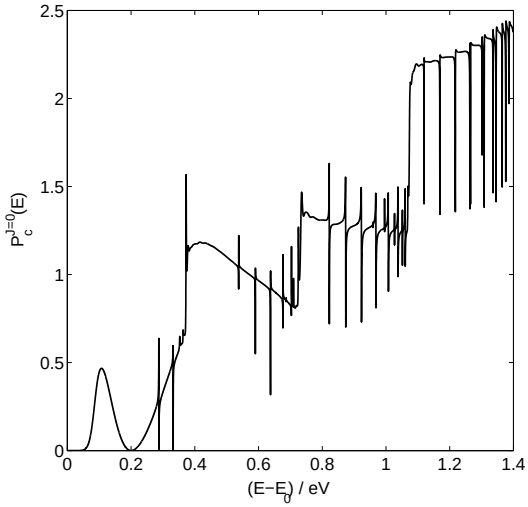

(a) $J = 0$ cumulative reaction probability as a function of total energy.

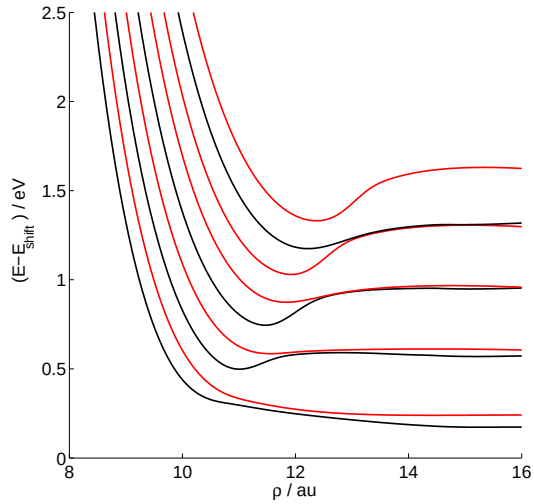

(b) Hyperspherical adiabats for channels open at 1.4 eV. (Black: product; red: reactant)

Figure 6.15: Reactivity of the CH_3+HCl →CH_4+Cl ($^2P_{\frac{3}{2}}$) on the ground adiabatic potential energy surface.

In general, there is quantum oscillatory structure typical of heavy-light heavy systems. The approximate surface barrier height (0.0935 eV on this energy scale) lies after the onset of reaction, indicating that tunnelling plays a significant role in the R1 reaction process. The hyperspherical adiabats for the ground adiabatic state are also given in Figure 6.15; the assignment of the states is reported in Table 6.10.

The initial state selected probabilities (Figure 6.16) exhibit oscillating reaction probability for the $s = 0$ and 1 initial states, possibly indicative of quantum interference effects due to the near degeneracy of reactant and product hyperspherical adiabats in the asymptotic region [52]. Furthermore, sharp resonance features at high collision energies are seen for all four transitions. This is expected given the deep wells in the hyperspherical adiabats (Figure 6.15), which are capable of supporting metastable bound states. By analysis of the state-to-state reaction probabilities, the ground adiabatic reaction was found to be primarily vibration-

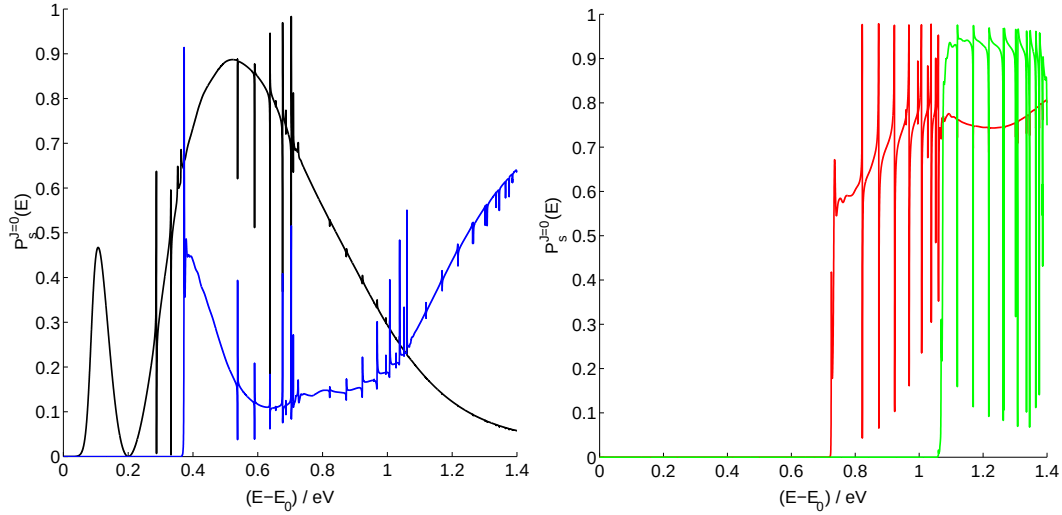

(a) $s = 0$ (black), $s = 1$ (blue). (b) $s = 2$ (red), $s = 3$ (green).

Figure 6.16: Initial state selected reaction probabilities ($s \rightarrow$all) for the CH_3+HCl $\rightarrow CH_4$+Cl ($^2P_{\frac{3}{2}}$) reaction on the ground adiabatic potential energy surface.

ally adiabatic, with the exception of reactions out of state $s = 1$. Incidence of vibrationally nonadiabatic pathways increased with total energy.

Resonances.

Hyperspherical adiabat analysis. The sharp resonance peaks in the $J = 0$ CRP can be analysed and assigned by performing a one-dimensional DVR analysis on the adiabatic hyperspherical adiabat potentials, ε_s. The Schrödinger equation

$$\left[-\frac{1}{2\mu}\frac{\partial^2}{\partial\rho^2} + \varepsilon_s\right]\Theta(\rho) = E_k^n\Theta(\rho) \tag{6.9}$$

is solved using the same DVR basis implemented for solving the δ-dependent portion of the scattering Hamiltonian in Chapter 2 [53]. Each hyperspherical adiabat potential, ε_s, is restricted to ρ values less than the local maximum. In general, the locations of the predicted bound states accurately reproduce the location of the

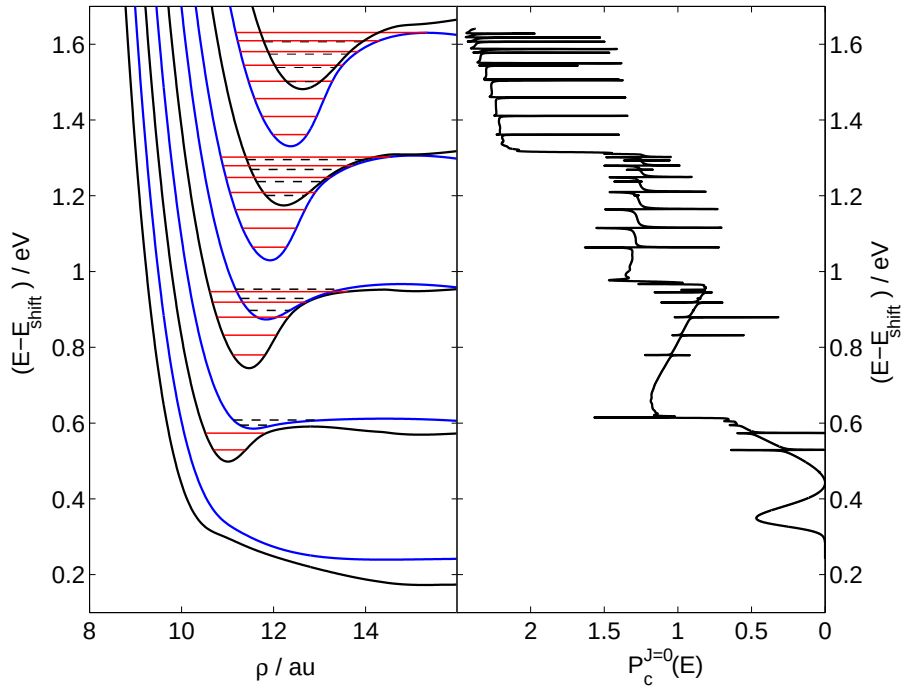

Figure 6.17: Bound state analysis of resonances for the CH_3+HCl →CH_4+Cl ($^2P_{\frac{3}{2}}$) reaction on the adiabatic ground state surface. **Left:** hyperspherical adiabats (Blue: reactant, black: product). Red solid and black dashed lines are overlapping resonances predicted by DVR analysis. **Right:** Cumulative reaction probability, $J = 0$.

CRP resonances, though small discrepancies arise that are most likely due to the approximation made in restricting the ρ value of the potential. The bound states of each hyperspherical adiabat are shifted by an average value to correlate with the location of the CRP resonances. The bound states, their quantum assignment, energies, shifted energies and ρ-location of the positive maximum are all given in Table 6.13. The shifted bound states are plotted in Figure 6.17 alongside the CRP and correlate well with observed resonance behaviour. High-energy hyperspherical adiabats possess deep wells and therefore support more bound states in both reactant and product hyperspherical adiabats, creating complex overlapping resonance behaviour, especially for $s = 4$. One would thus expect resonances to be a dominant factor in the reaction of vibrationally excited states.

Table 6.13: Resonances on the adiabatic surface for reaction $CH_3 + HCl \longrightarrow CH_4 + Cl(^2P_{\frac{3}{2}})$ (p=product, r=reactant). Energies in parentheses are shifted DVR energies. s=adiabat label, γ=eigenstate label, TD=time delay.

s	γ	ρ_{max} / au	DVR (E-E_0) / eV	TD #	TD (E-E_0) / eV
0 (p)	n/a	n/a	No bound states		
0 (r)	n/a	n/a	No bound states		
1(p)	0	12.8278	0.2818 (0.2873)	1	0.2874
	1		0.3262 (0.3317)	2	0.3320
1 (r)	0	14.4192	0.3557 (0.3526)		
	1		0.3693 (0.3662)		
2 (p)	0	14.4192	0.5301 (0.5383)	3	0.5378
	1		0.5820 (0.5902)	4	0.5903
	2		0.6294 (0.6376)	5	0.6378
	3		0.6691 (0.6773)	6	0.6767
	4		0.6968 (0.7050)	7	0.7035
2 (r)	0	14.7824	0.6495 (0.6555)		
	1		0.6811 (0.6871)		
	2		0.7056 (0.7116)		
3 (r)	0	14.9426	0.8133 (0.8223)	8	0.8222
	1		0.8637 (0.8727)	9	0.8735
	2		0.9124 (0.9214)	10	0.9229
	3		0.9579 (0.9669)	11	0.9685
	4		0.9975 (1.0065)	13	1.0080
	5		1.0284 (1.0374)	15	1.0380
	6		1.0514 (1.0604)	17	1.0600
3 (p)	0	14.6435	0.9520 (0.9590)		
	1		0.9885 (0.9955)	12	0.9958
	2		1.0205 (1.0275)	14	1.0270
	3		1.0467 (1.0537)	16	1.0520
4 (r)	0	15.3485	1.1126 (1.1196)	18	1.1190
	1		1.1603 (1.1673)	19	1.1690
	2		1.2076 (1.2146)	20	1.2180
	3		1.2533 (1.2603)	22	1.2660
	4		1.2955 (1.3025)	24	1.3080
	5		1.3317 (1.3387)	26	1.3460
	6		1.3602 (1.3672)	28	1.3650
	7		1.3820 (1.3890)		
4 (p)	0	15.0494	1.2591 (1.2651)	21	1.2630
	1		1.2968 (1.3028)	23	1.3020
	2		1.3322 (1.3382)	25	1.3360
	3		1.3640 (1.3700)	27	1.3650

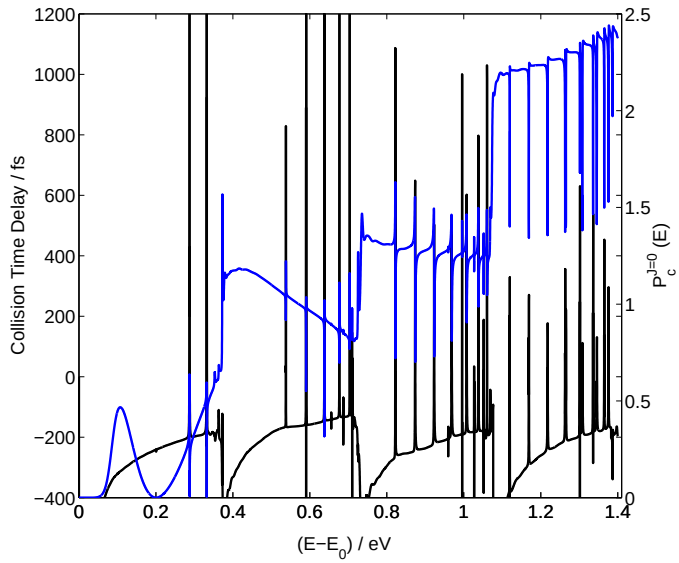

Figure 6.18: Collision time delay for the CH_3+HCl →CH_4+Cl ($^2P_{\frac{3}{2}}$) reaction on the adiabatic ground state surface. Time delay (black), $J = 0$ CRP (blue).

Time delay analysis. The presence of reactive resonances can also be confirmed by time delay analysis as discussed in Chapter 4. A positive maximum peak in the time delay indicates the presence of resonances, as shown in Figure 6.18[23]. Several bound states predicted by analysis of the hyperspherical adiabats were not indicated to be resonances by time delay theory (Table 6.13). With increasing total energy (especially for the $s = 4$ hyperspherical adiabats), overlap between the bound states for reactant and product hyperspherical adiabats made exact assignment difficult. A best estimate of the ordering and assignment of the time delay resonances is given alongside the DVR results in Table 6.13[24].

Thermal rate constants.

[23]Only clear, large positive peaks were analysed, although the presence of some small peaks in the time delay positive relative to the negative baseline energy indicate that additional resonances could be present in the system. The complicated nature of the overlapping resonances makes analysis of small peaks difficult.

[24]Figure 6.17 is presented on a total E-E_{shift} scale whereas Figure 6.18 and Table 6.13 give resonances on a E-E_0 scale.

Experimental results. The experimental thermal rate constants for the reverse process $CH_3 + HCl \longrightarrow CH_4 + Cl$ have been determined in a number of studies [153–155]; the corresponding Arrhenius expressions are given in Table 6.14. The recent data reported by Eskola *et al* [155] is also used for comparison.

Table 6.14: Experimental thermal rate constants for $HCl + CH_3 \longrightarrow CH_4 + Cl$ ($^2P_{3/2}$). Rates given in cm^3 $molecule^{-1}$ s^{-1} unless otherwise specified.

Study	Arrhenius Expression	Temperature
Pohjonen 1979 [153]	$10^{8.63} \exp(\frac{-8.9 kJ/mol}{RT})$ dm^3 mol^{-1} s^{-1}	298-473 K
Russell 1988 [154]	$5.0(\pm 0.7) \times 10^{-13} \exp(\frac{-1.4(\pm 0.3) kcal/mol}{RT})$	296-495 K

Theoretical results. Transition state theory and 2D J-shifted thermal rate constants are given in Table 6.15 alongside the CUS/μOMT results by Rangel, *et al.* [119].

The experimental and theoretical thermal rate constants are shown in Figure 6.19. The results of Russell *et al.* and Eskola *et al.* are generally in good agreement with each other, whereas the earlier results Pohjohnen *et al.* introduce ambiguity by predicting a much lower experimental thermal rate constant. The TST and 2D quantum scattering results are in relatively good agreement with the Pohjonen results but are too low, especially at low temperatures, compared to the Russell and Eskola studies. The quantum results predict a large degree of high temperature recrossing by comparison with TST; this difference at high temperature is primarily due to the post-projection change in the vibrational partition function. Significant low-temperature tunnelling is predicted, as expected because of the HLH nature of the reaction.

There is relatively good agreement between the CUS/μOMT results of Rangel, *et al.* and the 2D quantum scattering results, in terms of the shape and curvature of the thermal rate constant as a function of temperature. However, Rangel predicts

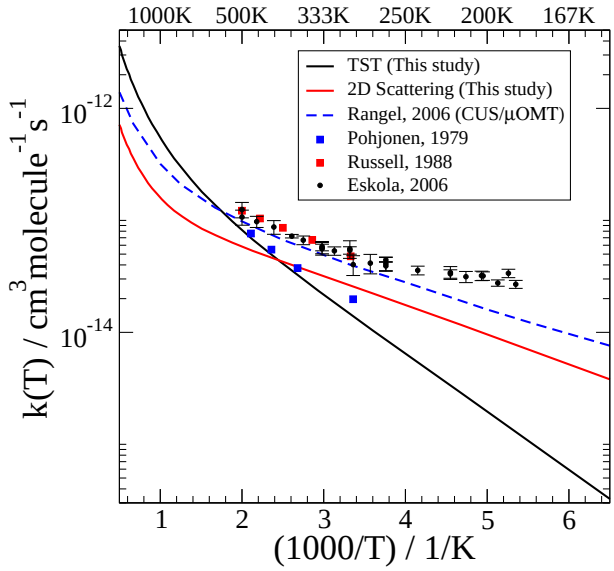

Figure 6.19: J-shifted thermal rate constants for the HCl + CH_3 ⟶ Cl + CH_4 reaction.

Table 6.15: Theoretical thermal rate constants for CH_3+HCl ⟶ CH_4 + Cl ($^2P_{3/2}$) on the adiabatic surface. Rates given in cm^3 $molecule^{-1}$ s^{-1}; powers of ten shown in parentheses.

T / K	TST	J-shifted 2D	Rangel, 2006
150	2.6546(-16)	3.4294(-15)	7.0000(-15)
180	1.0100(-15)	6.8041(-15)	1.2000(-14)
200	1.9602(-15)	9.5758(-15)	1.6000(-14)
250	6.4497(-15)	1.7574(-14)	2.8000(-14)
300	1.4381(-14)	2.6113(-14)	4.0000(-14)
400	4.0928(-14)	4.2657(-14)	6.7000(-14)
500	8.1740(-14)	5.8268(-14)	9.8000(-14)
600	1.3769(-13)	7.4046(-14)	1.3000(-13)
800	3.0209(-13)	1.1073(-13)	2.1000(-13)
1000	5.5068(-13)	1.6000(-13)	3.2000(-13)
1500	1.6492(-12)	3.6550(-13)	7.3000(-13)
2000	3.6095(-12)	7.1579(-13)	1.4000(-12)
2500	6.6221(-12)	1.2249(-12)	2.3000(-12)

a higher TRC by an almost constant factor ranging from 1.5-2.0 across the temperature grid. The discrepancy between the two methods could relate to surface barrier height differences, given that *ab initio* calculation of the reaction barrier is difficult for this system.

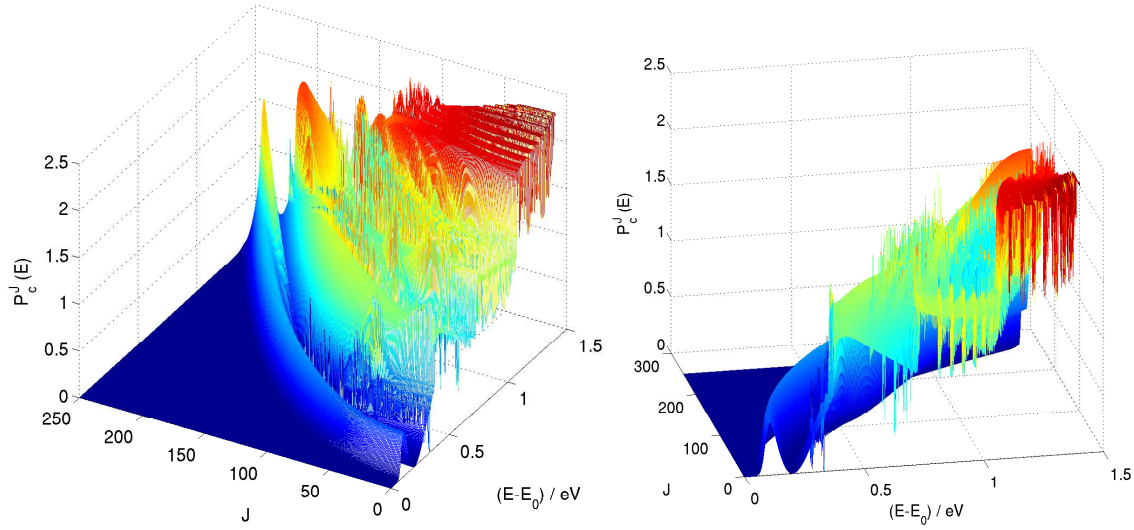

Figure 6.20: Two perspectives of the cumulative reaction probability of reaction CH_3+HCl →CH_4+Cl ($^2P_{\frac{3}{2}}$) on the adiabatic ground state surface with respect to increasing J.

6.5.2.2 Adiabatic: $CH_3 + HCl \longrightarrow CH_4 + Cl\ (^2P_{\frac{3}{2}})$ $(J > 0)$.

Quantum scattering calculations were performed up to $J = 250$ for the reverse R1 reaction. The dependence of the cumulative reaction probability on total angular momentum (Figure 6.20) shows that the shape the CRP is preserved but shifted to higher energies with increasing J (thus providing additional justification for the use of the J-shifting approximation in calculation of the thermal rate constant).

The initial state selected integral and differential cross sections were also determined from the $J > 0$ results. The initial state selected and state-to-state cross sections are plotted as a function of collision energy ($E - \varepsilon_s$ for initial state s) in Figures 6.21. As the calculations are performed on a total energy scale, reaction out of excited reactant states is only computed for lower collision energies. Initial state selected cross sections for $s = 0,\ 1,\ 2$ are dominated by vibrationally adiabatic processes at low energy. Furthermore, the $s = 0$ cross section has a shoulder at approximately 0.2 eV, which is most likely due to preservation of the

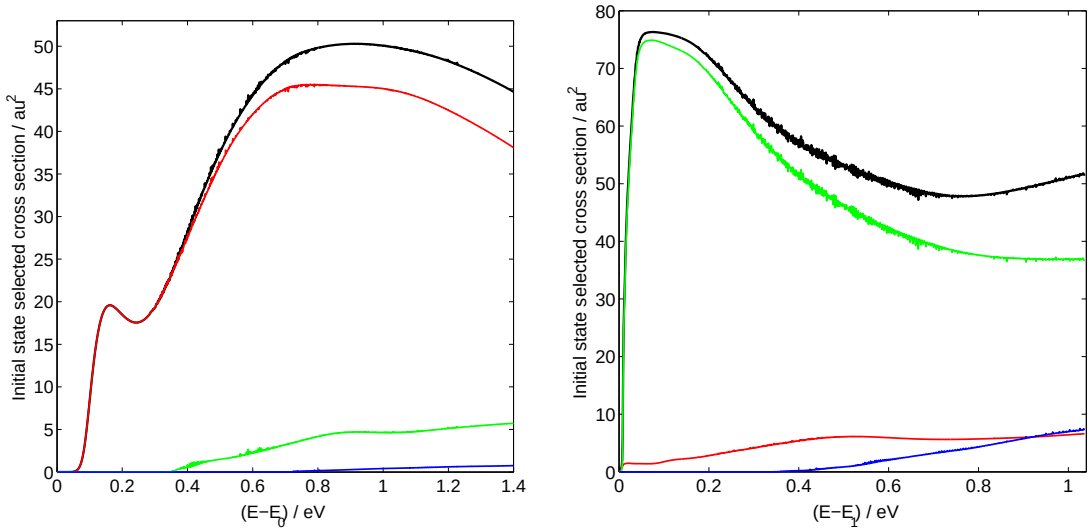

(a) $s = 0$ (b) $s = 1$

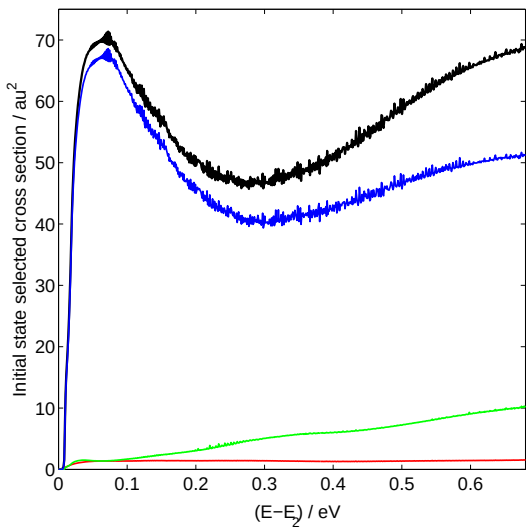

(c) $s = 2$

Figure 6.21: Initial state selected integral cross sections for the CH_3+HCl $\rightarrow$$CH_4$+Cl ($^2P_{\frac{3}{2}}$) reaction on the adiabatic ground state surface. $s \rightarrow$all (black), $s \rightarrow 0$ (red), $s \rightarrow 1$ (green), $s \rightarrow 2$ (blue).

first CRP peak with increasing J. Vibrationally nonadiabatic effects play a larger role at higher collision energies, though the adiabatic pathway remains the most important mechanism of reaction.

The ground state (0$\rightarrow$0) differential cross section was also computed and is

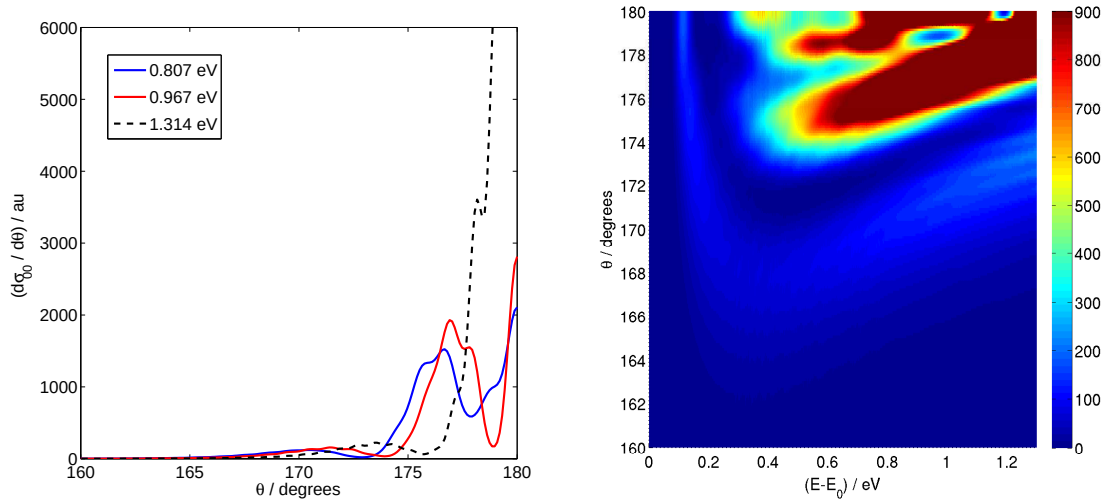

(a) (b)

Figure 6.22: Energy dependence of the 0→0 differential cross section for the $CH_3 + HCl \longrightarrow CH_4 + Cl(^2P_{\frac{3}{2}})$ reaction on the adiabatic ground state surface. (a): For three collision energies E_c(eV): 0.807 (blue), 0.967 (red), 1.314 (black). (b): As a function of collision energy.

given in Figure 6.22. The products of reaction are primarily backward-scattered, with a maximum sideways scattering distribution of 160°. The experimental collision energies associated with the fast, slow, and average distributions are given along with the energy dependence of the cross section, which shows a decreased propensity for sideways scattering at higher collision energies.

Explicitly summed rate constant. The explicitly summed thermal rate constant (calculated with 250 partial wave cumulative reaction probabilities) is given in Figure 6.23, and is in relatively good agreement with the J-shifted TRC. In general, it can be seen that the J-shifting method results in rate constants which are slightly too high at high temperatures, and slightly low at low temperatures.

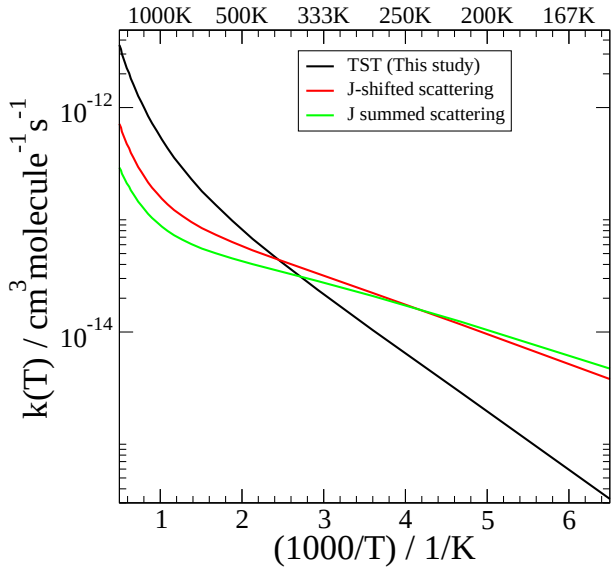

Figure 6.23: TST, reduced dimensionality J-shifted and J-summed thermal rate constants for the $CH_3 + HCl \longrightarrow CH_4 + Cl(^2P_{\frac{3}{2}})$ reaction on the adiabatic ground state surface.

6.5.2.3 Adiabatic: $\mathbf{Cl\ (^2P_{\frac{3}{2}}) + CH_4 \longrightarrow HCl + CH_3}$ $(J = 0)$.

The state-to-state dynamics and resonances of the forward F1 reaction process are identical to the reverse reaction by microscopic reversibility (differing only by an energy shift equal to the difference in initial reactant energy). However, the thermal rate constant differs significantly.

Experimental results. Many more experimental studies have been performed to characterise the rate of the F1 $Cl + CH_4$ process in comparison with the reverse reaction. The Arrhenius expression for several experimental studies [148, 150–152] and one evaluated rate constant result [154] are presented in Table 6.16. In general, these studies are in good agreement with one another and report non-Arrhenius curvature.

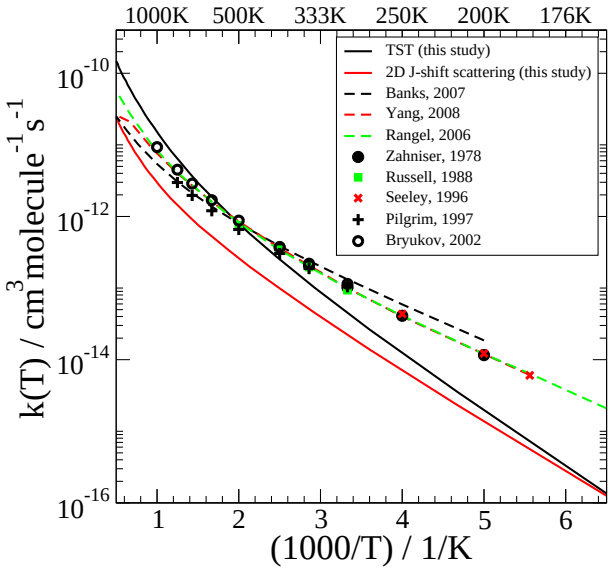

Figure 6.24: TST and reduced dimensionality J-shifted thermal rate constants for the $Cl(^2P_{\frac{3}{2}})$+CH_4 ⟶ HCl + CH_3 reaction on the adiabatic ground state surface in comparison with previous theoretical [13, 119, 125] and experimental [148, 150–152, 154] studies.

Table 6.16: Experimental thermal rate constants for Cl ($^2P_{3/2}$) + CH_4 ⟶ CH_3 + HCl. Rates given in cm^3 $molecule^{-1}$ s^{-1} unless otherwise specified.

Study	Arrhenius Expression	T / K
Zahniser 1978 [150]	$8.6 \times 10^{-18} T^{2.11} e^{-795/T}$ cm^3 s^{-1}	200-500
Russell 1988 [154]	$1.7(\pm 0.2) \times 10^{-11} e^{-3.1 \pm 0.3 \text{ kcal mol}^{-1}/RT]}$	298-504
Seeley 1996 [148]	$7.0(\pm 1.6) \times 10^{-12} e^{-(1270 \pm 60)/T}$	181-291
Pilgrim 1997 [152]	$3.7(+8.2, -2.5) \times 10^{-13} (T/298)^{2.6 \pm 0.7} e^{-385(\pm 320)/T}$	292-800
Bryukov 2002 [151]	$1.30 \times 10^{-19} T^{2.69} e^{-497/T}$	295-1104

Theoretical results. The TST and 2D J-shifted quantum results are given in Table 6.17 alongside the 2D time-independent quantum scattering results of Banks *et al.* [13], the CUS/μOMT results of Rangel *et al.* [119] and the 4D time-dependent quantum results of Yang *et al.* [125].

These results are also shown in Figure 6.24, where it can be seen that TST predicts a much higher TRC than the 2D quantum scattering; the latter grossly overestimates the significance of recrossing dynamics. The Yang, 2008 [125] and

Table 6.17: Theoretical thermal rate constants for Cl ($^2P_{3/2}$) + $CH_4 \longrightarrow CH_3$+HCl on the ground adiabatic surface. Rates given in cm^3 $molecule^{-1}$ s^{-1}; powers of ten shown in parentheses.

T / K	TST	2D J-shifted	Yang [125]	Banks [13]	Rangel [119]
150	9.97(-17)	9.58(-17)			1.70(-15)
180	7.18(-16)	5.55(-16)	6.10(-15)		6.40(-15)
200	1.95(-15)	1.34(-15)	1.20(-14)	1.86(-14)	1.20(-14)
250	1.23(-14)	7.08(-15)	4.00(-14)	5.91(-14)	4.10(-14)
300	4.46(-14)	2.21(-14)	1.00(-13)	1.32(-13)	9.90(-14)
350	1.17(-13)	5.12(-14)		2.40(-13)	
400	2.51(-13)	9.87(-14)	3.60(-13)	3.86(-13)	3.40(-13)
500	7.98(-13)	2.61(-13)	8.50(-13)	7.96(-13)	8.20(-13)
600	1.88(-12)	5.28(-13)	1.60(-12)	1.37(-12)	1.60(-12)
700	3.69(-12)	9.17(-13)		2.12(-12)	
800	6.41(-12)	1.44(-12)	4.00(-12)	3.05(-12)	4.10(-12)
1000	1.52(-11)	2.99(-12)	7.60(-12)	5.41(-12)	8.30(-12)
1250	3.37(-11)	6.05(-12)			
1500	6.17(-11)	1.05(-11)	2.10(-11)		2.70(-11)
2000	1.48(-10)	2.41(-11)	2.60(-11)	2.51(-11)	5.70(-11)
2500	2.75(-10)	4.33(-11)			9.70(-11)

Rangel, 2006 [119] results are in good agreement[25] and correlate well with experiment. The Banks, 2007 [13] results slightly overestimate low-temperature rate constants but are in generally good agreement with experimental results. The 2D quantum scattering results of this study are low in comparison with previous experimental and theoretical results; this discrepancy most likely relates to the increased surface barrier height due to explicit inclusion of spin-orbit effects in the $Cl + CH_4$ reactant channel.

6.5.2.4 Diabatic ground state model

Quantum scattering calculations were also performed for the forward and reverse reactions on the diabatic ground state, in order to evaluate the single-surface (adiabatic) effects of including spin-orbit coupling in the PES description. Hyperspher-

[25]This is expected given that these studies are based upon similar surfaces.

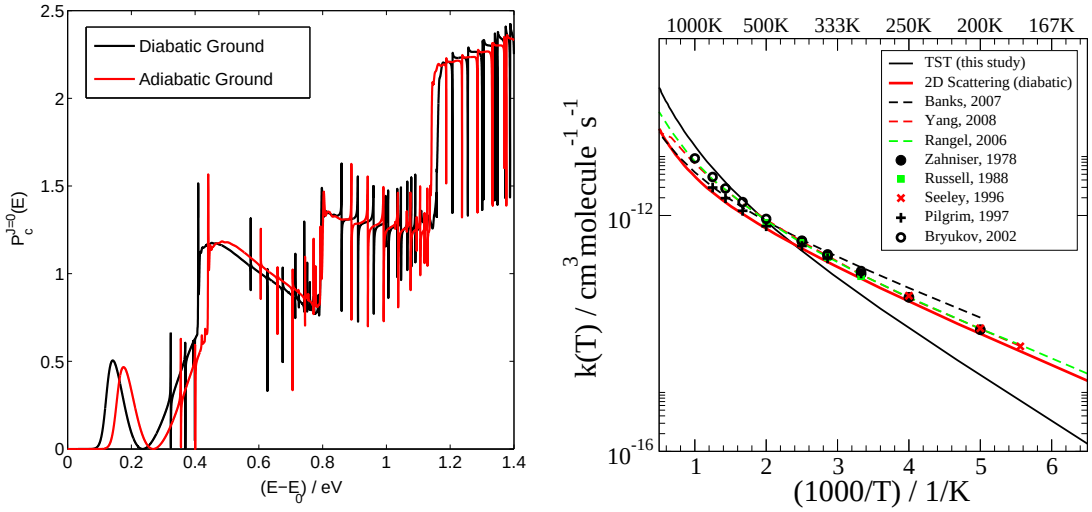

(a) (b)

Figure 6.25: Reactivity of the $Cl(^2P_{\frac{3}{2}}) + +CH_4 \longrightarrow HCl + CH_3$ system on the ground state diabatic and ground state adiabatic potential energy surfaces. (a): $J = 0$ cumulative reaction probability for the ground state diabatic (black) and adiabatic (red) surfaces. (b): TST and reduced dimensionality J-shifted thermal rate constant results for the diabatic ground state potential in comparison with previous theoretical [13, 119, 125] and experimental [148, 150–152, 154] results.

ical adiabats were found to be similar, with the exception of energy shifts for the $Cl + CH_4$ states. For the reverse R1 process, there is little difference in the cumulative reaction probability or thermal rate constant, thus providing evidence that spin-orbit coupling has little effect on the $CH_3 + HCl$ channel or transition state.

The forward F1 scattering results differ significantly for the diabatic ground state because of the differences in the F1 reactant channel. The hyperspherical adiabats and thermal rate constant (Figure 6.25) both indicate the increase in surface barrier height for the adiabatic surface, thus leading to a delayed onset of reaction and a decreased TRC. The diabatic ground state TRC agrees well with experiment and theory, suggesting that the spin-orbit coupling correction decreases TRC accuracy. The accuracy of the diabatic ground state TRC could be due to error cancellation; explicit treatment of spin-orbit coupling may also require more accurate, basis-set extrapolated *ab initio* methods, investigated in section 6.6.

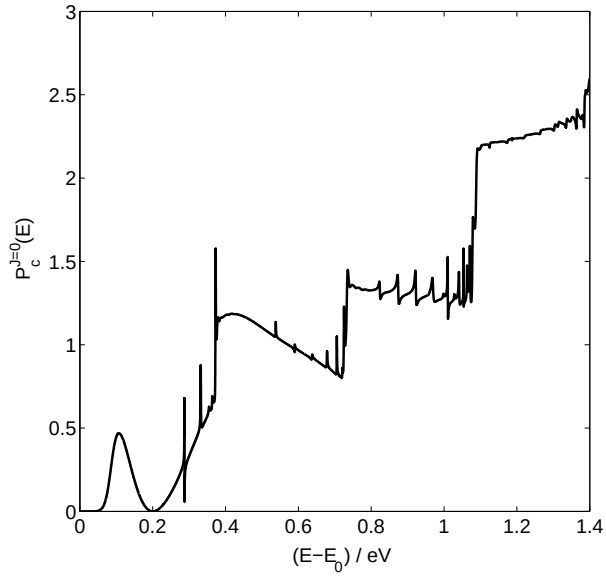

Figure 6.26: $J = 0$ Cumulative reaction probability for the $CH_3 + HCl \longrightarrow CH_4 + Cl(^2P)$ reaction system with the three surface model.

6.5.3 Multi-surface model

6.5.3.1 $\mathbf{CH_3 + HCl \longrightarrow CH_4 + Cl\ (^2P)\ (}J = 0\mathbf{)}$.

Cumulative reaction probability. The cumulative reaction probability for the R1 reaction process is shown in Figure 6.26. Many of the same features seen in the adiabatic ground state CRP, such as oscillating reactivity and resonances, are observed. However, the resonance peaks are not as well resolved, possibly because of interference effects arising from the complicated pattern of avoided crossings present only in the interaction of the three-state hyperspherical adiabats (Figure 6.13).

Initial state selected reaction probabilities. The initial state selected reaction probabilities also display similar behaviour to that predicted by the ground state adiabatic model, especially the oscillating reactivity observed for reactions

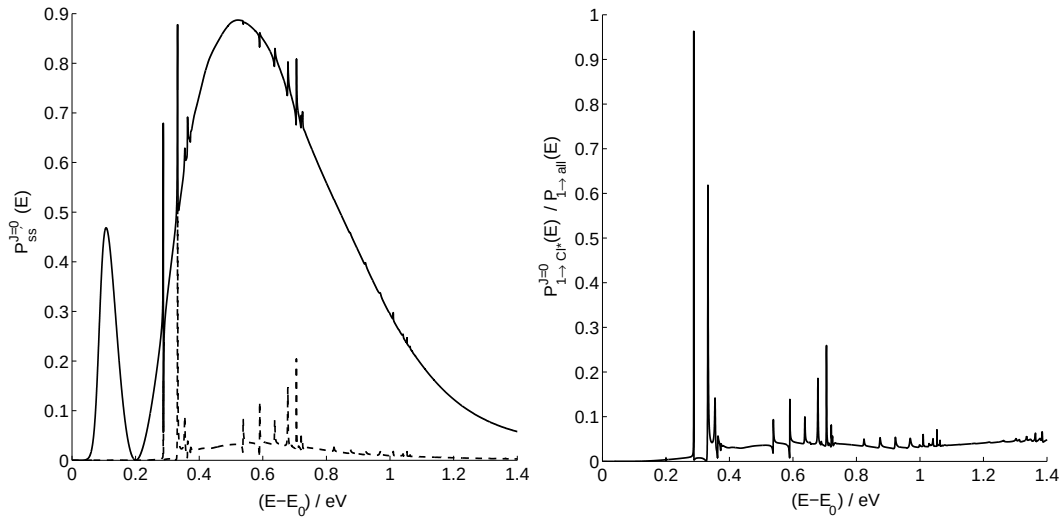

(a) (b)

Figure 6.27: $J = 0$ Initial state selected probabilities and nonadiabatic branching ratios for the CH_3 + HCl($\nu = 0$) $\longrightarrow$ CH_4 + $Cl(^2P)$ reaction. (a): 0 $\rightarrow$ all reaction probability (solid line); 0 $\rightarrow$Cl* reaction probability (dashed). (b): Nonadiabatic branching ratio $P^{J=0}_{0\rightarrow Cl^*}(E)$ / $P^{J=0}_{0\rightarrow all}(E)$.

out of $\nu = 0$ and 1[26]. Furthermore, state-to-state probabilities afford a means to analyse the contribution of electronically nonadiabatic pathways. In Figures 6.27 and 6.28, the initial state selected probabilities have been plotted with the probabilities associated with nonadiabatic production of Cl*, thus allowing for the calculation of probability branching ratios.

Nonadiabatic production of Cl* from initial state $\nu = 0$ is delayed relative to reaction to ground Cl (Figure 6.27). The onset occurs through two sharp resonance peaks at $E_c = 0.2874$ and 0.3318 eV, possibly indicating the importance of resonances in mediating nonadiabatic transition. The nonadiabatic branching ratio increases with collision energy, reaching an approximately constant value of 4% of total reaction probability out of state $\nu = 0$.

Electronically nonadiabatic reaction occurs immediately upon opening of the

[26]The R1 reactant states are described by compound vibronic quantum number $s = i\nu$; however, only the ground electronic state is important for the reactant states and therefore the vibrational quantum number ν may be used.

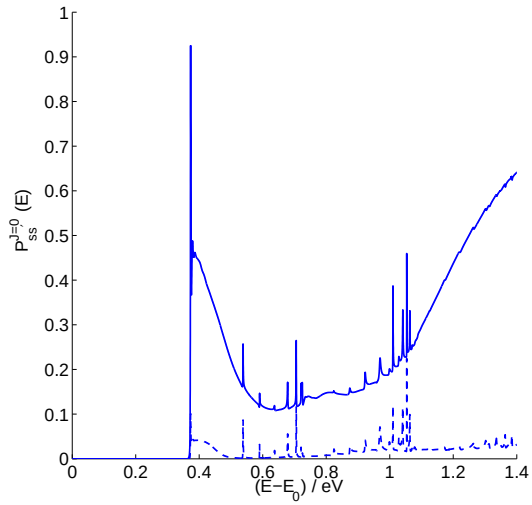

(a) 1 → all (solid); 1 →Cl* (dashed).

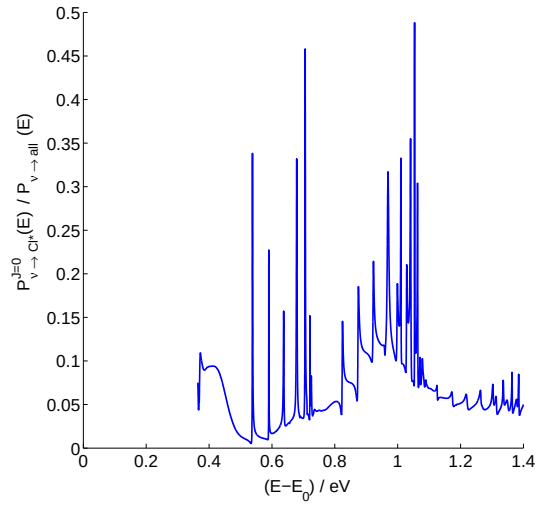

(b) $P^{J=0}_{1\to Cl^*}(E)$ / $P^{J=0}_{1\to all}(E)$.

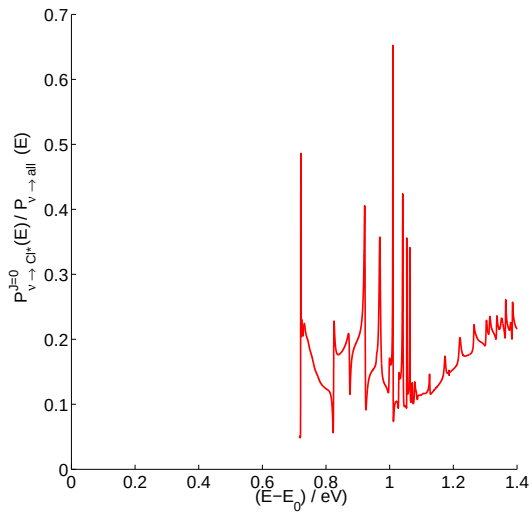

(c) $P^{J=0}_{2\to Cl^*}(E)$ / $P^{J=0}_{2\to all}(E)$.

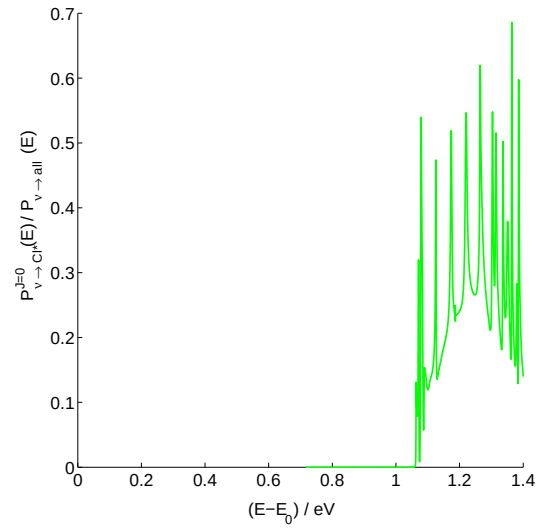

(d) $P^{J=0}_{3\to Cl^*}(E)$ / $P^{J=0}_{3\to all}(E)$.

Figure 6.28: $J = 0$ Initial state selected probabilities and nonadiabatic branching ratios for the $CH_3 + HCl(\nu = 1, 2, 3) \longrightarrow CH_4 + Cl(^2P)$ reaction.

$\nu = 1$ reaction channel (Figure 6.28); this pathway also appears to be dominated by resonance features. The nonadiabatic branching ratio displays oscillatory behaviour, indicating that (at some collision energies) nonadiabatic production of Cl* comprises over 10% of the total reaction from $\nu = 1$.

Similarly, the probability branching ratios for reactions out of $\nu = 2$ and $\nu = 3$

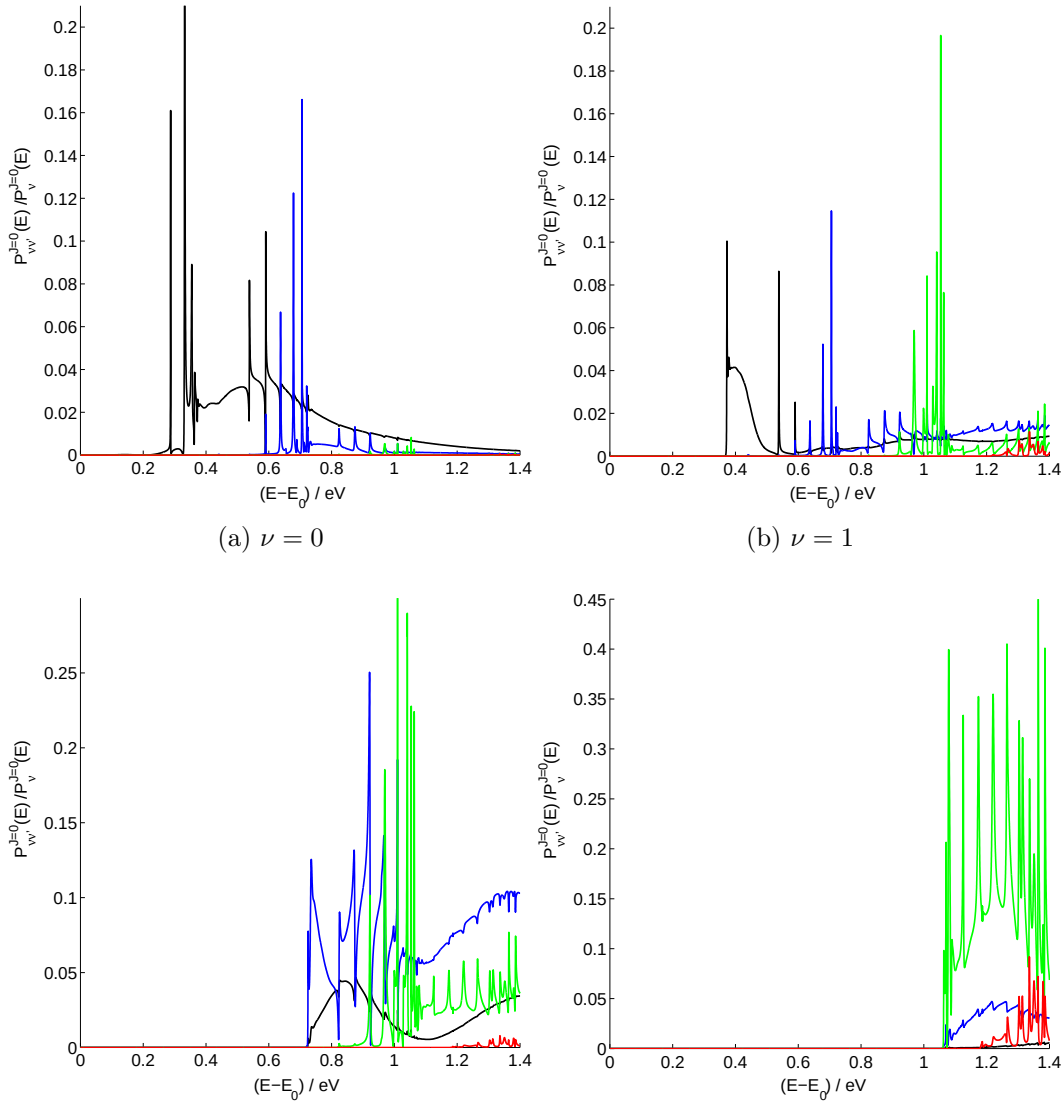

(a) $\nu = 0$ (b) $\nu = 1$

(c) $\nu = 2$ (d) $\nu = 3$

Figure 6.29: $J = 0$ State-to-state electronically nonadiabatic branching ratios for HCl (ν) + CH_3 $\rightarrow$Cl ($^2P_{\frac{1}{2}}$) + $CH_4(\nu')$. $\nu' = 0$ (black), $\nu' = 1$ (blue), $\nu' = 2$ (green), and $\nu' = 3$ (red).

indicate that electronically nonadiabatic transitions comprise a maximum of 20% and 30% of the initial state selected reaction probabilities, respectively (Figures 6.28).

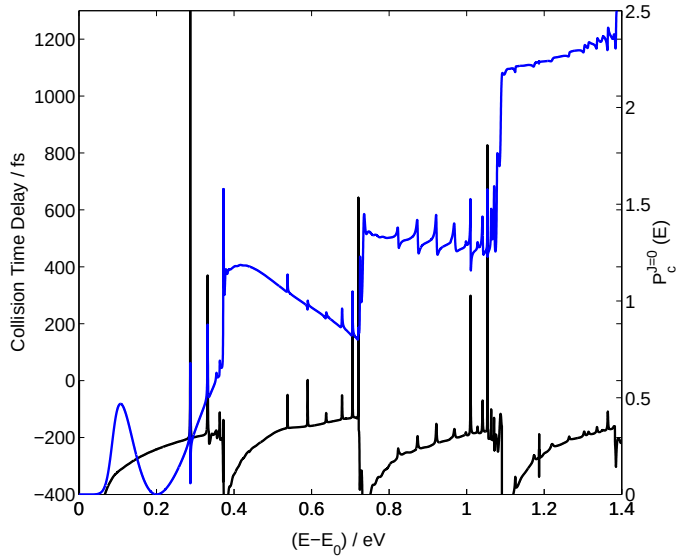

Figure 6.30: Time delay analysis for identification of resonances in the CH_3 + HCl $\longrightarrow$ CH_4 + Cl(^{2}P) reaction (black). $J = 0$ cumulative reaction probability (blue).

State-to-state reaction probabilities. The state-to-state dynamics are also useful in evaluating vibrational adiabaticity associated with electronically non-adiabatic transitions[27]. The state-to-state branching ratios for the production of Cl* states with vibrational excitation $\nu' = 0, 1, 2$ and 3 are given in Figure 6.29, and indicate that, with the exception of reaction from $\nu = 0$, electronically non-adiabatic transitions are not associated with vibrational adiabaticity. The $0 \rightarrow 0$, $1 \rightarrow 0$, $2 \rightarrow 1$, and $3 \rightarrow 2$ transitions are seen to dominate at low collision energies, although additional pathways are significant for higher values of E_c[28]. This loss of vibrational energy associated with nonadiabatic excitation of Cl$\rightarrow$Cl* is a common result witnessed in previous studies of the forward reaction process Br* + H_2 [43].

[27] As the A_1 and E_{low} product electronic states are indistinguishable, differentiation between R1 product states $s' = 0/1;\ 3/4;\ 6/7;\ 9/10$ is not possible.

[28] $\nu \rightarrow \nu'$ indicates reaction from vibrational state ν to final vibrational state ν' on the excited, Cl* surface.

Table 6.18: Resonances in the $CH_3 + HCl \longrightarrow CH_4 + Cl$ reaction confirmed by time delay analysis.

Resonance	E-E_0(eV)	Nonadiabatic transition ($\nu \rightarrow$Cl*)
1	0.2867	1$\rightarrow$ Cl*
2	0.3313	1$\rightarrow$ Cl*
3	0.5901	2$\rightarrow$Cl*, (1$\rightarrow$ Cl*)
4	0.7061	2$\rightarrow$ Cl*, (1$\rightarrow$ Cl*)
5	0.7210	3$\rightarrow$ Cl*, (1$\rightarrow$ Cl*,2$\rightarrow$Cl*)
6	1.0100	3$\rightarrow$ Cl* , (1$\rightarrow$Cl*,2$\rightarrow$Cl*)
7	1.0540	2$\rightarrow$Cl*, (1$\rightarrow$Cl*, 3$\rightarrow$Cl*)

Resonances. The complicated set of avoided crossings present in the three-state hyperspherical adiabats prevents the detailed analysis of bound states that was used for the adiabatic ground state surface. Time-delay analysis was instead used to analyse $J = 0$ CRP resonance features (Figure 6.30). Fewer resonances were identified for the three-state model in comparison with the ground adiabatic case; the energies of these resonances are listed in Table 6.18. Exact assignment of the resonance states is not possible, however, resonance features are present on the electronically nonadiabatic state-to-state probabilities, potentially indicating the importance of resonances in nonadiabatic transitions (Table 6.18, minor correlations included in parentheses). Only resonances with large collision time-delays are analysed.

6.5.3.2 $\mathbf{Cl(^2P) + CH_4 \longrightarrow HCl + CH_3}$ $(J = 0)$.

Analysis of the forward reaction in the multi-surface model provides the opportunity to investigate the importance of nonreactive inelastic collisions, specifically with regards to the nonadiabatic production of Cl*[29]. For each initial F1 reactant state, there are three post-collision possibilities: (1) nonreactive elastic scatter-

[29] A smaller interval was chosen for the ρ coordinate in the scattering ($\rho_{max} = 15.6$ au) in order to avoid averaging probability matrix elements for asymptotically crossing F1 reactant states. Recall that the two ground electronic states are treated as indistinguishable in the asymptotic $Cl + CH_4$ channel.

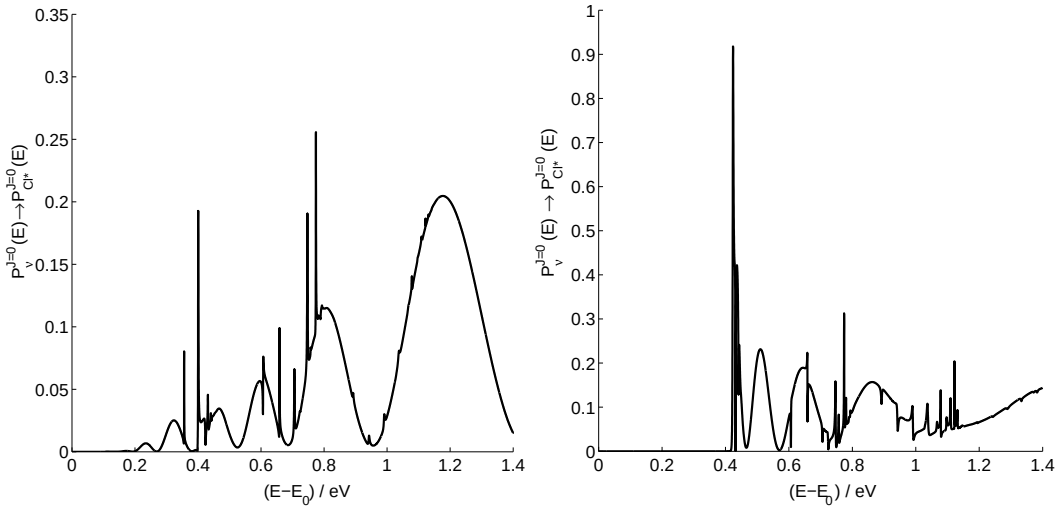

(a) Cl + CH_4 ($\nu = 0$) →Cl* + CH_4. (b) Cl + CH_4 ($\nu = 1$) →Cl* + CH_4.

Figure 6.31: Initial state selected nonreactive inelastic reaction probability for Cl + CH_4 (ν) →Cl* + CH_4.

ing to the same reactant state, (2) nonreactive inelastic scattering to a different reactant state and (3) reactive scattering to a product state. The probability of nonreactive inelastic scattering causing transition from an electronically ground to excited state (Cl → Cl*) is shown for vibrational states $\nu = 0,\ 1$ in Figures 6.31(a) and 6.31(b), respectively. The nonreactive nonadiabatic transition for the $\nu = 0$ reactant state is predominantly vibrationally adiabatic, whereas for $\nu = n,\ n > 0$ process, the most favourable nonadiabatic transition involves loss of one quantum of stretch excitation, leading to $\nu' = n - 1$ vibrational states. This result indicates the importance of vibrational energy in mediating electronic transitions, as has been previously reported in $X + H_2$ studies [43], and as was witnessed for reactive transitions in section 6.5.3.1. Furthermore, strong oscillatory reaction probability characteristic of HLH processes is observed, consistent with previous studies [31]. Such behaviour could be associated with interference affects arising from the two degenerate ground Cl electronic states in the Cl + CH_4 channel.

Furthermore, characterisation of the nonadiabatic reaction of the Cl*(ν) state

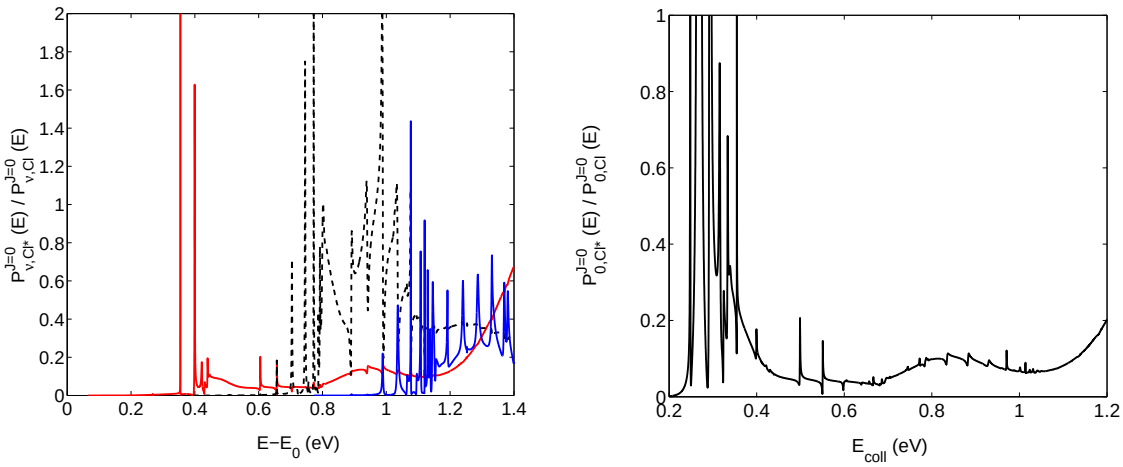

(a) (b)

Figure 6.32: (a). $J = 0$ initial state selected probability branching ratio for the nonadiabatic reaction $Cl^* + CH_4(\nu) \longrightarrow HCl + CH_3$. $\nu = 0$ (red), $\nu = 1$ (black, dashed), $\nu = 2$ (blue). (b). Ratio of ground state nonadiabatic reaction to ground state electronically adiabatic reaction ($P^{J=0}_{0\rightarrow Cl^*}(E)/P^{J=0}_{0\rightarrow Cl}(E)$), on a collision energy scale.

provides opportunity for comparison with experimental results for the $Cl + CH_2D_2$ reaction [166]. Reaction out of Cl* states are generally associated with the release of one quantum of stretch excitation; resulting in the mechanism

$$Cl^* + CH_4\,(\nu = n) \rightarrow HCl\,(\nu' = n+1) + CH_3 \qquad (n = 1, 2). \tag{6.10}$$

This result was more complex for the ground vibrational state reaction ($\nu = 0$), where the vibrationally adiabatic pathway ($\nu' = 0$) was seen to have a significant effect in addition to the ($\nu' = 1$) channel.

The initial state selected probability branching ratio for the reaction of Cl* compared to ground state Cl is given in Figure 6.32(a), for each initial vibrational quantum number ν. On this total energy scale, it is clear that increasing the vibrational level of the reactant states increases the contribution to reaction from nonadiabatic pathways.

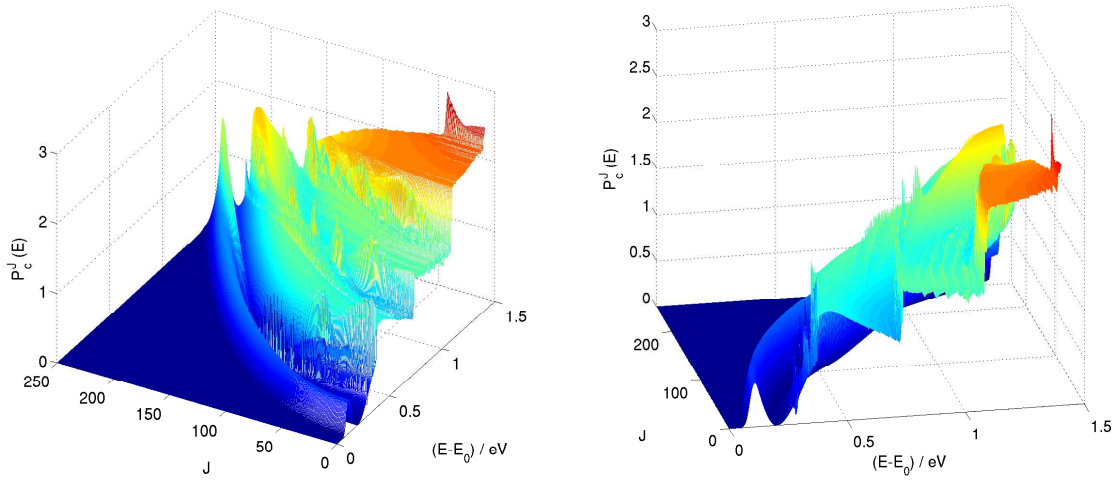

Figure 6.33: Two perspectives of the angular momentum (J) dependence of the cumulative reaction probability, for the $CH_3 + HCl \longrightarrow CH_4 + Cl\ (^2P)$ reaction.

It was estimated experimentally that the ratio of Cl*/Cl in the initial beam of reactants (n^*/n_0) was less than 1/2, resulting in a cross section branching ratio ($\sigma_{Cl^*}/\sigma_{Cl}$) of up to 9% at high collision energies ($\sim$ 0.867 eV) [166]. This result is consistent with the the $J = 0$ reaction probability branching ratio, plotted on a collision energy scale (Figure 6.32(b)); at 0.867 eV the probability ratio for $\nu = 0$ is 9.9%. The onset of nonadiabatic reaction is associated with resonance features causing a large ratio for low collision energies, however, this levels out at larger collision energies where the electronically adiabatic pathway is seen to dominate. Thus it is possible to conclude that for the $J = 0$ forward reaction process, the nonadiabatic pathway plays a small but significant role.

6.5.3.3 $CH_3 + HCl \longrightarrow CH_4 + Cl\ (^2P)$ ($J > 0$).

Cumulative reaction probability. The dependence of the CRP on the total angular momentum displays similar behaviour to the adiabatic ground state result (Figure 6.33), with the onset of reaction shifting to higher energy with J, yet

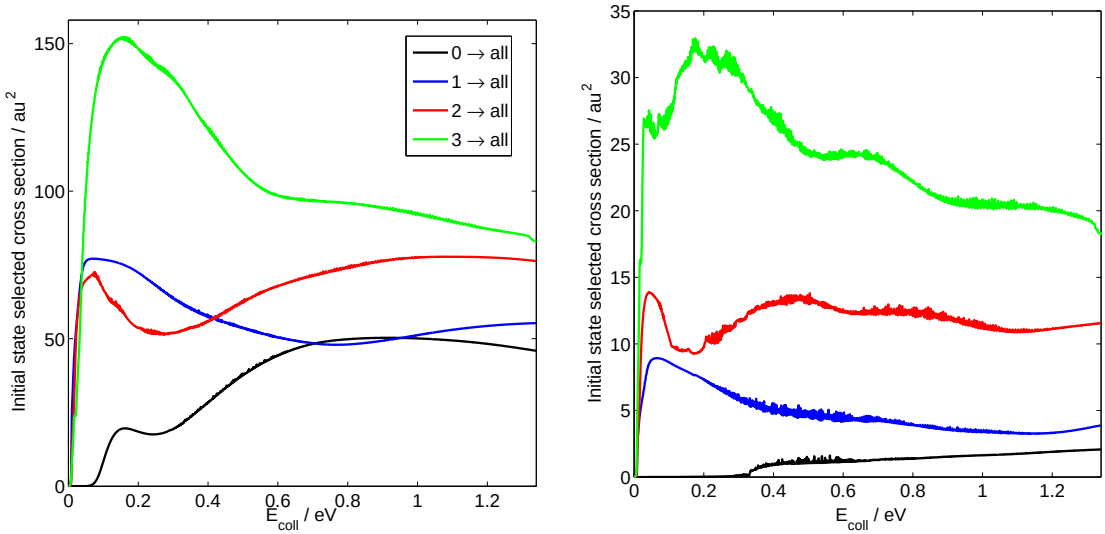

(a) All pathways ($\nu \rightarrow$all Cl, Cl*). (b) Nonadiabatic pathways ($\nu \rightarrow$all Cl*).

Figure 6.34: Initial state selected integral cross sections as a function of collision energy for the $HCl(\nu) + CH_3 \longrightarrow Cl + CH_4$ reaction. 0 →all (black), 1 →all (blue), 2 →all (red), 3 →all (green).

maintaining the basic oscillatory probability shape.

Nonadiabatic branching ratio. In order to compare the extent of nonadiabaticity with experiment, it is necessary to construct the nonadiabatic branching ratio of the total integral cross section on a collision energy scale[30]. The initial state selected cross sections ($J_{max} = 300$) are shown in Figure 6.34(a); the vibrationally excited channels open quickly once the state is accessible, whereas there is a delay associated with the onset of the $\nu = 0$ pathway. The initial state selected cross sections associated with nonadiabatic production of Cl* are shown in Figure 6.34(b).

Branching ratios for the nonadiabatic production of Cl* for each initial vibra-

[30]These cross sections must be computed on a collision energy scale up to the maximum experimental energy of 1.3 eV (30.3 kcal mol^{-1}), and therefore scattering must be performed at higher total energies for the excited vibronic states (2.4 eV). Convergence of the cross sections at high collision energy required calculations up to $J_{max} = 300$.

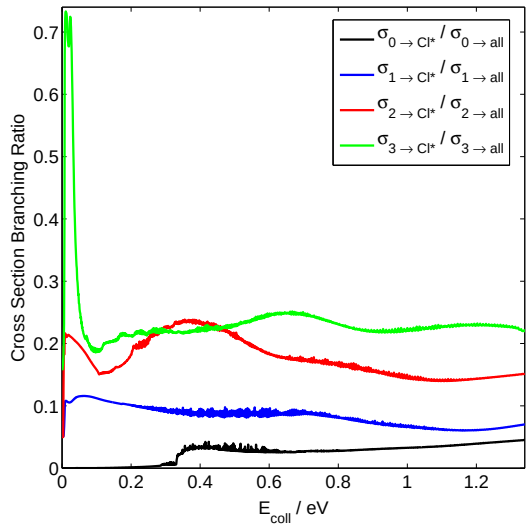

Figure 6.35: Initial state selected nonadiabatic branching ratios for the $HCl(\nu) + CH_3 \longrightarrow Cl + CH_4$ reaction.

tional state are calculated according to

$$\sigma_{\nu \rightarrow Cl*} = \frac{\sigma_{\nu \rightarrow Cl*}}{\sigma_{\nu \rightarrow all}}, \tag{6.11}$$

and shown in Figure 6.35. Nonadiabatic reaction for $\nu = 0$ only occurs at higher collision energies, whereas there is a large initial spike in nonadiabatic reactivity associated with the opening of the $\nu = 3$ reaction. At high collision energies the branching ratios level out, indicating that nonadiabatic transitions account for approximately 4% ($\nu = 0$) to 23% ($\nu = 3$) of the total reactivity, depending upon the initial vibrational state.

The large contribution of the nonadiabatic pathway at low collision energy for state $\nu = 3$ is a physically meaningful result. The electronically nonadiabatic, adiabatic and total transition probabilities for reaction $HCl(\nu = 3) + CH_3 \rightarrow Cl(^2P_J) + CH_4(\nu')$ are shown in Figure 6.36(a). The nonadiabatic pathway opens before the onset of the electronically adiabatic channels. This occurs through the presence of sharp resonance-like structures. The first peak, at 1.07 eV, corresponds to

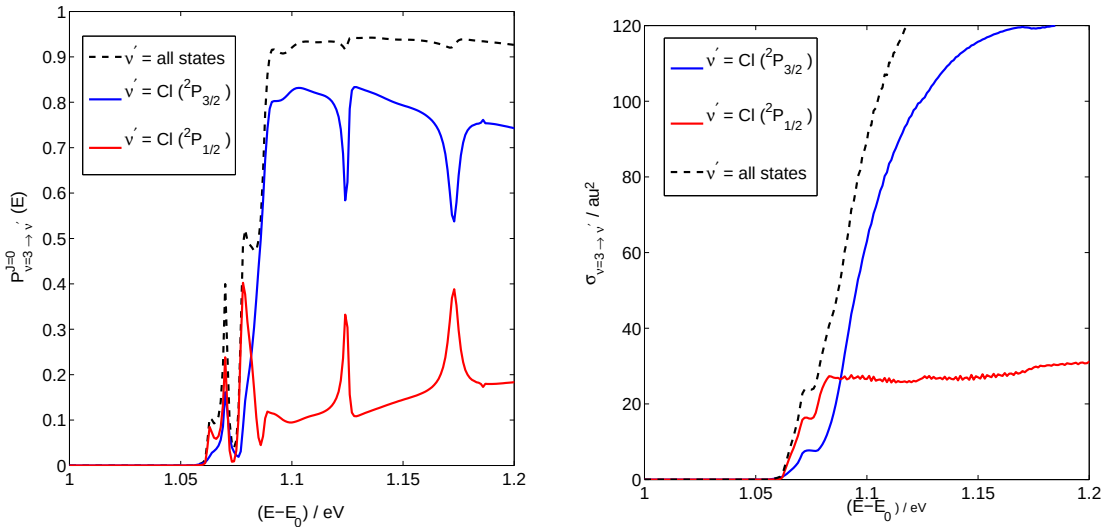

(a) Initial state selected probabilities ($\nu = 3$).

(b) Initial state selected integral cross section ($\nu = 3$).

Figure 6.36: Electronically adiabatic and nonadiabatic initial state selected probabilities (a) and integral cross sections (b) for reaction $HCl\ (\nu = 3) + CH_3 \rightarrow Cl + CH_4$.

a small positive maximum in the collision time delay (Figure 6.30, small positive peak with respect to negative time delay baseline), and therefore indicates that this nonadiabatic transition proceeds via a resonance mediated pathway. This is also supported by analysing the electronically adiabatic, nonadiabatic and total $\nu = 3$ integral cross sections (Figure 6.36(b)), where it is clear that the nonadiabatic reaction opens at lower collision energies. It is interesting to note the resonance at 1.07 eV survives averaging over all J states to produce a small shoulder in the integral cross section.

Experimental studies [115–118] report a total cross section branching ratio of $\Gamma = 0.14 \pm 0.02$ [115] at an average collision energy of 22.3 kcal mol^{-1}. However, two experimental factors must be considered when making a comparison: the bimodal experimental collision energy distribution and the initial vibrational population of the CH_3 radicals. In the case of the former, experimental work indicated that the slow (18.6 kcal mol^{-1}) distribution was ineffective in producing Cl*, such that it

Table 6.19: Vibrational energy distribution for CH_3 radicals produced from photodissociation of CH_3I.

CH_3 state	E_{vib} / cm^{-1}	P(ν) I* (slow)	P(ν) I (fast)
$\nu_2' = 0$	0	0.64	0.26
$\nu_2' = 1$	606	0.31	0.29
$\nu_2' = 2$	1288	0.04	0.21
$\nu_2' = 3$	2019	<0.01	0.09
$\nu_2' = 4$	2790	n/a	0.03
$\nu_1' = 1,\ \nu_2' = 0$	3004	n/a	0.07
$\nu_1' = 1,\ \nu_2' = 1$	3610	n/a	0.05
$<E_{vib}>$ / cm^{-1}		260	1100

could be neglected in considering nonadiabatic processes [117]. This was verified by subsequent experiments indicating that the fast (30.3 kcal mol^{-1}) distribution was found to be 7 times more reactive than the slow distribution in nonadiabatic pathways [118]. For simplicity, the current model assumes only the fast channel contributes to nonadiabatic reactivity.

The initial vibrational population of the methyl radicals following photolysis of ICH_3 has been measured experimentally [176] and is reported in Table 6.19. An average of 260 cm^{-1} and 1100 cm^{-1} of vibrational excitation exists for the slow and fast CH_3 distributions, respectively (rounded to the nearest 10 cm^{-1}). The majority of the internal energy is stored in the umbrella mode, with some additional C–H excitation. The HCl reactant is vibrationally cold [117].

Direct comparison between the current 2D scattering results and experiment is difficult given that the former only describes H–Cl stretching in the R1 reactants, whereas in the latter the CH_3 radical is umbrella excited. However, the correlation between vibrational excitation and nonadiabatic transition is clear even in the reduced dimensionality model. Therefore the approximation is made that the type of vibrational motion is not as significant as the amount of vibrational excitation available for reaction. The validity of this approximation is supported by previous

studies highlighting the importance of intramolecular vibrational redistribution along the reaction path [144].

The total nonadiabatic branching ratio can therefore be calculated according to the formula

$$\sigma_{\text{all}\rightarrow\text{Cl}*} = \frac{a \times \sigma_{0\rightarrow\text{Cl}*} + b \times \sigma_{1\rightarrow\text{Cl}*} + c \times \sigma_{2\rightarrow\text{Cl}*} + d \times \sigma_{3\rightarrow\text{Cl}*}}{a \times \sigma_{0\rightarrow\text{all}} + b \times \sigma_{1\rightarrow\text{all}} + c \times \sigma_{2\rightarrow\text{all}} + d \times \sigma_{3\rightarrow\text{all}}}, \tag{6.12}$$

where a, b, c and d are the variables that reflect the initial distribution of the reactant ensemble. Although the ratios displayed in Table 6.19 cannot be used directly, the amount of experimentally available vibrational excitation is used to develop a model for the theoretical initial reactant state population (a, b, c, d). Relative to the ground asymptotic reactant state $\nu = 0$, the excited reactant vibrational states ($\nu = 1, 2, 3$) have excitation energies of 2937, 5829, and 8517 cm^{-1} (Table 6.20).

A minimisation in Excel was used to model possible values for the population parameters, with the following restrictions:

1. $a + b + c + d = 1$. (The total distribution must equal 100%.)

2. $a - d \geq 0$. (The proportion of the initial ensemble in each of the available states must be positive.)

3. $d \leq c \leq b$,$c \leq a$. (The distribution in highly excited states d and c should be less than that in the lower energy states.)

4. $a\ E_{\text{vib},\nu=0} + b\ E_{\text{vib},\nu=1} + c\ E_{\text{vib},\nu=2} + d\ E_{\text{vib},\nu=3} \leq E_{\text{vib},max}$. (The amount of vibrational excitation should be within range of experiment (Table 6.19)).

The assumption is made that only the fast channel contributes to nonadiabatic reaction [117] and therefore it is assumed that there is approximately $<E_{\text{vib}}^{\text{exp}}> = 1100$

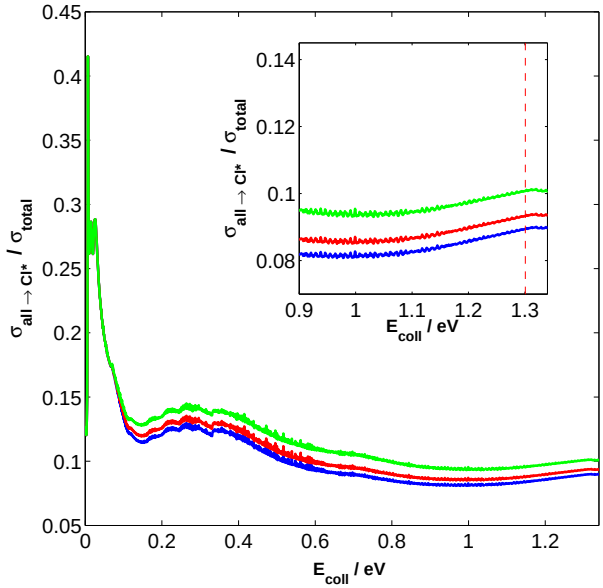

Figure 6.37: Total nonadiabatic branching ratio as a function of collision energy for reaction $CH_3 + HCl \longrightarrow CH_4 +$ Cl (^{2}P) . Three models for initial vibrational state population are shown accounting for 542 cm^{-1} (blue), 801 cm^{-1}(red) and 1095 cm^{-1}(green) of excess initial vibrational excitation (Table 6.20).

cm^{-1} of excess vibrational energy available to the reactant system. This amount of vibrational excitation is not sufficient to account for experimental levels of nonadiabatic reaction, and therefore three possible models are developed regarding the value of $E_{vib,max}$: (a) $E_{vib,max}$= 1.5 $<E_{vib}^{exp}>$, (b) $E_{vib,max}$= 1.75 $<E_{vib}^{exp}>$ and (c) $E_{vib,max}$= 2 $<E_{vib}^{exp}>$. A final model removes restrictions 3 and 4 in order to ascertain the amount of excess vibrational energy required to reproduce experimental branching ratios. The results of this analysis are given in Table 6.20 and displayed in Figure 6.37.

The nonadiabatic branching ratio models (Figure 6.37) clearly show large initial spikes in nonadiabatic reaction, which level out to approximately constant values at large collision energies. At the experimental fast channel collision energy of 1.3 eV, the models indicate approximately 8-11% contribution from the nonadiabatic reaction, depending upon the amount of initial vibrational excitation. This is in

Table 6.20: Branching ratio model for nonadiabatic production of Cl*. Energies in cm^{-1}, branching ratio at 1.3 eV.

Colour	a	b	c	d	$<E_{vib}>$	E_{excess}	Branching ratio
Blue	0.715	0.095	0.095	0.095	1642	542	8.74 %
Red	0.670	0.110	0.110	0.110	1901	801	9.33 %
Green	0.619	0.127	0.127	0.127	2195	1095	9.97 %
	0.250	0.250	0.250	0.250	4321	3221	13.8 %
E / cm^{-1}	0	2937	5829	8517			

relatively good agreement with the experimentally reported 14±0.2% branching ratio [115], although vibrational energy in excess of the experimentally measured value was required for the model branching ratios (Table 6.20)[31]. These results could indicate the importance of translation-into-vibration coupling along the reaction path, or that additional degrees of freedom (such as the umbrella mode) must be treated with more accuracy in order to achieve quantitative comparison with experiment. However, despite the additional vibrational energy required, the correlation between model and experiment indicates that the reduced dimensionality, spin-orbit coupling model provides a good theoretical foundation from which to understand the electronic nonadiabatic transitions in this reaction system.

6.6 Basis set extrapolated surface

A basis set extrapolated (T+d,T+d,Q+d) surface was also developed, and the parameters for the potential function are given in Table 6.21. The state-to-state and nonadiabatic dynamics remain very similar to the Q+d//T+d surface results, however, the basis set extrapolated surface has a decreased barrier height, thus counterbalancing the effects of the explicit inclusion of spin-orbit coupling.

The forward thermal rate constant for the ground adiabatic extrapolated sur-

[31] In order to exactly reproduce the experimental branching ratio, an unphysical population for each state ν (25%) is required (3221 cm^{-1} of excess vibrational excitation).

Table 6.21: Basis set extrapolated PES parameters. Powers of 10 in parentheses.

Parameter	$\mathbf{A_1}$	**E**	**A**	**B**
c_1	33.5333456	34.1142578	1.0278043(-4)	1.7837221(-5)
c_2	-9.5184794	-9.6565197	1.6730222(-1)	8.8885700(-2)
c_3	-0.2885825	-0.2942490	1.9180895	1.1052732
c_4	0.3394559	0.5232066	-7.6335945(-1)	-4.0910503(+1)
c_5	21.5331673	18.1823482	-1.1925541(+2)	4.1022580(+2)
c_6	-0.5922270	-0.1850375	6.2782817(+2)	-8.8115621(+2)
c_7	0.0472629	0.0311757	2.8241506(-1)	3.6444004(-3)
c_8	3.9444163	4.5762280	1.2686625(-3)	1.3401619(-3)
c_9	0.1981337	0.0718168		
c_{10}	-0.0127305	-0.0080245		
c_{11}	52.6235649	53.4881748		
c_{12}	251.7135322	253.0952975		
c_{13}	28.8394669	17.5819660		
c_{14}	12.6212925	17.6890044		
c_{15}	133.5273496	135.5749067		
c_{16}	-5.4643681	-5.3084698		
c_{17}	0.2449930	0.1591238		
c_{18}	0.3523492	0.5038674		
c_{19}	12.3022295	16.7745072		
c_{20}	0.9458117	-0.1866372		
c_{21}	-0.0257643	-0.0025329		
c_{22}	-7.2062625	-7.1338497		
c_{23}	-0.0440650	-0.1633082		
c_{24}	0.0033420	0.0033680		
c_{25}	-88.3174186	-83.5555132		
c_{26}	31.8401457	42.0927039		
c_{27}	-0.8966595	1.6035693		
c_{28}	-122.3617359	-120.3096212		
c_{29}	-540.7761851	-553.1711714		
Ab initio #	171 (171)	142 (585)	199 (199)	199 (199)
SSR (au^2)	2.15×10^{-4}	2.2×10^{-3}	2.08×10^{-9}	8.96×10^{-11}

face is shown in Figure 6.38(a). The extrapolated surface provides an improvement upon the thermal rate constant, and is in good agreement with experimental data. Thus, the TRC accuracy of the diabatic ground state model (section 6.5.2.4) is most likely due to fortuitous error cancellation; in explicit treatment of spin-orbit coupling higher-order basis sets must be used for accurate calculation of forward

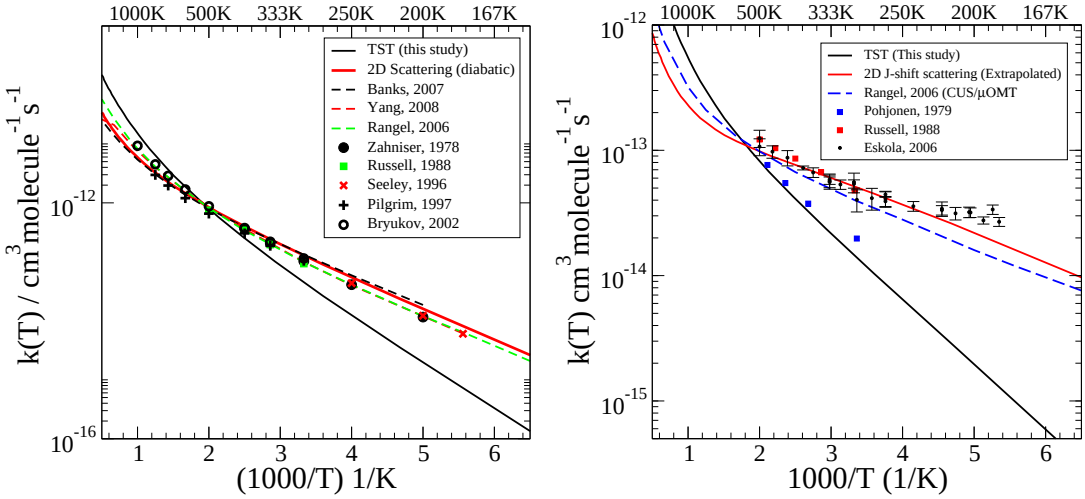

Figure 6.38: Thermal rate constants for the $Cl(^2P_{\frac{3}{2}}) + CH_4 \rightleftharpoons HCl + CH_3$ reaction system on the basis set extrapolated ground adiabatic potential energy surface. (a): $Cl + CH_4 \longrightarrow HCl + CH_3$ TST and J-shifted thermal rate constants in comparison with previous theoretical [13,119,125] and experimental [148,150–152,154] results. (b): $HCl + CH_3 \longrightarrow Cl + CH_4$ TST and J-shifted thermal rate constants in comparison with previous theoretical [119] and experimental [153–155] results.

Table 6.22: Theoretical thermal rate constants for Cl $(^2P_{3/2}) + CH_4 \rightleftharpoons CH_3 +$ HCl on the ground adiabatic basis set extrapolated surface. Rates given in cm^3 $molecule^{-1}$ s^{-1}; powers of ten shown in parentheses.

T / K	Reverse	Forward
150	8.8220(-15)	2.1436(-15)
180	1.6313(-14)	8.0710(-15)
200	2.2010(-14)	1.5824(-14)
250	3.6989(-14)	5.4530(-14)
300	5.1378(-14)	1.2809(-13)
350	6.4477(-14)	2.4168(-13)
400	7.6384(-14)	3.9756(-13)
500	9.8057(-14)	8.3942(-13)
600	1.1914(-13)	1.4584(-12)
700	1.4164(-13)	2.2621(-12)
800	1.6686(-13)	3.2631(-12)
1000	2.2883(-13)	5.9181(-12)
1250	3.3319(-13)	1.0598(-11)
1500	4.7189(-13)	1.6890(-11)
2000	8.6201(-13)	3.4168(-11)
2500	1.4082(-12)	5.6780(-11)

thermal rate constants. The reverse thermal rate constant is also improved on the basis set extrapolated surface (Figure 6.38(b)), and is a significant improvement upon the CUS/μOMT results of Rangel, *et al.* [119] at low temperatures. Thus, the basis set extrapolated surfaces provide the most accurate thermal rate constants for both the forward and reverse reaction processes. The rate constant results are given in Table 6.22.

6.7 Conclusions

The goal of this investigation was to provide a detailed understanding of the ground and excited state reaction properties of the $Cl + CH_4 \rightleftharpoons HCl + CH_3$ process, by developing a reduced dimensional, multiple electronic surface model. This theoretical characterisation bridges the gap between forward and reverse experimental results, seeking to develop a unified understanding of nonadiabatic processes in this fundamental polyatomic collision.

Many approximations have been applied to the scattering problem, and comparison of the results with experiment provides a means of evaluating the relative importance of these simplifications. The two dimensional surface system, consisting of three potential energy surfaces and coupling terms between them, describes the physical behaviour well in comparison with experimental data. In the $Cl+CH_4$ channel, the diabatic states are degenerate as expected, and diagonalisation of the potential matrix results in the correct asymptotic splitting behaviour for the adiabatic surfaces.

The ground-state thermal rate constants agree qualitatively with experimental results for the Q+d//T+d surface, and are quantitatively accurate for the basis set extrapolated model, thus providing further justification for the applicability of the surface system. The forward and reverse thermal rate constant results for the BSE

surface are in excellent agreement with experiment; the reverse reaction especially provides an improved description in comparison with previous theoretical models. The quantitative accuracy of the BSE surface is surprising given the results of previous work [13]; however, it is likely that use of BSE energies and explicitly including SOC in the ground state surface have opposite effects on the barrier height. The accuracy of the TRC reported at lower levels of theory [13] could be the result of fortuitous error cancellation. Furthermore, the J-shifting approximation was applied and shown to be in good agreement with explicitly summed results. Further justification of applying the method was found in the preserved shape of the CRP as a function of increased total angular momentum.

The close correlation between experiment and theory for the ground state TRC results indicates that approximately treating the reaction as a two dimensional system with zero-point corrections is an effective procedure. The umbrella bending mode has been indicated to be coupled to the reaction coordinate [135, 136]; in application of active mode projection at the TS, significant coupling was confirmed. Despite the good agreement of the kinetics results with experiment, it could be that the umbrella mode remains important in describing the reaction dynamics. Additional work would be required to evaluate the role of the umbrella bending mode in the multi-surface, nonadiabatic transitions. Additionally, the curvilinear projection method was found to be more accurate than its rectilinear counterpart in describing post-projected frequencies; however, the method offered less of an improvement than that seen for $CH_3 + CH_4$.

The HLH $Cl + CH_4 \rightleftharpoons HCl + CH_3$ system was found to be an endothermic reaction process with a collinear transition state as consistent with previous characterisations. The *ab initio* vibrationally corrected barrier height was found to be 3.57 kcal mol^{-1} and 2.78 kcal mol^{-1} for the forward and reverse reaction processes

at CCSD(T)/cc-pV(Q+d)Z-dk//MP2/cc-pV(T+d)Z-dk level of theory, respectively. Backwards scattering was found to the the dominant pathway, which is expected as the current model does not account for stripping mechanisms.

Nonadiabatic pathways were found to account for between approximately 8-11% of reactivity for the reverse reaction, in comparison with the 14 ± 2 % predicted by experiment [115]. The model used to calculate the theoretical branching ratio is approximate and requires more vibrational energy than available in experiment in order to achieve quantitative accuracy. This could indicate that coupling of translation into vibrational motion plays an important role in the reverse process. Alternately, it could be an indication that the 2D approach is not sufficient to completely describe the nonadiabatic pathway, and that more accurate 3D calculations explicitly accounting for the umbrella mode should be performed. Regardless, the model provides qualitative agreement with experiment regarding the extent of nonadiabaticity. Furthermore, for forward reaction out of the vibrational ground state, a ratio of approximately 10% of reaction was attributed to Cl*/Cl at high collision energies, in comparison with the 9% approximately reported by experiment [166]. Higher vibrational states indicated an even larger nonadiabatic branching ratio. These results are also consistent with those reported for past nonadiabatic characterisations of X + H_2 reactions: X=Cl was found to have 10% nonadiabatic reactivity [30, 35], X=F 10-25% [38, 40], and X=Br 10-40% [41].

The correlation between vibrational energy and nonadiabatic reaction reported in experiment [166] was witnessed for reactive forward, reverse, and nonreactive transitions. Reactive transitions of type

$$\mathrm{Cl}^* \ + \ \mathrm{CH_4}\ (\nu = n) \ \rightarrow \ \mathrm{HCl}\ (\nu' = n{+}1) \ + \ \mathrm{CH_3} \qquad (n = 1, 2) \qquad (6.13)$$

were found to dominate the forward reaction mechanism. The ground state $\nu = 0$

reaction also exhibited this behaviour, but additionally possessed a significant vibrationally adiabatic component. These results are consistent with those reported in recent experiments by Wu, *et al.* [166], where it was noted that reaction of excited spin-orbit state Cl* was associated with production of stretch excited HCl ($\nu = 1$). Furthermore, release of one quantum of stretch excitation was also shown theoretically to be a dominant pathway for the reaction of Br* + H_2 [42, 43].

Nonreactive, nonadiabatic production of Cl* also exhibited vibrational energy dependence; excitation of ground Cl to excited state Cl* was generally associated with the loss of one quantum of vibrational energy, with the obvious exception of the ground state transition. The dominant pathways were thus observed to be

$$\mathrm{Cl} + \mathrm{CH_4}\ (\nu = 0) \rightarrow \mathrm{Cl^*} + \mathrm{CH_4}\ (\nu' = 0) \tag{6.14}$$

$$\mathrm{Cl} + \mathrm{CH_4}\ (\nu = n) \rightarrow \mathrm{Cl^*} + \mathrm{CH_4}\ (\nu' = n - 1) \qquad (n > 0). \tag{6.15}$$

The loss of vibrational energy associated with nonadiabatic excitation was also previously reported for the Br + H_2 reaction system [43].

The nonadiabatic transition occurs in the Cl+CH_4 reaction channel, and can be identified by analysing the growth of the excited diabatic wavefunction as well as the location of the avoided crossings between reactant and Cl* states in the vicinity of the potential ridge. Within this collinear, C_{3v} reaction model, nonadiabatic transitions were found to occur with H–Cl distances varying from 1.4841 to 2.3428 Å, for vibrational levels $\nu = 0$ to $\nu = 3$. The dependence of transition location on vibrational quantum number ν is further indicative of the importance of vibrational energy in mediating the nonadiabatic transition. For larger vibrational excitation the nonadiabatic transition is shown to occur at increased molecular separation. Furthermore, the location of nonadiabatic transition supports the two-step reaction mechanism model [45]; electronic relaxation (or excitation) is followed (or preceded

by) reaction on the ground state surface.

Resonances were found to play a key role in the reverse reaction, as confirmed by analysis of bound states in the hyperspherical adiabats and via collision time-delay analysis. Strong resonance features were observed in state-to-state nonadiabatic reaction probabilities, and some were associated with the opening of the nonadiabatic pathway. The latter was seen for reaction from the HCl($\nu = 3$) +CH_3 state, where at low collision energies a resonance pathway caused the nonadiabatic mechanism to dominate the reaction probability and integral cross section. The importance of a resonance feature in the nonadiabatic reaction of Cl* + CH_4 was also reported by Wu *et al.* [166]; it was hypothesised that nonadiabatic relaxation to produce the $\nu = 1$ vibrationally excited state was followed by reaction through a ground state resonance pathway. In the current study, it is difficult to ascertain whether the resonance features are directly associated with the nonadiabatic transitions or occur separately on the ground state post (or pre) nonadiabatic transition. Given the strong pattern of resonance features shown for the adiabatic ground state scattering process, it is likely that the latter assertion is more accurate.

Chapter 7

Conclusions

In this thesis a reduced dimensionality quantum scattering model is applied to the study of two polyatomic heavy-light-heavy reactions: $CH_3 + CH_4 \longrightarrow CH_4 + CH_3$ and $Cl(^2P_J) + CH_4 \leftrightarrows HCl + CH_3$. The first study extended the method to a molecule + molecule reaction system and clearly showed its applicability in accurately characterising the kinetics of large polyatomic collision processes. For the study of the second system, the method was extended to account for multiple electronic surfaces and nonadiabatic reaction dynamics.

The overall approach involved a collinear, two dimensional quantum scattering technique derived from the triatomic bending corrected rotating linear model of Walker and Hayes [23, 25]. Spectator degrees of freedom were approximately treated by including their zero-point energies in the *ab initio* analytical potential energy surface description. Curvilinear [14,15] and rectilinear [66] projection methods were applied to obtain the zero-point corrections; the curvilinear method was observed to provide a significant improvement upon its rectilinear counterpart.

The multi-surface approach was similar to previous studies by Lepetit *et al.* [44,45,56]; vibronic basis sets were used such that the inelastic R-matrix propagation technique of Stechel, Walker and Light [55] could be applied without modi-

fication. Interpretation of scattering results for both the single and multi-surface calculations were presented in detail in Chapters 2 and 4. Thermal rate constants, reaction probabilities and integral and differential cross sections were all calculated in comparison with experiment; results for both systems compared favourably to available data. Both reactions were found to have exclusively backwards scattered mechanisms; this result is expected given that stripping mechanisms are not accounted for in the collinear model.

The main conclusions for characterisation of the $CH_3 + CH_4 \longrightarrow CH_4 + CH_3$ reaction process are presented in Chapter 5. Thermal rate constants for this reaction and deuterated variant $CD_3 + CD_4$ were found to be in excellent agreement with the evaluated kinetic data of Kerr and Parsonage [92], and Creak *et al.* [108], respectively. The reaction was found to be primarily vibrationally adiabatic, with broad oscillations in the cumulative reaction probability associated with quantum interference effects. Resonances were interpreted as combinations of heavy atom breathing and light atom chattering motions. Furthermore, the primary kinetic isotope effect was found to be more significant than secondary influences. In general, the quantitative agreement between theoretical and experimental thermal rate constants indicates that using this 2D method to characterise small molecule + molecule reactions is a realistic approach.

The main conclusions and results of the $Cl(^2P_J) + CH_4 \leftrightarrows HCl + CH_3$ reaction system are presented in Chapter 6. The nonadiabaticity of the forward, reverse, and nonreactive reaction processes were investigated in detail. Ground state thermal rate constants were found to be in good agreement with experiment for the reverse and forward processes, especially for the basis set extrapolated surfaces. This result thus justifies the use of a two-dimensional approach, despite significant coupling between the stretching and umbrella bending modes witnessed

by application of the projection method. The nonadiabatic branching ratio for the reverse reaction was presented in comparison with the experimental work of Orr-Ewing *et al.* [115–118]; an approximate nonadiabatic branching ratio of 8-11% was determined in comparison with the experimental value of 14±2% [117]. The forward reaction displayed a Cl* to Cl reactivity ratio of approximately 10% in comparison with results from Wu *et al.*, indicating a 9% ratio. Vibrational energy was found to mediate the nonadiabatic transition; excitation to Cl* states was associated with loss of one quantum of vibrational excitation. Nonadiabatic transition was found to occur via a two-step mechanism with the site of transition located in the $Cl + CH_4$ channel. Resonances were found to be important in the opening of nonadiabatic reaction pathways. The association between vibrational energy transfer and nonadiabatic reaction has been previously reported in several studies, which provide validation of the current approach.

In this thesis, it has been demonstrated that a relatively simple, two dimensional model based upon potential energy surfaces systematically derived from electronic structure calculations can be used to reliably characterise reactions of both polyatomic molecule + molecule reaction systems, as well as nonadiabatic transitions in multiple-surface studies. The good comparison that can be made between theoretical and experimental results validate the use of the method. It is likely that this approach can be extended further and applied to the study of larger, more complex reaction systems.

Appendix A

Scattering derivations

A.1 Reduced mass, μ, as arbitrary scaling mass

The reduced mass, μ, can be viewed as an arbitrary scaling mass in the scattering problem, and therefore does not effect the result of the scattering calculation. For example, in Tautermann's work on the adsorption of hydrogen onto nitrogen on a metal surface [177], μ is set to 1 amu. The effect of the value of μ can be analysed in the following way:

Assume a grid point A of energy -40.91 E_h at Jacobi coordinates (R (A), r(A)). The value for μ has no influence on the δ coordinate. We analyse the following two possible scenarios in order to ascertain the effect on the ρ dependent terms:

1. $\mu = \mu_1$, V(ρ_1(A), δ(A)) = -40.91 E_h

2. $\mu = \mu_2$, V$'$(ρ_2(A), δ(A)) = -40.91 E_h

We can define ρ_2 in terms of ρ_1 according to a square root ratio of the reduced

masses:

$$\rho_1 = \sqrt{\left(\frac{M_1}{\mu_1}\right) R^2 + \left(\frac{M_2}{\mu_1}\right) r^2} \tag{A.1}$$

$$\rho_2 = \sqrt{\frac{\mu_1}{\mu_2}}\sqrt{\left(\frac{M_1}{\mu_1}\right) R^2 + \left(\frac{M_2}{\mu_1}\right) r^2} \tag{A.2}$$

$$\rho_2 = \sqrt{\frac{\mu_1}{\mu_2}}\rho_1. \tag{A.3}$$

The total system Hamiltonian is given by [13, 16]

$$H = \frac{-1}{2\mu}\left[\frac{\partial^2}{\partial\rho^2} + \frac{1}{\rho^2}\frac{\partial^2}{\partial\delta^2} - \frac{3}{4\rho^2} - \frac{\hat{J}^2}{\rho^2}\right] + V(\rho,\delta). \tag{A.4}$$

In the two possible coordinate definitions (relying on μ_1 and μ_2), the potential ($V(\rho,\delta)$) at point A is by definition equivalent regardless of the choice of coordinate system. Therefore we analyse the kinetic energy operators:

$$T_1 = \frac{-1}{2\mu_1}\left[\frac{\partial^2}{\partial\rho_1^2} + \frac{1}{\rho_1^2}\frac{\partial^2}{\partial\delta^2} - \frac{3}{4\rho_1^2} - \frac{\hat{J}^2}{\rho_1^2}\right] \tag{A.5}$$

$$T_2 = \frac{-1}{2\mu_2}\left[\frac{\partial^2}{\partial\rho_2^2} + \frac{1}{\rho_2^2}\frac{\partial^2}{\partial\delta^2} - \frac{3}{4\rho_2^2} - \frac{\hat{J}^2}{\rho_2^2}\right] \tag{A.6}$$

$$= \frac{-1}{2\mu_2}\left[\frac{\partial^2}{\partial\frac{\mu_1}{\mu_2}\rho_1^2} + \frac{1}{\frac{\mu_1}{\mu_2}\rho_1^2}\frac{\partial^2}{\partial\delta^2} - \frac{3}{4\frac{\mu_1}{\mu_2}\rho_1^2} - \frac{\hat{J}^2}{\frac{\mu_1}{\mu_2}\rho_1^2}\right] \tag{A.7}$$

$$= \frac{-1}{2\mu_2}\frac{\mu_2}{\mu_1}\left[\frac{\partial^2}{\partial\rho_1^2} + \frac{1}{\rho_1^2}\frac{\partial^2}{\partial\delta^2} - \frac{3}{4\rho_1^2} - \frac{\hat{J}^2}{\rho_1^2}\right] \tag{A.8}$$

$$= \frac{-1}{2\mu_1}\left[\frac{\partial^2}{\partial\rho_1^2} + \frac{1}{\rho_1^2}\frac{\partial^2}{\partial\delta^2} - \frac{3}{4\rho_1^2} - \frac{\hat{J}^2}{\rho_1^2}\right] \tag{A.9}$$

$$= T_1\ . \tag{A.10}$$

Therefore the Hamiltonians are equal regardless of the choice of reduced mass, μ.

A.2 Scaling of the Hamiltonian operator

The BCRLM Hamiltonian is given according to (in au):

$$T_{RLM} = -\frac{1}{2\mu}\left[\frac{1}{\rho^3}\frac{\partial}{\partial\rho}\rho^3\frac{\partial}{\partial\rho} + \frac{1}{\rho^2}\frac{\partial^2}{\partial\delta^2}\right] + \frac{\hat{J}^2}{2\mu\rho^2}. \tag{A.11}$$

Expanding the first term within the brackets yields

$$T_{RLM} = -\frac{1}{2\mu}\left[\frac{\partial^2}{\partial\rho^2} + \frac{3}{\rho}\frac{\partial}{\partial\rho} + \frac{1}{\rho^2}\frac{\partial^2}{\partial\delta^2}\right] + \frac{\hat{J}^2}{2\mu\rho^2}. \tag{A.12}$$

Therefore, the entire Hamiltonian is expressed as

$$H_{RLM} = -\frac{1}{2\mu}\left[\frac{\partial^2}{\partial\rho^2} + \frac{3}{\rho}\frac{\partial}{\partial\rho} + \frac{1}{\rho^2}\frac{\partial^2}{\partial\delta^2}\right] + \frac{\hat{J}^2}{2\mu\rho^2} + V, \tag{A.13}$$

where V represents the potential of the system.

However, this form of the Hamiltonian is cumbersome to solve, and so we seek to express the kinetic energy operator in a scaled form. The scaling factor is applied to the wavefunction and the Hamiltonian transformed such that the original Hamiltonian acting on the original wavefunction yields the same eigenvalues as the transformed Hamiltonian acting on the scaled wavefunction:

$$H_{RLM}\Psi = E\Psi$$
$$H_{RLM}(\rho^{-3/2}\Psi) = E^{'}(\rho^{-3/2}\Psi).$$

It is easy to see that $E = E'$ if and only if the following relation holds:

$$H_{RLM}(\rho^{-3/2}\Psi) = \rho^{-3/2}H_{RLM}(\Psi). \tag{A.14}$$

As suggested by Walker and Hayes [23], the most appropriate scaling factor for the rotating linear model (RLM) Hamiltonian (and subsequent reduced dimensionality and bending-corrected extensions) is $\rho^{-3/2}$. This is most easily demonstrated by expressing the Hamiltonian as a sum of two operators:

$$\begin{aligned} H &= H_0 + H_1 \\ H_0 &= -\frac{1}{2\mu}\left[\frac{\partial^2}{\partial\rho^2} + \frac{3}{\rho}\frac{\partial}{\partial\rho} + \frac{1}{\rho^2}\frac{\partial^2}{\partial\delta^2}\right] \\ H_1 &= \frac{\hat{J}^2}{2\mu\rho^2} + V. \end{aligned} \tag{A.15}$$

It is easily shown that the $H_1(\rho^{-3/2}\Psi) = \rho^{-3/2}H_1(\Psi)$, as H_1 does not contain any operators that would transform the scaled wavefunction.

This result is also true for H_0, albeit less obvious:

$$\begin{aligned} H_{RLM}(\rho^{-3/2}\Psi) &= -\frac{1}{2\mu}\left[\frac{\partial}{\partial\rho}\left(\rho^{-3/2}\frac{\partial\Psi}{\partial\rho} - \frac{3\Psi}{2}\rho^{-5/2}\right) + \frac{3}{\rho}\left(\rho^{-3/2}\frac{\partial\Psi}{\partial\rho} - \frac{3\Psi}{2}\rho^{-5/2}\right)\right] \\ &= -\frac{1}{2\mu}[\rho^{-3/2}\frac{\partial^2\Psi}{\partial\rho^2} + \frac{\partial\Psi}{\partial\rho}\left(\frac{-3}{2}\rho^{-5/2}\right) - \left(\frac{-3\Psi}{2}\left(\frac{-5}{2}\rho^{-7/2}\right)\rho^{-5/2}\frac{3\partial\Psi}{2\partial\rho}\right) + \\ &+ \frac{3}{\rho}\left(\rho^{-3/2}\frac{\partial\Psi}{\partial\rho} - \frac{3\Psi}{2}\rho^{-5/2}\right)] \\ &= -\frac{1}{2\mu}\left[\rho^{-3/2}\frac{\partial^2\Psi}{\partial\rho^2} + \Psi\left(\frac{15}{4}\rho^{-7/2} - \frac{9}{2}\rho^{-7/2}\right)\right] \\ &= -\frac{1}{2\mu}\left[\rho^{-3/2}\frac{\partial^2\Psi}{\partial\rho^2} - \frac{3}{4}\rho^{-7/2}\right] \\ &= -\frac{1}{2\mu}\left[\rho^{-3/2}\right]\Psi. \end{aligned}$$

Appendix B

Acronym definitions

BCRLM	Bending corrected rotating linear model
BO	Born-Oppenheimer
BP	Breit-Pauli
BSE	Basis set extrapolation
CVT	Canonical variational transition state theory
CC	Coupled channel
CEQ	Colinear exact quantum
CEQB	Colinear exact quantum with bending corrections
CRP	Cumulative reaction probability
CS	Coupled states
DOF	Degrees of freedom
DVR	Discrete variable representation
HO	Harmonic oscillator
IRC	Intrinsic reaction coordinate
ISS	Initial state selected
KIE	Kinetic isotope effect

PES	Potential energy surface
PIB	Particle in a box
QCT	Quasi-classical trajectory
RBU	Rotating bond umbrella
RD	Reduced dimensionality
RDEQ	Reduced dimensionality exact quantum
RLA	Rotating line approximation
RLM	Rotating linear model
RLU	Rotating line umbrella approximation
SCT	Small curvature tunnelling corrections
SO	Spin-orbit
SOC	Spin-orbit coupling
SPE	Single point energy
TD	Time-dependent
TI	Time-independent
TRC	Thermal rate constant
TST	Transition state theory
vdW	van der Waals
ZPE	Zero-point energy

References

[1] *Tutorials in Molecular Reaction Dynamics*; Brouard, M.; Vallance, C., Eds.; Royal Society of Chemistry, 2012.

[2] Henriksen, H. E.; Hansen, F. Y. *Theories of Molecular Reaction Dynamics*; Oxford University Press, 2008.

[3] Manolopoulos, D. E. *Encyclopedia of Computational Chemistry*; John Wiley & Sons, Ltd, 2002.

[4] Althorpe, S. C.; Clary, D. C. *Annu. Rev. Phys. Chem.* **2003**, *54*, 493.

[5] J. Aoiz, F.; Banares, L.; F. Castillo, J.; Menendez, M.; E. Verdasco, J. *Phys. Chem. Chem. Phys.* **1999**, *1*, 1149.

[6] Collepardo-Guevara, R.; Suleimanov, Y. V.; Manolopoulos, D. E. *J. Chem. Phys.* **2009**, *130*, 174713.

[7] Schiffel, G.; Manthe, U. *J. Chem. Phys.* **2010**, *132*, 084103.

[8] Bowman, J. M. *J. Phys. Chem.* **1991**, *95*, 4960.

[9] Kerkeni, B.; Clary, D. C. *Mol. Phys.* **2005**, *103*, 1745.

[10] Kerkeni, B.; Clary, D. C. *Chem. Phys. Lett.* **2007**, *438*, 1.

[11] Kerkeni, B.; Clary, D. C. *J. Phys. Chem. A* **2003**, *107*, 10851.

[12] Kerkeni, B.; Clary, D. C. *J. Chem. Phys.* **2004**, *120*, 2308.

[13] Banks, S. T.; Clary, D. C. *Phys. Chem. Chem. Phys.* **2007**, *9*, 933.

[14] Banks, S. T.; Clary, D. C. *J. Chem. Phys.* **2009**, *130*, 024106.

[15] Banks, S. T.; Tautermann, C. S.; Remmert, S. M.; Clary, D. C. *J. Chem. Phys.* **2009**, *131*, 044111.

[16] Remmert, S. M.; Banks, S. T.; Clary, D. C. *J. Phys. Chem. A* **2009**, *113*, 4255.

[17] Schatz, G. C. In *The Theory of Chemical Reaction Dynamics*; Clary, D., Ed.; D. Reidel Publishing Company: Dordrecht, 1985, p 1.

[18] Bowman, J. M.; Wagner, A. In *The Theory of Chemical Reaction Dynamics*; Clary, D. C., Ed.; D. Riedel Publishing Company: Dordrecht, 1985, p 47.

[19] McGuire, P.; Kouri, D. J. *J. Chem. Phys.* **1974**, *60*, 2488.

[20] Child, M. S. *Mol. Phys.* **1967**, *12*, 401.

[21] Connor, J. N. L.; Child, M. S. *Mol. Phys.* **1970**, *18*, 653.

[22] Wyatt, R. E. *J. Chem. Phys.* **1969**, *51*, 3489.

[23] Walker, R. B.; Hayes, E. F. In *The Theory of Chemical Reaction Dynamics*; Clary, D., Ed.; D. Reidel Publishing Company: Dordrecht, 1985, p 105.

[24] Walker, R. B.; Hayes, E. F. *J. Phys. Chem.* **1983**, *87*, 1255.

[25] Walker, R. B.; Hayes, E. F. *J. Phys. Chem.* **1984**, *88*, 1194.

[26] Bowman, J. M.; Ju, G.-Z.; Lee, K. T. *J. Chem. Phys.* **1981**, *75*, 5199.

[27] Bowman, J. M.; Ju, G. Z.; Lee, K. T. *J. Phys. Chem.* **1982**, *86*, 2232.

[28] Sun, Q.; Bowman, J. M. *J. Chem. Phys.* **1990**, *92*, 5201.

[29] Brooks, A. N.; Clary, D. C. *J. Chem. Phys.* **1990**, *92*, 4178.

[30] Wang, X. et al. *Science* **2008**, *322*, 573.

[31] Alexander, M. H.; Capecchi, G.; Werner, H.-J. *Science* **2002**, *296*, 715.

[32] Balucani, N.; Skouteris, D.; Capozza, G.; Segoloni, E.; Casavecchia, P.; Alexander, M. H.; Capecchi, G.; Werner, H.-J. *Phys. Chem. Chem. Phys.* **2004**, *6*, 5007.

[33] Alexander, M. H.; Capecchi, G.; Werner, H.-J. *Faraday Discuss.* **2004**, *127*, 59.

[34] Capecchi, G.; Werner, H.-J. *Phys. Chem. Chem. Phys.* **2004**, *6*, 4975.

[35] Balucani, N.; Skouteris, D.; Cartechini, L.; Capozza, G.; Segoloni, E.; Casavecchia, P.; Alexander, M. H.; Capecchi, G.; Werner, H.-J. *Phys. Rev. Lett.* **2003**, *91*, 013201.

[36] Liu, K. *Annu. Rev. Phys. Chem.* **2001**, *52*, 139.

[37] Whiteley, T. W. J.; Dobbyn, A. J.; Connor, J. N. L.; Schatz, G. C. *Phys. Chem. Chem. Phys.* **2000**, *2*, 549.

[38] Alexander, M. H.; Manolopoulos, D. E.; Werner, H.-J. *J. Chem. Phys.* **2000**, *113*, 11084.

[39] Tzeng, Y.-R.; Alexander, M. H. *J. Chem. Phys.* **2004**, *121*, 5812.

[40] Alexander, M. H.; Werner, H.-J.; Manolopoulos, D. E. *J. Chem. Phys.* **1998**, *109*, 5710.

[41] Maierle, C. S.; Schatz, G. C.; Gordon, M. S.; McCabe, P.; Connor, J. N. L. *J. Chem. Soc., Faraday Trans.* **1997**, *93*, 709.

[42] Mielke, S. L.; Truhlar, D. G.; Schwenke, D. W. *J. Phys. Chem.* **1995**, *99*, 16210.

[43] Takayanagi, T.; Kurosaki, Y. *J. Chem. Phys.* **2000**, *113*, 7158.

[44] Lepetit, B.; Launay, J. M.; Dourneuf, M. L. *Chem. Phys.* **1986**, *106*, 103.

[45] Lepetit, B.; Launay, J. M.; Dourneuf, M. L. *Chem. Phys.* **1986**, *106*, 111.

[46] Yagi, K.; Takayanagi, T.; Taketsugu, T.; Hirao, K. *J. Chem. Phys.* **2004**, *120*, 10395.

[47] Jasper, A. W.; Zhu, C.; Nangia, S.; Truhlar, D. G. *Faraday Discuss.* **2004**, *127*, 1.

[48] Hickman, A. P. *Int. Rev. Phys. Chem.* **1997**, *16*, 177.

[49] Aquilanti, V.; Cavalli, S.; De Fazio, D.; Volpi, A. *Int. J. Quantum Chem.* **2001**, *85*, 368.

[50] Janssen, L. *Master's Thesis*, University of Oxford, Radboud University Nijmegen, 2007.

[51] Palma, J.; Clary, D. C. *J. Chem. Phys.* **2000**, *112*, 1859.

[52] Romelt, J. In *The Theory of Chemical Reaction Dynamics*; Clary, D. C., Ed.; D. Riedel Publishing Company: Dordrecht, 1985, p 77.

[53] Muckerman, J. T. *Chem. Phys. Lett.* **1990**, *173*, 200.

[54] Colbert, D. T.; Miller, W. H. *J. Chem. Phys.* **1992**, *96*, 1982.

[55] Stechel, E.; Walker, R. B.; Light, J. C. *J. Chem. Phys.* **1978**, *69*, 3518.

[56] Lepetit, B.; Launay, J. M.; Le Dourneuf, M.; Gadéa, F. X. *Chem. Phys.* **1987**, *117*, 17.

[57] Light, J. C.; Walker, R. B.; Stechel, E. B.; Schmalz, T. G. *Comp. Phys. Comm.* **1979**, *17*, 89.

[58] Römelt, J. *Chem. Phys. Lett.* **1980**, *74*, 263.

[59] Nyman, G.; Yu, H.-G.; Walker, R. B. *J. Chem. Phys.* **1998**, *109*, 5896.

[60] Clary, D. C. *J. Chem. Phys.* **1991**, *95*, 7298.

[61] Frisch, M. J. et al. *Gaussian 03, Revision C.02*, Gaussian, Inc., Wallingford, CT, 2004.

[62] Werner, H.-J. et al. *MOLPRO, version 2008.3, a package of ab initio programs*, 2008.

[63] *Matlab, version 7.1.0.183 (R14) Service Pack 3*, 2007.

[64] McQuarrie, D. A.; Simon, J. D. *Physical Chemistry: A Molecular Approach*; University Science Books, 1997.

[65] Ochterski, J. W. *Vibrational Analysis in Gaussian [White paper]*, 1999.

[66] Lu, D. H.; Truhlar, D. G. *J. Chem. Phys.* **1993**, *99*, 2723.

[67] Berning, A.; Schwiezer, M.; Werner, H.-J.; Knowles, P. J.; Palmieri, P. *Mol. Phys.* **2000**, *98*, 1823.

[68] Fedorov, D. G.; Koseki, S.; Schmidt, M. W.; Gordon, M. S. *Int. Rev. Phys. Chem.* **2003**, *22*, 551.

[69] Marian, C. M. *Rev. Comput. Chem.* **2001**, *17*, 99.

[70] *European Summerschool in Quantum Chemistry*; Widmark, P.-O., Ed.; Lund University, 2009, pp 547–567.

[71] Bearkpark, M. J.; Handy, N. C.; Palmieri, P.; Tarroni, R. *Mol. Phys.* **1993**, *80*, 479.

[72] Stanton, A. C. *Chem. Phys. Lett.* **1985**, *122*, 385.

[73] Bowman, J. M. *Theor. Chem. Acc.* **2002**, *108*, 125.

[74] Bowman, J. M. In *Reaction and molecular dynamics: proceedings of the European School on Computational Chemistry*; Lagana, A., Ed.; Springer, 1999, p 101.

[75] Maczek, A. *Statistical Thermodynamics (Oxford Chemistry Primers, No 58)*; Oxford University Press, 1998.

[76] Brouard, M. *Reaction Dynamics (Oxford Chemistry Primers, No 61)*; Oxford University Press, 1998.

[77] Child, M. S. *Molecular Collision Theory*; Dover Publications, Inc., 1974.

[78] Levine, R. D.; Bernstein, R. B. *Molecular Reaction Dynamics and Chemical Reactivity*; Oxford University Press, 1987.

[79] Skodje, R. T.; Skouteris, D.; Manolopoulos, D. E.; Lee, S.-H.; Dong, F.; Liu, K. *J. Chem. Phys.* **2000**, *112*, 4536.

[80] Chao, S. D.; Skodje, R. T. *J. Chem. Phys.* **2003**, *119*, 1462.

[81] Castillo, J. F.; Manolopoulos, D. E.; Stark, K.; Werner, H.-J. *J. Chem. Phys.* **1996**, *104*, 6531.

[82] Cavalli, S.; Fazio, D. D. *Phys. Scr.* **2007**, *76*, C21.

[83] Manolopoulos, D. E. *J. Chem. Soc., Faraday Trans.* **1997**, *93*, 673.

[84] Smith, F. T. *Phys. Rev.* **1960**, *118*, 349.

[85] Back, M. H.; Back, R. A. *Pyrolisis: Theory and Industrial Practice*; Academic Press, Inc., 1983.

[86] Kungwan, N.; Truong, T. N. *J. Phys. Chem. A* **2005**, *109*, 7742.

[87] McNesby, J.; Gordon, A. *J. Am. Chem. Soc.* **1954**, *76*, 4196.

[88] Derwish, G.; Galli, A.; Giardini-Guidoni, A.; Volpi, G. *J Chem. Phys.* **1964**, *40*, 5.

[89] Dainton, F.; McElcheran, D. *Trans. Faraday Soc.* **1955**, *51*, 657.

[90] Dainton, F.; Ivin, K.; Wilkinson, F. *Spec. Publ. - Chem. Soc.* **1958**, *9*, 187.

[91] Dainton, F.; Ivin, K.; Wilkinson, F. *Trans. Faraday Soc.* **1959**, *55*, 929.

[92] Kerr, J.; Parsonage, M. *Evaluated Kinetic Data on Gas Phase Hydrogen Transfer Reactions of Methyl Radicals*; Butterworths: London, 1976.

[93] Arthur, N.; Bell, T. *Rev. Chem. Intermed.* **1978**, *2*, 37.

[94] Canadell, E.; Olivella, S.; Poblet, J. M. *J. Phys. Chem.* **1984**, *88*, 3545.

[95] Chandra, A. K.; Malar, E. P.; Gupta, D. S. *Int. J. Quantum Chem.* **1992**, *41*, 371.

[96] Fradera, X.; Duran, M.; Mestres, J. *Can. J. Chem.* **2000**, *78*, 328.

[97] Gillion, R. D. *J. Comput. Chem.* **1984**, *5*, 237.

[98] Jursic, B. S. *Chem. Phys. Lett.* **1995**, *244*, 263.

[99] Litwinowicz, J.; Ewing, D.; Jurisevic, S. *J. Phys. Chem.* **1995**, *99*, 9709.

[100] Mestres, J.; Duran, M.; Bertran, J. *Can. J. Chem.* **1996**, *74*, 1253.

[101] Pederson, M. R. *Chem. Phys. Lett.* **1994**, *230*, 54.

[102] Jayatilaka, D.; Lee, T. J. *J. Chem. Phys.* **1993**, *98*, 9734.

[103] Lee, T. J.; Rice, J. E.; Scuseria, G. E.; Schaefer, H. F. I. *Theor. Chim. Acta* **1989**, *75*, 81.

[104] Hernandez, M. I.; Campos-Martinez, J.; Villarreal, P.; Schmatz, S.; Clary, D. C. *Phys. Chem. Chem. Phys.* **1999**, *1*, 1197.

[105] Aquilanti, V. In *The Theory of Chemical Reaction Dynamics*; Clary, D. C., Ed.; D. Reidel Publishing Company: Dordrecht, 1985, p 383.

[106] Clary, D. C.; Connor, J. N. L. *Chem. Phys. Lett.* **1983**, *94*, 81.

[107] Schatz, G. C.; Sokolovski, D.; Connor, J. N. L. *Faraday Discuss. Chem. Soc.* **1991**, *91*, 17.

[108] Creak, G. A.; Dainton, F. S.; Ivin, K. J. *Trans. Faraday Soc.* **1962**, *58*, 326.

[109] Douglass, A. R.; Schoeberl, M. R.; Stolarski, R. S.; Waters, J.; Russell, J. M.; Roche, A. E.; Massie, S. T. *J. Geophys. Res.* **1995**, *100*, 13967.

[110] Michelsen, H. A.; Webster, C.; Manney, G.; Scott, D.; Margitan, J.; May, R.; Irion, R.; Gunson, M.; Russell, J.; Spivarkovsky, C. *J. Geophys. Res.* **1999**, *104*, 26419.

[111] Sanee, M.; Froidevaux, L.; Manney, G.; Read, W.; Waters, J.; Chipperfield, M.; Roche, A.; Kumer, J.; Mergenthaler, J.; Rusell, J. *J. Geophys. Res.* **1996**, *101*, 18835.

[112] Prather, M.; Jaffe, A. H. *J. Geophys. Res.* **1990**, *95*, 3473.

[113] Tanaka, N.; Xiao, Y.; Lasaga, A. C. *J. Atmos. Chem.* **1996**, *23*, 37.

[114] Wu, Y.; Lin, Y.-F. *Combust. Flame* **2004**, *137*, 376.

[115] Retail, B.; Pearce, J. K.; Greaves, S. J.; Rose, R. A.; Orr-Ewing, A. J. *J. Chem. Phys.* **2008**, *128*, 184303.

[116] Retail, B.; Pearce, J. K.; Murray, C.; Orr-Ewing, A. J. *J. Chem. Phys.* **2005**, *122*, 101101.

[117] Retail, B.; Greaves, S. J.; Pearce, J. K.; Rose, R. A.; Orr-Ewing, A. J. *Phys. Chem. Chem. Phys.* **2007**, *9*, 3261.

[118] Rose, R. A.; Greaves, S. J.; Orr-Ewing, A. J. *Mol. Phys.* **2010**, *108*, 981.

[119] Rangel, C.; Navarrete, M.; Corchado, J. C.; Espinosa-García, J. *J. Chem. Phys.* **2006**, *124*, 124306.

[120] Truong, T. N.; Truhlar, D. G.; Baldridge, K. K.; Gordon, M. S.; Steckler, R. *J. Chem. Phys.* **1989**, *90*, 7137.

[121] Troya, D.; Millán, J.; Banos, I.; González, M. *J. Chem. Phys.* **2002**, *117*, 5730.

[122] Duncan, W. T.; Truong, T. N. *J. Chem. Phys.* **1995**, *103*, 9642.

[123] Castillo, J. F.; Aoiz, F. J.; Banares, L. *J. Chem. Phys.* **2006**, *125*, 124316.

[124] Zhou, Z.; Chen, G.; Zhou, X.; Fu, H. *Int. J. Quantum Chem.* **2002**, *87*, 49.

[125] Yang, M.; Yang, C.-L.; Chen, J.; Zhang, Q. *Chem. Phys.* **2008**, *354*, 180.

[126] Michelsen, H. A. *Acc. Chem. Res.* **2001**, *34*, 331.

[127] Simpson, W. R.; Rakitzis, T. P.; Kandel, S. A.; Lev-On, T.; Zare, R. N. *J. Phys. Chem.* **1996**, *100*, 7938.

[128] Wang, X.; Ben-Nun, M.; Levine, R. *Chem. Phys.* **1995**, *197*, 1.

[129] Martínez, R.; González, M.; Defazio, P.; Petrongolo, C. *J. Chem. Phys.* **2007**, *127*, 104302.

[130] Troya, D.; Weiss, P. J. E. *J. Chem. Phys.* **2006**, *124*, 074313.

[131] Klos, J. *Chem. Phys. Lett.* **2002**, *359*, 309.

[132] Yu, H.-G.; Nyman, G. *J. Chem. Phys.* **1999**, *111*, 6693.

[133] Garcia, E.; Sanchez, C.; Saracibar, A.; Lagana, A. *J. Phys. Chem. A* **2004**, *108*, 8752.

[134] Rudić, S.; Murray, C.; Harvey, J. N.; Orr-Ewing, A. J. *J. Chem. Phys.* **2004**, *120*, 186.

[135] Espinosa-Garcia, J.; Corchado, J. C. *J. Chem. Phys.* **1996**, *105*, 3517.

[136] Corchado, J. C.; Truhlar, D. G.; Espinosa-Garcia, J. *J. Chem. Phys.* **2000**, *112*, 9375.

[137] Garcia, E.; Sánchez, C.; Rodríguez, A.; Laganà, A. *Int. J. Quantum Chem.* **2006**, *106*, 623.

[138] Teslja, A.; Valentini, J. J. *J. Chem. Phys.* **2006**, *125*, 132304.

[139] Orr-Ewing, A. J.; Simpson, W. R.; Rakitzis, T. P.; Kandel, S. A.; Zare, R. N. *J. Chem. Phys.* **1997**, *106*, 5961.

[140] Nyman, G.; Zhou, J.; Zhang, B.; Liu, K. *Isr. J. Chem.* **2007**, *47*, 1.

[141] Zhou, J.; Zhang, B.; Lin, J. J.; Liu, K. *Mol. Phys.* **2005**, *103*, 1757.

[142] Yu, H.-G.; Nyman, G. *J. Chem. Phys.* **1999**, *110*, 7233.

[143] Espinosa-Garcia, J. *J. Phys. Chem. A* **2007**, *111*, 9654.

[144] Sansón, J.; Corchado, J. C.; Rangel, C.; Espinosa-Garcia, J. *J. Chem. Phys.* **2006**, *124*, 074312.

[145] Sanson, J.; Corchado, J.; Rangel, C.; Espinosa-Garcia, J. *J. Phys. Chem. A* **2006**, *110*, 9568.

[146] Skokov, S.; Bowman, J. M. *J. Chem. Phys.* **2000**, *113*, 4495.

[147] Yu, H.-G.; Nyman, G. *Phys. Chem. Chem. Phys.* **1998**, *1*, 1181.

[148] Seeley, J. V.; Jayne, J. T.; Molina, M. J. *J. Phys. Chem.* **1996**, *100*, 4019.

[149] Takahashi, K.; Yamamoto, O.; Inomata, T. *Proc. Combust. Inst.* **2002**, *29*, 2447.

[150] Zahniser, M. S.; Berquist, B. M.; Kaufman, F. *Int. J. Chem. Kinet.* **1978**, *10*, 15.

[151] Bryukov, M. G.; Slagle, I. R.; Knyazev, V. D. *J. Phys. Chem. A* **2002**, *106*, 10532.

[152] Pilgrim, J. S.; McIlroy, A.; Taatjes, C. A. *J. Phys. Chem. A* **1997**, *101*, 1873.

[153] Pohjonen, M.-L.; Koskikallio, J. *Acta Chem. Scand.* **1979**, *33*, 449.

[154] Russell, J. J.; Seetula, J. A.; Senkan, S. M.; Gutman, D. *Int. J. Chem. Kinet.* **1988**, *20*, 759.

[155] Eskola, A. J.; Seetula, J. A.; Timonen, R. S. *Chem. Phys.* **2006**, *331*, 26.

[156] Michelsen, H. A.; Simpson, W. R. *J. Phys. Chem. A* **2001**, *105*, 1476.

[157] Roberto-Neto, O.; Coitino, E. L.; Truhlar, D. *J. Phys. Chem. A* **1998**, *102*, 4568.

[158] Martinez-Nunez, E.; Fernandez-Ramos, A.; Vazquez, S. A.; Rios, M. A. *Chem. Phys. Lett.* **2002**, *360*, 59.

[159] Simpson, W. R.; Rakitzis, T. P.; Kandel, S. A.; Orr-Ewing, A. J.; Zare, R. N. *J. Chem. Phys.* **1995**, *103*, 7313.

[160] Kim, Z. H.; Bechtel, H. A.; Camden, J. P.; Zare, R. N. *J. Chem. Phys.* **2005**, *122*, 084303.

[161] Kandel, S. A.; Zare, R. N. *J. Chem. Phys.* **1998**, *109*, 9719.

[162] Zhou, J.; Lin, J. J.; Zhang, B.; Liu, K. *J. Phys. Chem. A* **2004**, *108*, 7832.

[163] Zhang, B.; Liu, K. *J. Chem. Phys.* **2005**, *122*, 101102.

[164] Yan, S.; Wu, Y.-T.; Zhang, B.; Yue, X.-F.; Liu, K. *Science* **2007**, *316*, 1723.

[165] Yan, S.; Wu, Y.-T.; Liu, K. *PNAS* **2008**, *105*, 12667.

[166] Wu, Y.-T.; Liu, K. *J. Chem. Phys.* **2008**, *129*, 154302.

[167] Kawamata, H.; Tauro, S.; Liu, K. *Phys. Chem. Chem. Phys.* **2008**, *10*, 4378.

[168] Feller, D. J. *Comp. Chem.* **1996**, *17*, 1571–1586.

[169] Schuchardt, K.; Didier, B.; Elsethagen, T.; Sun, L.; Gurumoorthi, V.; Chase, J.and Li, J.; Windus, T. *J. Chem. Inf. Model* **2007**, *47*, 1045–1052.

[170] Truhlar, D. G. *Chem. Phys. Lett.* **1998**, *294*, 45.

[171] Halkier, A.; Helgaker, T.; Jørgensen, P.; Klopper, W.; Koch, H.; Olsen, J.; Wilson, A. K. *Chem. Phys. Lett.* **1998**, *286*, 243.

[172] *CRC Handbook of Chemistry and Physics, 78th ed.*; CRC Press, Inc.: Boca Raton, FL., 1998.

[173] *ANAF Thermochemical Tables, 3rd Ed.*; Jr, M. C.; Davies, C. A.; Jr., J. D.; Frurip, D.; McDonald, R., Eds.; Natl. Stand. Ref. Data Ser. Natl. Bur. Stand, Vol 14., 1985.

[174] Clary, D. C. *J. Phys. Chem.* **1994**, *98*, 10678.

[175] Ohsaki, A.; Nakamura, H. *Phys. Rep.* **1990**, *187*, 1.

[176] Li, G.; Hwang, H. J.; Jung, H. C. *Rev. Sci. Instrum.* **2005**, *76*, 023105.

[177] Tautermann, C. S.; Clary, D. C. *J. Chem. Phys.* **2005**, *122*, 134702.